Quantum States Engineering in Graphene Nanoribbons



Fanmiao Kong

Trinity College

University of Oxford

Supervisor: Prof. Lapo Bogani

A thesis submitted for the degree of

Doctor of Philosophy

Trinity 2023

Abstract

The new upcoming generation of quantum devices requires the creation of solid state systems that display prominent quantum properties. This search, which is intensifying, has allowed identifying excellent quantum systems in molecular magnets, defect centres, low-dimensional materials, among others. Most efforts are directed towards systems produced with a top-down approach, e.g. by exfoliation or shaping of two-dimensional materials. This, however, prevents achieving the precise atom-by-atom control of the morphology that is usually necessary for topological and quantum properties to emerge distinctively in experiments.

One class of systems that holds the promise of overcoming many present difficulties are graphene nanoribbons (GNRs) made by molecular synthesis. GNRs display a graphitic backbone, whose edges, terminations, and morphology can all be altered synthetically, with atomic precision, thus changing the electronic, optical, and magnetic properties. Synthesis of these systems is booming, as new pathways for the bottom-up synthesis of novel systems are reported frequently. At the same time, new theoretical developments now allow understanding that GNRs can also display non-trivial topologies. On the other hand, their quantum behaviour, and the relationship with theoretically-predicted topological and quantum properties remain largely unexplored.

In this thesis I present a theoretical and experimental investigation of molecular GNRs, integrating computation and experiments, so as to unravel the interplay between morphology and quantum properties. The focus of my thesis lies on their electronic properties, with attention to topological phases, quantum spin, and vibrational states.

The development of theoretical methods and programs for numerical calculations allowed classifying and understanding the topological phases in GNRs, and we could use these tools to design novel structures exhibiting distinct topological phases, and directly suggest innovative applications for topological states. Most importantly, we could relate the topological properties to some of the old rules concerning the stability of aromatic compounds, producing a direct connection between modern theoretical physics and the very empirical, rule-of-thumb guidelines developed at the organic synthesis hoods in the 1970s. We also find that dissipationless transport becomes possible, under certain conditions, and that different compounds known since decades, such as fused porphyrin tapes, can display interesting topological states.

As the quantum properties are most evident in spin states, we first investigate theoretically how topology can influence them. Then we investigate experimentally, using pulsed EPR techniques, two types of spin centres introduced through external functionalisation groups in GNRs.

In the final part we examine two ways of probing directly the electronic states: through optical spectroscopy and through electron transport in devices. We show how, in both cases, the vibrational states are fundamental, and we can identify unambiguously their role in ultra-clean quantum transport devices at millikelvin temperatures and in optical spectra. We extract the electron–phonon coupling strength and offer a unified vision, which could set the interpretative basis for both transport and optical measurements.

Contents

List of Figures **ix**

1 Motivation **1**

2 Background **9**

2.1 Electronic structure of GNRs 9

2.1.1 Armchair and zigzag GNRs 10

2.1.2 The emergence of edge states 16

2.1.2.1 Understanding the origin of edge states 16

2.1.2.2 Edge states in general GNRs 19

2.1.2.3 Applications of edge states 20

2.1.2.4 Experimental realisations of edge states 21

2.1.3 Tuning electronic properties by structure modification 23

2.1.3.1 Modifying backbone structure and width 23

2.1.3.2 Doping and edge decoration 25

2.1.3.3 Heterostructures 27

2.1.4 The effect of finite length 29

2.2 Band topology of GNRs 33

2.2.1 The arise of topology in condensed matter 33

2.2.2 Topological classification of GNRs 42

2.2.3 Experimental verification 48

2.2.4 Topology in quantum spin chains 53

2.3 Spin states in GNRs 55

2.3.1 Spin qubits and spin relaxation 55

2.3.2 Quantum properties of electron spins in GNRs 58

2.3.3 Incorporating spin states into GNRs 61

2.4 Vibrational properties of GNRs 66

3 Methods **71**

3.1 Theoretical methods 71

3.1.1 Tight-binding model 71

3.1.2 DFT 77

3.1.3 Topology . . . 83
3.1.4 Wannier functions . . . 86
3.2 Experimental methods . . . 89
3.2.1 EPR spectroscopy . . . 89
3.2.1.1 CW EPR . . . 90
3.2.1.2 Pulsed EPR . . . 92
3.2.2 Single-molecule transistor . . . 101
3.2.3 Optical spectroscopy . . . 105
3.2.3.1 Photoluminescence spectroscopy . . . 105
3.2.3.2 Raman spectroscopy . . . 108

4 Topological States in GNRs 111
4.1 Introduction . . . 111
4.2 Designing topologically nontrivial GNRs . . . 113
4.2.1 Tuning the topology via unit-cell design . . . 120
4.2.2 Tuning the topology via connection between unit cells . . . 123
4.2.3 Topology at different energy gaps . . . 127
4.3 Relationship between $\mathbb{Z}$ topology and Clar's sextet rule . . . 131
4.3.1 Relationship between $\mathbb{Z}$ index and Wannier functions . . . 131
4.3.2 $\mathbb{Z}$ index, Wannier functions, and Clar's sextet rule . . . 136
4.4 Topology in porphyrin nanoribbons . . . 147
4.5 Dissipationless transport channels in beard–zigzag GNRs . . . 155
4.6 Summary and outlook . . . 161
4.7 Project overview . . . 163

5 Spin States and Quantum Coherence in GNRs 165
5.1 Introduction . . . 165
5.2 Spin states and topological phase . . . 166
5.3 Spin states from functionalisation groups . . . 177
5.3.1 Cyano functionalisation . . . 178
5.3.2 Vanadyl-porphyrin functionalisation . . . 187
5.4 Summary and outlook . . . 194
5.5 Project overview . . . 195

6 Interplay between Electronic States and Phonons in GNRs 197
6.1 Introduction . . . 197
6.2 Manifestation of vibrational states in single-molecule transport . . . 199
6.2.1 Comparison of GNRs with different solubilities . . . 199
6.2.2 Signature of vibrational modes in stability diagrams . . . 202
6.3 Manifestation of vibrational states in optical spectra . . . 208

6.3.1 Band structure analysis 209
6.3.2 Vibrational and optical properties 214
6.4 Summary and outlook 224
6.5 Project overview 226

7 Conclusions **227**

8 Appendix **235**

References **243**

List of Figures

1.1 Different ways of quantum states engineering in bottom-up synthesised graphene nanoribbons 2

2.1 Graphene lattice and its band structure 10
2.2 GNRs with different edge shapes 11
2.3 Schematic structure of AGNR and ZGNR 11
2.4 Approximation of 5-AGNR's band structure by zone-folding 12
2.5 Band structure of three types of AGNRs 13
2.6 The band gap of AGNRs versus ribbon width 14
2.7 Band structure of 12-ZGNR and magnetic edge states 15
2.8 Band gap calculated from DFT versus GW approximation 16
2.9 Magnetic interaction strength between edge states versus ZGNR width 18
2.10 Edge states of chiral GNRs. 19
2.11 Experimental verification of edge states in ZGNRs 22
2.12 Designing GNRs with different backbone structures and widths . . . 23
2.13 Band-gap engineering of chevron GNRs by different dopants 26
2.14 Heterojunction built from pristine and N-doped chevron GNR 28
2.15 Energy levels of finite 5-AGNRs as a function of ribbon length . . . 30
2.16 Zigzag end states in finite 7-AGNRs 31
2.17 Zigzag end states of 7-AGNR with different lengths 32
2.18 Quantum Hall effect 34
2.19 Torus surfaces with different genus 36
2.20 Edge modes in quantum Hall and quantum spin Hall state 39
2.21 Structural representation of SSH model 43
2.22 SSH model in topologically distinct phases 43
2.23 Winding number of the SSH model 44
2.24 Interface between topologically equivalent and distinct GNRs 46
2.25 Chiral-phase index of AGNRs 48
2.26 Experimental verification of topological states by STM 49
2.27 Probing the magnetic nature of topological states by STM 51
2.28 Excitonic emission from topological end states 52
2.29 Topological phase in triangulene spin chains 54

2.30 Quantum units from tailoring the graphene 59
2.31 Different strategies of incorporating spin states in GNRs 63
2.32 Mapping of the fundamental modes and overtones of ZGNR and AGNR onto graphene's phonon dispersion 67
2.33 RBLM and LCM of GNRs 68

3.1 Fat bands, Bloch function, and Wannier function 87
3.2 Principle of CW EPR for $S = 1/2$ 91
3.3 Hyperfine splitting in an EPR spectrum for $S = 1/2$, $I = 1/2$. 93
3.4 Pictorial representation of the transformation of spin angular momentum operators 96
3.5 Hahn echo pulse sequence and related measurements 98
3.6 Picket-fence pulse sequence and T_1 measurement 99
3.7 HYSCORE technique 100
3.8 Charge transport through a single molecule 103
3.9 Single-molecule device and dilution fridge 105
3.10 Optical absorption and emission 106
3.11 Rayleigh scattering and Raman scattering 109

4.1 Topological classification of GNR **1**–**6** 115
4.2 LDOS of GNR **1**–**6** at the bulk cell and the end cell 117
4.3 Fat bands and Wannier-interpolated bands of GNR **2** 118
4.4 Maximally localised Wannier functions of GNR **2** 119
4.5 Wannier centres of GNR **1**–**6** 120
4.6 GNR **2** and a derivative of it with the same bulk structure but different end terminations 121
4.7 Tuning GNR topology by changing the unit cell 122
4.8 Tuning GNR topology by changing connection between unit cell . . 124
4.9 Distinct topological phases of GNR **4a** with different connections. . 126
4.10 Distinct topological phases in different energy gaps. 128
4.11 More examples of distinct topological phases in different energy gaps 129
4.12 Three different unit cells of 7-AGNR with different $\mathbb{Z}$ indices 132
4.13 Wannier functions of a 7-AGNR 134
4.14 $\mathbb{Z}$ indices, Wannier functions, and Clar's sextets of different 7-AGNR unit cells 137
4.15 Structural models of 7-AGNRs with maximum and non-maximum number of Clar's sextets 138
4.16 $\mathbb{Z}$ indices, Wannier functions, and Clar's sextets in other AGNR examples 139

4.17 Three different configurations of Wannier funtions that correspond to the same Clar's sextet 140
4.18 $\mathbb{Z}$ index and Clar's sextet of AGNRs 141
4.19 Ambiguity of topological phases in 8-AGNRs 143
4.20 Pattern of the most densely packed Clar's sextets 145
4.21 Relationship between $\mathbb{Z}$ indices, Wannier functions, and Clar's sextets for GNR **3** and its derivatives 146
4.22 Structure of porphyrin 148
4.23 Fat bands and projected density of states (PDOS) of a fused Zn-porphyrin nanoribbon 149
4.24 Three end states of a fused Zn-porphyrin nanoribbon 150
4.25 Energy levels and end states of finite Zn-porphyrin nanoribbons . . 151
4.26 Double SSH-chain model 153
4.27 Chiral dissipationless modes in beard–zigzag GNRs with transverse electric fields 157
4.28 Dependence of the ZEB on the electric field and ribbon width 159
4.29 Chiral dissipationless modes in cove–zigzag GNRs with transverse electric field 160

5.1 Spin-polarised topological end states in GNR **4a** 169
5.2 Spin-polarised topological end states in 8-AGNR 171
5.3 Clar's sextet rule and spin polarised states in periacenes 173
5.4 Peri-tetracene and 8-AGNR synthesised in solution phase 175
5.5 EPR spectra, spin–lattice relaxation time, and spin coherence time of peri-tetracene molecule 176
5.6 Spin density and band structure of GNR-CN 179
5.7 EPR Spectra, T_1, and T_m of GNR-Br and GNR-CN powders 180
5.8 HYSCORE spectrum of GNR-CN power sample 184
5.9 EPR spectrum, T_1, and T_m of GNR-CN solution sample 185
5.10 Structure and spin density of GNR-VO 188
5.11 EPR spectra, T_1, T_m of GNR-VO powder and solution samples . . . 190
5.12 HYSCORE spectra of the GNR state and the VO state of GNR-VO 191
5.13 Comparison of T_1 and T_m of the VO states in GNR-VO and vanadyl porphyrin 193

6.1 Structure of cove-edge GNRs and single-molecule device 200
6.2 Stability diagrams of the devices fabricated using GNRs with alkyl and bulky groups 201
6.3 Signatures of electron–phonon coupling in single-molecule measurements on GNR-AOM 203

6.4 Transverse bending mode of cove-edge GNR 206
6.5 Transverse bending mode of cove-edge GNRs with different side groups 207
6.6 Band structure and projected DOS of GNR-AOM 210
6.7 Valley mixing and twilight states 211
6.8 Band unfolding of a (6,6) carbon nanotube 212
6.9 Band unfolding of a cove-edge GNR 213
6.10 Photoluminescence and absorption spectra of GNR-alkyl and GNR-AOM 215
6.11 Raman spectrum of GNR-AOM 217
6.12 Photoluminescence and absorption spectra of GNR-AOM fitted with the Franck–Condon model 218
6.13 Electron–phonon coupling in optical transitions, temperature dependence and temporal evolution of PL 219
6.14 Photoluminescence excitation (PLE) spectra of GNR-AOM 222
6.15 Temperature dependence of ZPL position and FWHM 223

8.1 Nontrivial topology in an alternative unit cell of GNR **5** 236
8.2 Distinct topological phases of GNR **5a** with different connections. . 237
8.3 Band structures of fused nanoribbons from pristine porphyrin and N2O2-porphyrin 238
8.4 HYSCORE spectra of VO state of GNR-VO powder sample 238

1 Motivation

Graphene, a single layer of carbon atoms where electrons behave as relativistic particles, provides a fascinating platform for both investigating fundamental physics and designing innovative materials and devices. Discovered nearly two decades ago [1], graphene is known for its exceptional properties, including high carrier mobility, superior mechanical strength, remarkable flexibility, excellent thermal conductivity, and large surface area [2]. These unique characteristics have paved the way for its applications in a variety of sectors, such as sensors [3], energy harvesting [4], energy storage [5], photonics [6], and spintronics [7]. The gapless feature of graphene, however, poses a hurdle for the development of one of the key components of today's electronics: the transistor. One possible way to overcome this is by structuring graphene into long and thin strips, known as nanoribbons, where lateral confinement induces a band gap. This allows us to use graphene nanoribbons (GNRs) for semiconductor electronics. Meanwhile, owing to graphene's inherent properties and quantum confinement effects, GNRs can showcase extremely rich physics, leading to a plethora of intriguing properties that can be exploited in devices. Long before the experimental discovery of graphene, theoretical studies on GNRs had already commenced. In 1996, the dependence of the band gap on

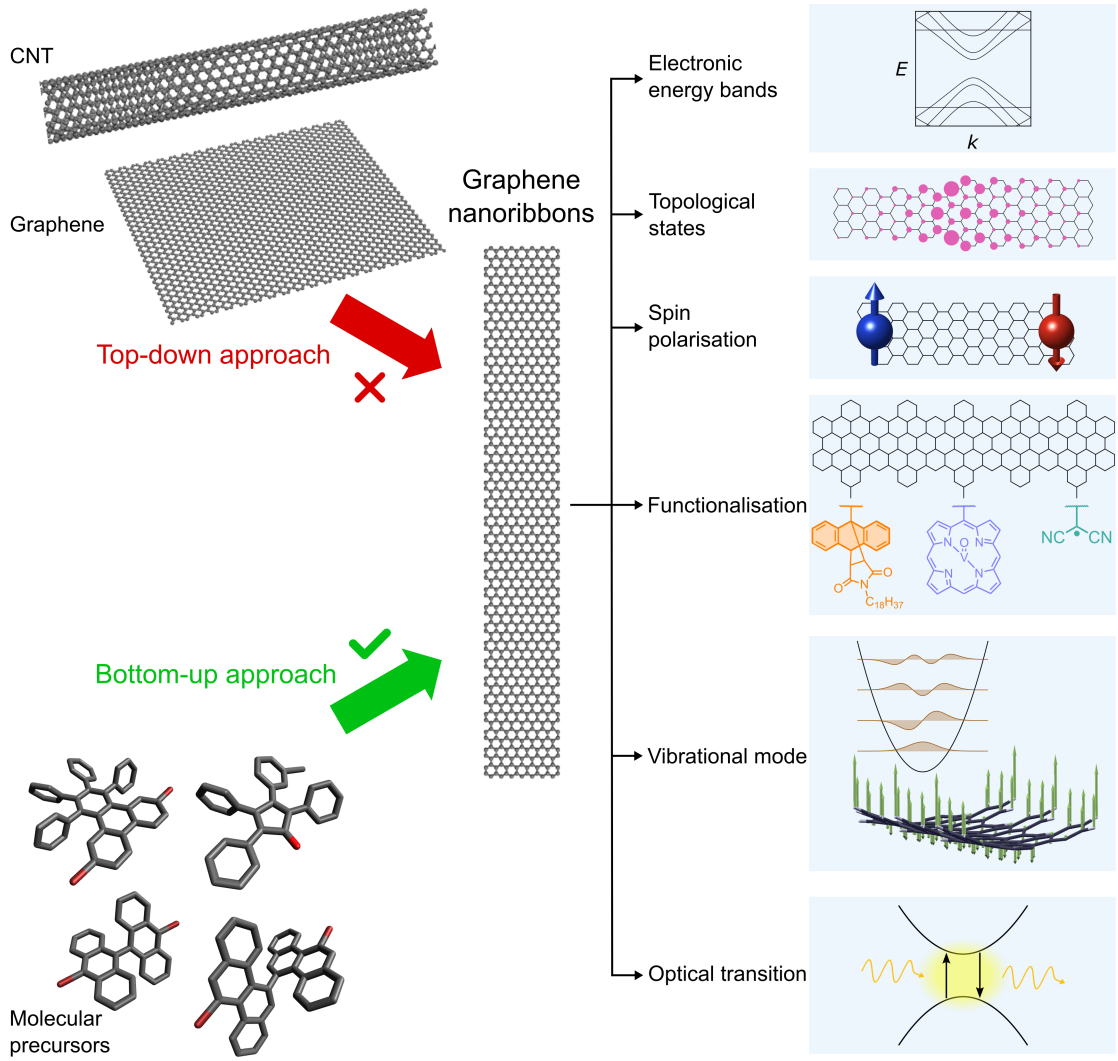


Figure 1.1: Different ways of quantum states engineering in bottom-up synthesised graphene nanoribbons. The principles of the top-down and the bottom-up approaches are illustrated on the left. In the top-down approach, graphene or carbon nanotube (CNTs) are trimmed to graphene nanoribbons (GNRs). In the bottom-up approach, molecular precursors are polymerised and then cyclodehydrogenated, leading to structurally well-defined GNRs. We focused on the bottom-up approach in this thesis. The quantum states of GNRs can be engineered through different ways, including electronic energy bands, topological states, spin polarisation, functionalisation, vibrational modes, and optical transitions.

the GNR's edge morphology was reported for the first time [8]. Over the years, and with the successful fabrication of graphene itself, this theoretical interest has surged to impressive levels.

Following the discovery of graphene in 2004 [1], the fabrication of GNRs remained challenging. Meanwhile, theoretical predictions of appealing properties of

GNRs began to appear. In addition to band structure calculations, new predicted properties of GNRs encompass half-metallicity [9], large magnetoresistance [10], spin-semiconducting [11], topological phase [12], and many more. Initial fabrication methods of GNRs leveraged top-down approaches, including unzipping carbon nanotubes (CNTs) [13–17], lithographical patterning [18, 19], catalytic-particle cutting [20–23], or sonochemical breaking [24, 25]. However, it quickly became apparent that these top-down methods are prone to scattering events and disorder, which easily wash out the desirable properties. In persuit of smoother edges and narrower ribbons, significant efforts have been devoted to the improvement of fabrication strategies and to the development of bottom-up synthetic approaches. Early bottom-up strategies included chemical-vapor deposition (CVD) [26–29] and epitaxial growth [30], resulting in some improvements in producing GNRs with smoother edges. Nevertheless, later studies demonstrated that an alternative bottom-up approach, based on molecular precursors, significantly outperformed the previous fabrication methods in making atomically well-defined structures [31–34]. The brief principles of the top-down approach, and the bottom-up synthesis based on molecular precursors, are schematically illustrated in Figure 1.1. In the subsequent part of this thesis, the term "bottom-up synthetic approach" is exclusively used to denote the synthetic method based on molecular precursors. This technique has witnessed a series of major breakthroughs in recent years. By designing molecular monomers, the structure can be precisely tuned, thereby also allowing the engineering of GNRs' properties that are closely related to structural parameters, such as width, edge morphology, and chemical functionalisation. These bottom-up synthetic protocols have enabled the design of a wide variety of GNRs with novel structures [34]. With the availability of nanoribbons of desired cleanliness, researchers are now beginning to investigate the possibility of integrating them into nanoelectronic devices, such as field-effect transistors (FETs) [35–38]. Owing to their properties including strong ballistic transport, high electron mobility, and

tunable energy bands, GNRs hold great potential as a replacement for silicon to build next-generation electronic devices [39, 40].

The ultimate miniaturisation of transistors based on CMOS technology is hampered by the quantum tunneling effect, whereas novel nanodevices based on GNRs can follow different design principles and exploit quantum effects. GNR-based devices exhibit unconventional functionalities that are inaccessible in traditional electronic devices. For example, an array of spin qubits with long-distance coupling between the individual qubit units can be achieved in a GNR [41]. Such a feature is crucial for scalable and fault-tolerant quantum computation [41]. In recent years, the topological aspects of the electronic states in GNRs have started to capture the interests of both theoreticians and experimentalists. Topology, initially a mathematical concept, was later introduced to condensed-matter physics to describe energy bands, leading to a subfield of physics, known as topological insulators [42–44]. Topological insulators are insulating in the bulk while conducting at the boundary. For one-dimensional GNRs, a topologically nontrivial phase implies that the ribbon possesses mid-gap[1] states localised at the ends. These localised end states in finite ribbons are often spin polarised when considering electron–electron interactions. The spin states in GNRs deserve particular attention because of their ultra-long spin coherence time [45], a critical property when considering using electron spins as qubits. Additionally, the electronic properties of GNRs can be flexibly tuned by bottom-up design. Numerous GNRs have been synthesised to date. A vast number of applications are being explored, including molecular electronics [35–38], spintronics [9, 46–48], single-photon sources [49–51], photovoltaics [52–54], quantum spin chains [12, 55–57], Majorana zero modes [12, 58, 59], quantum computation and quantum sensing [60–63].

[1]Mid-gap state refers to the electronic state whose energy is positioned in the middle of the band gap.

The quantum states of GNRs can be engineered in different ways, such as through electronic energy bands, topological states, spin polarisation, functionalisation, vibrational mode, and optical transitions, as summarised in Figure 1.1. In this work we focused on theoretical calculations of three aspects of GNRs: the topological states, the spin states, and the vibrational states. On the one hand, we aim at gaining a deeper understanding of electronic properties, specifically about topological phases, and guide the synthesis of novel GNRs. On the other hand, with the experimental testing of practical applications of GNRs already underway, we performed theoretical modelling to unveil the quantum states of GNRs manifested in experiments, for instance, the vibrational states and their coupling with electronic states in quantum transport and optical measurements. A central theme of our study is the development of experimentally more accessible GNRs. Most of bottom-up synthesised GNRs reported in recent years can only be synthesised and characterised on metal surfaces in a scanning tunneling microscope (STM). Only a very limited amount of GNRs, however, can be synthesised on surfaces [34, 64]. For this work, novel GNRs with bulky functionalisation groups that will make GNRs soluble were designed. In this way, the GNRs can not only be mass produced, but also be more easily studied using a large variety of experimental techniques, such as electron paramagnetic resonance (EPR) spectroscopy, single-molecule transistors (SMTs), and optical spectroscopy. In the experimental sections of this thesis, we focused on a type of soluble GNRs, whose superior solubility has significantly enhanced physical properties of GNRs, including spin coherence time, SMT yield, and photoluminescence quantum efficiency (PLQE).

This thesis is organised as follows. We begin with a comprehensive literature review about GNRs in Chapter 2. Various aspects of the electronic properties of GNRs are covered, including band structure, edge states, effects of structure modification, and finite-length effect. Then we will introduce the topological phase in GNRs, covering both the theoretical background and recent experimental characterisations. Following this, we present the spin states in GNRs, including

both their quantum properties and approaches to incorporate spin states in GNRs. In the last section, we briefly review the vibrational properties of GNRs.

Chapter 3 is dedicated to the theoretical and experimental methods used in our study. We outline the theoretical framework of the tight-binding (TB) model and density-functional theory (DFT). We then present a detailed theory of the topological phases in GNRs and practical methodologies to calculate them. We also formulate the theory in the Wannier representation, which serves as an important tool in our theoretical calculations. Regarding the experimental methods, we focus on EPR spectroscopy since all other complementary experimental characterisations were carried out by my collaborators. The basic theory of single-molecule transistors and optical spectroscopy are also briefly outlined.

The results are presented in Chapter 4–Chapter 6, which discuss the topological states, spin states, and vibrational states of GNRs, respectively. In Chapter 4, we first investigate three approaches to tune the topological phases of GNRs, and design a large number of novel structures. We then progress to study the relationship between the topological phase, a concept in condensed-matter physics, and the Clar's sextet rule, an empirical rule in organic chemistry. We also extend the study of topological phases to fused porphyrin nanoribbons. Finally, we discuss a possible way to realise chiral dissipationless transport by exploiting the topological zero-energy mode in sublattice-imbalanced GNRs under a transverse electric field. In Chapter 5, we first discuss the intrinsic spin states that arise from the spin polarisation of the end states in topological GNRs by carrying out DFT calculations. Subsequently, we experimentally investigate two novel GNRs with spin-polarised states from external functionalisation groups. The spin dynamics in these GNRs are characterised using EPR spectroscopy. In Chapter 6, we reveal the manifestations of vibrational states of GNRs in two types of experimental measurements: the single-molecule transport measurement, and optical measurement. Specifically,

we discuss the role of electron–phonon coupling in these experimental datasets. Meanwhile, we compare the performance of two GNRs with different solubilities.

2 Background

Contents

2.1 Electronic structure of GNRs 9
2.1.1 Armchair and zigzag GNRs 10
2.1.2 The emergence of edge states 16
2.1.3 Tuning electronic properties by structure modification . . 23
2.1.4 The effect of finite length 29
2.2 Band topology of GNRs 33
2.2.1 The arise of topology in condensed matter 33
2.2.2 Topological classification of GNRs 42
2.2.3 Experimental verification 48
2.2.4 Topology in quantum spin chains 53
2.3 Spin states in GNRs 55
2.3.1 Spin qubits and spin relaxation 55
2.3.2 Quantum properties of electron spins in GNRs 58
2.3.3 Incorporating spin states into GNRs 61
2.4 Vibrational properties of GNRs 66

2.1 Electronic structure of GNRs

In this chapter, I will first give an overview of the basic electronic properties of GNRs. We introduce the band structures of the two most basic GNRs: armchair graphene nanoribbons (AGNRs) and zigzag graphene nanoribbons (ZGNRs). In particular, we discuss the emergence of spin-polarised edge states, their fascinating

properties and wide-ranging applications. We also review current strategies for modifying the electronic properties via structure engineering. The finite-length effect in some GNRs gives rise to nontrivial end states, which are related to topological phases. We elaborate on the band topology of GNRs in Section 2.2 by starting from introducing a broader scope of topology in condensed-matter physics. Following that we will present the quantum properties of spin states in GNRs, which have profound potential in quantum-technology applications. Finally, we will give a brief review of GNRs' vibrational properties.

2.1.1 Armchair and zigzag GNRs

As it is well known, graphene is a gapless semimetal. The real lattice, reciprocal lattice, and band structure of graphene are shown in Figure 2.1. The conduction band and valence band of graphene join each other in the Dirac points. The dispersion around Dirac points is almost linear, which implies vanishing mass and exceptional high mobility of the fermion. The lack of band gap, however, limits the application of graphene in logic devices. There have been various approaches to open a band gap in graphene, for example by doping [67], heterojunction formation [68],

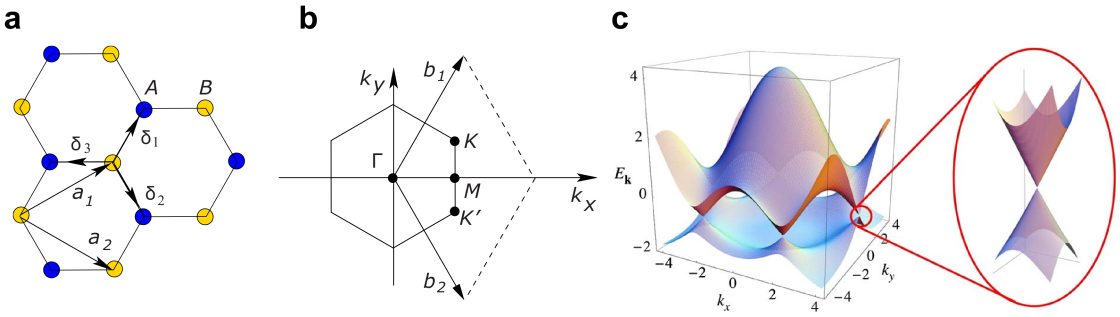


Figure 2.1: Graphene lattice and its band structure. (a) Honeycomb lattice of graphene, consisting of two sublattices marked by yellow and blue dots. The two lattice translation vectors are labelled as $\mathbf{a_1}$ and $\mathbf{a_2}$, and δ_1, δ_2, and δ_3 are the three nearest-neighbour vectors. (b) Brillouin zone of graphene, with two reciprocal lattice vectors $\mathbf{b_1}$ and $\mathbf{b_2}$. The hexagonal Brillouin zone has two inequivalent vertices, denoted as $\mathbf{K}$ and $\mathbf{K'}$. They are the Dirac points where conduction band touches valence band. (c) Band structure of graphene. A zoom-in view of the Dirac cone is shown on the right. Adapted from Ref. [65].

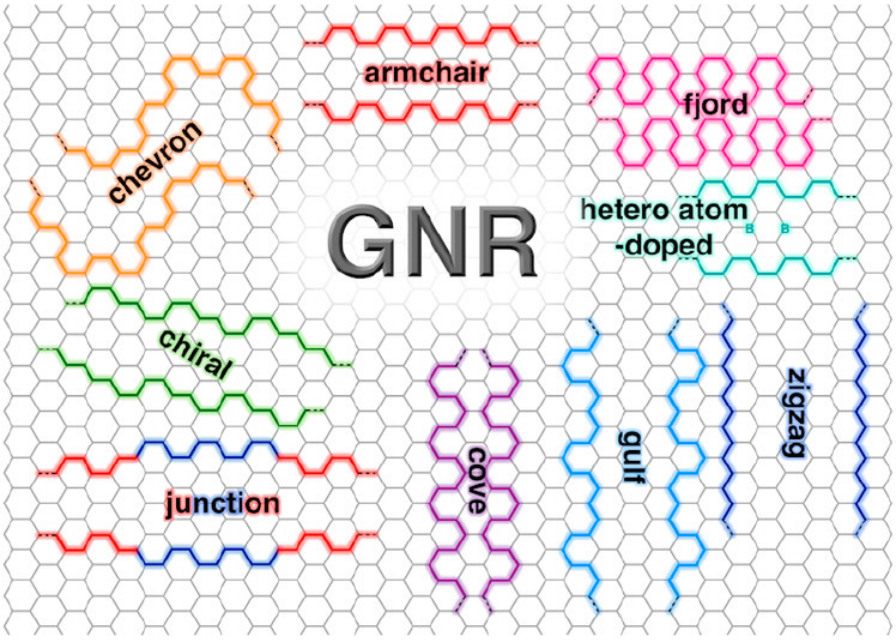


Figure 2.2: GNRs with different edge shapes. Adapted from Ref. [34].

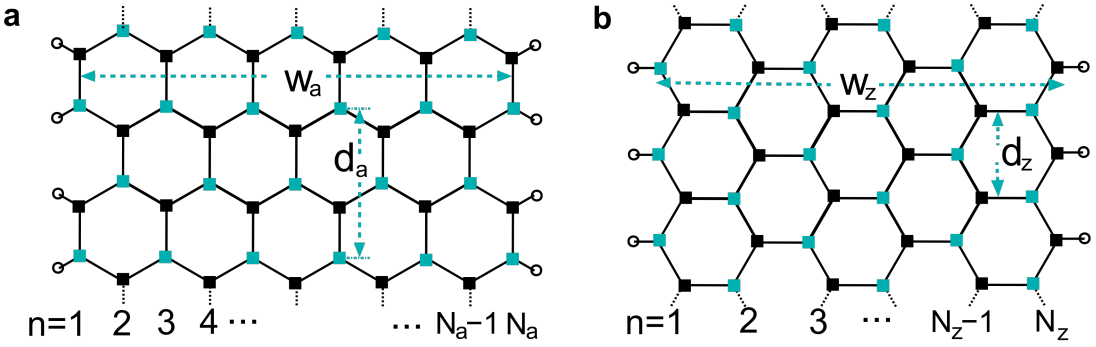


Figure 2.3: Schematic structure of (a) AGNR and (b) ZGNR. The structures are confined in the horizontal direction, but infinite along the vertical direction. A and B sublattices are represented as black and green squares. The empty circles are hydrogen atoms that passivate the edge carbon atoms. The number of columns of carbon atoms are counted as N_a and N_z, respectively. The unit-cell translation vectors d_a and d_z are along the periodic directions, while w_a and w_z are the ribbon width. Adapted from Ref. [66].

bilayer stacking [69], or local electric fields [70]. Here we focus on the approach of creating a strip of graphene, i.e. a GNR. The lateral quantum confinement in GNRs can effectively introduce a tunable band gap.

The electronic band structure of GNRs is crucially dependent on their edge morphology. There is a large degree of freedom in designing GNRs' edge shape. Some examples are given in Figure 2.2, among which the armchair edge and zigzag

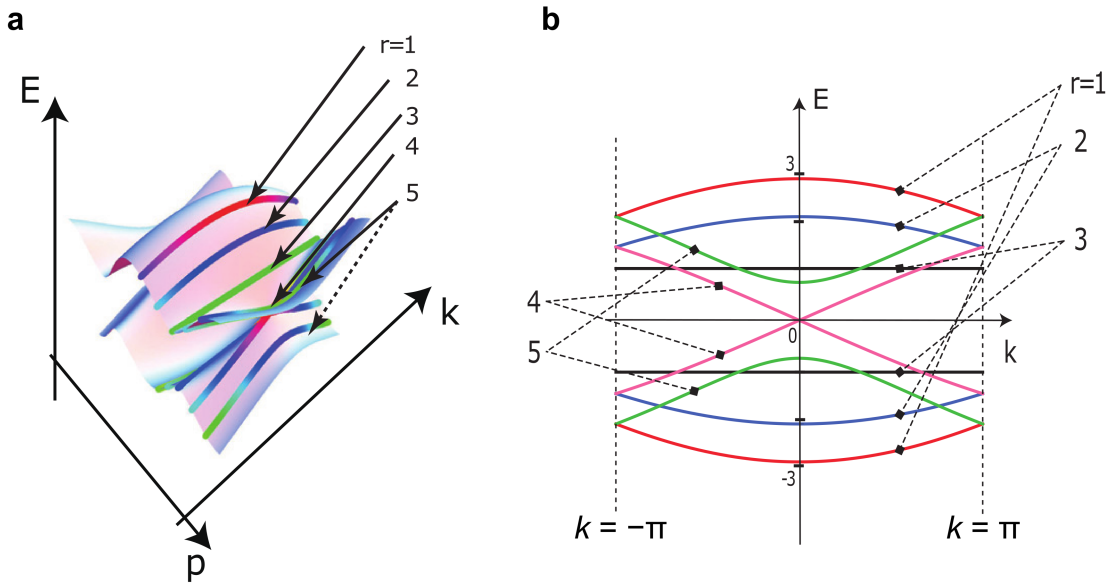


Figure 2.4: Approximation of 5-AGNR band structure by zone-folding. (a) 3D graphene band structure with k lines corresponding to discrete transverse wavenumber p. The k lines are along the armchair direction. The sub-band indices are denoted as r. (b) Energy-band structure of 5-AGNR, where each sub-band is obtained by projecting the 3D graphene band structure onto the 2D E–k plane. Adapted from Ref. [71].

edge are the two most fundamental types. All the other edge shapes can be decomposed into armchair and zigzag segments. Hence here we only introduce the band structure of GNRs with armchair and zigzag edges.

To begin with, we need to introduce the convention of defining the widths of AGNRs and ZGNRs. The width of an AGNR, or ZGNR, is defined by the number of rows of carbon atoms in transverse direction. We denote the width as N_{a} for AGNRs and N_{z} for ZGNRs. When counting rows in AGNRs, a zigzag (or dimer line) is considered a row. Therefore, in Figure 2.3a there are 11 rows of carbon atoms, and we denote this GNR as 11-AGNR. Similarly the ribbon in Figure 2.3b is labelled as 6-ZGNR.

The zone-folding approximation can be used to determine the band structure of GNRs, just as it can for CNTs [72], from that of graphene. For one-dimensional (1D) GNRs, the wavenumber is continuous along the periodic direction (denoted as k), but discrete along the transverse direction (denoted as p). The band structure

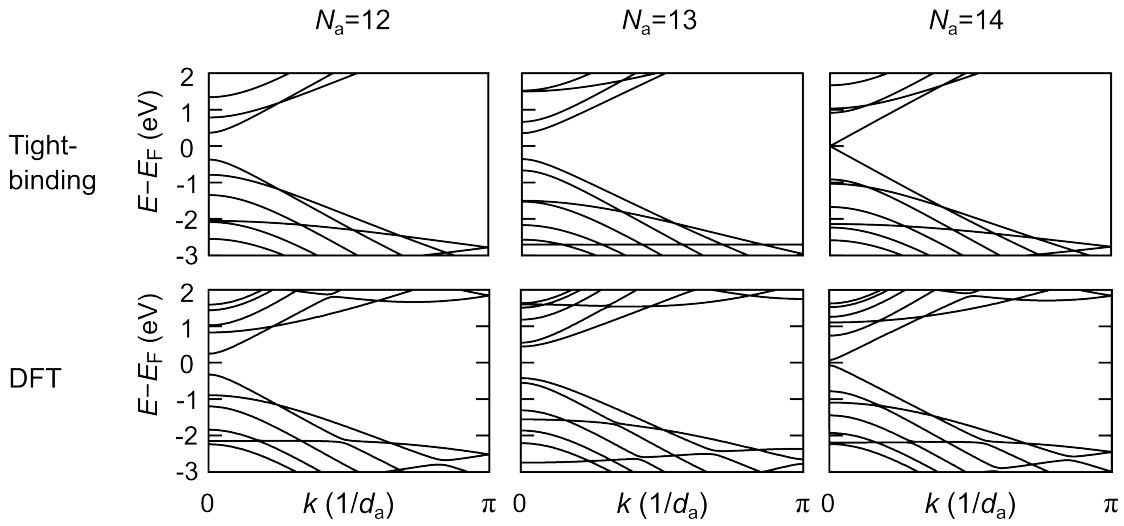


Figure 2.5: Band structure of 12-AGNR, 13-AGNR, 14-AGNR calculated from the tight-binding model and DFT. The definition of N_a and d_a are given in Figure 2.3. DFT calculations are reproduced from Ref. [66].

of a GNR can be approximated by the graphene bands along certain allowed k lines. As illustrated in Figure 2.4, the band structure of 5-AGNR can be obtained by projecting the graphene band structure onto five k paths along the armchair direction with equidistant transverse wavenumbers along the zigzag direction. This approximation can give a reasonable estimation of the band structure for many ribbons. For example, if one of the discrete k lines pass through Dirac points, then the ribbon will be metallic under this approximation, otherwise it is semiconducting. This approach, however, fails to estimate GNRs with complicated edge shape.

The earliest calculation of band structures of GNRs used mainly the tight-binding model and the mean-field Hubbard model. We discuss the band structure of AGNRs first. AGNRs can be classified into three categories based on their width N_a. When $N_a = 3p + 2$, where p is a positive integer, the ribbon is gapless. The frontier bands have linear dispersion around the Γ point, such as in 5-AGNRs (Figure 2.4) and 14-AGNRs (Figure 2.5). This can be understood from the zone-folding approximation as mentioned before. Meanwhile, when $N_a = 3p, 3p+1$, the ribbon is semiconducting, such as in 12-AGNRs and 13-AGNRs (Figure 2.5). First-principle calculations

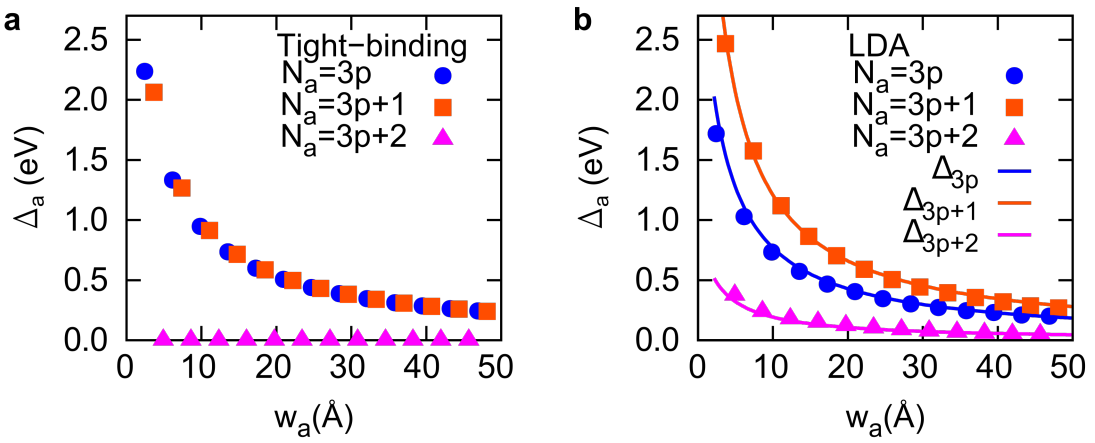


Figure 2.6: The band gap Δ_a of AGNRs versus ribbon width w_a calculated from (a) Tight-binding model, and (b) DFT with LDA functional. The definition of N_a and w_a are given in Figure 2.3. The solid line in (b) are fit by $\Delta_a \sim w_a^{-1}$. Adapted from Ref. [66].

using DFT with local-density approximation (LDA) functional give very similar estimates of the band gap as the tight-binding model, except that for AGNRs of $N_a = 3p + 2$ type there is a small gap opening at the Γ point. The variation of band gaps in AGNRs as a function of ribbon width is given in Figure 2.6. As shown in the solid-line fit, the band gap is almost perfectly proportional to the inverse of ribbon width. This relation is an important guideline for searching for ribbons that have a similar band gap as silicon.

In contrast to AGNRs, ZGNRs are predicted to have zero band gap by the tight-binding model [73]. In the range of $2\pi/3 < k/d_z < \pi$, the valence band and conduction band join at zero energy. The high density of states (DOS) of the flat bands will trigger magnetic instability upon considering electron–electron interactions [73], which is ignored by the tight-binding model. The inclusion of on-site Coulomb repulsion energy will induce a separation of the flat bands, leading to an energy gap [71, 73]. DFT calculation with local spin-density approximation (LSDA) functional produces similar results [66], as shown in Figure 2.7b. What's more, spontaneous magnetic order is formed at the two zigzag edges. As illustrated in Figure 2.7c, the two edges are spin polarised, with ferromagnetical coupling between spins belonging to same edge, and antiferromagnetical coupling betweeen

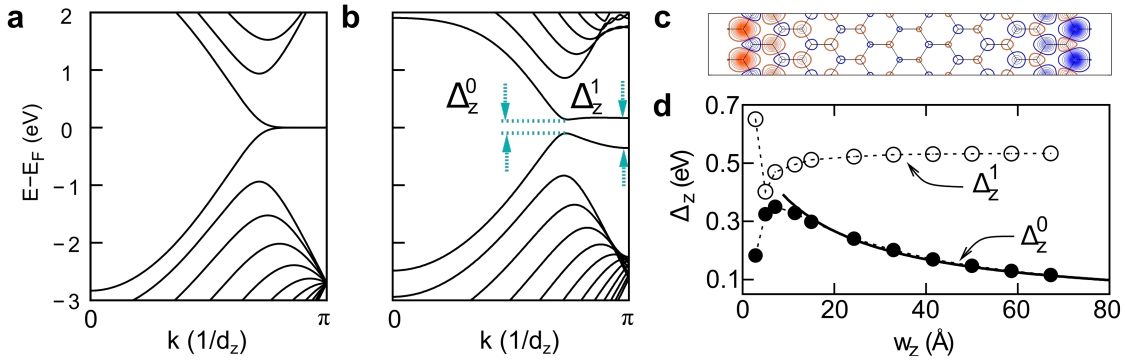


Figure 2.7: Band structure of 12-ZGNR calculated from (a) Tight-binding model, and (b) DFT with LSDA functional. The definition of d_z and w_z are given in Figure 2.3. In (b) the α-spin and β-spin bands are degenerate. Δ_z^0 and Δ_z^1 are the direct band gap and the energy gap at $k = \pi/d_z$, respectively. (c) The contour of spin density of 12-ZGNR. The density is integrated over the direction normal to the ribbon plane. (d) The dependence of Δ_z^0 and Δ_z^1 against ribbon width w_z. Dotted lines are guide to the eyes. Solid line is a reciprocal function fit to the data for $N_z \geq 8$. (b–d) are reproduced from Ref. [66].

spins belonging to opposite edges. This is called the edge states of ZGNRs. We will provide more details of the zigzag edge states in the next section. It is worth noting that for wider ZGNRs with $N_z \geq 8$, the direct gap is also inversely proportional to the ribbon width, similar as AGNRs as introduced in preceding paragraph. This trend holds not only for pure zigzag or armchair GNRs, but also for general GNRs with any edge morphology, and it has been corroborated by many experiments [74–76].

Although DFT calculations give much better predictions of the electronic structure of GNRs compared with the tight-binding model, they still fail to match the experimental results. The main reason is that the electron–electron interaction is enhanced in nanometre-sized confined systems like GNRs. Kohn–Sham DFT can map the many-electron system to a system of non-interacting particles (Kohn–Sham orbitals) in an effective potential, which includes the effects of electron–electron interactions. The effective potential consists of the external potential, the classical electrostatic interaction, and the exchange–correlation potential. In principle, all the many-body interactions can be captured if the exact form of the exchange–correlation functional is known. However, in practice, the typical approximations to the exchange–correlation functional may not capture these effects

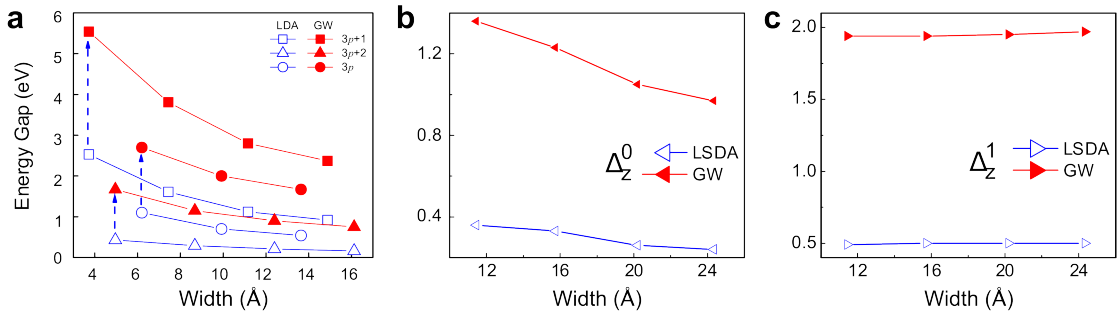


Figure 2.8: Comparison of energy-band gap calculated from DFT and GW approximations for (a) AGNRs and (b–c) ZGNRs. For AGNRs, the ribbon is divided into three families as explained before. The solid lines within each group serve as visual guides. DFT calculation was carried out using LDA functional. The dashed arrows represent the self-energy correction. For ZGNRs, DFT calculation was implemented with the LSDA functional. The direct band gap Δ_z^0 and the energy gap Δ_z^1 at zone boundary are plotted in (b) and (c), respectively. Adapted from Ref. [77].

adequately. In contrast, the GW approximation directly addresses the quasiparticle interactions, and, thus, captures effects like electron screening more naturally, therefore producing much more accurate estimations on band gaps [78]. Compared with band gaps calculated with LDA functional, GW calculations result in a larger value by adding a self-energy correction term to the band gap, as denoted by the dashed arrows in Figure 2.8a. The GW-corrected quasiparticle band gap is larger than the LDA band gap for all ribbons [77]. The calculation has been verified by various experiments [53, 79, 80].

Besides the tight-binding model, Hubbard model, DFT, and GW approximation mentioned above, there are some other approaches to calculate the band structure of GNRs. For instance, the combination of $k \cdot p$-perturbation theory and Dirac equation gives similar results as the tight-binding model for all but the narrowest ribbons [81, 82].

2.1.2 The emergence of edge states

2.1.2.1 Understanding the origin of edge states

The presence of magnetic edge states in ZGNRs was first reported in the 1990s [8, 73], and soon after that it attracted tremendous interest from theoreticians. Note

that the spin-polarised zigzag-edge states here are different from the edge states in the quantum spin Hall (QSH) system as proposed by Kane and Mele [83, 84]. The latter edge states are a pair of gapless, helical edge states where electrons with opposite spins move in opposite directions along the boundary of the material. QSH effect can be realised in graphene by adding external, staggered sublattice potentials and spin–orbit coupling (SOC) [83, 84], whereas the intrinsic SOC in graphene is very weak. Here we will focus on the edge states in ZGNRs. It results from on-site Coulomb interaction, which is non-negligible in confined systems.

The origin of zigzag edge states had drawn the attention of many theoreticians since being firstly reported. So far there have been many different perspectives on that. For example, Akhmerov and Beenakker studied terminated graphene with the Dirac equation [85], and showed that edge states is an intrinsic property of zigzag boundary condition in Dirac materials. The dispersionless zigzag edges states can be turned into propagating states by adding staggered potentials near the edge. Furthermore, Tkachov also employed the Dirac equation and explicitly proved that the zigzag edge states are a result of isospin rotation-symmetry breaking, where the isospin represents the two nonequivalent nodal points of graphene's Brillouin zone [86]. On the other hand, Ryu and Hatsugai pointed out that zero-energy edge modes in zigzag and bearded edges of GNRs have a topological origin [87]. For a two-dimensional (2D) system, the Hamiltonian can be parameterised in $k_{\parallel}$ and $k_{\perp}$, the wavenumber parallel and perpendicular to the edge, respectively. For each $k_{\parallel}$, by expressing the Hamiltonian $H(k_{\perp}; k_{\parallel}$ fixed) in the vector space of Pauli matrices, a topological invariant, viz., the winding number, can be defined for the Hamiltonian if the system has particle-hole symmetry and chiral symmetry. When the winding number is 1 the Hamiltonian has a pair of zero-energy edge states. By calculating the winding number at different $k_{\parallel}$, one can determine the range of zero-energy flat bands that correspond to edge states. Delplace et al. further explained the emergence of edge states in graphene by calculating the Zak phase

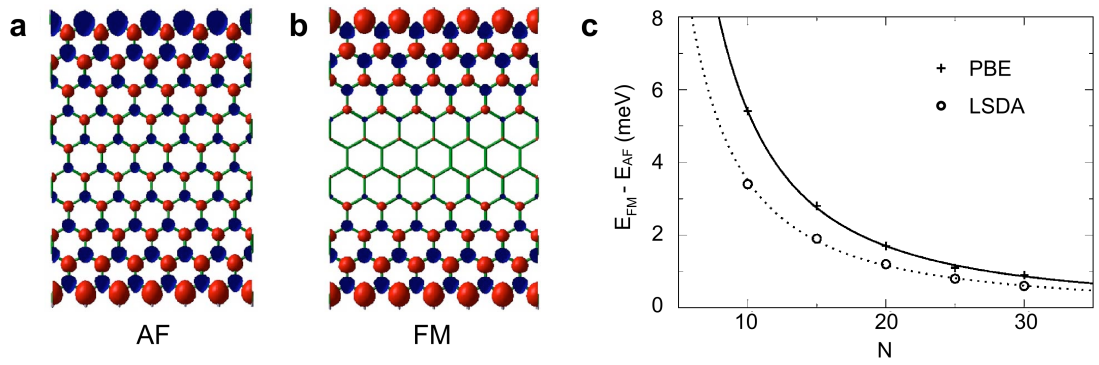


Figure 2.9: Magnetic-interaction strength between edge states versus ZGNR width N. (a) and (b) show the spin-density isosurface for antiferromagnetic (AF) case (a) and ferromagnetic (FM) case (b), respectively. The red and blue surface represent α and β spin, respectively. (c) The energy difference between ferromagnetic state and antiferromagnetic state is plotted as a function of ZGNR width N. The energies are calculated from DFT with both PBE and LSDA functional. The power-law fitting results in $1/N^{1.44}$ and $1/N^{1.39}$ for PBE and LSDA functional, respectively. Adapted from Ref. [88].

from the Hamiltonian $H(k_\perp; k_\parallel \text{ fixed})$ for GNRs with more general edge shapes [89]. This approach shares the same core principle with the approach using the winding number calculation. Later, Miert et al. extended this result to systems without chiral symmetry, which implies that the edge states are not limited to graphene and can exist in more general 2D materials [90].

The analytical theories about edge states mentioned above all treat GNRs as 2D objects, where the zigzag edge is the boundary of the graphene. Whereas in very narrow ribbons the perpendicular wavenumber $k_\perp$ is no longer a good quantum number, and the electron–electron interaction is nonnegligible because of the high density of states at zero energy. As introduced before in Figure 2.7, DFT predicts a non-zero energy gap and spin-polarised edge states. In ground state the two edges are antiferromagnetically coupled, which can be labelled as antiferromagnetic states (Figure 2.9a). The two edges can have parallel spin (ferromagnetic state) in excited states, as illustrated in Figure 2.9b. The energy difference between the ferromagnetic state and the antiferromagnetic state is linked to the strength of magnetic interaction between the two spin-polarised edges. Pisani et al. demonstrated by DFT calculations that this magnetic interaction decays

with the ribbon width [88]. As shown in Figure 2.9c, the Perdew–Burke–Ernzerhof (PBE) and LSDA functionals generate slightly different results but both data sets can be fit by a power law very well. This result implies that for wide ZGNRs the magnetic ordering becomes weak and will be destroyed at room temperature [88]. In addition, while edge states in an antiferromagnetic state is semiconducting, the ribbon is metallic when edge states are in a ferromagnetic state. A metal–insulator transition can thus be very interesting for practical applications [88].

2.1.2.2 Edge states in general GNRs

In fact, the edge states appear not only in ZGNRs, but also in other GNRs that possess zigzag fragments in the edge. For example, Yazyev et al. systematically studied the presence of magnetic edge states in chiral GNRs whose translation vector is a combination of zigzag edge and armchair edge, as displayed in Figure 2.10a [91]. In this study, the electronic band structures were computed by mean-field Hubbard model, which includes an empirical parameter, the on-site Coulomb repulsion potential U, to account for electron–electron interactions, and it provides comparable

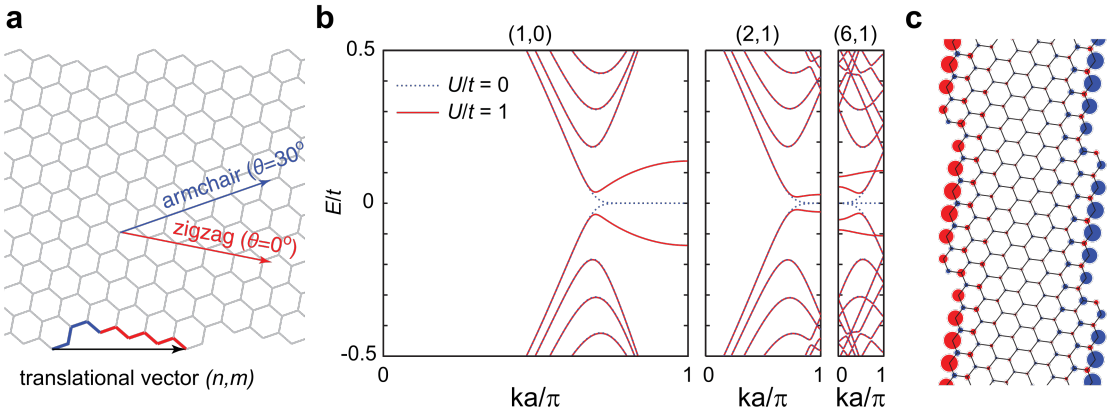


Figure 2.10: Edge states of chiral GNRs. (a) Model structure of chiral GNR, where the edge translation vector is comprised of zigzag units (red) and armchair units (blue). In this case this ribbon is denoted as (4,1) chiral GNR. (b) The band structure of (1,0), (2,1), (6,1) chiral GNR calculated with the tight-binding model (dashed blue curve, $U/t = 0$) and mean-field Hubbard model (solid red curve, $U/t = 1$. The width of the band structure plots scale with the varying Brillouin zone size of different ribbons. (c) Spin density distribution of (6,1) chiral GNR, where red and blue circles represent α and β spin, respectively. Adapted from Ref. [91].

results as spin-unrestricted DFT results. As shown in Figure 2.10c, antiparallel edge states also exist in chiral GNR with zigzag fragments. On top of this, edge states were also reported in GNRs with other edge morphology like bearded edge [92] and some cove-decorated zigzag edges [93]. Furthermore, Jaskólski et al. proposed a simple rule to determine the presence of edge states by projecting the edge translation vector onto zigzag direction [93].

2.1.2.3 Applications of edge states

The edge states in GNRs attracted the interest of researchers because they have many potential applications in nanoelectronics and spintronics devices. Sawada et al. studied the edge states in ZGNRs using non-collinear DFT and found that the band gap gradually closed as the relative angle between the spins in opposite edges decreases from 180° to 0°, i.e. from antiferromagnetic state to ferromagnetic state [94]. This can be potentially controlled by an external magnetic field. In 2006, Son et al. proposed that ZGNRs will be half-metallic upon applying transverse electric fields [9]. The band gap is closed for α spin while widened for β spin. Therefore only electrons with α spin can pass, but electrons with β spin are blocked. Such spin-filter behaviour can be very useful for spintronic devices. Son et al. also found that there is a critical electric-field strength to trigger half-metallicity [9]. Many approaches, like doping or chemical decoration, have been proposed to regulate the half-metallicty and reduce the critical electric-field strength [95–97]. Wang et al. calculated the sawtooth-edge GNRs under transverse electric fields [11]. Unlike the ZGNRs, sawtooth GNRs are spin-semiconductors where the charge carriers are not only spin-polarised but also spatially separated. The spin-up electrons move along one edge while the spin-down holes move along the opposite edge. Moreover, Rycerz et al. proposed that a quantum point-contact system built from zigzag edges of graphene can work as a valley filter with tuning of gate potential [98]. Qiao et al. [48] and Yao et al. [99] reported that spin-polarised and valley-helical edge modes

can be created by introducing a staggered sublattice potential. Sasaki et al. also studied the superconductivity supported by the zigzag edge states of graphene [100].

2.1.2.4 Experimental realisations of edge states

In the last section we have shown that there are a plethora of opportunities to employ the edge states in novel electronic and spintronic devices. Experiments, however, had been hampered by the chemical instability of zigzag edges. In 2007, Jiang et al. investigated the chemical reactivity of zigzag edges of GNRs with common radicals by first-principle DFT calculations [101]. Huang et al. demonstrated that the spin polarisation in zigzag edge states can be destroyed by defects and impurities [102]. Therefore, obtaining a defect-free zigzag edge and keeping it in a chemically inert environment is vital for observing the edge states. In 2011, Tao et al. reported the fabrication of (8,1) chiral GNRs by unzipping CNTs [75]. The chiral edges were resolved by high-resolution STM, and the edge states were observed by scanning tunneling spectroscopy (STS). The chirality of such GNRs, however, is poorly controlled. Later, the development of the bottom-up synthesis approach that used molecular precursors successfully produced atomically well-defined GNRs that were inaccessible by other approaches. In 2015, Ruffieux et al. reported the on-surface synthesis of 6-ZGNRs by bottom-up approach [103]. As shown in Figure 2.11a, the monomers were polymerised on a gold surface under ultra-high vacuum (UHV) conditions, followed by cyclodehydrogenation. The UHV condition can effectively protect the zigzag edge from being oxidised by air. Atomically precise 6-ZGNR is clearly resolved by non-contact atomic force microscopy (AFM). Since the electronic states of GNRs are often obscured by the metal surface because of strong electronic coupling, GNRs are often transferred to NaCl crystals by STM tip manipulation to detect the electronic states. Afterwards the local density of states (LDOS) of GNRs can be characterised by differential conductance measurement. As shown in Figure 2.11d, the differential conductance trace measured at the zigzag edge (marked

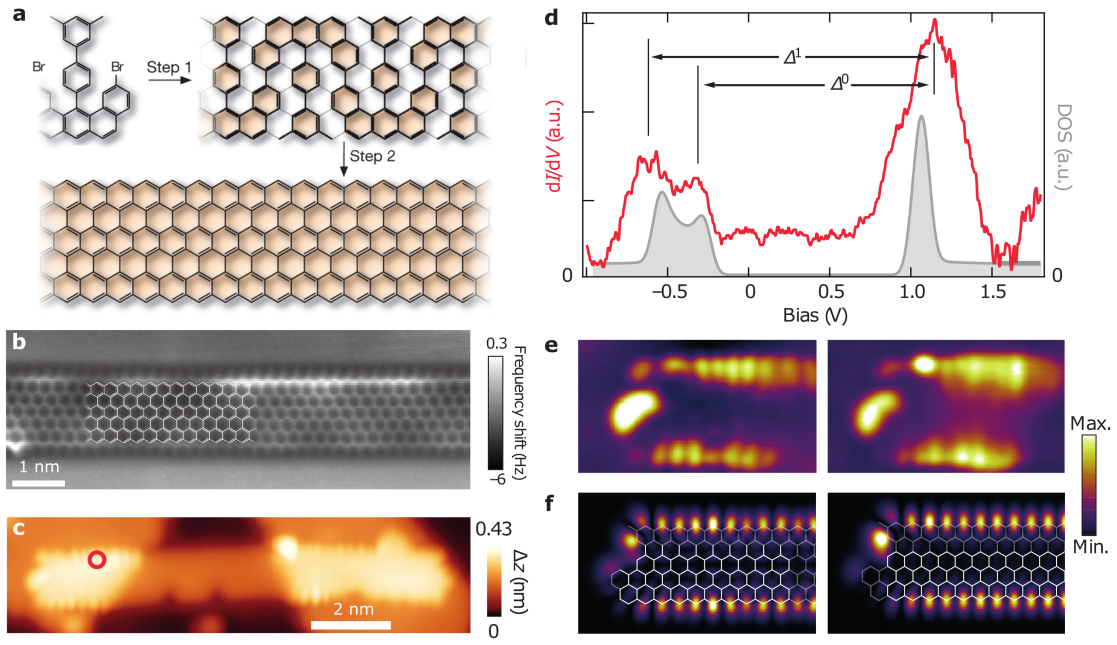


Figure 2.11: On-surface surface of ZGNR and verification of edge states. (a) Synthesis of 6-ZGNRs by polymerisation (step 1) of molecular precusor and subsequent cyclisation (step 2). (b) Atomically precise zigzag edges of a 6-ZGNR, resolved by constant height non-contact AFM frequency shift image, obtained with a CO-functionalised tip. The bright spot in the bottom left corner is a CH_2 defect. (c) STM topography image of a 6-ZGNR bridging between two NaCl islands. (d) Calculated quasiparticle DOS (grey) and differential conductance (dI/dV) spectrum (red) taken at the zigzag edge marked by the red circle in (c). Δ^0 and Δ^1 correspond to the energy gaps as labelled in Figure 2.7b. (e) Differential-conductance maps of occupied (left) and unoccupied (right) edge states, measured at sample bias voltage of −0.3 V and 1.0 V, respectively. (f) Local density of states (LDOS) calculated from DFT at 4 Å above the ribbon, correspond to the filled (left) and empty (right) edge states in (e), respectively. Structural model is overlaid on top of the LDOS spatial distribution. Adapted from Ref. [103]

by red circle in Figure 2.11c) matches perfectly with the peaks in DOS calculated by the GW approximation. The occupied and unoccupied zigzag edge states can also be visualised by measuring LDOS maps (Figure 2.11e–f) for the whole ribbon.

The spin ordering of zigzag edge states was untested until Blackwell et al. reported the on-surface synthesis and characterisation of nitrogen-doped 6-ZGNRs in 2021 [104]. Although the conduction band and valence band were modified by nitrogen atoms, the magnetic edge states remained intact. The electron lone pairs of nitrogen atoms also introduced two flat bands, which were split in energy because of exchange coupling with the magnetic edge states. The results provided strong

evidence for the existence of spin-polarised edge states in ZGNRs.

2.1.3 Tuning electronic properties by structure modification

2.1.3.1 Modifying backbone structure and width

One of the most important applications of GNRs is miniaturised FETs. To achieve this goal it is pivotal for scientists to be able to design the band gap of the materials. For instance, Barone et al. predicted that in order to get similar band gap as in silicon and GaAs, GNRs with widths of 1–2 nm are needed [105]. Besides, GNRs can also be applied in photovoltaics, where the materials need to have strong optical absorption as well as a suitable energy-level shift between donor and acceptor [54]. For these purposes, the electronic structure of GNRs should be carefully engineered. As introduced in Section 2.1.1, the electronic properties of GNRs are basically determined by their geometric structures. Especially in recent years the advances in bottom-up synthesis of GNRs have provided us many techniques to design GNRs with various edge shapes, including but not limited to armchair-type, zigzag-type, chiral-type, chevron-type and cove-type.

Figure 2.12 gives three examples of getting a well-defined backbone and width through monomer design. The monomers are connected by polymerisation, then

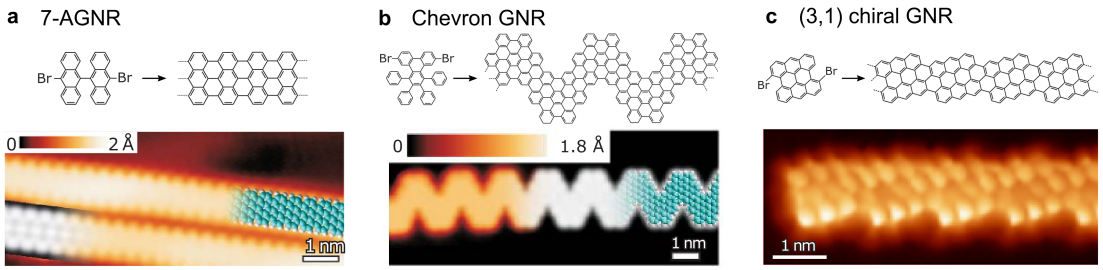


Figure 2.12: Designing GNRs with different backbone structures and widths. (a) Synthesis of 7-AGNRs from polymerisation and cyclisation of 10,10'-dibromo-9,9'-bianthryl monomer. High resolution STM image with partially overlaid structure model (blue) is shown below. Adapted from Ref. [106]. (b) Synthesis of chevron-type GNRs from 6,11-dibromo-1,2,3,4-tetraphenyltriphenylene monomer, with STM image and superimposed structure model below. Adapted from Ref. [106]. (c) Synthesis of (3,1) chiral GNR from 2,2'-dibromo-9,9'-bianthracene monomer, with STM image below. Adapted from Ref. [107].

fused to flat ribbons by cyclisation. As introduced in Section 2.1.1, AGNRs can be divided into three categories. The band gap can be easily tuned by changing the ribbon width. The most basic strategy of controlling the ribbon width is designing the molecular precursors. So far, chemists have successfully synthesised AGNRs of width 5 [108], 6 [109], 7 [106], 8 [110], 9 [111–113], 12 [114], 13 [115], 15 [116], 18 [117] from molecular precursors. The other way of modifying the width of AGNRs is by fusing narrower GNRs along the lateral direction under certain reaction conditions. For instance, Chen et al. synthesised 10-AGNRs and 15-AGNRs by fusing chemical-vapor-deposited 5-AGNRs [118]. Merino-Díez et al. synthesised AGNRs of width 6, 9, 12, and 15 by fusing poly-*para*-phenylene nanowires, which can also be considered as 3-AGNRs [119]. Sun et al. synthesised 8-AGNRs and 10-AGNRs by fusing 3-AGNRs with 5-AGNRs and 7-AGNRs, respectively [120]. The electronic band gaps of AGNRs were also experimentally characterised, and they are all in line with theoretical predictions [119, 121]. ZGNRs are relatively more challenging to synthesise because of their highly reactive edges. Alternatively, researchers have extensively explored chiral-edge GNRs [107, 122, 123], as these GNRs also host spin-ordered edge states as ZGNRs do. The chevron-edge GNRs are also one of the earliest ribbons synthesised from the bottom-up approach [106, 124], and they have been shown to be useful in building heterojunction structures, which we will detail later. Moreover, Narita et al. have also reported some cove-edge GNRs [125]. It is worth noting that these cove-edge GNRs are synthesised in liquid phase rather than on metal surfaces [125]. Such an approach is able to produce GNRs in much larger scales. In summary, the past advances of GNRs' bottom-up synthesis has shown the striking ability of this approach to produce atomically precise ribbons with various backbones and different widths, and thus with desirable electronic properties.

2.1.3.2 Doping and edge decoration

Although backbone structure and width modification are powerful tools for controling the band gap, they usually bring considerable change to the gap. As complementary tactics, heteroatom doping and edge decoration have been explored as possible ways to more finely tune the band gap. Normal GNRs consist only of carbon atoms in the backbone, with their edges passivated by hydrogen atoms. In the doping and edge decoration approaches, the backbone carbon atoms can be replaced with nitrogen, boron, sulfur, oxygen, or other atoms. The hydrogen atoms at the edge can also be replaced by other decoration groups. The band gap can be affected by both the type and concentration of doping atoms [64]. The dopants can also create either n-type or p-type semiconductors. Next, we will give an overview of the experimental advances in creating chemically doped and functionalised GNRs.

The nitrogen doping is firstly investigated in chevron GNRs. In 2013, Bronner et al. fabricated chevron GNRs with edge carbon atoms selectively substituted with nitrogen atoms [126]. The band gap changes only slightly, while the whole band structure linearly shifts toward lower energies upon nitrogen doping. Later, Carbonell-Sanromà et al. decorated 7-AGNRs' edges by attaching nitrile (CN) groups [127]. Because of the strong electron-withdrawing effect of nitrile groups, the bands are collectively shifted downward by about 0.5 eV per CN group. The CN groups can also effectively extend the π-network, so that the band-gap size is reduced by around 0.1 eV. Marangoni et al. devised a carbazole-functionalised precursor, providing a more reliable doping strategy for chevron GNRs that can turn six-member rings to five-member rings [128]. In 2018, Durr et al. proposed an improved method to incorporate diversified dopants, including N, O, and S into chevron GNRs [129]. As shown in Figure 2.13, the inclusion of these orbital-matched doping atoms induces significant upward shifts of bands and shrinkages of band-gap sizes. The doped GNRs can be clearly identified in high resolution STM images.

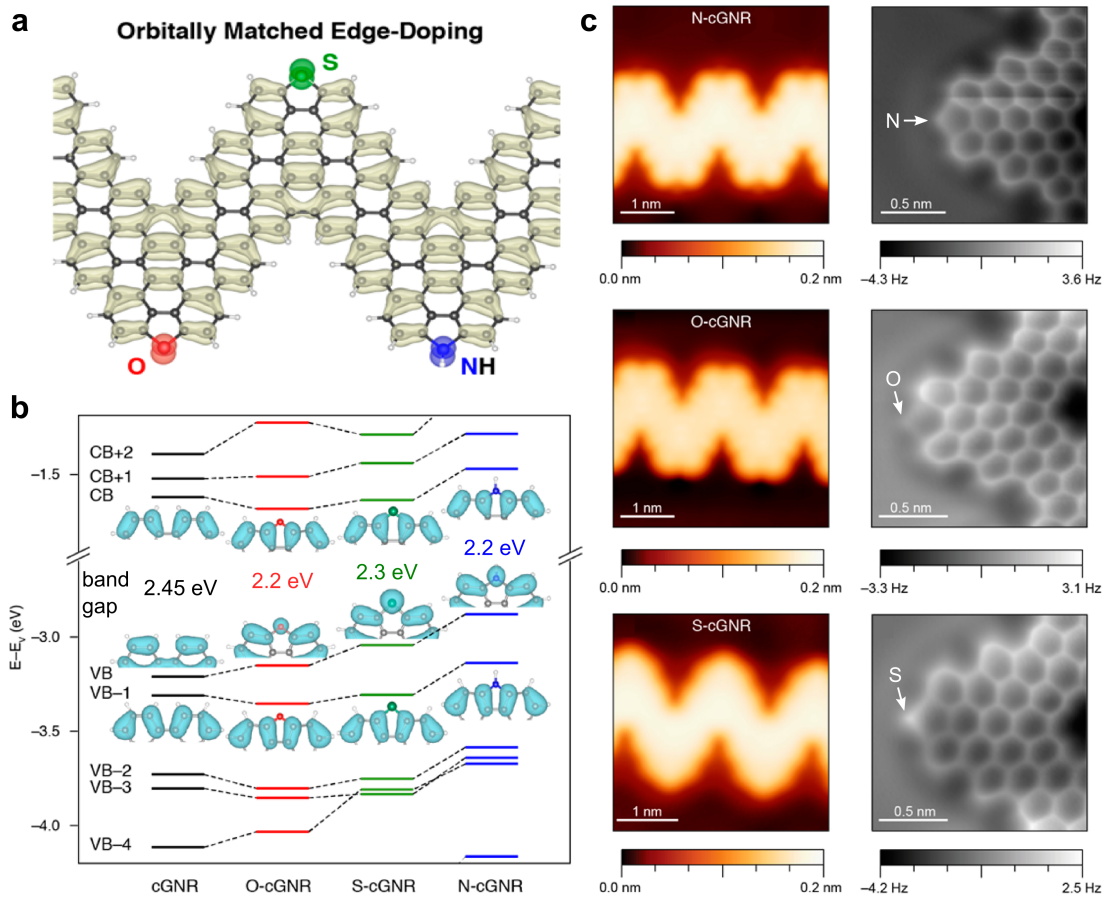


Figure 2.13: Band-gap engineering of chevron GNRs by different dopants. (a) Schematic illustration of orbitally matched edge doping by trigonal planar dopant heteroatoms O, S, and N. (b) Theoretically calculated energy levels around the Fermi level at the Γ point of pristine (cGNR, black) and oxygen-doped (O-cGNR, red), sulfur-doped (S-cGNR, green), and nitrogen-doped (N-cGNR, blue) chevron GNRs. The cyan insets are the wavefunctions of each ribbon at conduction band (CB), valence band (VB), and VB−1 near the GNR edges. (c) STM topographic images (left) and nc-AFM frequency-shift images (right) of N-cGNR, O-cGNR, and S-cGNR. The dopant atoms are highlighted by arrows. Adapted from Ref. [129].

Besides using nitrogen as dopant atom, researchers have also extensively explored using sulfur and boron [130–133] . Boron doping not only shifts the bands, but also introduces donor or acceptor states in the energy gap [132]. The effect of doping concentration has also been clarified [133]. Recently, many research groups have investigated the doping of GNRs with multiple heteroatoms, such as in the oxygen–boron–oxygen- (OBO-) doped chiral GNRs [134], boron–nitrogen- (BN-) doped 7-AGNRs [135], and nitrogen–boron–nitrogen- (NBN-) doped ZGNRs [136].

In summary, the development of chemical-modification strategies, including doping and edge decoration, has tremendously enriched the toolbox of tuning electronic properties of GNRs, and laid the foundation for future applications of GNRs in electronic and spintronic devices.

2.1.3.3 Heterostructures

So far, we have examined a variety of approaches to modify the electronic properties of a single type of GNR. By combining different GNRs, we can create heterojunctions with diverse new properties that can have direct applications in optoelectronic and electronic devices [52, 137–139], such as diodes, transistors, and solar cells. Herein we will give an brief overview of the latest experimental development of GNR-based heterojunctions. As introduced in the last section, doped chevron GNRs have shifted bands compared with pristine GNRs. Such a difference can be adopted to fabricate type-II heterojunctions. For example, as shown in Figure 2.14, Cai et al. integrated the pristine and nitrogen-doped chevron GNRs [140]. The doped part has a narrower band gap than the pristine GNRs, and in the meantime both the conduction band and valence band are positioned at lower energies. The LDOS map along the ribbon in Figure 2.14e exhibits a typical alignment of type-II heterojunctions. The interface region contains a built-in electric field that exceeds $2 \times 10^8\,\mathrm{V/m}$, a field which surpasses the strength of that in traditional semiconductor p–n junctions by at least two orders of magnitude [140]. Therefore we can envision the promising application of such heterojunctions in photovoltaics as well as electronic components that involve p–n junctions, where the depletion region is always the limiting factor [140].

Similarly, Nguyen et al. designed a heterojunction between chevron GNRs and oxygen-doped chevron GNRs that were derived from a single precursor [141]. In contrast, Bronner et al. fabricated a novel heterojunction between chevron GNRs and laterally extended chevron GNRs, which displays type-I heterojunctions behaviour [142]. Besides chevron GNRs, armchair GNRs are also a viable

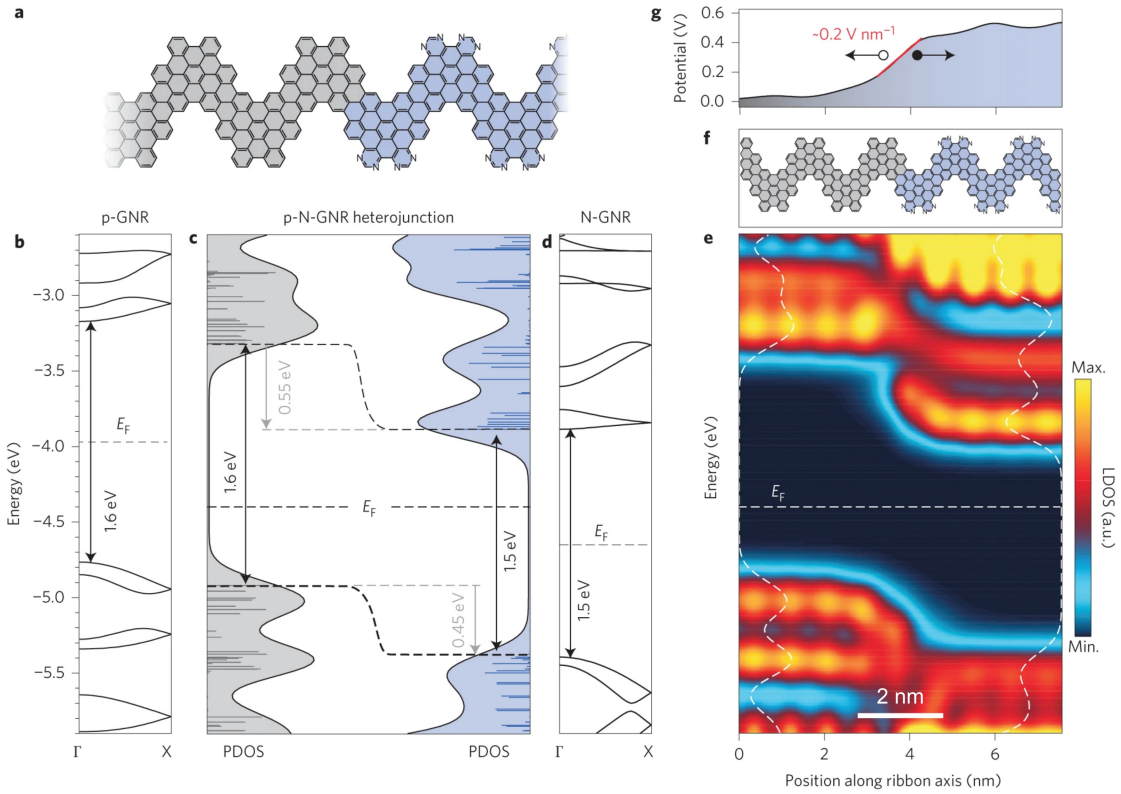


Figure 2.14: Heterojunction built from pristine and N-doped chevron GNRs. (a) Structure of the heterojunction between pristine GNR (p-GNR, grey) and nitrogen-doped GNR (N-GNR, blue). (b, d) The band structure of p-GNR (b) and N-GNR (d), taking vacuum energy as zero. (c) Projected density of states (PDOS) of the p-GNR part (left, grey) and N-GNR part (right, blue) of the heterojunction. The conduction band and valence band are shifted downwards by 0.55 eV and 0.45 eV, respectively. (e–g) LDOS (e) for the heterojunction segment in (f), showing ~ 0.5 eV band offset across the ~ 2 nm interface region. A high electric field of about 0.2 V/nm is built up, as illustrated by the potential slope in (g). The electrons and holes can therefore be separated efficiently, indicated by the circles and directed arrows in (g). Adapted from Ref. [140].

platform for heterostuctures. For example, Wang et al. creates a 7–14–7 AGNRs heterostructure by fusing 7-AGNRs [143]. Rizzo et al. synthesised quantum dots from 7-AGNRs and 9-AGNRs, where the quantum dots host localised interface states [144]. As will be elucidated in Section 2.2, these interface states are related to the topological phases in GNRs.

Finally, it bears mentioning that more heterostructures have been explored over the past decade, besides the examples listed above [145–148]. Researchers have significantly improved the techniques of producing heterostructures with

atomic precision, and also have proposed abundant novel structures with innovative functionalities. In the next stage it will be necessary to study the devices built from these heterostructures.

2.1.4 The effect of finite length

In condensed-matter physics, we always use periodic boundary conditions (PBCs) to describe crystals. Since GNRs are 1D crystals, PBC imply that the ribbon is infinite. In reality, however, ribbons are always finite. Early theoretical studies suggested that the properties of finite GNRs longer than 40 nm are similar to those of the infinite ribbon [149]. The truncation of some GNRs, such as AGNRs, will lead to end states, which cannot be overlooked for nanoscale GNRs. The emergence of zigzag end states (also known as Tamm states [150, 151]) of AGNRs had attracted the interest of theorists before the bottom-up synthesis of AGNRs. Shemella et al. noticed that the zigzag end states are more localised in AGNRs with larger band gaps, such as 7-AGNRs, but more delocalised in AGNRs with narrower band gaps, such as 8-AGNRs [152]. Ijäs et al. carried out a systematic study of the end states in 7-AGNRs, and pointed out that the energy splitting between end-localised states decays exponentially with respect to ribbon length [153]. Moreover, the zigzag end states are actually spin polarised, and the two end states couple to each other antiferromagnetically in the ribbon's ground state. This can be intuitively understood from a Hubbard dimer model that includes a kinetic exchange term (electron hopping) and a Coulomb interaction term. Electrons prefer to have opposite spins (antiferromagnetic coupling) on the two sites to minimise the total energy through the kinetic exchange, as opposed to having the same spin on the two sites (ferromagnetic alignment) which would prevent hopping due to the Pauli exclusion principle. For an AGNR, the kinetic exchange term dominates in the ground state and favours an antiferromagnetic alignment of the two spin-polarised end states.

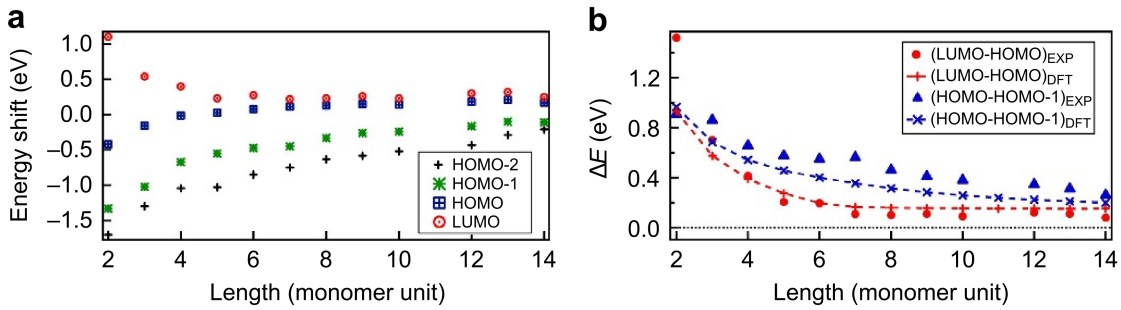


Figure 2.15: Energy levels of finite 5-AGNRs as a function of ribbon length. (a) Energies of the molecular orbitals from HOMO−2 to LUMO as a function of ribbon length. (b) Energy gaps obtained from experiments and DFT as a function of ribbon length. Adapted from Ref. [108].

With the advent of atomically precise on-surface synthesis, many of the electronic properties of GNRs can be experimentally validated. For instance, Koch et al. measured the conductance of a single 7-AGNR on a gold substrate using an STM tip, and identified the effect of localised end states [150]. They also mapped the spatial distribution of the ribbon's end states. Bronner et al. used high-resolution electron-energy-loss spectroscopy (HREELS) and two-photon photoemission (2PPE) techniques to study the electronic structure of 7-AGNR on an Au(111) surface, and they also found the signature of the in-gap end states [151]. Kimouche et al. synthesised 5-AGNRs of various lengths on gold surfaces [108]. They determined the energy levels of these molecules by STS. As presented in Figure 2.15, the highest occupied molecular orbital (HOMO) and lowest unoccupied molecular orbital (LUMO) (the end states) converge faster with ribbon length compared with the bulk states lower in energy. The measured energy gaps are also in line with theoretical calculations. Besides 5-AGNRs, the relationship between energy gap and ribbon length has been tested in multiple GNRs [154–157].

For GNRs synthesised on surfaces, the electronic structures are usually strongly hybridised with the metal substrates [154]. The intrinsic electronic properties of GNRs can be unravelled by transferring the ribbon to an insulating surface, such as a NaCl crystal. Wang et al. have studied the properties of the zigzag

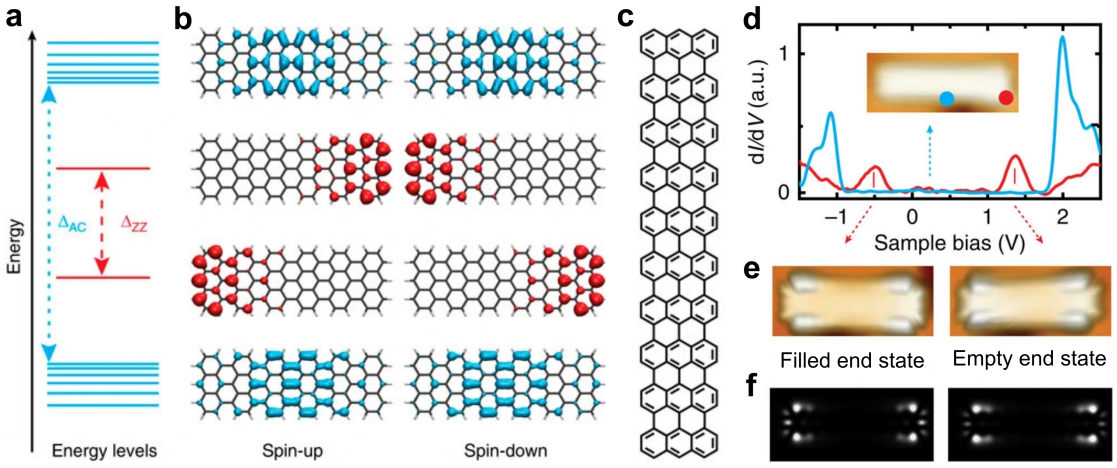


Figure 2.16: Zigzag end states in finite 7-AGNRs. (a) Energy-level diagram of a finite (7,12)-GNR, where localised end states are plotted in red lines. Δ_{AC} and Δ_{ZZ} indicate the bulk energy gap and end-state splitting, respectively. (b) DFT-calculated spin orbitals of localised end states (red) and their energetically similar bulk states (blue). (c) Structure model of a (7,20)-GNR. (d) dI/dV spectra recorded in the zigzag terminus (red) and centre of armchair edge (blue) of a decoupled (7,20)-GNR on a NaCl crystal, as shown in the STM topographic image in the inset. (e) STM topographic image with higher resolution, showing the occupied (left) and unoccupied (right) end states. (f) Calculated LDOS map at 4 Å above the ribbon. Adapted from Ref. [154].

end states in 7-AGNRs using this technique [154]. As shown in Figure 2.16a, the energy levels and Kohn–Sham orbitals of (7,12)-GNRs calculated from DFT are depicted. (7,12)-GNR stands for a 7-AGNR with 12 repeating units, and all the other ribbons in this paper are named in the same convention. The bulk energy gap Δ_{AC} will converge to the band gap of an infinite ribbon as the ribbon length increases. A significant splitting was found between the empty and filled end states, as labelled by Δ_{ZZ}. The mean-field Hubbard model and non-interacting Kohn–Sham DFT tend to severely underestimate this splitting [153]. This splitting can also be destroyed if ribbons interact with gold substrates, but become observable when they are placed on NaCl crystals. As shown in Figure 2.16d, differential conductance measurements and STM topographic images revealed the end states and energy splitting of (7,20)-GNRs, and are also corroborated by theoretically calculated LDOS. The end states of 7-AGNRs were investigated for ribbons with different lengths. As illustrated in Figure 2.17, the zigzag terminus states remain localised

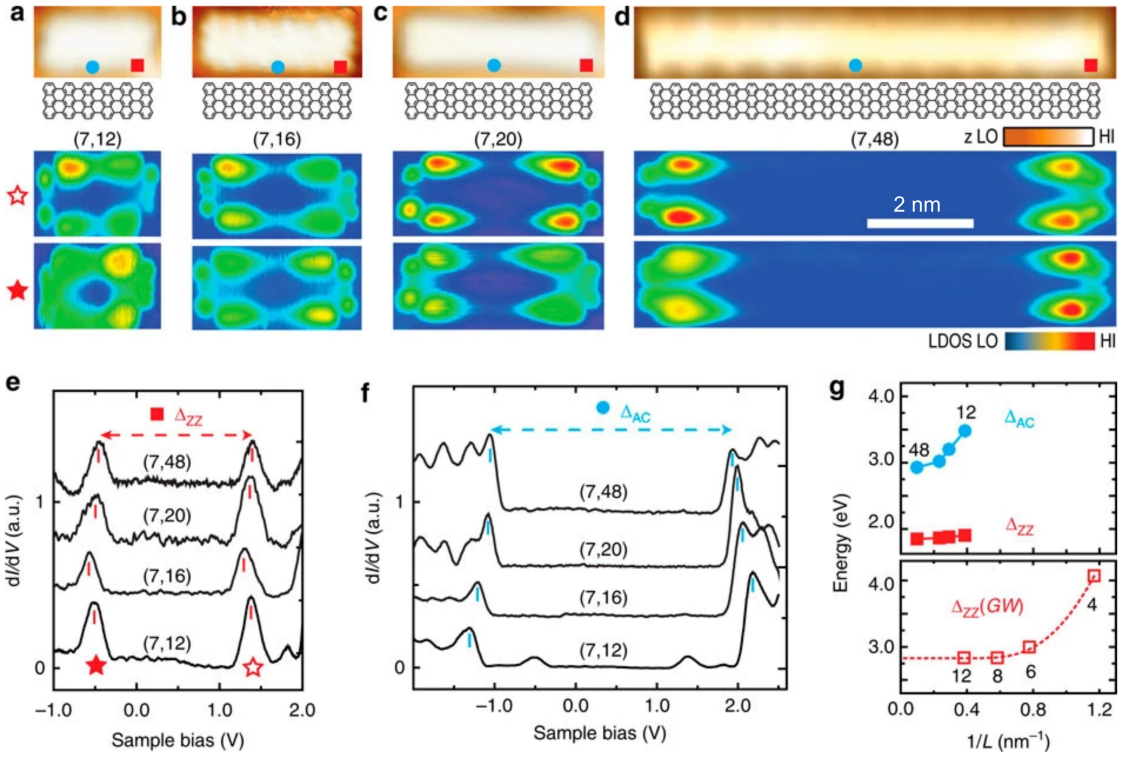


Figure 2.17: Zigzag end states of 7-AGNR with different lengths. (a–d) STM topography images (top), structure models (middle), STS maps of occupied and unoccupied end states (bottom) of (7,12)-, (7,16)-, (7,20)-, and (7,48)-GNRs. LO and HI in the colour bar stand for low and high, respectively. (e, f) dI/dV spectra measured at the end (e) and centre (f) of the ribbons in (a–d). (g) DFT-calculated bulk energy gap Δ_{AC} and end-state splitting Δ_{ZZ} (top) and GW-calculated Δ_{ZZ} as a function of inverse ribbon length (bottom). The dashed line is a guide to the eye. Adapted from Ref. [154].

for all ribbons. The bulk energy gap gradually converges for longer ribbons because of reduced longitudinal confinement, whereas the end-state splitting is not sensitive to the length for the measured ribbons. GW calculations in Figure 2.17g show that the end-state splitting has already converged in shorter ribbons like (7,8)-GNR.

In fact, these zigzag end states can be understood in a similar way as the zigzag edge states introduced in Section 2.1.2. They always appear at the zigzag boundary of a honeycomb lattice. Likewise, the zigzag end states are also spin-polarised. The magnetic nature of end states has been justified by the characteristic Kondo peaks in STM lifting measurements [158]. The interplay between the two magnetic end states has been studied theoretically, and may have profound potential for spin qubits [159]. Su et al. have also explored coupling the end states with porphyrin,

which opens prospects for applications in optoelectronics and gas sensing [160]. Finally, it is worth noting that the end states actually have a topological nature. In the next section we will introduce the theory of topological phases in GNRs, where we will formulate the end states in the theoretical framework of topology.

2.2 Band topology of GNRs

2.2.1 The arise of topology in condensed matter

The concept of topology was introduced to condensed-matter physics when physicists realised that Landau's approach of phase classification based on spontaneous symmetry breaking failed in some cases [43]. Since the discovery of the quantum Hall (QH) effect (referring to the integer QH effect unless specified) in the 1980s [161], it was found that the QH state did not conform to any previous theoretical framework. Consequently, an alternative classification approach was adopted, centered on topological order [162, 163]. Traditionally, the electronic structure of solids is described by the energy-band theory. The band theory rests upon the discrete translational symmetry in crystals. The eigenstates of the Hamiltonian are so-called Bloch states $|u_n(\boldsymbol{k})\rangle$. The eigenvalues $E_n(\boldsymbol{k})$ outline energy bands, which together create the band structure. The band structure is filled up to Fermi surface by electrons. If the Fermi level falls into a gap between two bands, the filled valence band and the empty conduction band are separated, and thus the material is considered an insulator. In contrast, if the Fermi surface passes through an energy band, then the material is in a metallic phase. Semiconductors have smaller band gaps, but they are considered to be in the same phase as insulators. The QH effect, however, falls entirely out of this paradigm.

The experimental setup to realise the QH state is illustrated in Figure 2.18a. A strong magnetic field is applied normal to the plane of a two-dimensional electron gas (2DEG) device, which is fabricated from semiconductors heterostructures, and the

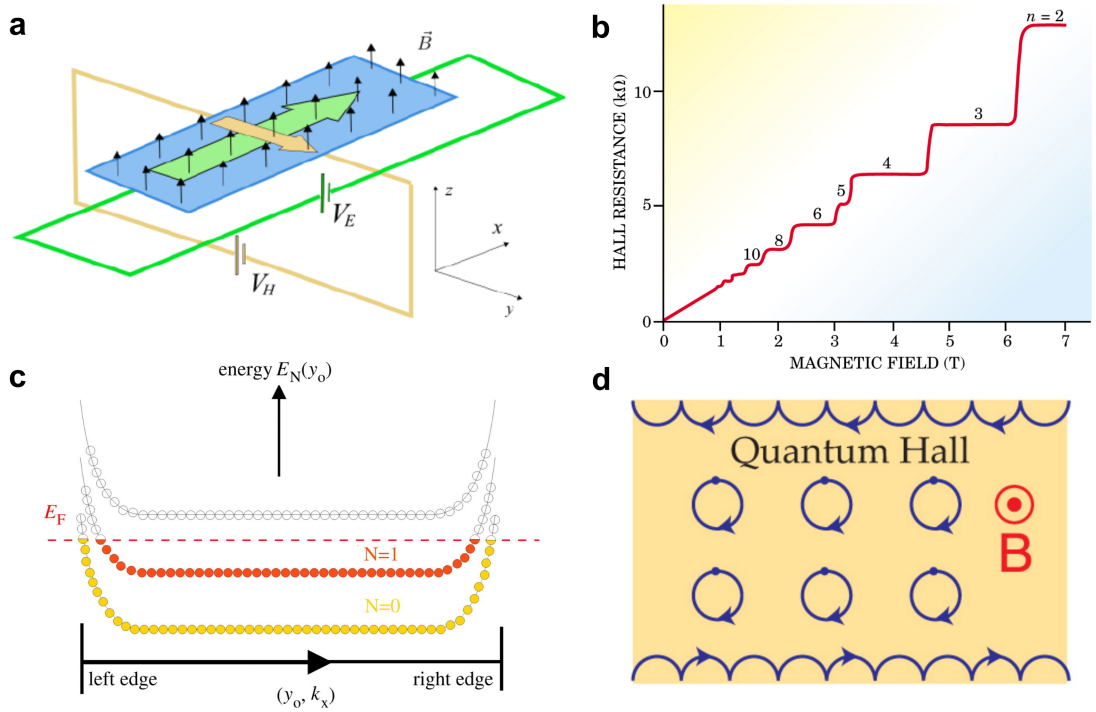


Figure 2.18: Quantum Hall effect. (a) Schematic diagram illustrating the experimental arrangement for the QH effect. Two-dimensional electron gas is subjected to magnetic field (black arrows) directed perpendicular to the sample. Electromotive force (green arrow) runs along the x-axis, while the resulting Hall current (yellow arrow) flows in the y-direction. Adapted from Ref. [164]. (b) Hall resistance (reciprocal of conductance) of the sample at low temperatures as a function of the perpendicular magnetic field. The Hall conductance at plateaus equals exactly Ne^2/h, with N marked in the graph. The resistance unit is defined as approximately 26 kΩ. Figure adapted from Ref. [165], and data reproduced from Ref. [166]. (c) Landau levels of the device. The bulk is gapped and insulating, whereas at the left and right boundaries electrons have non-zero and opposite velocities. The number of filled Landau levels is related to the conductance quantisation. Adapted from Ref. [167]. (d) Cyclotron orbitals of electrons in QH device. The electrons at each boundary have a skip motion and transport in one direction. Adapted from Ref. [168].

electrons are confined within a two-dimensional plane. The voltage is applied along the x direction and the Hall conductance σ_{xy} is measured along the y direction at low temperatures. Strikingly, in Figure 2.18b, one can find a staircase-like quantised Hall conductance. In the plateaus the Hall conductance is equal to Ne^2/h, and the precision reaches, incredibly, one part in 10^9 [167]. This counterintuitive phenomenon can be explained by the Landau levels, as depicted in Figure 2.18c. When we include the strong magnetic field in the Bloch Hamiltonian, the energy

bands in the bulk become quantised Landau levels with energy $E_n = \hbar\omega_c(n + 1/2)$. The occupied levels are separated from the empty levels by a sizeable energy gap. When the Fermi energy aligns with a Landau level, electrons can scatter between different states within the same level, causing a peak in the material's longitudinal resistance. When the Fermi energy lies between two Landau levels, the longitudinal conductance is essentially zero, since there is no available state for electrons to scatter into. The bulk sample behaves like an insulator. Meanwhile, the confinement potential at the edges, which keeps electrons within the 2DEG, interacts with the magnetic field and modifies the Landau levels. This interaction causes the Landau levels to bend upwards or downwards near the edge, forming what are known as edge channels or edge states. These edge channels are spatially separated from the bulk and are localised at the sample boundaries. The electric current flows in one direction along the edge. The prohibited backscattering thus avoids the heat dissipation. The electric current can be visualised in a classical orbital picture, as shown in Figure 2.18d. The electrons in the bulk move in circular orbitals, while the electrons at the edge have a skipping motion and are able to circumvent defects or barriers.

Nevertheless, the Landau levels fall short in explaining the robustness and precision of the QH conductance's quantisation. The topological nature of the QH effect was revealed by Thouless, Kohmoto, Nightingale and den Nijs (TKNN) in their seminal paper [162]. Here we will introduce the concept of topology briefly. Topology is a branch in mathematics that describes the properties of objects that remain unchanged under continuous deformations, such as twisting, stretching, or bending. Topology focuses on the qualitative aspects of shapes, disregarding such details as lengths, angles, and distances. Topologically equivalent objects can be classified into a group using a common topological invariant, and they can be smoothly transformed into each other without tearing or gluing. A classic example is that a donut and a coffee cup are considered topologically equivalent because they each have a single hole. A graphical representation of a topological invariant

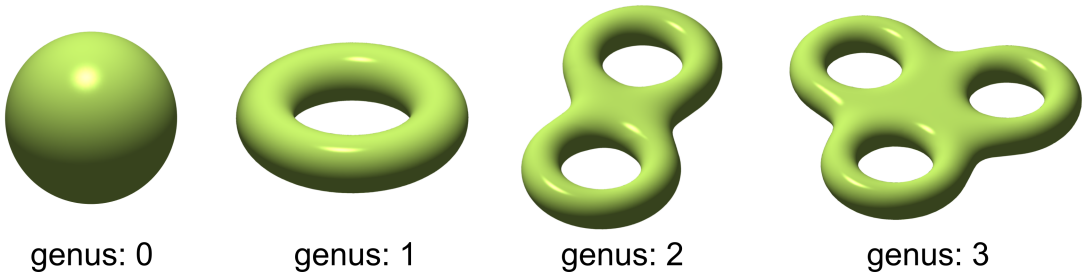


Figure 2.19: Torus surfaces with genus of 0 to 4. The genus counts the number of holes in the geomtry. Adapted from Ref. [169].

is illustrated in Figure 2.19. The geometrical surfaces are labelled by the number of holes, called the genus. The genus g is related to Euler characteristic χ that can be calculated through integration of Gaussian curvature $\boldsymbol{G}$ over the surface $\boldsymbol{S}$ according to the Gauss–Bonnet theorem:

$$\chi = 2 - 2g = \frac{1}{2\pi} \int_{\boldsymbol{S}} \boldsymbol{G} \, \mathrm{d}\boldsymbol{S}. \tag{2.1}$$

The Euler characteristic χ remains the same when the surfaces are smoothly deformed, as long as the number of holes is kept the same, and thereby can be regarded as a topological invariant.

It is remarkable that TKNN revealed the connection between the Hall conductance and the topological invariant, Chern number, which has similar properties to the Euler characteristic [162]. By using the Kubo formula, they derived the expression of Hall conductance σ_{xy}:

$$\sigma_{xy} = \frac{e^2}{h} \sum_n C_n = N \frac{e^2}{h}, \tag{2.2}$$

where the Chern number C_n of band n is given by

$$C_n = \frac{1}{2\pi} \int_{\mathrm{BZ}} \boldsymbol{\Omega}_n(\boldsymbol{k}) \, \mathrm{d}\boldsymbol{k}. \tag{2.3}$$

In the above equation, the integration of Berry curvature $\boldsymbol{\Omega}_n(\boldsymbol{k})$ is called the Berry phase, as introduced by Michael Berry in 1984 [170]. The Berry curvature

is defined as the curl of the Berry connection $A_n(\boldsymbol{k})$, which is calculated from the Bloch wavefunctions $|u_n(\boldsymbol{k})\rangle$:

$$\boldsymbol{\Omega}_n(\boldsymbol{k}) = \nabla \times \boldsymbol{A}_n(\boldsymbol{k}); \tag{2.4}$$

$$\boldsymbol{A}_n(\boldsymbol{k}) = \mathrm{i}\langle u_n(\boldsymbol{k})|\nabla_{\boldsymbol{k}}|u_n(\boldsymbol{k})\rangle. \tag{2.5}$$

It should be highlighted that Equation (2.2) perfectly reproduced the experimental results shown in Figure 2.18b. The integer number observed in experiments is actually the sum of Chern numbers for all occupied Landau levels, also called the TKNN number [162]. And the expression for the Chern number in Equation (2.3) closely resembles that of the Euler characteristic in Equation (2.1). In fact, the Chern number has deep roots in fiber bundles, as it measures the nontriviality of the mapping between the base parameter space defined by the Brillouin zone and the Hilbert space that Bloch fibers inhabit [171]. The quantisation of the Chern number is similar to the topological invariant χ defined for geometrical surfaces. Therefore the robustness of the Hall conductance's exact quantisation is due to the fact that the Chern number (or Chern invariant) remains the same when the Hamiltonian is smoothly affected by defects or other perturbations, as long as the band gap does not close. On the other hand, the calculation of the topological Chern invariant involves Bloch wavefunctions, which are the eigenstates of the Bloch Hamiltonian, whereas conventional band theory uses only the eigenvalues of the Bloch Hamiltonian to explain the electronic properties. In fact, the Berry phase was later found to cause various physical phenomena, including quantum (anomalous, spin) Hall effects, electronic polarisation, orbital magnetism, and quantum charge pumping. These phenomena have been comprehensively reviewed by Xiao et al. [172].

In 1988, Haldane made the seminal discovery that, in order to realise topological states in 2D insulators, it is not necessary to use a strong magnetic field, but the more fundamental requirement is the breaking of time reversal symmetry (TRS) [173]. In the original honeycomb system, the Berry curvatures at $\mathbf{K}$ and $\mathbf{K}'$ are opposite and

cancel each other upon integration [172]. Haldane devised a toy model to achieve TRS-breaking by applying a periodic magnetic field in the honeycomb lattice, but with no net flux. This modification can make the Berry curvatures at two valleys have the same sign. The full form of Haldane's Hamiltonian is written as

$$H = t \sum_{\langle i,j \rangle} c_i^\dagger c_j + M \sum_i \xi_i c_i^\dagger c_i + t' \sum_{\langle\langle i,j \rangle\rangle} \mathrm{e}^{\mathrm{i}\phi_{ij}} c_i^\dagger c_j, \tag{2.6}$$

where t and t' are nearest-neighbour $\langle i, j \rangle$ and next-nearest-neighbour $\langle\langle i, j \rangle\rangle$ hopping amplitudes, respectively. The creation and annihilation operators for electrons at sites i and j are denoted as $c_i^\dagger$ and c_j, respectively. The staggered on-site potential is represented by $M\xi_i$, with ξ_i being either +1 or −1 depending on whether site i belongs to sublattice A or B. This terms breaks the sublattice symmetry and opens a band gap at Dirac point. In the third term, we use ϕ_{ij} to represent the phase acquired by an electron hopping between next-nearest-neighbour sites i and j, determined by the direction of hopping, and this term breaks the time reversal symmetry. By doing similar calculations as for the QH effect using the Haldane Hamiltonian, we will also get a non-zero Chern number for occupied bands. This type of insulator is also called a Chern insulator. The Haldane model is a close relative to the QH effect, where broken TRS in 2D insulators leads to a non-vanishing Chern number and chiral metallic surface states, as shown in Figure 2.20. Importantly, in the models we have mentioned above, we have calculated the topological invariant from the bulk Hamiltonian, which characterises the number of gapless modes at the boundaries. This rule is called the bulk–boundary correspondence (BBC), and it is a unifying feature of all topological states. In the terminology of band topology, systems described by the Haldane Hamiltonian are trivial if they have null topological invariants, while those with non-zero topological invariants are non-trivial. We can also regard a vacuum as a topologically trivial insulator, by considering the valence band (positrons) and conduction band (electrons) according to Dirac's relativistic quantum theory [43]. Therefore, for the simply truncated

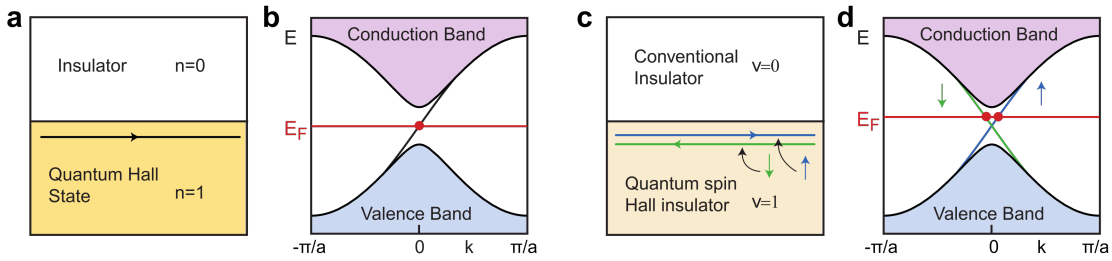


Figure 2.20: Edge modes in quantum Hall and quantum spin Hall state. (a) The chiral edge mode of a quantum Hall state and (b) band structure of a semi-infinite strip governed by Haldane model. The band that connects valence band and conduction band in (b) leads to same unidirectional edge channel as quantum Hall. (c) The pair of spin up and spin down edge modes propagating along opposite direction along the edge and (d) band structure of a graphene system displaying quantum spin Hall state. Adapted from Ref. [43].

system, the interface between a non-trivial topological insulator and a trivial vacuum will host chiral gapless conducting states. More generally, the topological states at any interface between two materials are determined by the difference in topological invariants of the bulk materials on either side.

For many years, Haldane model has stimulated the interests of many physicists and led to a plethora of studies on topological electronic states, especially after the experimental discovery of graphene [1]. In 2005, Kane and Mele uncovered a new class of topological states protected by time reversal symmetry [83, 84]. They developed a model for graphene with spinful fermions, a model that effectively combines two copies of Haldane models with opposite spin projections and a unique intrinsic SOC. The Kane–Mele Hamiltonian is written in the form

$$H = t\sum_{\langle i,j\rangle} c_i^\dagger c_j + M\sum_i \xi_i c_i^\dagger c_i + \mathrm{i}\lambda_{\mathrm{SO}}\sum_{\langle\langle i,j\rangle\rangle} \nu_{ij} c_i^\dagger \sigma_z c_j + \mathrm{i}\lambda_{\mathrm{R}}\sum_{\langle i,j\rangle} c_i^\dagger(\boldsymbol{\sigma}\times\boldsymbol{d}_{ij})_z c_j, \qquad (2.7)$$

where the first and second terms represent the nearest-neighbour hopping and staggered sublattice potential, respectively. These two terms are the same as those in the Haldane model. The third term describes the mirror-symmetric SOC that involves spin-dependent next-nearest-neighbour hopping. In this term, $\nu_{ij} = (2/\sqrt{3})(\boldsymbol{d}_1 \times \boldsymbol{d}_2)_z = \pm 1$, where $\boldsymbol{d}_1$ and $\boldsymbol{d}_2$ are unit vectors along the two bonds through which the electron traverses when hopping from site j to i. The Pauli matrix

σ_z is used to describe the electron's spin. The last term is the nearest-neighbour Rashba SOC term, which arises from a perpendicular electric field or interaction with a substrate [84]. It explicitly breaks the mirror symmetry. The combination of these terms in the Hamiltonian leads to the QSH effect in graphene. The Chern number for spin-up electrons ($C_\uparrow$) and spin-down electrons ($C_\downarrow$) are opposite to each other; therefore the total Chern number satisfies $C = C_\uparrow + C_\downarrow = 0$. Instead, the topological invariant $\mathbb{Z}_2 = (C_\uparrow - C_\downarrow)/2 \bmod 2$ can be defined, which must be either 0 or 1, for topologically trivial and non-trivial insulators, respectively. Unlike the Haldane model, the Kane–Mele model converses S_z, which produces a pair of counterpropagating edge states that have spins locked to their momentum, thus preventing backscattering by non-magnetic impurities. The edge modes of two spin species are depicted in Figure 2.20c. These gapless, helical edge states remain robust against staggered-potential and Rashba spin–orbit perturbations, as long as the bulk gap does not fully close [174]. Nonetheless, a perturbation that breaks TRS, such as a transverse magnetic field, would disrupt the metallic nature of the helical edge [174]. In other words, the Kane–Mele model is protected by TRS. This type of insulator is called a 2D topological insulator.

Although the Kane–Mele model was a revolutionary breakthrough in the field of topological electronic states, the SOC in graphene is extremely weak. Therefore, heavier elements with stronger SOC are more desirable for creating QSH phase. With this intention, Bernevig, Hughes, and Zhang (BHZ) proposed a band-inversion mechanism based on HgTe/CdTe quantum-well structures, in which HgTe is sandwiched between CdTe layers [175]. By tuning the thickness of the HgTe layer, one can invert the band structure, leading to a nontrivial $\mathbb{Z}_2$ invariant. Soon after this theoretical proposal, König et al. conducted experiments and observed convincing signatures of quantum spin Hall states [176]. Later, the $\mathbb{Z}_2$ topology was extended to three-dimensional (3D) structures [177–179], resulting in a multitude of experimental realisations [180–182]. In addition, inspired by the significant progress

of the QH and QSH effects, another type of quantised Hall effect has also been extensively explored, known as the quantum anomalous Hall (QAH) effect. The QAH effect is similar to the QH effect, except that TRS is broken by the insulator's intrinsic ferromagnetism, rather than an external magnetic field. In this sense, the Haldane model can also be classified as a QAH insulator. On the other hand, the chiral edge states in the QAH insulator are spin-polarised, implying that they can be regarded as QSH states with one suppressed spin channel. Several theoreticians proposed various material systems with intrinsic ferromagnetism and strong SOC, which are necessary for the QAH effect [183–185]. Following these, Chang et al. experimentally observed the QAH effect in magnetically doped $(Bi,Sb)_2Te_3$ [186].

In more recent years, the study of topological electronic states has emerged as a thriving field in physics. Just as electrons can have spin up or down in the QSH effect, Dirac fermions in graphene can have pseudospin up or down, corresponding to the two valleys of graphene's band structure, giving rise to quantum valley Hall (QVH) states [48, 99, 187]. The concept of topological insulators, which are protected by abstract symmetry such as TRS, has been further extended to topological crystalline insulators, which are protected by crystal symmetry [188]. With regards to the conceptual framework of the topological phase, theorists have established powerful classification methods based on symmetry and dimensions [189, 190]. Additionally, various computational methods have been proposed to determine the topological phase [177, 191–193], leading to the discovery of a broad range of novel topological materials [194–196]. In recent years, topological phase has been applied to not only various electronic states like semimetals [197], superconductors [198], and spin chains [199, 200], but also other branches of physics, such as photonics [201], mechanics [202], and superfluids [203]. We will not delve into the details of these at this moment. Instead, the following section will concentrate on the topological phases that were discovered in GNRs.

2.2.2 Topological classification of GNRs

In Section 2.1, we discussed various aspects of the electronic structures of GNRs. It was later established that conventional band theory falls short in explaining the electronic states in GNRs. Hence, topological band theory needed to be adopted. Prior to reviewing the theory of topological classification of GNRs, we must introduce the Su–Schrieffer–Heeger (SSH) model, which is the simplest example of topological phase in 1D. Initially proposed in 1979 by Su, Schrieffer, and Heeger [204] to describe the electronic structure of polyacetylene (a polymer composed of alternating single and double carbon–carbon bonds), this model has since become a paradigmatic model for studying topological insulators and other topological phenomena in condensed-matter physics [205].

The SSH model considers a chain of carbon atoms, with each atom interacting with its nearest neighbours through two distinct hopping parameters, v (intracell) and w (intercell). The structural model is presented in Figure 2.21. The SSH Hamiltonian is written as

$$H = \sum_n v c_B^\dagger(n) c_A(n) + w c_B^\dagger(n) c_A(n+1) + \text{h.c.}, \tag{2.8}$$

where $c_{A/B}^\dagger(n)$ and $c_{A/B}(n)$ are the creation and annihilation operators of atom A/B in the n-th unit cell, and h.c. means hermitian conjugate. The band structure can be solved analytically by diagonalising the momentum-space Hamiltonian $H(k)$,

$$H(k) = \begin{pmatrix} 0 & v + w\mathrm{e}^{-\mathrm{i}k} \\ v + w\mathrm{e}^{\mathrm{i}k} & 0 \end{pmatrix}. \tag{2.9}$$

The band-gap size depends on the difference between the hopping parameters v and w. Hence, the SSH chain can be either metallic or insulating based on this difference.

A key feature of the SSH model is its topology. Depending on the relative strength of their hopping parameters, systems can have exactly identical band structures but belong to distinct topological phases. As shown in Figure 2.22, the band structures in the two phases are identical, and they cannot be distinguished

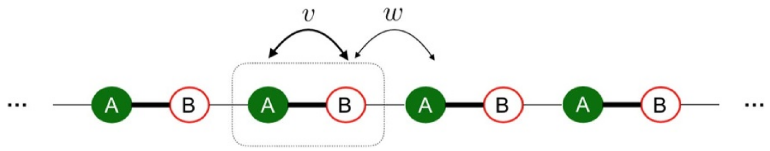


Figure 2.21: Structural representation of the SSH model, where v and w represent the intracell and intercell hopping amplitudes, respectively. Adapted from Ref. [174].

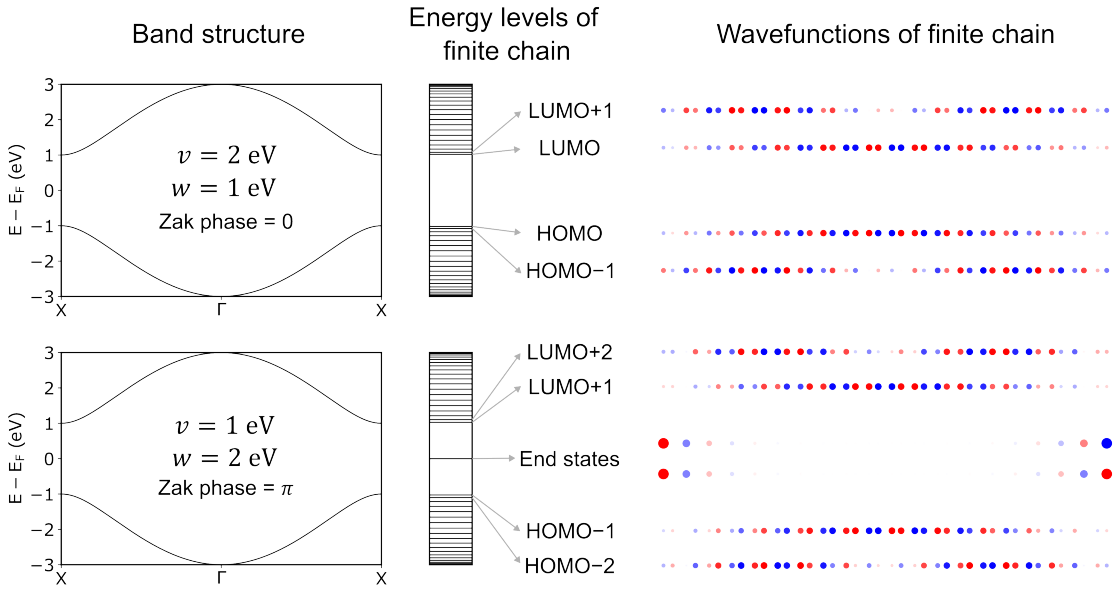


Figure 2.22: SSH model in topologically distinct phases. The model with $v = 2\,\text{eV}$, $w = 1\,\text{eV}$ is trivial and has no end states. The model with $v = 1\,\text{eV}$, $w = 2\,\text{eV}$ is nontrivial and has a pair of localised end states. The finite SSH chain in both cases consists of 20 unit cells.

from each other using conventional energy-band theory. The distinction between the two systems becomes apparent when considering their topological phases, which can be revealed by calculating the Berry phase, using an equation similar to Equation (2.3). For 1D systems, the Berry phase is also referred to as the Zak phase, named after Joshua Zak [206], and it can be determined using

$$\gamma_n = \int_{\text{BZ}} A_n(k)\,\mathrm{d}k \mod 2\pi, \quad A_n(k) = \mathrm{i}\langle u_n(k)|\nabla_k|u_n(k)\rangle, \tag{2.10}$$

where n represents the n-th band, and mod 2π means the value takes either 0 (trivial) or π (nontrivial). This phase quantifies the Berry phase accumulated by an electron as it traverses the Brillouin zone in reciprocal space. For the two-band SSH model, we only calculate the Zak phase γ for a single occupied band, resulting in 0

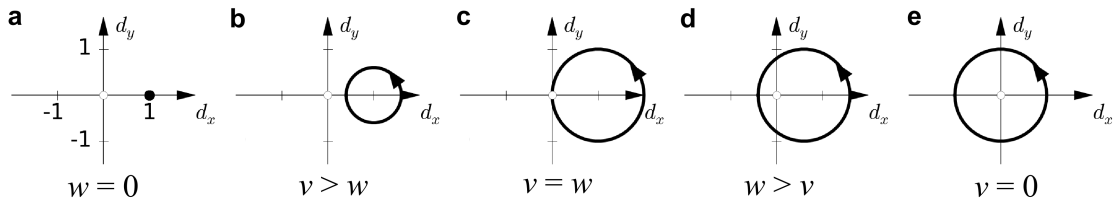


Figure 2.23: Winding number of the SSH model. The trajectory of the endpoints of vector $\mathbf{d}(k)$ defined by momentum-space Hamiltonian is plotted with different parameter settings: (a) $v = 1$, $w = 0$; (b) $v = 1$, $w = 0.6$; (c) $v = w = 1$; (d) $v = 0.6$, $w = 1$; (e) $v = 0$, $w = 1$. Adapted from Ref. [207].

and π for the two cases in Figure 2.22. In the topologically nontrivial phase, the system exhibits localised end states. These end states are robust against disorder and perturbations, which is a characteristic feature of topological insulators.

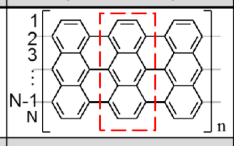
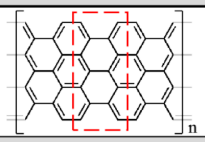
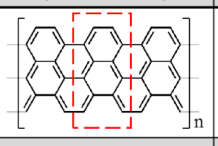
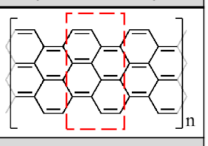
Another way to characterise the topological phase of the SSH model is using the so-called winding number. The momentum-space Hamiltonian, Equation (2.9), can be written in a basis spanned by the Pauli matrices:

$$H(k) = \mathbf{d}(k) \cdot \boldsymbol{\sigma} = d_x(k)\sigma_x + d_y(k)\sigma_y, \quad d_x(k) = v + w\cos k, d_y(k) = w\sin k. \quad (2.11)$$

Following this, one can get a circle by plotting the path of the endpoint of vector $\mathbf{d}(k)$ as k changes from 0 to π, as illustrated in Figure 2.23. The winding number denotes the number of times that the circle winds around origin. The cases where $v = 1$, $w = 0.6$ and $v = 0.6$, $w = 1$ will result in equivalent band structures, but the winding numbers are 0 and 1 for the two cases, respectively, as shown in Figure 2.23b and Figure 2.23d. When the circle passes through the origin, the system is gapless, and it is at the critical point of a topological phase transition.

We are now ready to introduce topological phases in GNRs, which, like SSH chains, are 1D periodic systems. The Louie group pioneered the study of topological properties of GNRs. In a seminal paper published in 2017, the Louie group calculated the Z_2 invariant of armchair GNRs with different unit-cell geometries using an analytical approach [12]. The Zak phase of GNRs is obtained by integrating the Berry connection in the 1D Brillouin zone using Equation (2.10), as before. The

Table 2.1: $\mathbb{Z}_2$ topological classification of AGNRs with different unit-cell shape and termination type. The number of rows of carbon atoms is denoted as N. The red dashed rectangle in the second row highlights the bulk unit cell. The bracket indicates the specific termination that is commensurate with the unit cell. The $\lfloor\ \rfloor$ sign in last row denotes the floor function. Adapted from Ref. [12].

Termination type	Zigzag (N = Odd)	Zigzag' (N = Odd)	Zigzag (N = Even)	Bearded (N = Even)
Unit cell shape				
Bulk Symmetry	Inversion/mirror	Inversion/mirror	Mirror	Inversion
Z_2	$\frac{1+(-1)^{\lfloor\frac{N}{3}\rfloor+\lfloor\frac{N+1}{2}\rfloor}}{2}$	$\frac{1-(-1)^{\lfloor\frac{N}{3}\rfloor+\lfloor\frac{N+1}{2}\rfloor}}{2}$		$\frac{1-(-1)^{\lfloor\frac{N}{3}\rfloor}}{2}$

Zak phase can be separated into two parts: the intracellular and intercellular Zak phase. Only the latter is quantised to 0 or π and is appropriate to use to characterise the topological phase [208]. The $\mathbb{Z}_2$ value can then be computed from the (intercellular) Zak phase using

$$(-1)^{\mathbb{Z}_2} = \exp\left(\mathrm{i}\sum_n \gamma_n\right), \tag{2.12}$$

where the sum runs over all occupied bands. Besides the approach using numerical integration of the Berry connection [209], another method for calculating the $\mathbb{Z}_2$ invariant, discovered by Fu and Kane, uses the parity of wavefunctions at high symmetry points in the Brillouin zone for systems with inversion symmetry [177]. Using the Fu–Kane method, Cao et al. derived analytical formulas for the $\mathbb{Z}_2$ invariants of AGNRs with different unit-cell geometries, as summarised in Table 2.1 [12].

Figure 2.24 provides an example of topological phases in GNRs. Based on the formulas listed in Table 2.1, one can see that both the 9-AGNR and the 7-AGNR, both with zigzag termination, yield $\mathbb{Z}_2 = 1$. Therefore, the two segments forming the heterojunction are topologically equivalent. According to the bulk–boundary correspondence, there should be an even number (including zero) of localised

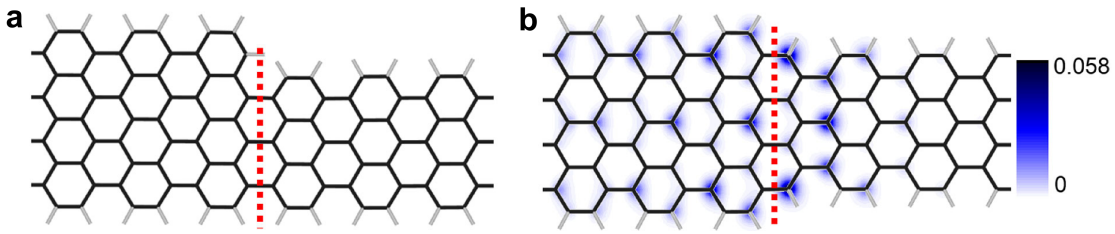


Figure 2.24: Interface between topologically equivalent and distinct GNRs. (a) Both GNR segments adjacent to the interface (red dashed line) have $\mathbb{Z}_2 = 1$. (b) The segments in the left and right side have $\mathbb{Z}_2 = 1$ and 0, respectively. The charge density distribution of the localised interface states is overlaid on top of the structure. Adapted from Ref. [12].

junction states appearing in the middle of the band gap. The DFT calculations, as expected, showed that there is no such junction state for this heterstructure. Interestingly, a lateral shift in the 7-AGNR segment alters its $\mathbb{Z}_2$ index to 0, implying the emergence of an odd number of midgap states localised at the interface between the topologically distinct segments. This prediction was confirmed by DFT results, as shown in Figure 2.24b. Such localised interface states are the 0D counterpart of topological edge states and surface states at the boundaries of 2D and 3D topological insulators. Furthermore, Cao et al. suggested that boron-doping can modify the topological phases of AGNRs [12]. By combining the pristine and boron-doped AGNRs, they designed a 1D antiferromagnetic Heisenberg spin 1/2 chain, enabling the exploration of spin physics within GNRs. Moreover, Majorana fermion states were predicted to exist at the terminations of such spin chain when coupled to a superconductor under specific conditions [210].

The $\mathbb{Z}_2$ classification can predict the appearance of many topological boundary states, but it fails in certain cases. For instance, the 13-AGNR, having $\mathbb{Z}_2 = 0$, hosts two topological end states. The $\mathbb{Z}_2$ index cannot determine if there are no end states or more than one end state. In addition, it can be difficult to accurately determine the $\mathbb{Z}_2$ index of GNRs without spatial symmetry. To resolve this, Jiang et al. proposed a more powerful classification protocol which requires only chiral symmetry [55]. They introduced the chiral-phase index (CPI), also called the $\mathbb{Z}$

index, which eliminates the ambiguity inherent in $\mathbb{Z}_2$ classification and quantifies the number of topological end/interface states within the system. The $\mathbb{Z}$ index can be calculated from the following formula:

$$\begin{aligned}\mathbb{Z} &= -\frac{\mathrm{i}}{\pi}\sum_{n\in\mathrm{occ}}\mathrm{inter}\left(\int_{\mathrm{BZ}}\langle u_{nk}|\hat{\Gamma}\partial_k|u_{nk}\rangle\,\mathrm{d}k\right)\\ &= -\frac{\mathrm{i}}{\pi}\int_{\mathrm{BZ}}\mathrm{d}k\sum_{n\in\mathrm{occ}}\left(\alpha_{nk}^{\dagger}\partial_k\alpha_{nk}-\beta_{nk}^{\dagger}\partial_k\beta_{nk}\right),\end{aligned} \tag{2.13}$$

where "inter" means taking the intercellular part. The A-sublattice part and B-sublattice part of the Bloch wavefunction u_{nk} are denoted as α_{nk} and β_{nk}, respectively. "occ" stands for all occupied bands. The chiral operator $\hat{\Gamma}$ satisfies the following relation:

$$\hat{\Gamma}\begin{pmatrix}\alpha_{nk}\\ \beta_{nk}\end{pmatrix}_E = \begin{pmatrix}\alpha_{mk}\\ \beta_{mk}\end{pmatrix}_{-E} = \begin{pmatrix}\alpha_{nk}\\ -\beta_{nk}\end{pmatrix}_E, \tag{2.14}$$

where E is the eigenvalue of the Hamiltonian. A key distinction between CPI and the intercellular Zak phase defined in Equation (2.10) is that the former takes the difference between the contributions of the A sublattice and B sublattices, while the latter sums them up. Upon application of the above formula to AGNRs, Jiang et al. found a simple relationship between the $\mathbb{Z}$ index and the geometrical descriptors of AGNR unit cells:

$$\mathbb{Z} = N_{\mathrm{notco}} - \left\lfloor\frac{N}{3}\right\rfloor \tag{2.15}$$

where N refers to the number of rows of carbon atoms along the width direction of the AGNR, and N_{notco} counts the rows within the unit cell that contain carbon pairs not connected by σ-bonds, as depicted in Figure 2.25a.

For example, as illustrated in Figure 2.25b, the unit cells on the two sides of the junction, commensurate with the interface, are from a bearded 7-AGNR and a bearded 9-AGNR, respectively. Their $\mathbb{Z}$ indices are -2 and -3, respectively. Hence, by subtracting the $\mathbb{Z}$ indices, we deduce that a single topological junction state exists within the band gap, a prediction which aligns with the DFT calculation

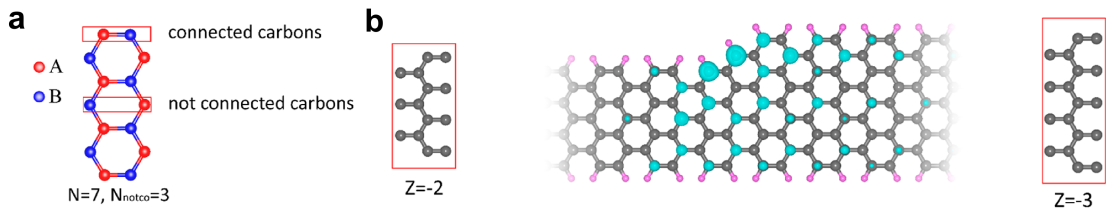


Figure 2.25: Chiral-phase index of AGNRs. (a) The unit cell of a 7-AGNR with zigzag-type termination, where A and B sublattices are depicted in red and blue, respectively. A–B pairs connected and unconnected within the unit cell are highlighted by red rectangles. (b) A heterojunction formed between a bearded 7-AGNR and a 9-AGNR. Unit cells on either side of the junction, which are commensurate with the interface, are depicted. The wavefunction norm of the in-gap junction states calculated from LDA-DFT, coloured in blue, is visualised at a 5% isosurface level. Adapted from Ref. [55].

result. This result inspires the design of junction states with any arbitrary spin quantum number. Moreover, topological classification based on CPI is not solely applicable to GNRs; it can be extended to other 1D structures with chiral symmetry.

In recent years, the investigation of topological phases in GNRs has become a focal point for numerous researchers. After initial studies on AGNRs [12, 211], researchers have conducted comprehensive topological classifications for cove-GNRs [212, 213], chevron-GNRs [212], and cove-zigzag GNRs [214]. Furthermore, Zhao et al. demonstrated that the topological phase in doped AGNRs can be tuned by a transverse electric field [215]. Other research includes the examination of interface magnetism and spin correlations in topologically nontrivial GNRs [216–219], as well as exploration into potential applications of topological states [49, 144]. The subsequent section will review recent experimental advances in studying topological GNRs.

2.2.3 Experimental verification

Prior to theoretically studying topological phases in GNRs, researchers had already observed zigzag end states in various experiments [108, 154, 220], as discussed in Section 2.1.4. Nevertheless, the nontrivial topology of these end states was not recognised until several years later. In 2018, two research teams from Berkeley and

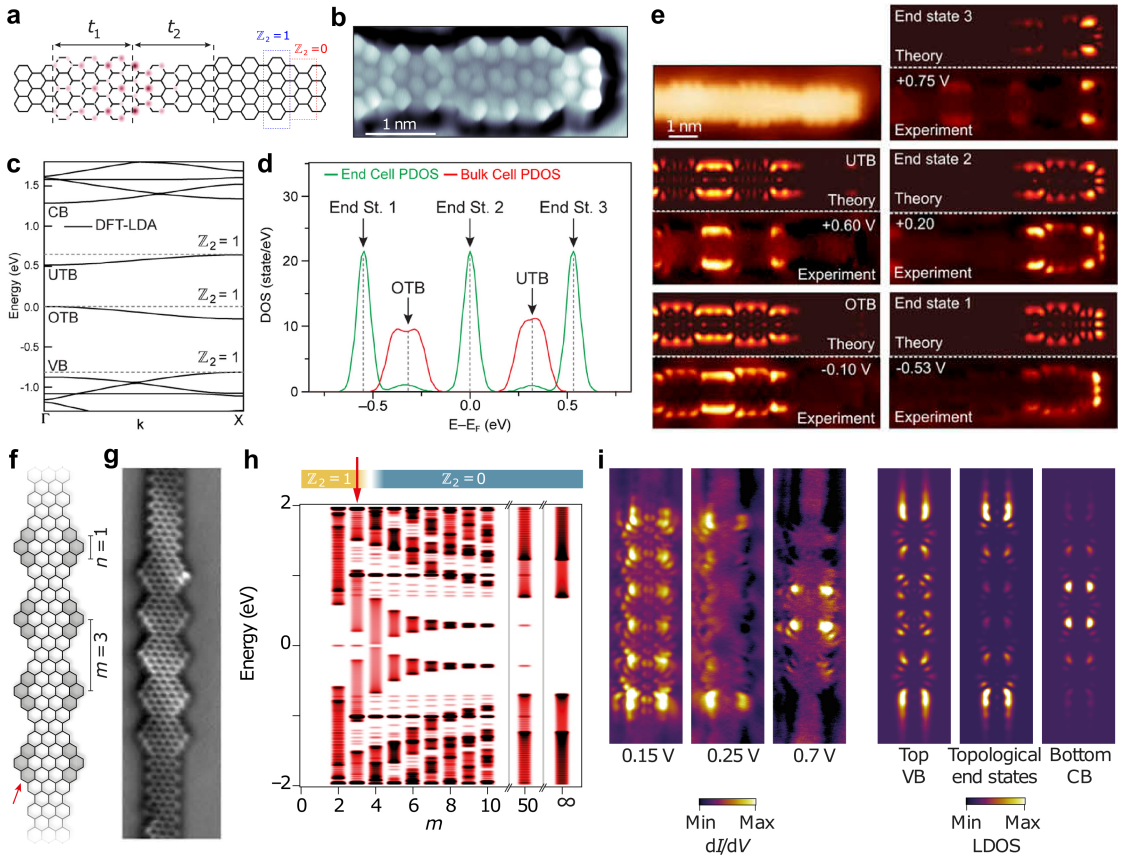


Figure 2.26: Experimental verification of topological states by STM. (a–e) Topological states in a 7/9-AGNR superlattice. (a) Sketch of the structure with charge density of the topological interface state between the nontrivial 9-AGNR ($\mathbb{Z}_2 = 1$) and trivial 7-AGNR ($\mathbb{Z}_2 = 0$) segments. The hopping magnitudes between the interface states are represented by t_1 and t_2. (b) High-resolution STM image of the end segment. (c) DFT-calculated band structure. Between the valence band (VB) and conduction band (CB) are the occupied (OTB) and unoccupied (UTB) topologically induced bands. $\mathbb{Z}_2$ invariants are evaluated for electrons occupying up to the corresponding energy gaps. (d) Projected DOS (PDOS) of a finite (octamer) superlattice with 0.05 eV Gaussian broadening, exhibiting the contribution from end cell (green) and bulk cell (red) separately. (e) STM topography (top-left corner), experimentally obtained dI/dV maps and DFT-simulated LDOS of the UTB, OTB, and three end states. Adapted from Ref. [221]. (f–i) Topologically nontrivial phase in a 7-AGNR with inline edge extensions. (f) Structural model and (g) nc-AFM image. The length of edge-extension segments and distance between them are characterised by n and m, respectively. (h) LDOS at the termination of the edge extension (arrow in (f)) as a function of m. The synthesised structure with m = 3 is highlighted by the red arrow on top. (i) Experimentally measured dI/dV maps and theoretically calculated LDOS of valence-band top, topological end states, and conduction-band bottom, respectively. Adapted from Ref. [59].

Switzerland reported that they had independently verified topological GNRs in experiments. Their findings are summarised in Figure 2.26. As discussed previously, the topological phase of AGNRs can be controlled by width and termination type. Based on this concept, Rizzo et al. fabricated a superlattice structure comprising 7- and 9-AGNR fragments [221], shown in Figure 2.26a–b. This structure is same as the theoretically proposed example in Figure 2.24b. As expected, topological in-gap states emerge at the interfaces between the topologically nontrivial 9-AGNR ($\mathbb{Z}_2 = 1$) part and the trivial 7-AGNR ($\mathbb{Z}_2 = 0$) part. Because the alternating segments are so short, these interface states couple with each other, leading to two topologically induced bands (OTB and UTB). These bands can be effectively described by the aforementioned SSH model. By examining the $\mathbb{Z}_2$ invariants of the superlattice repeating cell – which includes both 7- and 9-AGNR segments – we discover that all three energy gaps appearing in the band structure are topologically nontrivial. This suggests that when electrons fill up to these gaps, the ribbon exhibits nontrivial phases and supports topological end states positioned within each energy gap. This prediction agrees well with the local projected DOS results in Figure 2.26d–e and is further supported by the differential conductance measurements.

In contrast, Groning et al. synthesised an edge-extended 7-AGNR, as shown in Figure 2.26f, where the shaded area can be approximated by a dimer, and all the shaded segments together can be described by the SSH model [59]. The topological phase of this SSH Hamiltonian can be tuned through geometrical features, including segment length n and distance m. As indicated by the LDOS calculation in Figure 2.26h, the ribbon changes from a nontrivial phase to a trivial one as the inter-segment distance m increases. Experimental results shown in Figure 2.26i have validated the presence of topological end states between the valence band and conduction band for the ribbon with m = 3 and n = 1.

In addition to the examples mentioned, the occurrence of topological phases has also been validated in other types of GNRs [223–225], as well as in π-conjugated

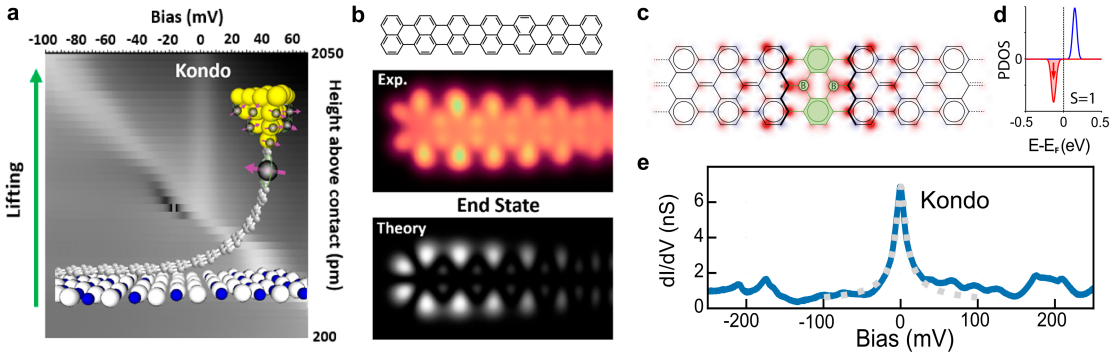


Figure 2.27: Probing the magnetic nature of topological states by STM. (a–b) Topological end states of 5-AGNRs. (a) Zero-bias Kondo resonance measured during lifting of the ribbon by a STM tip. (b) Structural model and end states of 5-AGNR from experiments and theory. Adapted from Ref. [158]. (c–e) Topological interface states in boron-doped 7-AGNR. (c) Structure of 2B-7-AGNR and superimposed spin-density map from DFT simulation. (d) Projected DOS of up (blue) and down (red) spin at the position of boron. (e) dI/dV spectrum acquired by STM lifting, showing a Kondo peak. The peak is fit by a Frota function (dashed line). Adapted from Ref. [222].

polymers [226, 227]. Several research groups have made use of the STM-lifting technique to verify the magnetic nature of topological boundary states. For instance, Lawrence et al. synthesised 5-AGNRs and performed transport measurements by suspending the ribbon between a STM probe and the substrate [158]. As displayed in Figure 2.27a, the existence of a zero-bias Kondo peak provides compelling evidence for spin-polarised end states. The spin centre is quenched when the zigzag end is oxidised. The authors also discovered that as the ribbon is shortened, the two ends exhibit strong coupling, changing from singly occupied spin-polarised states to closed-shell states. Around the same time, Friedrich et al. synthesised a boron-doped 7-AGNR, shown in Figure 2.27c [222]. The introduction of two boron atoms and two Clar's sextets disrupts the π-conjugation network, isolating the two 7-AGNR boundaries. In such configurations, the two spin centres display a ferromagnetic coupling and can be treated as an $S = 1$ component. The dI/dV spectrum, recorded by lifting the ribbon, also exhibits a Kondo feature, aligning with theoretical predictions. The authors also established that increasing the separation of boundary states by introducing more boron-doped segments would

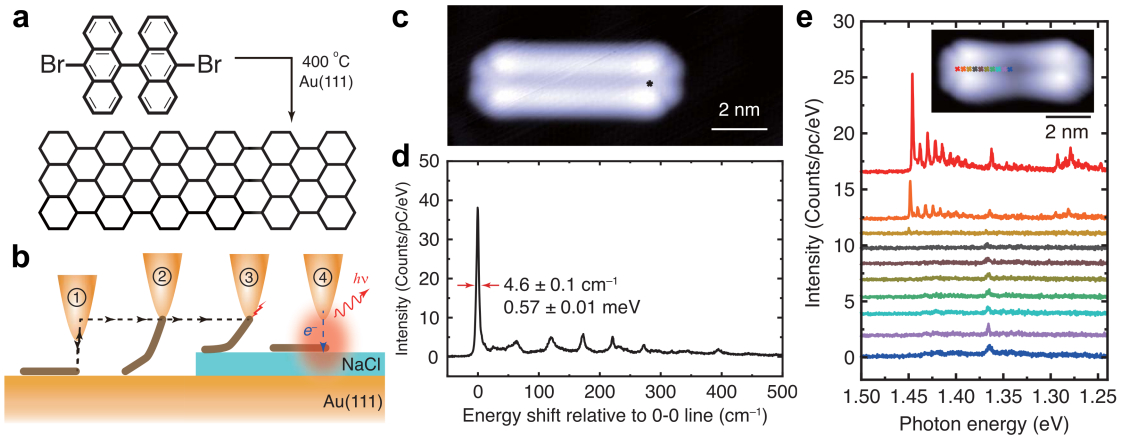


Figure 2.28: Excitonic emission from topological end states. (a) 7-AGNR synthesised on a surface from molecular precursors. (b) Transfer of a 7-AGNR from an Au surface to a NaCl island, followed by STM-induced luminescence (STML) measurement. (c) STM image of the ribbon on the NaCl island. (d) High-resolution STML spectrum recorded at the terminus of the ribbon (black dot in (c)). (e) STML spectra recorded along the line from the end to the bulk of the ribbon, as marked by corresponding dots in the inset. Adapted from Ref. [51].

favour an antiferromagnetic coupling.

Recently, the electron transport properties and optoelectronic properties of topological states in GNRs have been explored [37, 51, 223]. Mangnus et al. demonstrated that electron transport is suppressed for the localised topological boundary states, and they observed negative differential conductance in their experiments [37]. Jiang et al. fabricated 7-AGNRs and conducted STM-induced luminescence (STML) measurements after transferring the ribbon from a gold surface to a NaCl crystal [51]. As presented in Figure 2.28, the STML spectrum acquired at a zigzag terminus exhibits an extremely sharp peak with a spectral width of 0.57 meV, which is referred to as the 0–0 line. This line represents the emission from the vibrational ground state of the electronic excited state to the vibrational ground state of the electronic ground state. The 0–0 line arises from topological end states, as can be seen when comparing the spectra recorded at different locations (Figure 2.28e). Beyond the 0–0 line, the spectra display additional peaks that result from the topologically localised excitons and longitudinal acoustic modes. These results suggest that GNRs can serve as an ideal platform for studying the interplay

of electronic topology, vibrons, and excitons. Furthermore, topological GNR are promising materials for applications in quantum sensing, single-photon sources, etc.

2.2.4 Topology in quantum spin chains

Topological phases are not exclusive to topological insulators or superconductors, but also extend to other systems such as quantum spin chains. Haldane conjectured in 1983 that periodic integer-spin chains should have a finite energy gap between the ground state and the first excited state [229], a concept now recognised as the Haldane gap. Subsequent studies indicated the existence of a $S = 1/2$ edge excitation state, or end state, within the Haldane gap in open-ended spin chains [230–232]. This phenomenon is another manifestation of topological phases, and resonates with the aforementioned end states in 1D topological insulators (SSH model and topological GNRs).

Despite the significant efforts devoted to the experimental realisation of the Haldane phase in transition-metal-ion systems [233, 234], limitations often arise because of interchain exchange interaction and magnetic anisotropy [228]. Recently, Mishra et al. successfully demonstrated that the Haldane spin chain could also be produced in a nanographene-based system through on-surface synthesis and STM characterisation [228]. Using a bottom-up synthetic approach, they fabricated a molecular spin chain from triangulene units, called a triangulene spin chain (TSC), as shown in Figure 2.29a. A single triangulene molecule has two unpaired electrons because of sublattice imbalance and exists in its triplet form in ground state [235]. For the TSC, each triangulene unit can be modeled by a $S = 1$ component, as depicted in Figure 2.29b. Mishra et al. showed that this system's properties are better captured by a spin Hamiltonian that includes both bilinear and biquadratic (BLBQ) terms. The BLBQ model is explicitly written as $\hat{H}_{\mathrm{BLBQ}} = J\sum_i [\boldsymbol{S}_i \cdot \boldsymbol{S}_{i+1} + \beta(\boldsymbol{S}_i \cdot \boldsymbol{S}_{i+1})^2]$. For an open system (oTSC), the spin chain hosts a fractional edge excitation. The $S = 1/2$ spin at each of the two ends has an

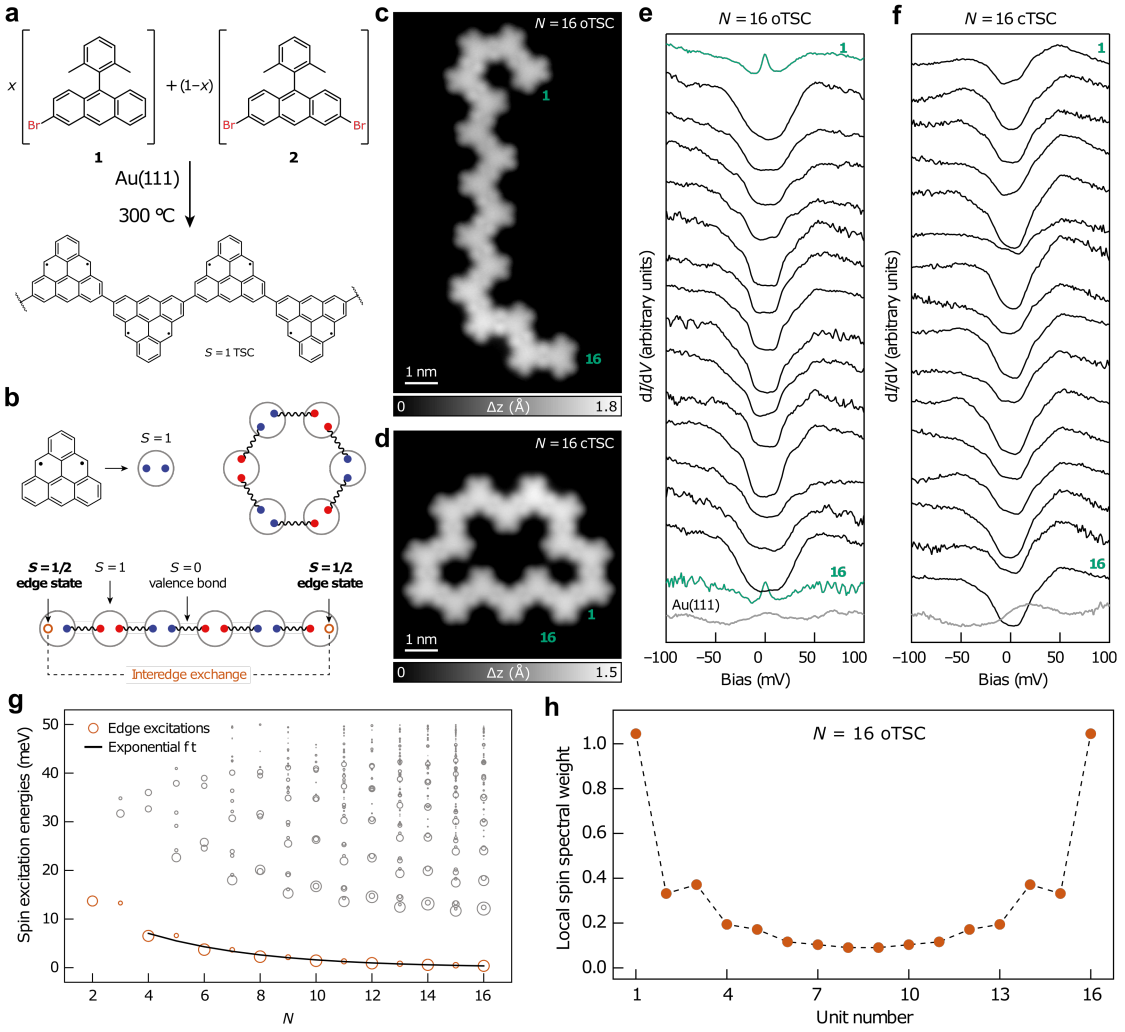


Figure 2.29: Topological phase in triangulene spin chains. (a) On-surface synthesis of triangulene spin chains (TSCs) from a mixture of two precursors. (b) Triangulene modeled by a $S = 1$ unit comprising two 1/2 spins. Also depicted are the diagrams of closed (cTSC) and open TSC (oTSC) with $N = 6$, where edge excitations are present only in the latter case. Neighbouring $S = 1/2$ units from adjacent triangulenes are connected by valence bonds, represented by wavy lines. Spin-up and spin-down electrons are indicated by blue and red dots, respectively. (c) $N = 16$ oTSC and (d) $N = 16$ cTSC visualised by highly resolved STM images, where Δ_z denotes the height. (e,f) $\mathrm{d}I/\mathrm{d}V$ spectra measured on each repeating unit in (e) oTSC and (f) cTSC, uncovering the zero-energy excitations in the terminations of only oTSC (green traces). (g) Excitation spectrum of oTSC with varying number of triangulene units calculated from exact diagonalisation of BLBQ model. Size of the circles quantifies the spin spectral weight. Edge excitations are highlighted by orange circles, which are fitted by an exponential model $Ae^{-N/\zeta}$, where the coefficient A equals 19 meV and the spin-correlation length ζ equals four. (h) Spin spectral weight of the edge state of $N = 16$ oTSC with $|S, S_z\rangle = |1, +1\rangle$, determined using BLBQ model. Adapted from Ref. [228].

effective inter-edge coupling with the other, a feature absent in the closed TSC (cTSC). This contrast is validated by the dI/dV measurements of an oTSC and cTSC molecule, as displayed in Figure 2.29c–f. The Kondo resonance is observed only at the two ends of the oTSC molecule. The experimental findings were strongly supported by the solutions of the BLBQ model, as shown in the local spin spectral weight calculation (Figure 2.29h). The authors also calculated the evolution of the excitation spectrum of TSC molecules over the number of repeating units N (Figure 2.29g), and found the results to be consistent with experimental data.

The nanographene spin-chain molecule discussed herein closely relates to GNRs in that both are synthesised from molecular precursors, with the distinction that GNRs are planarised. GNRs could also serve as an exceptional platform for exploring quantum spin physics in the future. This opens up numerous opportunities for testing theoretical models and designing novel structures with substantial potential in spintronics and quantum technologies.

2.3 Spin states in GNRs

2.3.1 Spin qubits and spin relaxation

Most electronic devices in widespread use today are primarily based on classical physics. Currently, we are in a stage where quantum properties are being harnessed to develop innovative functional devices. Quantum properties like entanglement, quantum tunneling, superposition state, and quantum coherence could lead to novel technologies such as quantum computation, quantum sensing, quantum optics, and quantum cryptography [236]. Unlike a classical binary unit used for information storage, which can either be 0 or 1, a qubit, or quantum bit, can be in a coherent superposition of 0 and 1 states. Qubits represent the fundamental units of quantum information technology.

Various two-level systems can function as qubits, including the electron spin. In 2000, DiVincenzo outlined five essential criteria for a qubit: (1) long coherence time, (2) initialisation capability, (3) good scalability, (4) individual measurability, and (5) the ability to construct universal quantum gates [237]. The first important requirement is that the qubit needs to remain in a coherence superposition state when quantum operations are implemented. However, spin–lattice relaxation and spin decoherence are the limiting factors of many types of qubit nowadays Leon et al. When an external magnetic field is applied, an electron spin has two eigenstates with different energies, either parallel or antiparallel to the magnetic field. The spin qubit can then be put in any superposition state by microwave pulses. Spin–lattice relaxation refers to the process when the longitudinal component of the spin magnetic moment gradually relaxes to the thermodynamic equilibrium state. It is characterised by the spin–lattice relaxation time, denoted as T_1. Spin decoherence refers to the process when the expectation value of the transverse component of the spin magnetic moment gradually vanishes. In other words, spin decoherence means that the phase relationship between quantum states is lost and, consequently, the superposition state is destroyed. This phenomenon is also known as spin–spin relaxation, and is characterised by the spin coherence time, T_2. In practical experiments, however, it is difficult to measure the real T_2 of a material. Instead, the quantity obtained from pulsed EPR measurements is called T_m, which includes the effects of both intrinsic spin coherence and external factors, such as instantaneous diffusion caused by microwave pulses. For simplicity, we will use T_m to refer to the spin coherence time.

Both T_1 and T_m are important figures of merits to describe the performance of a qubit. T_m determines the time window during which the qubit can be controlled, while T_1 sets an upper limit to T_m, and meanwhile the inverse of T_1 is related to the speed of qubit operation [239]. In Chapter 3 we will introduce experimental methods to measure T_1 and T_m using pulsed EPR spectroscopy. Here, we briefly

review the mechanisms of spin–lattice relaxation and spin decoherence. Spin–lattice relaxation involves an energy exchange between a spin system and the "lattice", which does not necessarily mean an actual crystal lattice, but can also refer to the general surrounding that establishes thermal equilibrium [240]. At low temperatures (typically below 20 K), spin–lattice relaxation is often dominated by a direct process, where a spin flips its orientation when the Zeeman energy matches the energy of a lattice phonon. This mechanism is characterised by a linear relationship between the relaxation rate ($1/T_1$) and temperature (T) [240]. At intermediate temperatures (usually between 20 K and 150 K), spin–lattice relaxation is mainly mediated by a Raman process, which describes a two-phonon process. The energy transferred between the spin system and the lattice matches the energy difference between the absorbed phonon and emitted phonon that are associated with a virtual excited state. The Raman process leads to a T^9-dependence of the relaxation rate at temperatures below the Debye temperature, and T^2-dependence above [240]. At higher temperatures (between 150 K and room temperature), Orbach relaxation may play a role, which is similar to the Raman process but instead of a virtual state it involves an actual excited state. Furthermore, we can obtain the energy of an excited state of the system by measuring T_1 here [240]. For molecular materials, local vibrational modes, rather than long-range phonon modes, may contribute to the spin–lattice relaxation as well, and this phenomenon is called local-mode process. Moreover, spin–lattice relaxation may also be mediated by other mechanisms depending on the environment of the spin qubit. For example, in the liquid state, rotational tumbling of molecules can be a very efficient relaxation mechanism. In amorphous solids with high concentration of unpaired spins, triplet states may exist in large clusters of spin centres. In such a situation, simultaneous transitions within a spin doublet and a triplet state may happen, leading to a cross-relaxation process. These different relaxation mechanisms have different lineshapes and are applicable

to different scenarios. In practice, appropriate relaxation mechanisms will be chosen to fit the temperature dependence of the spin–lattice relaxation rate.

On the contrary, spin–spin relaxation, or spin decoherence, is caused by different sources. In general, a qubit becomes more immune to decoherence if it is more isolated from its surrounding environment. One decoherence mechanism is through spin–orbit coupling when the spins are coupled to lattice vibrations. However, this effect is usually weak for spin qubits in graphene quantum dots [241]. Dipolar interactions between unpaired spins may have a large influence on the coherence time. Furthermore, concentration effects play an important role. With increasing spin concentration, spin coherence decreases [240]. By using solvents or embedding in diamagnetic matrices, we can control the spin concentration. Another major source of spin decoherence is the hyperfine interaction between the electron spin and the fluctuating nuclear spins in the local environment [240]. Graham et al. showed that the nuclear spins at intermediate distances with the electron spin have most significant effect on the decoherence, while the nuclear spins closer to the electron spin do not contribute much. Meanwhile, the nuclear spins far away only affect decoherence in a longer time scale [243]. By using nuclear-spin-free isotopes or isotopes with lower gyromagnetic ratios, coherence times can be enhanced [244].

2.3.2 Quantum properties of electron spins in GNRs

A good qubit requires not only a fast operating speed, but also a long coherence time. So far, several pathways to fabricate a practical qubit have been explored by researchers, including superconducting qubits, gate-defined semiconducting quantum dots, nitrogen-vacancy colour centres in diamonds, ion traps, photons, and Majorana zero mode [238]. The electron spin in a carbon-based quantum dot, as an alternative qubit candidate, has drawn significant attention because of its long coherence time [245]. Spin relaxation in graphene is primarily mediated by SOC, electron–phonon coupling, and hyperfine coupling [245]. The SOC in graphene

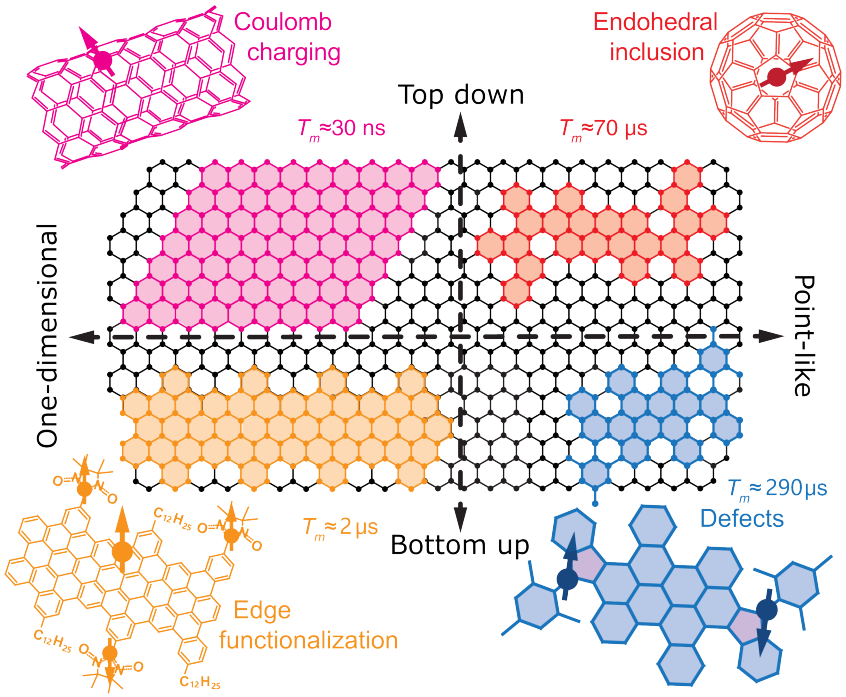


Figure 2.30: Quantum units from tailoring the graphene. The spin qubits in CNTs with Coulomb charging (magenta), and heteroatom included in endohedral fullerenes (red) are fabricated using a top-down approach. The side-functionalised GNRs (orange) and nanographene molecule with pentagonal defects (blue) are synthesised using a bottom-up approach. Adapted from Ref. [63].

is very weak for two main reasons. On the one hand, carbon has a low nuclear charge and SOC is weaker in light elements [246]. On the other hand, graphene has a relatively planar surface, making it largely immune to SOC induced by local curvature, unlike carbon nanotubes [247]. Additionally, the quantum coherence of an electron spin in a graphene quantum dot benefits from the low abundance of ^{13}C isotopes. The random nuclear spin flip-flop is detrimental to the coherence of an electron spin coupled to the nuclear-spin bath [60]. Only ^{13}C possesses a nuclear spin, while ^{12}C does not. Consequently, the overall hyperfine coupling between an electron spin in graphene and nuclear spins is very weak, leading to minimal dephasing of the electron spin [45].

GNRs, as graphene quantum dots, have been theoretically studied as a qubit [60, 61]. Slota et al. investigated the cove-edge GNRs functionalised by nitronyl nitroxide side groups [62]. They diffused spin density from the radical-bearing side groups

into the GNR backbone. Using EPR spectroscopy, they determined the spin–lattice-relaxation time T_1 and the spin-coherence time (or phase-memory time) T_m. At room temperature, T_1 reached approximately 12 µs, and T_m reached around 300 ns at X-band frequency [62]. When measured at W-band, T_m increased to around 2 µs. This is considerably higher than that of CNT, as illustrated in Figure 2.30. It is noteworthy that these GNRs were measured in the powder state. Therefore, the spin-coherence times are intrinsically limited by the spin–spin coupling, and the hyperfine coupling with surrounding protons. There is ample room to further improve the spin–lattice-relaxation time and coherence time through chemical modification, isotopic substitution, or dynamic decoupling [62]. We also presented an example of the zero-dimensional limit of a GNR, a nanographene molecule, in Figure 2.30. The spin states in this molecule were generated by the pentagonal defects. Similar to the previous example of GNR, this nanographene molecule is also synthesised using a bottom-up approach. Upon optimisation by dynamic decoupling, the spin-coherence time of the spin states localised at defect sites reached 290 µs at 80 K at X-band frequency [63]. This molecule was measured in the CS_2 solution and was, therefore, free from dephasing caused by nuclear spins.

To summarise, the superior quantum properties of GNRs and nanographene molecules have been experimentally verified. Although the coherence time of such carbon-based nanostructures is still lower than that of some semiconducting quantum dots, the former outperforms the latter at room temperature. Furthermore, these nanostructures are all synthesised using a bottom-up approach, which permits fine tuning of atomically precise structures. Bottom-up synthesised GNRs and other nanographene molecules may provide unprecedented options for room-temperature quantum devices.

2.3.3 Incorporating spin states into GNRs

In this section, we provide an overview of strategies to incorporate spin states into GNRs and their potential applications. The magnetism in graphene nanostructures, which encompasses a larger family that includes GNRs, has been extensively studied in the literature. As summarised by Song et al., there are four categories of π-magnetism in graphene nanostructures [248]. The first type results from sublattice imbalance in the bipartite honeycomb lattice. As all the π-bonds are formed between two neighbouring atoms, which belong to different sublattices, sublattice imbalance means that not all p_z electrons can form π-bonds, leaving unpaired electrons. According to Lieb's theorem [249], the spin quantum number of the ground state of such sublattice-imbalanced structures is given by $S = (N_A - N_B)/2$, where N_A and N_B are the number of atoms in A and B sublattices, respectively [248]. Such structures with radical centres are often called non-Kekulé structures. The second type of π-magnetism arises from aromatic stabilisation [248]. These structures have a balanced sublattice, but have multiple resonance forms, including both Kekulé and non-Kekulé forms. As per Clar's sextet rule, the resonance form containing the maximum number of Clar's sextets (defined as a hexagonal ring with six localised π-electrons) is the most chemically stable one [250, 251]. The creation of radicals in this type of molecule is driven by aromatic-stabilisation energy gained from maximising the number of Clar's sextets [248]. The third type of π-magnetism originates from the Coulomb repulsion among electrons in molecular orbitals near the Fermi level, which exist primarily in graphene nanostructures with zigzag edges [8, 252]. The magnetic edge states in ZGNRs are an example of this category. Another example is the rhombus-shaped nanographene that has four zigzag edges, and provided it is above a certain size limit, the Coulomb repulsion energy among valence electrons is stronger than the hybridisation effect between orbitals near the Fermi level [253]. The fourth type of π-magnetism is induced by topological

frustration [254, 255]. It is noteworthy that the concept of topology in this context differs from the topology discussed in Section 2.2. While the former refers to the geometrical connections amongst carbon atoms, the latter describes a more abstract topology associated with the band structure. Topologically frustrated nanographene molecules also exhibit a balanced sublattice, but not all the p_z-orbitals can be simultaneously paired. This phenomenon can be interpreted using graph theory. The number of unpaired spins is determined by the nullity η of the hexagonal graph representing the atoms and bonds of the molecule. Nullity is defined as $\eta = \alpha - \beta$, where α and β denote the maximum number of nonadjacent vertices and edges in the graph, respectively. A typical example of this is Clar's goblet, which has been synthesised and characterised experimentally [256].

The previously discussed four approaches for inducing π-magnetism are all applicable to finite-length GNRs. Additionally, there are also new methods to introduce spin states to GNRs, including topological states and external functionalisation groups. In Figure 2.31, we present several examples of recently published GNRs exhibiting spin-polarised states. As we have already comprehensively reviewed the magnetic edge states in GNRs that result from the Coulomb repulsion between electrons, we have opted to omit them in Figure 2.31. Figure 2.31a depicts a chevron GNR, which has each unit cell doped with two nitrogen atoms. These ribbons form a strong bond with the gold substrate, and electrons are transferred from the ribbons to the substrate, leaving the ribbons positively charged [56]. Each unit cell harbours a $S = 1/2$ spin centre, so that the entire ribbon can be viewed as a 1D Kondo spin chain. The $\mathrm{d}I/\mathrm{d}V$ spectrum is measured at zero-bias voltage, showing the spatial distribution of the zero-bias resonance.

Figure 2.31b illustrates a spin chain constructed from the topological junction state between topologically distinct segments [55]. Although the definition of A and B sublattice can be arbitrary for a standalone structure, the sublattice definition for structures containing two kinds of substituent segments must remain

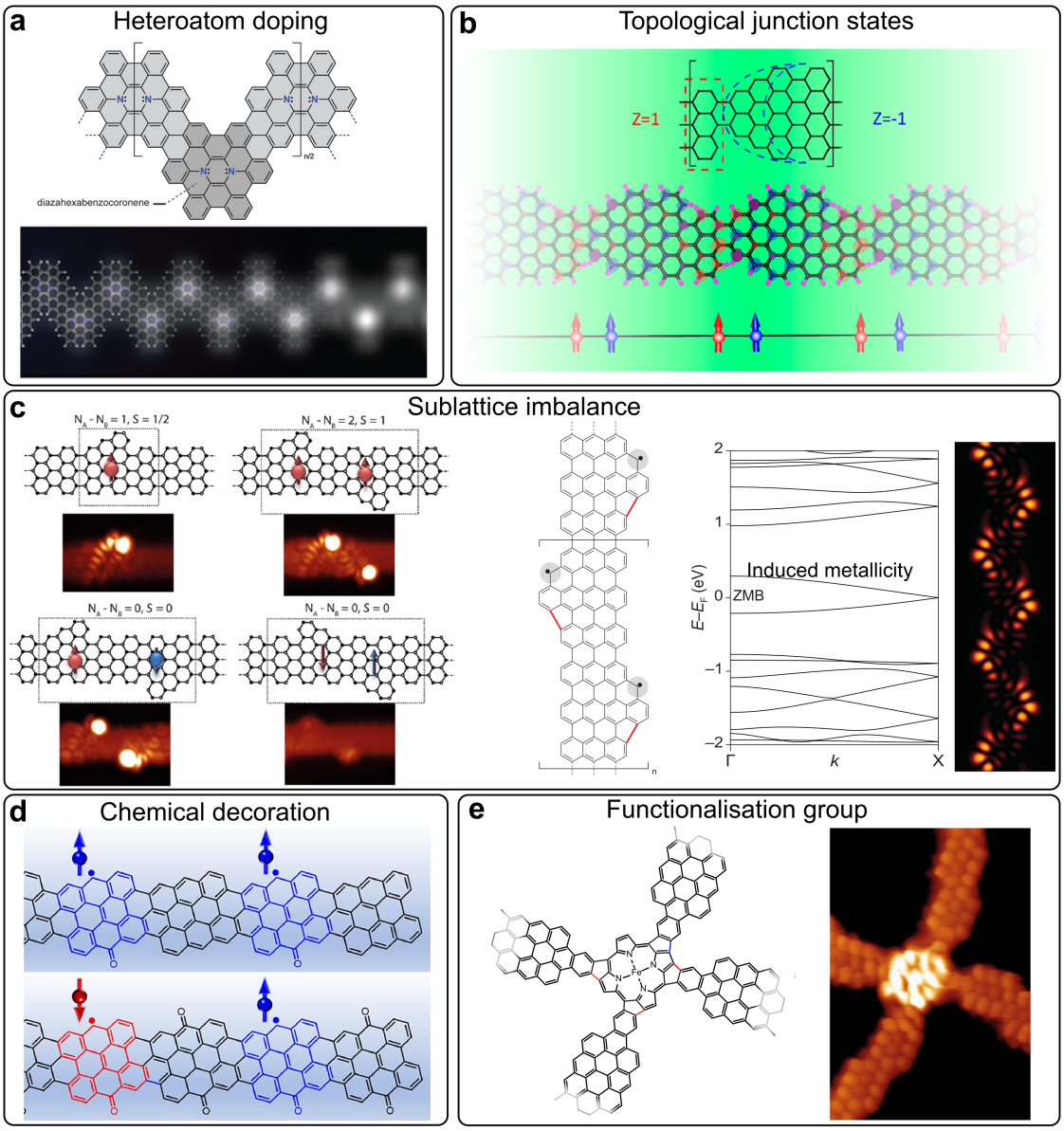


Figure 2.31: Different strategies of incorporating spin states in GNRs. (a) Double-nitrogen-doped chevron GNR. The spatial distribution of the zero-bias resonance measured by STS shows a Kondo spin-chain feature. The structural model is superimposed on the left half of the ribbon. Adapted from Ref. [56]. (b) A spin chain formed by topological junction states. The unit cell is composed of two segments, having $\mathbb{Z} = -1$ and $\mathbb{Z} = 1$, respectively. Two spin-polarised in-gap states emerge at each junction between the two segments. Adapted from Ref. [55]. (c) Different spin states generated from sublattice imbalanced GNRs. Shown on the left are four instances built from 7-AGNR with asymmetric zigzag-edge extensions (adapted from Ref. [57]). The four unit cells are in doublet ($S = 1/2$), triplet ($S = 1$), open-shell singlet ($S = 0$), and closed-shell singlet ($S = 0$) state, respectively. The ribbon displayed on the right is synthesised from a similar repeating unit, but with additional bonds (red) forming pentagonal rings at the edge (adapted from Ref. [257]). The radicals interact with each other and create dispersive metallic bands (ZMB) around the Fermi level. The DFT-simulated LDOS map of the ZMB is presented on the right. (d) Different coupling between spin states in the chiral edges achieved by controlling the chemical decoration of the GNR edges. Adapted from Ref. [258]. (e) Spin states in a hybrid structure derived from Fe-porphyrin and GNRs. Adapted from Ref. [259].

consistent. Theoretical calculations revealed that the two segments have $\mathbb{Z} = -1$ and $\mathbb{Z} = 1$, respectively [55]. According to bulk–boundary correspondence, the difference between their $\mathbb{Z}$ indices indicates the number of in-gap zero-energy modes. DFT calculations demonstrated that these two in-gap modes are spin-polarised, giving rise to a ferromagnetic spin chain [55]. These spin-polarised topological states have been extensively studied in recent years. We have already provided a comprehensive review in Section 2.1.4 and Section 2.2.3.

Sublattice imbalance is also a strategy for creating magnetic states in GNRs. Sun et al. synthesised a series of AGNRs with asymmetric zigzag edge extensions, as depicted in the left panels of Figure 2.31c [57]. The top-left panel presents a unit with sublattice imbalance. There is one radical state localised at the zigzag-edge extension. By arranging such units in different alignments, scientists produced various magnetic couplings between these radicals. The two neighbouring radicals within the unit cell can be either in the triplet (top-right panel), open-shell singlet (bottom-left panel), or closed-shell singlet (bottom-right panel) configurations. Rizzo et al. synthesised a similar ribbon using the same unit cells, but additionally, they induced five-membered rings at the edge-extension components through secondary cyclodehydrogenation [257]. These pentagonal rings enhanced the coupling between neighbouring spin centres, transforming the dispersionless zero-energy bands into dispersive metallic zero-energy bands, as confirmed by band structure calculation and STS measurements. This study showcased the numerous possibilities achievable by manipulating spin states in GNRs through bottom-up synthesis.

Figure 2.31d provides two examples of chiral GNRs with varying chemical decorations at the edge. In the upper case, the ketone functionalisation introduces an additional p_z electron, resulting in an unpaired spin in the unit cell. In the lower case, all the unit cells are functionalised with ketone at the edge except for two, where the ketone groups are remove, creating two radicals as well. The two spin centres exhibit ferromagnetic and antiferromagnetic coupling in two instances,

respectively. These findings offer new insights for tuning magnetic interactions in carbon-based spin chains and networks [258].

Spin states can also be incorporated into GNRs by grafting external spin-bearing groups onto them. For instance, as we introduced in the previous section, spin states can be injected into GNRs from nitronyl nitroxide side groups [62]. Figure 2.31e presents another example of a hybrid structure produced by linking a Fe-porphyrin with four GNRs. This structure could be beneficial for connecting a single molecule to GNR electrodes, enabling the study of spin states in single-molecule devices. Moreover, Su et al. synthesised a hybrid structure by fusing a 7-AGNR and a manganese phthalocyanine (MnPc) molecule [160], facilitating the investigation of the interaction between the spin states at the zigzag end of the 7-AGNRs and the spin states in the MnPc molecule.

Next, we will review the multitude of applications of spin states in GNRs. We mentioned in the previous section that spin states in GNRs could be promising candidates for qubits in quantum-information technologies. One of the present challenges for molecular spins as qubits is scalability [260]. GNRs could potentially provide a platform to integrate multiple spin centres, which could be either locally addressed or globally addressed at distinct frequencies [261]. Furthermore, the spin states in GNRs could be exploited to build spintronic devices, such as magnetic tunnel junctions and spin FETs [262–264]. The localised spin state at the zigzag end could potentially be used as a single-photon emitter [51]. The high sensitivity of the coherent superposition state of a spin qubit could be utilised to build a quantum sensor [265]. GNR-based quantum spin chains also have a wide variety of applications, such as quantum communication [266, 267], quantum spin transistor [268], and topological quantum computation [58, 210, 269].

2.4 Vibrational properties of GNRs

The vibrational properties of GNRs can be used to characterise their structures. In this section, we will review the basic vibrational properties of AGNRs and ZGNRs, which are the two most basic GNRs. The vibrational modes of a hydrogen-passivated GNR include the fundamental modes, overtones, and C–H vibrational modes. The fundamental modes and overtones can be mapped onto the phonon dispersion of graphene using a zone-folding approximation, analogous to what can be done for band structures, as introduced in Section 2.1.1. Let us assume the phonon wave is expressed as $Ae^{i(\boldsymbol{k}\boldsymbol{r}-\omega t)}$, where A is the normalisation factor, $\boldsymbol{k}$ is the wavevector, ω is the mode frequency. The longitudinal component of the wavevector $k_{\parallel}$ is continuous, while the transverse component $k_{\perp}$ is discrete, because the edges allow only standing waves perpendicular to the ribbon. Hence, the perpendicular wavevector can be written as:

$$k_{\perp,n} = \frac{n\pi}{w}, \tag{2.16}$$

where n is the mode index, and w is the ribbon width. In Figure 2.32a, we depict the Brillouin zone of graphene, AGNRs, and ZGNRs. The Brillouin zone of a ZGNR is continuous along the Γ–K direction, but quantised along the Γ–M direction. The Γ-point phonon frequencies of an 8-ZGNR are mapped onto the phonon dispersion of graphene, as illustrated in Figure 2.32b. Here, the letters L, T, and Z represent the longitudinal, transverse, and out-of-plane modes, respectively. The optical and acoustic branches are represented by O and A, respectively. The Brillouin zone of an AGNR is continuous along the Γ–M direction, but quantised along the Γ–K–M direction. Figure 2.32c demonstrates the mapping of the Γ-point phonon frequencies of a 15-ZGNR onto the phonon dispersion of graphene. It can be found that the graphene phonon dispersion can roughly provide an estimation of the phonon frequencies of AGNRs and ZGNRs.

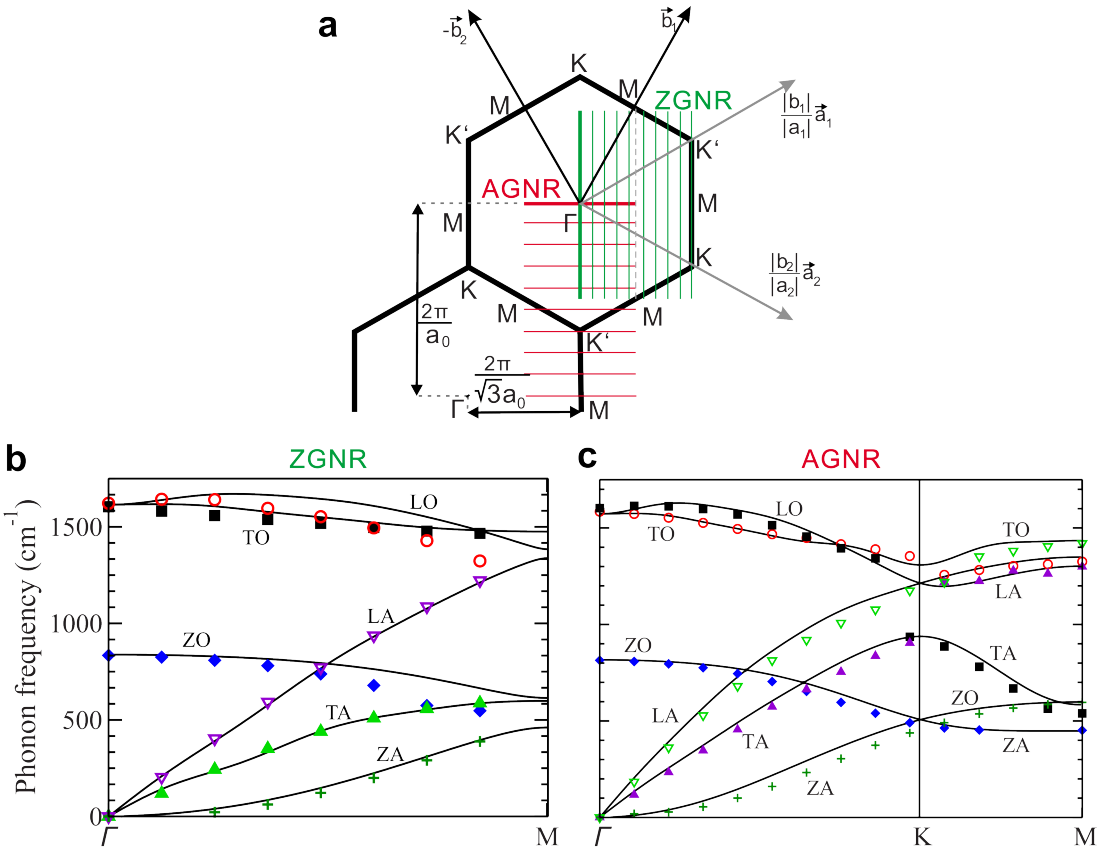


Figure 2.32: Mapping of the fundamental modes and overtones of ZGNR and AGNR onto graphene's phonon dispersion. (a) The Brillouin zone of graphene, zigzag (10-ZGNR) and armchair (10-AGNR) nanoribbons. The real-space lattice vectors of graphene are denoted as $\vec{a}_1$ and $\vec{a}_2$. The reciprocal-space lattice vectors are denoted as $\vec{b}_1$ and $\vec{b}_2$. The green lines and red lines represent the Brillouin zone of a ZGNR and a AGNR, respectively. (b) Mapping of the LA (filled triangles), TA (open triangles), ZA (crosses), LO (filled squares), TO (circles), ZO (filled diamonds) fundamental and overtone frequencies of an 8-AGNR on the phonon dispersion of graphene (solid lines). (c) Mapping of the LA (filled triangles), TA (open triangles), ZA (pluses), LO (circles squares), TO (filled squares), ZO (filled diamonds) fundamental and overtone frequencies of a 15-AGNR on the phonon dispersion of graphene (solid lines). Adapted from Ref. [270].

Vibrational modes can offer very valuable information of the structure of GNRs. For instance, the first overtone of the fundamental transverse acoustic mode, often referred to as radial breathing-like mode (RBLM) and which is Raman-active, can be utilised to characterise the ribbon's width [273–276]. As shown in Figure 2.32, the three acoustic branches of graphene's phonon dispersion are approximately linear at the long-wave limit (small k). Therefore, based on Equation (2.16), the acoustic mode frequencies of GNRs can be considered roughly proportional to the

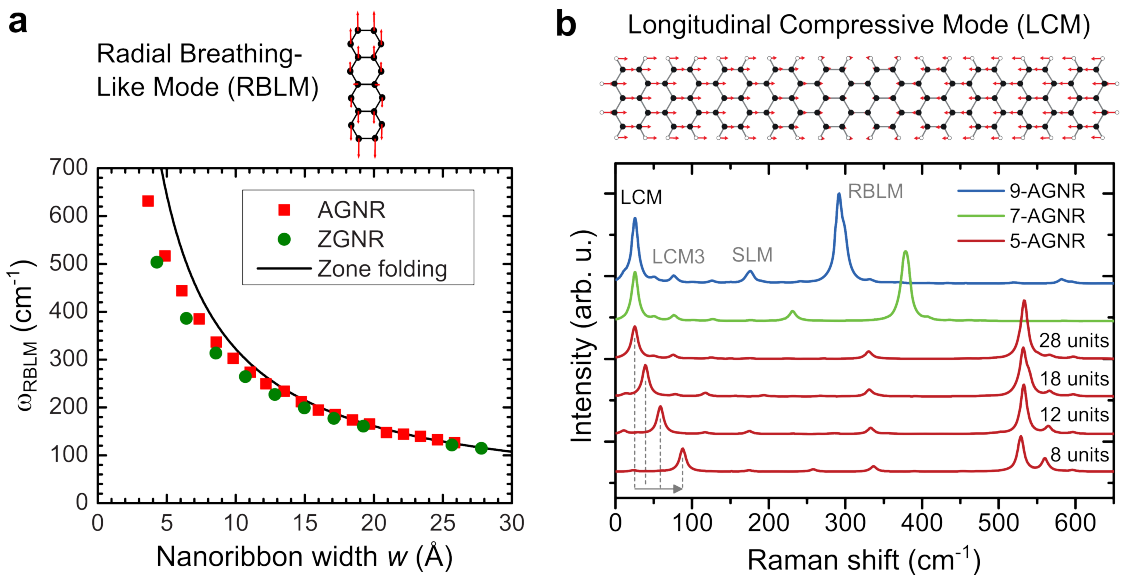


Figure 2.33: Radial breathing-like mode (RBLM) and longitudinal compressive mode (LCM) of GNRs. (a) Frequencies of the RBLM of AGNRs (red squares) and ZGNRs (green dots) as a function of ribbon width w. Atomic displacement of the RBLM of a 9-AGNR unit cell is depicted on the top. The solid line in the lower graph is a zone-folding approximation using the linear part of the LA branch of graphene's phonon dispersion. The relation is written as $\omega_{\mathrm{RBLM}} = a\pi/w$, where $a = 1025.6\,\text{Å}\text{cm}^{-1}$ is the sound velocity in graphene. Adapted from Ref. [271]. (b) Manifestation of LCM in Raman spectra of AGNRs with varying widths and lengths. Atomic displacement of the LCM of a 10-unit finite 5-AGNR is displayed on the top. Simulated Raman spectra of a 28-unit finite 9-AGNR (blue), a 28-unit finite 7-AGNR (green), and finite 5-AGNRs with 8, 12, 18, and 28 units (red) are plotted below. The peaks resulting from LCM, LCM3 (the second overtone of LCM), SLM, and RBLM are labelled in the graph. Adapted from Ref. [272].

inverse of the ribbon width. Figure 2.33a demonstrates that the DFT-calculated RBLM frequencies of AGNRs and ZGNRs align well with the relation $\omega_{\mathrm{RBLM}} = a\pi/w$ derived from zone-folding approximation, particularly for wide GNRs where RBLM wavevectors are closer to the Γ point. Similarly, the first overtone of the fundamental longitudinal acoustic mode, or the longitudinal compressive mode (LCM), can be used to characterise the length of GNRs. Figure 2.33b illustrates that for the 5-AGNR, 7-AGNR, and 9-AGNR of identical lengths, the Raman shifts of the LCM modes are the same. In contrast, for the 5-GNRs with varying lengths, the LCM modes have distinct Raman shifts.

To conclude, vibrational properties can provide unique information for characterising the structure of GNRs. This is particularly advantageous for future

applications of GNRs that require both precision in fabrication and accuracy in characterisation of the structures.

3 Methods

Contents

3.1 Theoretical methods 71
3.1.1 Tight-binding model 71
3.1.2 DFT 77
3.1.3 Topology 83
3.1.4 Wannier functions 86
3.2 Experimental methods 89
3.2.1 EPR spectroscopy 89
3.2.2 Single-molecule transistor 101
3.2.3 Optical spectroscopy 105

3.1 Theoretical methods

3.1.1 Tight-binding model

The tight-binding model is a widely-used theoretical framework in condensed-matter physics and materials science for understanding the electronic structure of solids. This model is particularly relevant for systems where electrons are strongly localised around their respective atomic sites, leading to discrete energy levels or energy bands. The tight-binding model provides a simple yet powerful description of these bands, capturing essential features of the electronic behavior in complex materials.

It is based on the superposition of atomic orbitals (or localised Wannier function) to construct the wavefunctions of the electrons in the crystal lattice. Hence, it is also called the Linear Combinations of Atomic Orbitals (LCAO) method. By considering the interactions between the atomic orbitals, the model derives a set of energy eigenvalues and eigenstates that describe the allowed energy levels of the electrons in the solid. This allows a detailed understanding of the band structure, density of states, and other electronic properties of various materials, from simple crystals to complex compounds [277]. Apart from the practical utility, the tight-binding model has also been a framework to construct effective models that provides an instructive insight to physical problems while also keeping the simplicity, such as the models as summarised in Section 2.2.1. In this section we will give a brief description of the tight-binding model. The text is mainly adapted from Ref. [277–279].

For a finite system like a molecule, we can choose the atomic orbitals as basis and write the eigenstates of the Hamiltonian as a linear combination of them [278]:

$$\Psi_n(\boldsymbol{r}) = \sum_j C_j^n \phi_j(\boldsymbol{r} - \boldsymbol{\tau}_j), \tag{3.1}$$

where ϕ_j is the j-th basis orbital, $\boldsymbol{r}$ is a general position in space, and $\boldsymbol{\tau}_j$ is the location of the j-th basis orbital. The coefficient of the j-th basis orbital of the n-th eigenstate is denoted as C_j^n. By inserting Equation (3.1) into the Schrödinger equation $H|\Psi_n\rangle = E_n|\Psi_n\rangle$, one can obtain the eigenvalues and eigenstates by solving the matrix equation:

$$(\mathcal{H} - E_n\mathcal{S})C_n = 0, \tag{3.2}$$

where $\mathcal{H}$ and $\mathcal{S}$ are the Hamiltonian matrix and the overlap matrix, respectively. The matrix elements can be written as:

$$\begin{aligned} \mathcal{H}_{ij} &= \langle\phi_i|H|\phi_j\rangle, \\ \mathcal{S}_{ij} &= \langle\phi_i|\phi_j\rangle. \end{aligned} \tag{3.3}$$

The diagonal and off-diagonal elements of the Hamiltonian matrix are often called on-site energies and hopping energies (or hopping integral, hopping matrix element), respectively. If we assume each atomic site to only contribute one basis orbital, and the basis orbitals from different atomic sites to be approximately orthonormal to each other, i.e.

$$\langle \phi_i | \phi_j \rangle \approx \delta_{ij}, \tag{3.4}$$

then the overlap matrix is equivalent to an identity matrix. In general, however, this is only true if one does not include multiple basis orbitals from the same atom.

For periodic systems, according to the Bloch theorem, the wavefunction is expressed as a plane wave multiplying a cell-periodic function [277]:

$$\Psi_{n\boldsymbol{k}}(\boldsymbol{r}) = \mathrm{e}^{\mathrm{i}\boldsymbol{k}\boldsymbol{r}} u_{n\boldsymbol{k}}(\boldsymbol{r}). \tag{3.5}$$

Using atomic orbitals as basis, the Bloch wavefunction can be written in the form of

$$\begin{aligned} \Psi_{n\boldsymbol{k}}(\boldsymbol{r}) &= \sum_j C_j^{n\boldsymbol{k}} |\chi_j^{\boldsymbol{k}}\rangle \\ &= \sum_j \sum_{\boldsymbol{R}} C_j^{n\boldsymbol{k}} \mathrm{e}^{\mathrm{i}\boldsymbol{k}\boldsymbol{R}} |\phi_{\boldsymbol{R}j}\rangle. \end{aligned} \tag{3.6}$$

The basis orbital $\phi_{\boldsymbol{R}j}$ now runs over not only each orbital j in the unit cell, but also over each unit cell, labelled by $\boldsymbol{R}$. It can also be written as $\phi_j(\boldsymbol{r} - \boldsymbol{R} - \boldsymbol{\tau}_j)$ [278]. By inserting the Equation (3.6) into the Schrödinger equation, we can obtain the secular equation again:

$$(\mathcal{H}_{\boldsymbol{k}} - E_{n\boldsymbol{k}} \mathcal{S}_{\boldsymbol{k}}) C_{n\boldsymbol{k}} = 0, \tag{3.7}$$

from which the eigenvalues and eigenstates can be easily obtained. Similar to Equation (3.3), the matrix elements of $\mathcal{S}_{\boldsymbol{k}}$ and $\mathcal{H}_{\boldsymbol{k}}$ are given by

$$\begin{aligned} \mathcal{S}_{ij}^{\boldsymbol{k}} &= \langle \chi_i^{\boldsymbol{k}} | \chi_j^{\boldsymbol{k}} \rangle \\ \mathcal{H}_{ij}^{\boldsymbol{k}} &= \langle \chi_i^{\boldsymbol{k}} | H | \chi_j^{\boldsymbol{k}} \rangle = \sum_{\boldsymbol{R}} \mathrm{e}^{\mathrm{i}\boldsymbol{k}\cdot(\boldsymbol{R}+\boldsymbol{\tau}_j-\boldsymbol{\tau}_i)} \mathcal{H}_{ij}^{\boldsymbol{R}}, \end{aligned} \tag{3.8}$$

where $\mathcal{H}_{ij}^{\boldsymbol{R}}$ is the matrix element of real space representation of the Hamiltonian. It is defined as

$$\mathcal{H}_{ij}^{\boldsymbol{R}} = \langle \phi_{\boldsymbol{R}',i} | H | \phi_{\boldsymbol{R}'+\boldsymbol{R},j} \rangle = \langle \phi_{\boldsymbol{0}i} | H | \phi_{\boldsymbol{R}j} \rangle. \tag{3.9}$$

Note that in practical calculations usually it is sufficient to consider only nearest-neighbour interactions, while other terms are ignored. Hence, this model is also called nearest-neighbour tight-binding model. This implies that $H_{ij}^{\boldsymbol{R}}$ is only non-zero for nearest neighbours and on-site terms. When nearest neighbouring pairs are equivalent, we can use a constant t to express it, where t is the so-called hopping integral. It is usually negative because the potential field in neighbouring sites attracts the tightly bound electrons [279].

The tight-binding model is often written using a second-quantisation formalism [279]. It is expressed as

$$H = \varepsilon_i \sum_i c_i^\dagger c_i - t_{\langle i,j \rangle} \sum_{\langle i,j \rangle} c_i^\dagger c_j, \tag{3.10}$$

where ε_i and $t_{\langle i,j \rangle}$ are the on-site energy at orbital i and hopping energy between orbital i and orbital j, respectively, and $c_i^\dagger / c_i$ are the annihilation/creation operators for electrons at orbital i.

Taking graphene as example, the simple tight-binding model can give a remarkably good estimation of the band structure. The tight-binding Hamiltonian of graphene is constructed by using carbon p_z-orbitals as basis [65]. Assuming the overlap between adjacent orbitals is negligible, the Hamiltonian reads as follows:

$$H = -t \sum_{\langle i,j \rangle} \left(a_i^\dagger b_j + b_j^\dagger a_i \right) = -t \sum_{i \in A} \sum_{\boldsymbol{\delta}} \left(a_i^\dagger b_{i+\boldsymbol{\delta}} + b_{i+\boldsymbol{\delta}}^\dagger a_i \right) \tag{3.11}$$

where $a_i^\dagger$ (a_i) creates (annihilates) an electron at site i in sublattice A, and $b_j^\dagger$ (b_j) creates (annihilates) an electron at site j in sublattice B. The summation $\langle i, j \rangle$ runs

over all nearest neighbours (A,B). The nearest-neighbour vector is denoted as $\boldsymbol{\delta}$, as illustrated in Figure 2.1. Subsequently, by performing the Fourier transformation:

$$a_i^\dagger = \frac{1}{\sqrt{N/2}} \sum_{\boldsymbol{k}} \mathrm{e}^{\mathrm{i}\boldsymbol{k}\boldsymbol{r}_i} a_{\boldsymbol{k}}^\dagger, \tag{3.12}$$

where N is the total number of atoms in both A and B sublattices, we can obtain the momentum-space representation of the Hamiltonian:

$$\begin{aligned} H &= -t \sum_{\boldsymbol{k},\boldsymbol{\delta}} \left(\mathrm{e}^{-\mathrm{i}\boldsymbol{k}\boldsymbol{\delta}} a_{\boldsymbol{k}}^\dagger b_{\boldsymbol{k}} + \mathrm{e}^{\mathrm{i}\boldsymbol{k}\boldsymbol{\delta}} b_{\boldsymbol{k}}^\dagger a_{\boldsymbol{k}} \right) \\ &= \sum_{\boldsymbol{k}} \boldsymbol{\Psi}^\dagger \mathcal{H}(\boldsymbol{k}) \, \boldsymbol{\Psi}, \end{aligned} \tag{3.13}$$

where

$$\boldsymbol{\Psi}^\dagger = \begin{pmatrix} a_{\boldsymbol{k}}^\dagger & b_{\boldsymbol{k}}^\dagger \end{pmatrix}, \quad \boldsymbol{\Psi} = \begin{pmatrix} a_{\boldsymbol{k}} \\ b_{\boldsymbol{k}} \end{pmatrix}, \tag{3.14}$$

$$\mathcal{H}(\boldsymbol{k}) = -t \begin{pmatrix} 0 & \Delta_{\boldsymbol{k}} \\ \Delta_{\boldsymbol{k}}^* & 0 \end{pmatrix}, \tag{3.15}$$

$$\Delta_{\boldsymbol{k}} = \sum_{\boldsymbol{\delta}} \mathrm{e}^{-\mathrm{i}\boldsymbol{k}\boldsymbol{\delta}}. \tag{3.16}$$

By diagonalising the Hamiltonian kernel $\mathcal{H}(\boldsymbol{k})$, we can obtain the energy bands of graphene:

$$E_\pm = \pm\sqrt{\Delta_{\boldsymbol{k}} \Delta_{\boldsymbol{k}}^*}, \tag{3.17}$$

where ± stands for the unoccupied and occupied energy bands, respectively.

For a simple system like graphene, it is relatively simple to carry out the tight-binding calculation analytically. For systems with larger bases and irregular geometries like GNRs, however, the analytical tight-binding calculations can be a daunting task. Therefore, a numerical approach is adopted for the tight-binding calculations presented in this thesis. The numerical tight-binding models were constructed with the help of the SISL code package [280].

It is worth noting that while the tight-binding model is a simple tool for gaining insights into the fundamental properties of materials, it fails to provide an accurate description of the electronic structure. For example, it is incapable of describing electron–electron interactions. The Hubbard model is another simple yet powerful

model that resembles the tight-binding approach but accounts for electron–electron interactions. It takes into account both the kinetic energy of the electrons and their mutual Coulomb repulsion, and has been used to study strongly-correlated electron systems in condensed-matter physics [279]. The Hubbard Hamiltonian is written as follows:

$$H = -t \sum_{\langle i,j\rangle,\sigma} (c^{\dagger}_{i\sigma} c_{j\sigma} + \text{h.c.}) + U \sum_{i} n_{i\uparrow} n_{i\downarrow}. \tag{3.18}$$

The first term represents the kinetic energy of the electrons and is modeled by a tight-binding approximation, which describes the hopping of electrons between lattice sites. The h.c. stands for Hermitian conjugate. The second term in Equation (3.18) describes the on-site Coulomb interaction, representing the energy cost of having two electrons with opposite spins occupying the same lattice site i. The on-site Coulomb repulsion energy is represented by U. The number operators for spin-up and spin-down electrons at site i are denoted as $n_{i\uparrow} = c^{\dagger}_{i\uparrow} c_{i\uparrow}$ and $n_{i\downarrow} = c^{\dagger}_{i\downarrow} c_{i\downarrow}$, respectively. The Hubbard model is similar to Equation (3.10), but additionally includes on-site Coulomb interactions between electrons. Meanwhile, this model neglects possible long-range Coulomb interactions. In graphene, however, long-range Coulomb interactions are quite important, because the density of states vanishes at the Fermi level, and, consequently, screening effects are expected to be low. Nevertheless, recent studies have shown that long-range Coulomb interactions have only negligible effects on the ferromagnetism of zigzag edge states in graphene [281]. Therefore, it is still appropriate to use this model when calculating magnetic properties.

The calculation of the Hubbard model is often very complicated to implement due to the exponential scaling of basis size [282]. In practice, to simplify the calculation, the on-site interaction term is often approximated with an averaged field term as follows [283]:

$$H_{\text{MF}} = -t \sum_{\langle i,j\rangle,\sigma} \left(c^{\dagger}_{i\sigma} c_{j\sigma} + \text{h.c.}\right) + U \sum_{i} \left(\langle n_{i\uparrow}\rangle n_{i\downarrow} + n_{i\uparrow}\langle n_{i\downarrow}\rangle - \langle n_{i\uparrow}\rangle\langle n_{i\downarrow}\rangle\right). \tag{3.19}$$

This approach greatly reduces the complexity by converting a many-body problem to a one-body problem. Compared with the pristine Hubbard model, the mean-field Hamiltonian can be solved through a self-consistent iterative procedure, making it more tractable for finding solutions. Despite its simplicity, the mean-field Hubbard model can capture some essential features of correlated electron systems, such as the emergence of antiferromagnetism and the Mott insulator phase [284].

3.1.2 DFT

In this section, we introduce the basics of DFT. The theory can be found in many textbooks. Here we mainly adapted the content from Ref. [279, 285]. DFT is a first-principles method based on quantum mechanics that does not rely on empirical parameters or phenomenological models. It provides a good balance between accuracy and computational efficiency and is suitable for a wide range of systems, including molecules and solids. Its philosophy is based on the key insight that the ground-state properties of a system can be determined entirely by its electron density, rather than by directly considering the many-body wavefunctions [285]. We start to introduce DFT from the many-body wavefunction:

$$\Psi = \Psi\left(\boldsymbol{r}_1, \boldsymbol{r}_2, \ldots, \boldsymbol{r}_N; \boldsymbol{R}_1, \boldsymbol{R}_2, \ldots, \boldsymbol{R}_M\right), \tag{3.20}$$

which is a function of the coordinates of both electrons $(\boldsymbol{r}_1, \boldsymbol{r}_2, \ldots, \boldsymbol{r}_N)$ and nuclei $(\boldsymbol{R}_1, \boldsymbol{R}_2, \ldots, \boldsymbol{R}_M)$. The Hamiltonian to describe this system is:

$$\begin{aligned} H = & \underbrace{-\sum_i \frac{\hbar^2}{2m_e}\nabla_i^2}_{\text{Kinetic energy of electrons}} \quad \underbrace{-\sum_I \frac{\hbar^2}{|2M_I|}\nabla_I^2}_{\text{Kinetic energy of nuclei}} \quad \underbrace{+\frac{1}{2}\sum_{i\neq j}\frac{e^2}{4\pi\epsilon_0}\frac{1}{|\boldsymbol{r}_i - \boldsymbol{r}_j|}}_{\text{Electron–electron Coulomb repulsion}} \\ & \underbrace{+\frac{1}{2}\sum_{I\neq J}\frac{e^2}{4\pi\epsilon_0}\frac{Z_I Z_J}{|\boldsymbol{R}_I - \boldsymbol{R}_J|}}_{\text{Nucleus–nucleus Coulomb repulsion}} \quad \underbrace{-\sum_{i,I}\frac{e^2}{4\pi\epsilon_0}\frac{Z_I}{|\boldsymbol{r}_i - \boldsymbol{R}_I|}}_{\text{Nucleus–electron Coulomb attraction}} , \end{aligned} \tag{3.21}$$

where $\hbar$ is the reduced Planck constant, m_e is the mass of an electron, M_I is the mass of the I-th nucleus, ∇^2 is the Laplacian operator for spatial coordinates, e is

the charge of an electron, ϵ_0 is the vacuum permittivity, Z_I is the atomic number of the I-th nucleus, r_i is the position vector of the i-th electron, and R_I is the position vector of the I-th nucleus. As the mass of nuclei is way larger than that of electrons, based on the Born–Oppenheimer approximation [285], one can treat the nuclei as static and reduce the Hamiltonian to the following simplified form:

$$\begin{aligned} H &= -\sum_i \frac{\hbar^2}{2m_e}\nabla_i^2 - \sum_{i,I}\frac{e^2}{4\pi\epsilon_0}\frac{Z_I}{|\boldsymbol{r}_i - \boldsymbol{R}_I|} + \frac{1}{2}\sum_{i\neq j}\frac{e^2}{4\pi\epsilon_0}\frac{1}{|\boldsymbol{r}_i - \boldsymbol{r}_j|} \\ &= -\sum_i \frac{\nabla_i^2}{2} - \sum_{i,I}\frac{Z_I}{|\boldsymbol{r}_i - \boldsymbol{R}_I|} + \frac{1}{2}\sum_{i\neq j}\frac{1}{|\boldsymbol{r}_i - \boldsymbol{r}_j|} \quad \text{(in atomic units)}\,. \end{aligned} \tag{3.22}$$

Meanwhile, the wavefunction only depends on the spatial positions of the electrons:

$$\Psi = \Psi\left(\boldsymbol{r}_1, \boldsymbol{r}_2, \ldots, \boldsymbol{r}_N\right). \tag{3.23}$$

Now, the energy of the many-body system can be calculated from the following equation:

$$E = \langle \Psi | H | \Psi \rangle = \int \mathrm{d}\boldsymbol{r}_1 \ldots \mathrm{d}\boldsymbol{r}_N \, \Psi^*(\boldsymbol{r}_1, \ldots, \boldsymbol{r}_N) H \, \Psi(\boldsymbol{r}_1, \ldots, \boldsymbol{r}_N). \tag{3.24}$$

To solve this equation, early attempts like the Hatree–Fock (HF) approximation simplified the problem by assuming that the many-body wavefunction can be approximated by a single Slater determinant, which is an antisymmetrised product of single-electron wavefunctions. With the HF approximation, one only needs to work with single-particle wavefunctions rather than with complicated many-body wavefunctions. Furthermore, it takes the exchange interaction into consideration. However, despite its success in providing qualitative insights into many systems, the HF approximation fails in accounting for electron correlations. In addition to that, within this theory, there is no rigorous justification for the use of single-particle solutions for the many-body problem.

In contrast, the density-functional theory approach provides a rigorous framework for single-particle approximations where exchange and correlation effects are taken into account by using functionals of electron densities. The foundation of DFT

theory is the Hohenberg–Kohn theorem [286], which states that the ground-state energy of a many-electron system is a functional of the electron density $n(\boldsymbol{r})$, i.e.

$$E = F[n(\boldsymbol{r})]. \tag{3.25}$$

This can be proven in three steps [285]: 1) the electron density $n(\boldsymbol{r})$ uniquely determines the external potential field generated by nuclei $V_n(\boldsymbol{r})$, i.e. the second term in Equation (3.22); 2) the external potential $V_n(\boldsymbol{r})$ uniquely determines the many-body wavefunction Ψ; 3) the total energy of the system is a functional of Ψ. Based on the Hohnberg-Kohn theorem, the total energy of the system can be derived:

$$E = \underbrace{-\sum_i \int \phi_i^*(\boldsymbol{r}) \frac{\nabla^2}{2} \phi_i(\boldsymbol{r}) \, \mathrm{d}\boldsymbol{r}}_{\text{Kinetic energy}} + \underbrace{\int n(\boldsymbol{r}) V_n(\boldsymbol{r}) \, \mathrm{d}\boldsymbol{r}}_{\text{External potential}} + \underbrace{\frac{1}{2} \iint \frac{n(\boldsymbol{r}) n(\boldsymbol{r}')}{|\boldsymbol{r} - \boldsymbol{r}'|} \, \mathrm{d}\boldsymbol{r} \, \mathrm{d}\boldsymbol{r}'}_{\text{Hartree energy}} + \underbrace{E_{\mathrm{xc}}[n]}_{\text{Exchange-correlation energy}}. \tag{3.26}$$

Subsequently, by employing the variational principle, the equation above leads to the famous Kohn–Sham equations [285]:

$$\left[-\frac{1}{2} \nabla^2 + V_n(\boldsymbol{r}) + V_{\mathrm{H}}(\boldsymbol{r}) + V_{\mathrm{xc}}(\boldsymbol{r}) \right] \phi_i(\boldsymbol{r}) = \varepsilon_i \phi_i(\boldsymbol{r}), \tag{3.27}$$

where

$$V_n(\boldsymbol{r}) = \sum_I \frac{Z_I}{|\boldsymbol{r} - \boldsymbol{R}_I|}, \tag{3.28}$$

$$V_{\mathrm{H}}(\boldsymbol{r}) = \int \frac{n(\boldsymbol{r}')}{|\boldsymbol{r} - \boldsymbol{r}'|} \, \mathrm{d}\boldsymbol{r}', \tag{3.29}$$

$$V_{\mathrm{xc}}(\boldsymbol{r}) = \frac{\delta E_{\mathrm{xc}}[n]}{\delta n(\boldsymbol{r})}, \tag{3.30}$$

$$n(\boldsymbol{r}) = \sum_i |\phi_i(\boldsymbol{r})|^2. \tag{3.31}$$

It is remarkable that the kinetic energy, external potential energy, and Hartree energy can be directly calculated from independent electron wavefunctions $\phi(\boldsymbol{r})$, and all the terms that are left out are included in the exchange-correlation (XC)

energy E_{xc}. The Equation (3.27)–Equation (3.31) can be solved in self-consistent cycles. Although the exact form of E_{xc} is unknown, the equation itself is exact. The challenge is to obtain an exchange-correlation functional as accurate as possible. Up to now many approximate XC functionals have been reported. For example, the simplest forms are the local-density approximation (LDA) [287] and the generalised-gradient approximation (GGA) [288]. The LDA functional assumes that the XC is only a function of the electron density, while the GGA improves it by including the gradient of the electron density. When electron spins are considered in the LDA calculation, it is also known as LSDA, and the calculation is called spin-unrestricted. Except for LDA and GGA, some hybrid functionals like B3LYP are also proposed to improve the accuracy of a calculation. Until now, they have been used to obtain a variety of important results in the field of condensed-matter physics and quantum chemistry [289–291].

In this thesis, we choose appropriate functionals for different types of calculations. For example, LDA and GGA functionals give correct predictions of the topological invariants, although the LDA and the GGA functionals underestimate band gaps [193]. That is because topological phases in GNRs are not affected significantly by moderate inaccuracies of the band gap. We chose the GGA functional for all calculations related to topological phases for consistency. For the calculations of vibrational properties, we chose the LDA functional because we found that it works better for avoiding negative frequencies. We furthermore compared the calculation results with experimental data, and we found that LDA provides better simulation results for the vibrational modes of GNRs in our case. In fact, the LDA functional is widely used in literature for the calculation of vibrational properties of GNRs [270, 292, 293]. For Raman simulations, we adopted the approach implemented in Quantum ESPRESSO, which has been reported in several studies [276, 294]. Also here we chose the LDA functional since, at the moment, only LDA is supported for Raman-intensity calculations in Quantum ESPRESSO.

In practice, besides the XC functionals, there are many other parameters that need to be carefully tuned to ensure the convergence and precision of DFT calculations, such as the basis set, the mesh cutoff, and the k-point sampling. In this thesis, we mainly employ DFT to calculate the electronic structure and phonon properties of GNRs. Topological phases can be calculated based on the DFT results and Wannierisation, which will be introduced in the next subsection. The band structure can be calculated by making use of the Bloch theorem. For a periodic system the single-particle wavefunction is written as the product of a plane wave and a cell-periodic function:

$$\phi_{i\boldsymbol{k}}(\boldsymbol{r}) = \mathrm{e}^{\mathrm{i}\boldsymbol{k}\boldsymbol{r}} u_{i\boldsymbol{k}}(\boldsymbol{r}) . \tag{3.32}$$

By inserting this into Equation (3.27), we obtain a modified version of the Kohn–Sham equation:

$$\left[-\frac{1}{2}(\nabla + \mathrm{i}\boldsymbol{k})^2 + V_n(\boldsymbol{r}) + V_{\mathrm{H}}(\boldsymbol{r}) + V_{\mathrm{xc}}(\boldsymbol{r})\right] u_{i\boldsymbol{k}}(\boldsymbol{r}) = \varepsilon_{i\boldsymbol{k}} u_{i\boldsymbol{k}}(\boldsymbol{r}) . \tag{3.33}$$

After solving the equation above iteratively, we obtain the eigenvalues $\varepsilon_{i\boldsymbol{k}}$ and plot their dispersion with respect to the wavevector k. Note that $\varepsilon_{i\boldsymbol{k}}$ and $u_{i\boldsymbol{k}}(\boldsymbol{r})$ are only single-particle eigenvalues and eigenstates. The electron–electron interaction is only approximated by an effective potential field, but is not calculated explicitly. Furthermore, DFT is only capable of calculating ground state properties. Although the Kohn–Sham band structure yields unoccupied states above the Fermi level, which can often provide a sensible prediction for the material properties, these unoccupied states are not real excited states. DFT often tends to underestimate the band gap in materials because it neglects many-body interactions. It also suffers from further problems, such as the self-interaction error, the delocalisation error, and the static correlation error [289, 295, 296]. Nevertheless, DFT has been proven to be a very successful tool for the modelling of materials properties in condensed-matter physics and quantum chemistry [285]. In this thesis, DFT is still

a legitimate tool to calculate the topological phase of GNRs since the topological properties are insensitive to the actual band gap size, but only sensitive to the closing or opening of the band gap.

On the other hand, DFT can be used to calculate the vibrational properties of materials. Within the Born-Oppenheimer approximation, the Hamiltonian for the nuclei can be written as:

$$H_n = -\sum_I \frac{\nabla_I^2}{2M_I} + U(\boldsymbol{R}_1, \ldots, \boldsymbol{R}_M), \tag{3.34}$$

where $U(\boldsymbol{R}_1, \ldots, \boldsymbol{R}_M)$ is the total potential energy of the nuclei given by:

$$U(\boldsymbol{R}_1, \ldots, \boldsymbol{R}_M) = \frac{1}{2}\sum_{I \neq J} \frac{Z_I Z_J}{|\boldsymbol{R}_I - \boldsymbol{R}_J|} + E(\boldsymbol{R}_1, \ldots, \boldsymbol{R}_M). \tag{3.35}$$

$E(\boldsymbol{R}_1, \ldots, \boldsymbol{R}_M)$ is the energy of all electrons when nuclei positions are fixed to $\boldsymbol{R}_1, \ldots, \boldsymbol{R}_M$. Considering atomic displacements to be small compared with interatomic distances, one can apply a harmonic approximation to the potential energy $U(\boldsymbol{R}_1, \ldots, \boldsymbol{R}_M)$ and obtain the interatomic force constant in real space:

$$C_{I\alpha,J\beta}(l, l') = \frac{\partial^2 U}{\partial u_{I\alpha}^l u_{J\beta}^{l'}}, \tag{3.36}$$

where $u_{I\alpha}^l$ is the atomic displacement of atom I from unit cell l along direction α, $C_{I\alpha,J\beta}(l, l')$ is the force constant between atom I, which is from unit cell l and moves along direction α, and atom J, which is from unit cell l' and moves along direction β. Since DFT is able to calculate the total potential energy for any positions of nuclei, it is straightforward to compute the interatomic force constants based on Equation (3.36). Subsequently, we can couple the Newton equations of motion for all the N nuclei and get $3N$ equations:

$$M_I \frac{\partial^2 u_{I\alpha}^l}{\partial t^2} = -\sum_{l',J,\beta} C_{I\alpha,J\beta}(l, l') u_{J\beta}^{l'}, \tag{3.37}$$

where M_I is the mass of nuclei I. For periodic systems, we assume the atomic displacement u is in the form of

$$u_{I\alpha}^l(t) = \frac{1}{\sqrt{M_I}} \sum_m \gamma_{m\boldsymbol{q}}(I\alpha)\, \mathrm{e}^{\mathrm{i}\boldsymbol{q}\boldsymbol{R}_I} \mathrm{e}^{-\mathrm{i}\omega_{m\boldsymbol{q}} t}, \tag{3.38}$$

where $\gamma_{m\boldsymbol{q}}(I\alpha)$ is the normalised phonon vector of I-th atom along the α direction of the m-th phonon mode at wavevector $\boldsymbol{q}$, $\omega_{m\boldsymbol{q}}$ is the phonon frequency. Meanwhile, we convert the interatomic force constants to the momentum space by a Fourier transformation, and normalise them by the atomic weight:

$$D_{I\alpha,J\beta}(\boldsymbol{q}) = \frac{1}{\sqrt{M_I M_J}} C_{I\alpha,J\beta}(\boldsymbol{q}) = \frac{1}{\sqrt{M_I M_J}} \sum_{l'} C_{I\alpha,J\beta}(0,l') e^{i\boldsymbol{q}\boldsymbol{R}_J}, \tag{3.39}$$

where $C_{I\alpha,J\beta}(\boldsymbol{q})$ is the interatomic force constant in reciprocal space, and $D_{I\alpha,J\beta}(\boldsymbol{q})$ is the dynamical matrix. Finally, we can combine Equation (3.37)–Equation (3.39) and derive the dynamical equation:

$$\sum_{J\beta} D_{I\alpha,J\beta}(\boldsymbol{q})\, \gamma_{m\boldsymbol{q}}(J\beta) = \omega^2_{m\boldsymbol{q}} \gamma_{m\boldsymbol{q}}(I\alpha)\,. \tag{3.40}$$

The normal frequencies and corresponding phonon vectors can be solved by diagonalising the above dynamical matrix.

So far, in this chapter we have reviewed the basic theories relevant to DFT methods that are employed in this thesis. There are many programs that can carry out the DFT calculations. They can be categorised based on the basis set, such as plane-wave type like Quantum ESPRESSO [297], VASP [298], or localised-orbital type like SIESTA [299], GAUSSIAN [300], or ORCA [301]. In this thesis we mainly use the open-source software SIESTA, which provides the advantage of linear scaling for large systems. It is capable of calculating both periodic system and molecules. Other softwares like Quantum ESPRESSO, GAUSSIAN, and ORCA are also used depending on the scenario.

3.1.3 Topology

We introduced the background of topology in Section 2.2. In this section we will explain the methodology of calculating topological phases in GNRs, primarily within the numerical tight-binding framework. For 1D systems, the topological phase is characterised by the Zak phase (Equation (2.10)). Rhim et al. proved that only

the intercellular part of the Zak phase is origin-independent and should be used to characterise the topological phase [208]. By using the tight-binding representation of the Bloch function in Equation (3.6) and the Bloch theorem (Equation (3.5)), the Zak phase is split into two parts as follows:

$$\gamma_n = \underbrace{\int_{\mathrm{BZ}} \mathrm{d}k \langle \Psi_{nk}|x|\Psi_{nk}\rangle - 2\pi\tilde{N}}_{\gamma_n^{\mathrm{intra}}} + \mathrm{i}\underbrace{\int_{\mathrm{BZ}} \mathrm{d}k \sum_{j,j'} C_j^{nk*}\partial_k C_{j'}^{nk}}_{\gamma_n^{\mathrm{inter}}}, \tag{3.41}$$

where $\gamma_n^{\mathrm{intra}}$ and $\gamma_n^{\mathrm{inter}}$ are the intracellular and intercellular Zak phase for band n, respectively, $\tilde{N}$ is an arbitrary integer that depends on the choice of the unit cell, C_j^{nk} are the eigenvectors calculated from the tight-binding model as introduced in Section 3.1.1. The intracellular Zak phase depends on the choice of origin, and is related to the classical electric polarisation, whereas the intercellular Zak phase reflects the extra charge accummulation at the boundary due to topological effects.

When the system has spatial symmetries, such as a mirror symmetry or an inversion symmetry, the intercellular Zak phase is quantised to 0 or π. Based on $\gamma_n^{\mathrm{inter}}$, the $\mathbb{Z}_2$ index can be calculated from Equation (2.12). According to bulk–boundary correspondence, the system has odd number of localised boundary states in the middle of a band gap when the $\mathbb{Z}_2$ index equals 1 ($\gamma^{\mathrm{inter}} = \pi$), and an even (including zero) number of boundary states when $\mathbb{Z}_2$ index equals 0 ($\gamma^{\mathrm{inter}} = 0$). When two different systems, for example, two different GNR segments, are connected, the number of localised junction states is determined by the difference between the $\mathbb{Z}_2$ indices of the two segments [12].

Note that the formula given in Equation (2.10) is in its continuous form. In practical calculations it can be very difficult to derive analytical solutions for some systems. In such cases, one has to resort to the discretised form of Zak phase to carry out numerical integration [278]. The Zak phase is a special Berry phase in 1D systems. The general discrete formulation of the Berry phase is written as:

$$\gamma = -\Im\left[\ln\left(\langle u_0|u_1\rangle\langle u_1|u_2\rangle \ldots \langle u_{N_k-1}|u_0\rangle\right)\right], \tag{3.42}$$

where $u_0, \cdots, u_{N_k-1}$ are the Bloch functions at the N_k discrete k points in the Brillouin zone. The k points are defined as:

$$k_m = \frac{2\pi}{a}\frac{m}{N_k}, \quad m = 1, 2, ..., N_k, \tag{3.43}$$

where a denotes the length of lattice vector in the 1D system.

For multiband systems, the intercellular Zak phase is expressed as [302]:

$$\gamma^{\text{inter}} = -\Im \ln \prod_{m}^{N_k} \det C^{\dagger}(k_m)\, S\left(k_m + \frac{\delta k}{2}\right) C(k_{m+1}), \tag{3.44}$$

where $C(k_m)$ is the coefficient matrix whose two dimensions correspond to all the occupied bands and all the basis orbitals at the m-th k point in the Brillouin zone, and its matrix element is same as the $C_j^{n\boldsymbol{k}}$ in Equation (3.6), δk is the interval between two adjacent k points, $S\left(k_m + \frac{\delta k}{2}\right)$ is the momentum-space representation of the overlap matrix at $k = k_m + \delta k/2$. Its matrix element is given by:

$$S_{jj'}^{k} = \sum_{R} \mathrm{e}^{\mathrm{i}kR} S_{jj'}^{R}, \quad S_{jj'}^{R} = \langle \phi_{0j} | \phi_{Rj'} \rangle, \tag{3.45}$$

where $S_{jj'}^{R}$ represents the real-space overlap matrix element. Once we have computed the intercellular Zak phase, the $\mathbb{Z}_2$ invariant can be obtained from Equation (2.12).

Next, we will briefly cover the numerical method to calculate the $\mathbb{Z}$ invariant. As reviewed in Section 2.2.2, the $\mathbb{Z}$ index can be analytically calculated from Equation (2.13). By using Equation (2.13) it is more obvious to see that the intercellular Zak phase sums up the contributions of two sublattices while the $\mathbb{Z}$ index computes the difference between them. The original definition of $\mathbb{Z}$, however, is given by:

$$\mathbb{Z} = -\frac{\mathrm{i}}{2\pi} \int_{\mathrm{BZ}} \mathrm{Tr}\left(U_k^{\dagger} \partial_k U_k\right) \mathrm{d}k, \tag{3.46}$$

where the matrix U_k is defined in the following expression:

$$\begin{aligned} Q_k &= \sum_{n \in \text{unocc}} |\Psi_{nk}\rangle \langle \Psi_{nk}| - \sum_{m \in \text{occ}} |\Psi_{mk}\rangle \langle \Psi_{mk}| \\ &= \begin{pmatrix} 0 & U_k \\ U_k^{\dagger} & 0 \end{pmatrix}. \end{aligned} \tag{3.47}$$

Here, Q_k is the Fermion operator constructed from the Bloch functions of all occupied bands (occ) and unoccupied bands (unocc). The Fermion operator can be regarded as a deformation of the Hamiltonian by changing all eigenvalues to ±1 while eigenvectors stay the same. For systems with chiral symmetry like graphene nanostructures, Q_k can be brought to a block off-diagonal form, where the off-diagonal blocks are represented by the U_k matrix. Similar to Equation (3.44), the discretised formula to calculate $\mathbb{Z}$ is expressed as:

$$\mathbb{Z} = -\Im \ln \prod_{m}^{N_k} \det U^{\dagger}\left(k_m\right) S\left(k_m + \frac{\delta k}{2}\right) U\left(k_{m+1}\right). \tag{3.48}$$

So far, we have introduced the basic methodology to calculate the $\mathbb{Z}_2$ and $\mathbb{Z}$ indices via a numerical integration approach. For some systems with inversion symmetry, the $\mathbb{Z}_2$ index can also be evaluated through the Fu–Kane method [177]. However, since this approach is limited to inversion-symmetric structures, the numerical integration approach is mainly adopted for the calculations in this thesis.

3.1.4 Wannier functions

In crystals, the wavefunctions are periodic in real space and are commonly represented by Bloch functions $\psi_{n\boldsymbol{k}}$. The theory we introduced before, including the tight-binding model and the topological phases, are also based on Bloch functions. Alternatively, there is another representation called Wannier function, which is related to Bloch functions via Fourier transformation. For a general three-dimensional system, the relation is written as:

$$\begin{aligned} |w_{n\boldsymbol{R}}\rangle &= \frac{V_{\text{cell}}}{(2\pi)^3} \int_{\text{BZ}} \mathrm{e}^{-\mathrm{i}\boldsymbol{k}\cdot\boldsymbol{R}} |\,\Psi_{n\boldsymbol{k}}\rangle \mathrm{d}^3k, \\ |\,\Psi_{n\boldsymbol{k}}\rangle &= \sum_{\boldsymbol{R}} \mathrm{e}^{\mathrm{i}\boldsymbol{k}\cdot\boldsymbol{R}} |w_{n\boldsymbol{R}}\rangle. \end{aligned} \tag{3.49}$$

Unlike the Bloch function $\Psi_{n\boldsymbol{k}}$, which is delocalised and periodic in real space, the Wannier function $w_{n\boldsymbol{R}}$ is localised in a single unit cell in real space. The Bloch functions are labelled by a wavevector $\boldsymbol{k}$, while the Wannier function are labelled

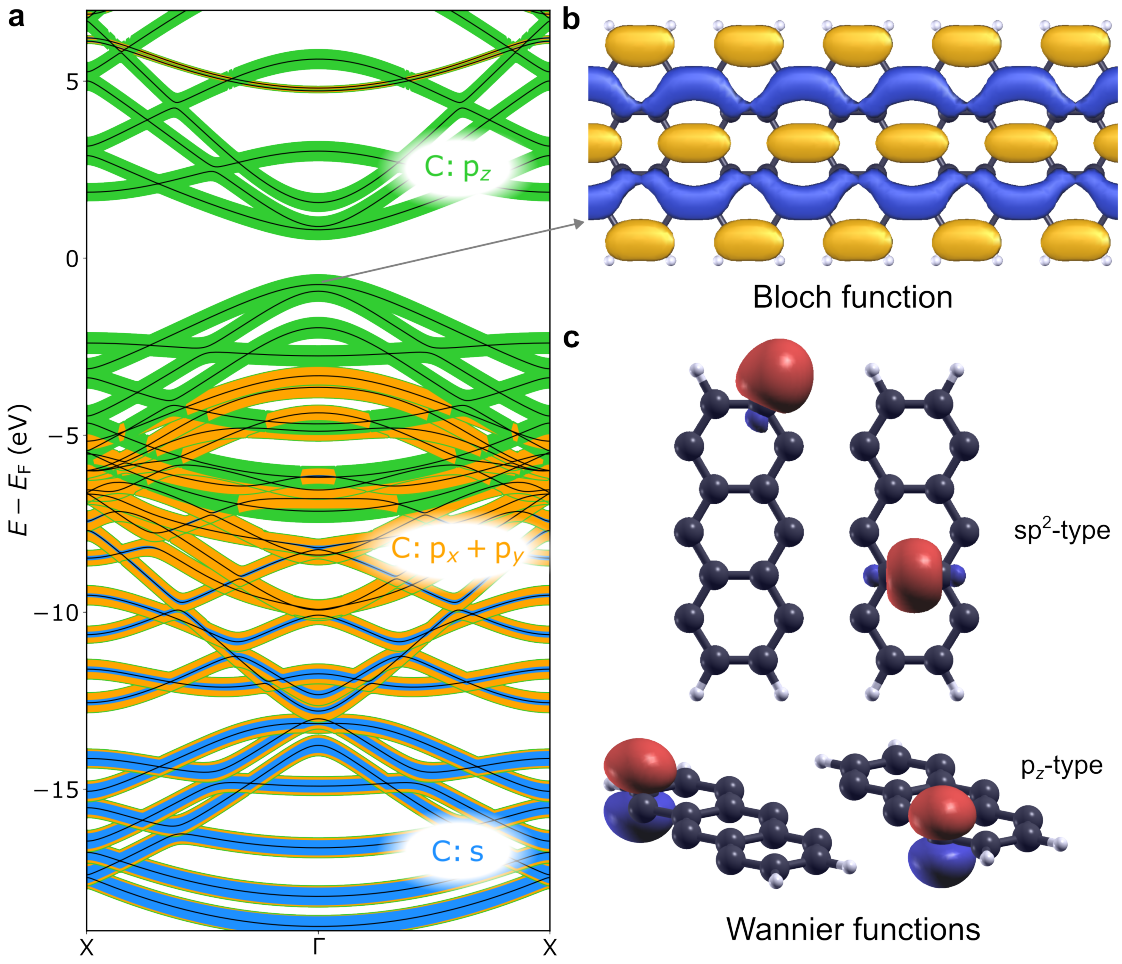


Figure 3.1: Fat bands, Bloch function, and Wannier function of 7-AGNR. (a) Fat bands representing the contribution of s-type (blue), p_x- and p_y-type (orange) and p_z-type (green) orbitals to the energy bands. (b) Bloch function of the valence band at the Γ point. (c) Examples of sp^2-type and p_z-type Wannier function obtained from Wannierising both occupied and unoccupied bands.

by a unit cell index $\boldsymbol{R}$. The Wannier function and Bloch functions are two different bases that represent the same quantum states. Although Bloch functions have the advantage of highlighting the periodicity and symmetry of a crystal, Wannier functions are particularly useful for intuitive physical and chemical interpretations of bonding or polarisation. For example, in Figure 3.1, we showed the character of each energy band of 7-AGNR by plotting the fat bands. The band structure is calculated from DFT. The bands are plotted with a certain width, and the width is divided into several parts based on the orbital type, with the width of each part

being proportional to the contribution of that type of orbital to this band. From the fat bands diagram we can analyse the type of bands. For instance, the bands close to the Fermi level are mainly constructed by p_z-orbitals of carbon atoms and are often called π-bands, because the p_z-orbitals have π-bonding character with each other. The bands deeper in energy are largely contributed by s-, p_x- and p_y-orbitals of carbon and they are highly hybridised. In chemistry, these states are regarded as resulting from sp^2 hybridisation. If we plot the Bloch function, shown in Figure 3.1b, not much information about the bonding character can be obtained. In contrast, with the Wannier function in Figure 3.1c we can visualise the chemical bonding such as π-bonds and sp^2-bonds that are associated with the energy bands. In Figure 3.1 we Wannierise both the occupied and unoccupied bands, so that we obtain all type of Wannier function. If, for instance, one only Wannierises the valence and conduction bands, only p_z-type Wannier function are obtained. In this way the bonding character of each band can be inspected separately.

Apart from visualising the chemical bonding, Wannier functions are also very powerful in many other occasions. For example, many physical quantities can be calculated from the Wannier representation, which has the advantage of linear-scaling, whereas the conventional methods based on the Bloch representation often have a third-power scaling and are thus computationally demanding [303]. The orthonormal tight-binding basis used earlier in this chapter are actually also a Wannier basis. For complicated structures, for which it is difficult to use a tight-binding approximation directly, we can Wannierise the Bloch states obtained from DFT calculations and use the Wannier functions as a rigorous tight-binding basis to calculate this system. It is important to note that while the Bloch functions for a given band are uniquely determined up to an overall phase factor, the corresponding Wannier functions are not unique. They can be chosen to be real and symmetric, which makes them useful for intuitive interpretations. In this

thesis we use the Wannier90 package [303–305] to calculate the so-called maximally localised Wannier functions (MLWFs).

In the field of band structure topology, Wannier functions also provide an alternative approach to calculate the topological index. For a certain Wannier function we can define the Wannier centre as:

$$\bar{\boldsymbol{r}}_n = \langle w_{n\mathbf{0}} | \boldsymbol{r} | w_{n\mathbf{0}} \rangle. \tag{3.50}$$

where the unit cell index is chosen to be $\mathbf{0}$ because the Wannier centre is modulo a (a is the lattice constant), therefore it is equivalent to choose any unit cell to evaluate the Wannier centre. In 1D, the Wannier centre is related to the Zak phase via [206, 278]

$$\bar{r}_n = a\frac{\gamma_n}{2\pi}, \quad \bar{r} = \sum_n \bar{r}_n = a\frac{\gamma}{2\pi}. \tag{3.51}$$

When the Wannier centre appears in the centre of the unit cell ($\bar{r} = 0$), it corresponds to $\gamma = 0$ and $\mathbb{Z}_2 = 0$. When the Wannier centre appears at the unit-cell boundary ($\bar{r} = a/2$), it corresponds to $\gamma = \pi$ and $\mathbb{Z}_2 = 1$. This offers an alternative approach to verify the topological phase calculation, as will be detailed in the next chapter.

3.2 Experimental methods

3.2.1 EPR spectroscopy

EPR, also known as electron spin resonance (ESR), is a powerful spectroscopic method used to investigate materials containing unpaired electrons, such as organic radicals, transition-metal complexes, defects in solids. In EPR, an external magnetic field B_0 is applied to a sample with unpaired electrons, creating an energy splitting between unpaired electrons aligned with or against this field, referred to as Zeeman splitting. Microwave radiation allows these spins to flip their alignment. This absorption only occurs when the microwave radiation's energy matches the energy

difference between the two spin states, a condition called resonance. The resonance condition can be represented by the following equation:

$$h\nu = g_e \mu_B B_0, \tag{3.52}$$

where ν is the microwave frequency. The frequencies typically available in experiments are often limited to several narrow frequency bands: X-band (9–10 GHz), Q-band (33–35 GHz), and W-band (95 GHz). The origins of these letter codes are from radar technology and carry no specific meaning [240]. The Landé g-factor, or simply g-factor, symbolised as g, characterises the magnetic moment of an electron. For free electrons, g is approximately 2.0023. The Bohr magneton is denoted by μ_B. The static external magnetic field and the oscillatory magnetic field driving the transition at a certain microwave frequency are represented by B_0 and B_1, respectively. In our experiments, when acquiring an EPR spectrum, the microwave frequency remains constant. By sweeping the magnetic field while recording the EPR signal, we can find the resonance peaks. By detecting these peaks, EPR can provide detailed information about the chemical environment surrounding the unpaired electrons, such as ligand fields, nuclear spins, and other unpaired electrons. EPR spectra can be measured either in the continuous-wave (CW) mode or the pulsed mode. The subsequent sections will provide a brief overview of the principles of CW and pulsed EPR. The text is mainly adapted from Ref. [240, 306].

3.2.1.1 CW EPR

In the CW EPR mode, a capillary tube that has a diameter of typically several millimeters and contains the sample is placed in the resonator's centre, where the microwave's magnetic-field component, B_1, is at a maximum, and the electric-field component, E_1, is at a minimum. The microwave radiation is continuously applied at a fixed frequency, and absorption is recorded while sweeping the static magnetic field B_0. At resonance, the magnetic field B_1 drives the transition between two

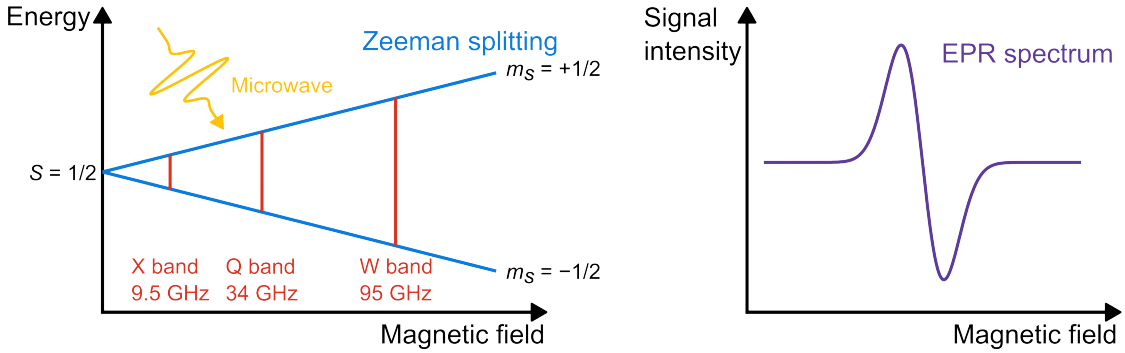


Figure 3.2: Principle of CW EPR for $S = 1/2$. The static magnetic field induces a Zeeman splitting between the energies of the spin doublet. Upon applying an oscillatory magnetic field at a certain microwave frequency (usually at X, Q, or W band), a transition occurs between the two spin states. A typical first derivative spectrum is shown on the right.

spin states, causing the population of the two spin states to oscillate sinusoidally, a phenomenon referred to as Rabi oscillation [307]. Ideally, the resonance condition results in a single line in the spectrum. In real systems, however, this line is usually broadened due to various factors. For instance, the random flip-flop of nuclear spins in proximity to the electron spin results in local magnetic field fluctuations, creating a homogeneous line broadening [306]. Inhomogeneous broadening of the spectrum may also occur because of factors such as unresolved hyperfine structures, spatial variations of the external static magnetic field, or anisotropic interactions in orientationally-disordered systems [306]. To enhance sensitivity, a modulation field, ΔB, typically operating at a frequency of 10–100 kHz, is added to B_0 using a lock-in detection technique. This process results in an absorption peak in its first-derivative lineshape, as depicted on the right of Figure 3.2.

The EPR spectrum in Figure 3.2 displays a single peak only. In real systems, however, various other interactions might lead to a more complicated spectrum,

which need to be included in the general spin Hamiltonian. It is written as

$$H = \underbrace{\mu_{\mathrm{B}} \boldsymbol{B}_0 \cdot \boldsymbol{g}_{\mathrm{e}} \cdot \hat{\boldsymbol{S}}}_{\text{Electron Zeeman energy}} + \underbrace{\sum_{i \neq j} \hat{\boldsymbol{S}}_i \cdot \boldsymbol{J}_{ij} \cdot \hat{\boldsymbol{S}}_j}_{\text{Exchange coupling}} + \underbrace{\sum_{i \neq j} \hat{\boldsymbol{S}}_i \cdot \boldsymbol{D}_{ij} \cdot \hat{\boldsymbol{S}}_j}_{\text{Zero-field splitting}} + \underbrace{\sum_i \hat{\boldsymbol{S}} \cdot \boldsymbol{A}_i \cdot \hat{\boldsymbol{I}}_i}_{\text{Hyperfine coupling}} - \underbrace{\sum_i g_{\mathrm{n},i} \mu_{\mathrm{n}} \boldsymbol{B}_0 \hat{\boldsymbol{I}}_i}_{\text{Nuclear Zeeman energy}} + \underbrace{\sum_{i \neq j} \hat{\boldsymbol{I}}_i \cdot \boldsymbol{P}_{ij} \cdot \hat{\boldsymbol{I}}_j}_{\text{Nuclear quadrupole interaction}} . \quad (3.53)$$

The electron Zeeman term describes the interaction of an electron spin $\hat{\boldsymbol{S}}$ with an external static magnetic field $\boldsymbol{B}_0$. The g-tensor of an electron is represented as $\boldsymbol{g}_{\mathrm{e}}$, which is generally anisotropic. The exchange-coupling tensor $\boldsymbol{J}$ describes the exchange interaction between electrons. The zero-field splitting term can stem from the dipolar coupling between electrons, spin–orbit coupling, or the ligand-field interactions. The hyperfine coupling between an electron and the surrounding nuclear spin i is indicated by $\boldsymbol{A}_i$. The remaining two terms – nuclear Zeeman energy and nuclear quadrupole interaction – typically have much lower magnitudes and are often neglected. To illustrate an EPR spectrum with multiple peaks, consider a simple example of a system composed of an electron spin and a nuclear spin. As shown in Figure 3.3, the electron Zeeman effect and hyperfine interactions lead to four energy levels. According to the selection rules, $\Delta m_s = \pm 1$ and $\Delta m_I = 0$, only two transitions are allowed at a certain frequency, as indicated by the red arrows in Figure 3.3. Consequently, two peaks appear in the EPR spectrum. In real EPR measurements, the hyperfine splitting is several orders smaller than the Zeeman splitting. The hyperfine coupling strength used for Figure 3.3 is exaggerated to make the hyperfine splitting more visible.

3.2.1.2 Pulsed EPR

In pulsed EPR, a short, high-power microwave pulse, typically with a length of tens to hundreds of nanoseconds, is applied to the sample. Instead of the continuous absorption, the transient emissive signal is recorded. There are a large number

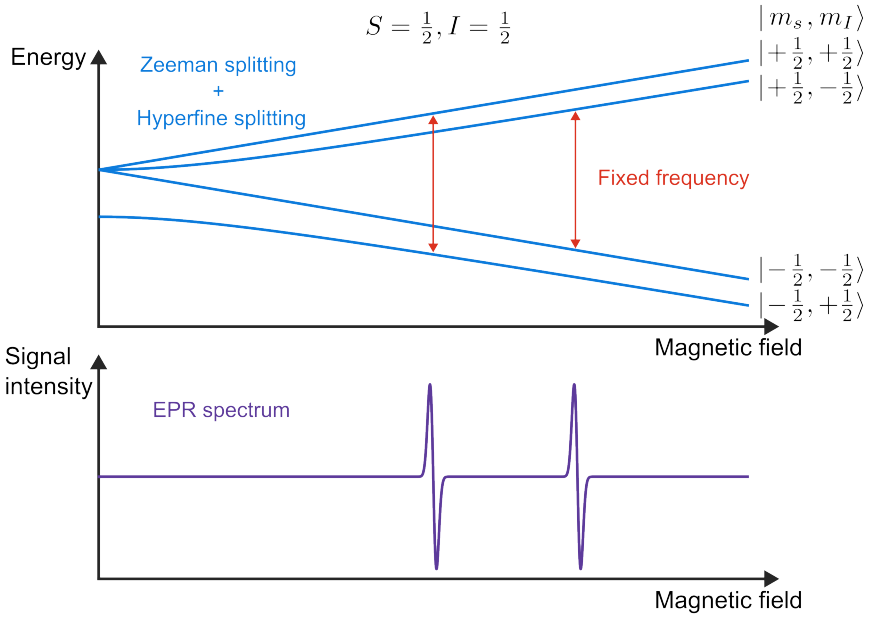


Figure 3.3: Hyperfine splitting in an EPR spectrum for $S = 1/2$, $I = 1/2$. The upper graph shows the energy-levels diagram of an electron spin coupled with a nuclear spin for varying magnetic field. The splitting of the four energy levels results from the Zeeman effect combined with hyperfine interactions. The red arrows represent the allowed EPR transitions at a fixed microwave frequency according to selection rules. The lower graph presents the resulting CW EPR spectrum as first derivative.

of pulse sequences, which have a wide range of applications. For example, in pulsed EPR small splittings that are unresolved by CW EPR spectra can be visible. More importantly, pulse EPR gives access to the spin dynamics, enabling the quantification of spin–lattice relaxation and spin-coherence times. This section will introduce the theoretical background of pulsed EPR and several pulse sequences that will be used in this thesis.

We assume the static magnetic field B_0 to be applied along the z direction. The spin Hamiltonian, in frequency unit, for electron Zeeman interaction can then be written as:

$$\hat{H}_{\mathrm{Z}} = -\hat{\mu}_z B_0 = g_{\mathrm{e}} \mu_{\mathrm{B}} \hbar^{-1} B_0 \hat{S}_z = \omega_0 \hat{S}_z, \tag{3.54}$$

where ω_0 is known as the Larmor frequency, and $\hat{S}_z$ is the z component of the spin (angular momentum) operator $\hat{S}$. Each component can be expressed in terms of

Pauli matrices. The complete set of spin operator components for a $S = \frac{1}{2}$ spin are:

$$\hat{S}_x = \frac{\hbar}{2}\begin{pmatrix} 0 & 1 \\ 1 & 0 \end{pmatrix}, \quad \hat{S}_y = \frac{\hbar}{2}\begin{pmatrix} 0 & -\mathrm{i} \\ \mathrm{i} & 0 \end{pmatrix}, \quad \hat{S}_z = \frac{\hbar}{2}\begin{pmatrix} 1 & 0 \\ 0 & -1 \end{pmatrix}. \tag{3.55}$$

They satisfy the cyclic commutation relations:

$$[\hat{S}_x, \hat{S}_y] = \mathrm{i}\hbar\hat{S}_z, \quad [\hat{S}_y, \hat{S}_z] = \mathrm{i}\hbar\hat{S}_x, \quad [\hat{S}_z, \hat{S}_x] = \mathrm{i}\hbar\hat{S}_y. \tag{3.56}$$

The two eigenstates of $\hat{H}_\mathrm{Z}$ are denoted as $|\alpha\rangle$ and $|\beta\rangle$, respectively. An arbitrary spin state at a time t can be written as the linear combination of these two eigenstates:

$$|\Psi(t)\rangle = c_\alpha(t)|\alpha\rangle + c_\beta(t)|\beta\rangle, \tag{3.57}$$

where $c_\alpha(t)$ and $c_\beta(t)$ are complex time-dependent coefficients. The signal measured in pulsed EPR, $\boldsymbol{m}(t)$, is proportional to the expectation value of the spin operator $\hat{\boldsymbol{S}}$:

$$\boldsymbol{m}(t) = -g_\mathrm{e}\mu_\mathrm{B}\langle\Psi(t)|\hat{\boldsymbol{S}}|\Psi(t)\rangle. \tag{3.58}$$

Therefore it is crucial to know the explicit expression of $\Psi(t)$ when applying external magnetic fields. We will derive the time evolution of $\Psi(t)$ in the density operator formalism in the following. A density operator is a matrix that describes the quantum states of a spin system. For $S = 1/2$, the density operator of the spin ensemble is defined as:

$$\hat{\sigma}(t) = \sum_k p_k|\Psi_k(t)\rangle\langle\Psi_k(t)| = \begin{pmatrix} \overline{c_\alpha(t)c_\alpha^*(t)} & \overline{c_\alpha(t)c_\beta^*(t)} \\ \overline{c_\beta(t)c_\alpha^*(t)} & \overline{c_\beta(t)c_\beta^*(t)} \end{pmatrix}. \tag{3.59}$$

The diagonal elements represent the probability of finding the spin ensemble in one of the states, while the off-diagonal elements describe electron coherences, or in other words, the phase relation between different states. As the time evolution of $\Psi(t)$ is determined by the Schrödinger equation:

$$\frac{\mathrm{d}}{\mathrm{d}t}|\Psi(t)\rangle = -\mathrm{i}\hat{H}(t)|\Psi(t)\rangle, \tag{3.60}$$

we can then derive the time evolution of the density operator by combining Equation (3.59) and Equation (3.60):

$$\frac{\mathrm{d}}{\mathrm{d}t}\hat{\sigma}(t) = -\mathrm{i}[\hat{H}(t), \hat{\sigma}(t)], \tag{3.61}$$

which is known as the Liouville–von Neumann equation. Here, the bracket means the commutation between two operators: $\left[\hat{A}, \hat{B}\right] = \hat{A}\hat{B} - \hat{B}\hat{A}$. The solution of Equation (3.61) is written as:

$$\hat{\sigma}(t) = \mathrm{e}^{-\mathrm{i}\hat{H}t}\hat{\sigma}(0)\mathrm{e}^{\mathrm{i}\hat{H}t}. \tag{3.62}$$

This equation becomes straightforward to solve if we express both the density operator and the spin Hamiltonian in the space spanned by the spin operators plus the identity matrix:

$$\hat{H}(t) = h_x(t)\hat{S}_x + h_y(t)\hat{S}_y + h_z(t)\hat{S}_z \tag{3.63}$$

$$\hat{\sigma}(t) = 2s_x(t)\hat{S}_x + 2s_y(t)\hat{S}_y + 2s_z(t)\hat{S}_z + s_0\hat{S}_0, \tag{3.64}$$

where $\hat{S}_0$ is the 2×2 identity matrix, and $h_p(t)$, $s_p(t)$ $(p = x, y, z)$, and s_0 are real coefficients. The expectation value of the spin angular momentum is given by $s_p(t)$:

$$\langle \hat{S}_p \rangle(t) = \mathrm{Tr}(\hat{\sigma}(t)\hat{S}_p) = s_p(t), \quad p = x, y, z. \tag{3.65}$$

Therefore, in the density operator formalism, solving the magnetic moment in Equation (3.58) is equivalent to finding the coefficients $s_p(t)$. For a set of operators $\hat{A}$, $\hat{B}$, and $\hat{C}$ that satisfy the cyclic commutation relations, like the spin operators do (Equation (3.56)), the following relation can be derived:

$$\mathrm{e}^{-\mathrm{i}\theta\hat{B}}\hat{A}\mathrm{e}^{\mathrm{i}\theta\hat{B}} = \hat{A}\cos\theta - \hat{C}\sin\theta. \tag{3.66}$$

This equation can also be expressed in the following form:

$$\hat{A} \xrightarrow{\theta\hat{B}} \hat{A}\cos\theta - \mathrm{i}[\hat{B}, \hat{A}]\sin\theta. \tag{3.67}$$

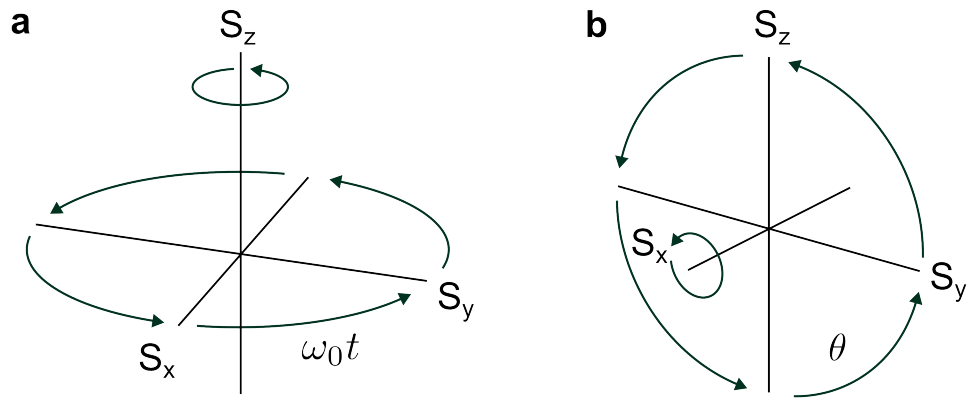


Figure 3.4: Pictorial representation of the transformation of spin angular momentum operators. (a) The evolution of $\hat{S}_x$ and $\hat{S}_y$ over time t under the Zeeman term of Hamiltonian ($\omega_0 \hat{S}_z$). (b) The transformation of $\hat{S}_y$ and $\hat{S}_z$ under a pulse along the x direction with a flip angle of θ. Adapted from Ref. [306].

Hence, we can solve the Equation (3.62) in a similar way. As an example, we consider a spin, whose angular momentum is along the x direction, subjected to Zeeman interaction. Ignoring the coefficients, the initial state of the density operator can be written as $\hat{\sigma}(0) = \hat{S}_x$. The spin Hamiltonian for the Zeeman interaction is given in Equation (3.54). In this case, the term $\theta\hat{B}$ in Equation (3.66) should be $\hat{H}t = \omega_0 t\hat{S}_z$. The evolution of the density operator at a time t, $\hat{\sigma}(t)$, can then be solved as follows:

$$\hat{\sigma}(0) = \hat{S}_x \xrightarrow{\omega_0 t\hat{S}_z} \cos(\omega_0 t)\hat{S}_x + \sin(\omega_0 t)\hat{S}_y = \hat{\sigma}(t). \tag{3.68}$$

This evolution describes a Larmor precession in the xy plane, and can be more intuitively understood from the pictorial representation in Figure 3.4a.

The influence of a microwave pulse on the spin density operator can also be solved in a similar manner. To deal with the oscillatory magnetic field of the microwave pulse, it is more convenient to work in the microwave's rotating frame as opposed to the lab frame. We assume that the magnetic field B_1 of the microwave is a linear cosine oscillating field along the x direction, and it oscillates at a frequency of ω_{MW}. After performing a unitary transformation, the spin Hamiltonian in the rotating frame (RoF) can be written as:

$$\hat{H}^{\mathrm{RoF}} = \Delta\omega\hat{S}_z + \omega_1\hat{S}_x, \tag{3.69}$$

where $\Delta\omega = \omega_0 - \omega_{\mathrm{MW}}$ is the off-resonance frequency, and $\omega_1 = g_e\mu_B\hbar^{-1}B_1/2$ is the nutation frequency. In the resonance condition, the first term vanishes. In a static magnetic field, the density operator in the equilibrium state can be written as $\hat{\sigma}(0) = \hat{S}_z$. When we apply the pulse for a time t_p such that the flip angle $\theta = \omega_1 t_p$ is equal to $\pi/2$, we can then derive the transformation of $\hat{\sigma}(0)$ under the $\pi/2$ pulse as follows:

$$\hat{\sigma}(0) = \hat{S}_z \xrightarrow{\frac{\pi}{2}\hat{S}_x} -\hat{S}_y = \hat{\sigma}(t). \tag{3.70}$$

In reality, the flip angle θ can be any arbitrary value. From the pictorial representation Figure 3.4b, such a flip can be visualised as the rotation of $\hat{S}_z$ by an angle θ driven by $\hat{S}_x$.

Pulse sequences

Next, we will introduce several pulse sequences that will be used in Chapter 5. The Hahn echo sequence is one of the basic pulse sequences used in EPR. It can either be a standalone pulse sequence or a component of more complex pulse sequences. As illustrated in Figure 3.5a, the Hahn echo sequences consists of a $\pi/2$ pulse and a π pulse, with a time interval τ between them. The Bloch representation (Figure 3.5b) is used here to explain the evolution of the spin packet when a Hahn echo sequence is performed. The spin vectors in a spin packet, represented by red arrows, have frequencies close to resonance. Upon applying a $\pi/2$ pulse, the spin vectors are rotated into the xy plane. Without loss of generality, here we suppose they are rotated to the x axis. During the following time interval τ, the spins of the rotated spin packet precess at their respective Larmor frequencies. The on-resonance spin vectors remain on the x axis in the rotating frame. Spin vectors with positive off-resonance frequencies ($\Delta\omega > 0$) rotate counterclockwise, while those with $\Delta\omega < 0$ rotate clockwise. Therefore, the spin packet gradually fans out. When the π pulse is applied, the spin vectors are rotated by 180° around the x or y axis, and then gradually converge to the x axis, generating an echo signal. In order to measure

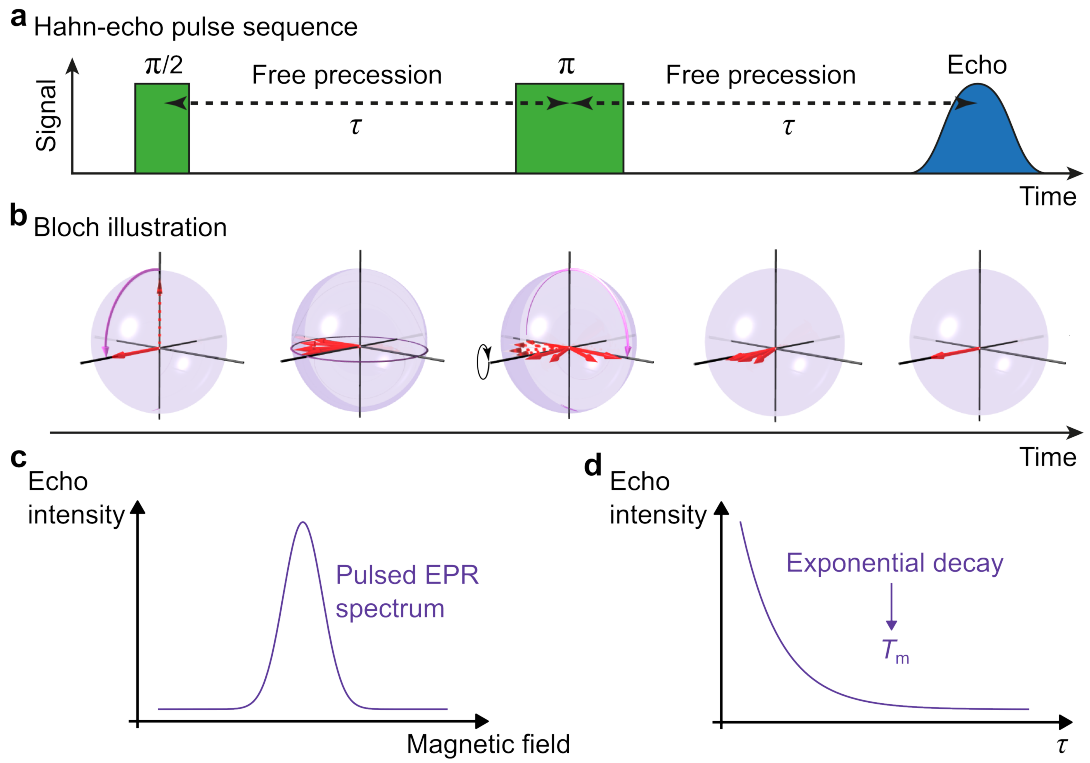


Figure 3.5: Hahn echo pulse sequence and related measurements. (a) The Hahn echo pulse sequence. An initial $\pi/2$ pulse is followed by a π pulse after time τ, leading to an echo formation at time 2τ. (b) Bloch representation of the evolution of spin packet during the process. (c) Pulsed EPR spectrum measured by plotting the echo intensity as a function of the magnetic field. (d) Echo intensity as a function of the time interval τ. The lineshape is typically an exponential decay, by fitting which the spin coherence time T_m can be obtained. Adapted and modified from Ref. [308].

an echo-detected field-swept (EDFS) EPR spectrum, we can record the integrated echo signal while varying the magnetic field B_0. Alternatively, the echo intensity can also be plotted as a function of the time interval τ, which typically exhibits an exponential or stretched-exponential decay shape. By fitting this decay, we can determine the spin coherence time T_m. Strictly speaking, T_m is called phase-memory time, or transverse relaxation time, as it includes both the true spin coherence time T_2 and unwanted factors in the spin ensemble, such as spectral diffusion and instantaneous diffusion. For simplicity, we will refer to T_m as the spin coherence time.

The picket-fence pulse sequence is employed to measure the spin–lattice relaxation time T_1, also known as the longitudinal relaxation time. As shown in Figure 3.6, a train of π pulses is initially applied to randomise the spin orientations

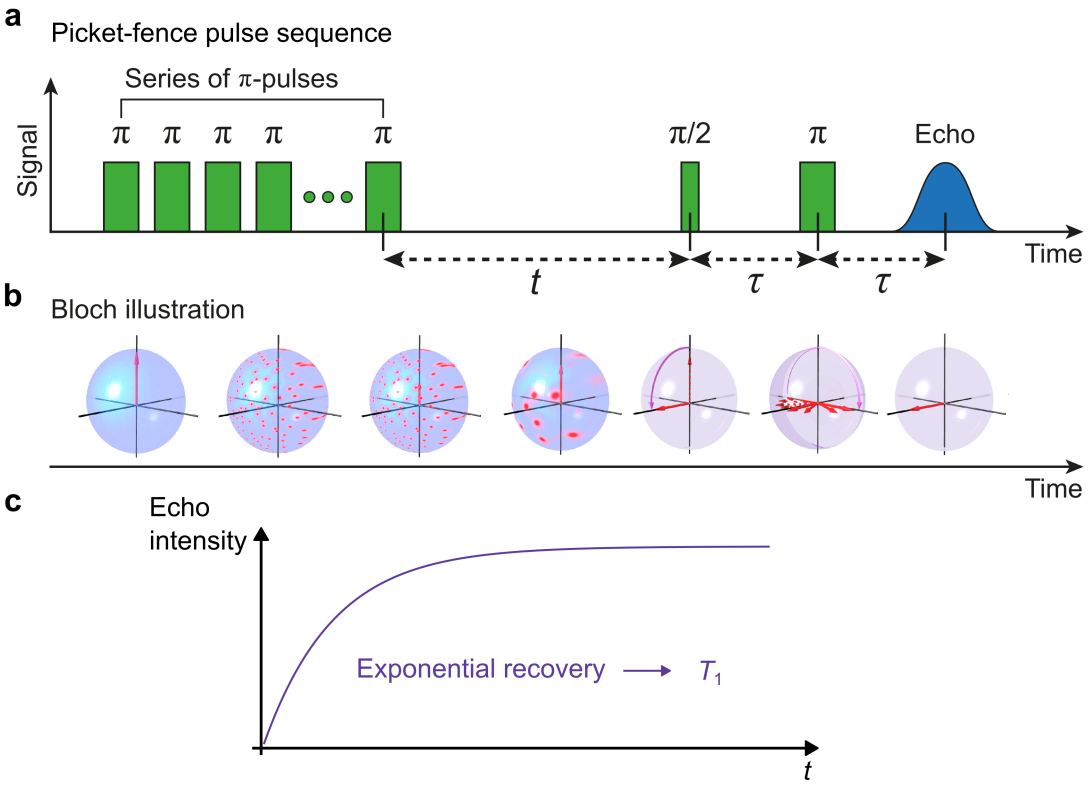


Figure 3.6: Picket-fence pulse sequence and T_1 measurement. (a) The picket-fence pulse sequence. First, a series of π-pulses randomise the spin orientations. After a relaxation time period t, a Hahn echo sequence is applied. (b) Echo intensity as a function of time t, exhibiting an exponential recovery. The exponential fitting's time constant is the spin–lattice relaxation time T_1. Adapted and modified from Ref. [308].

in the system (equalising the population of spins in two eigenstates). Following this, the spin vectors relax to their thermal equilibrium along the z direction over a time period t. A Hahn echo sequence is then used to detect the magnetic moment along the z direction. The echo intensity exhibits an exponential or bi-exponential recovery behaviour as a function of the recovery time t. The spin–lattice relaxation time can be obtained by fitting this curve.

The are many more complicated pulse sequences that have various capabilities. Now, we introduce the pulse sequence for hyperfine sublevel correlation spectroscopy (HYSCORE), which will be used to detect the hyperfine coupling of the spin species of interest. The HYSCORE technique, shown in Figure 3.7, consists of four pulses: $\pi/2$–$\pi/2$–π–$\pi/2$, with two variable time intervals t_1 and t_2 as variables. The system

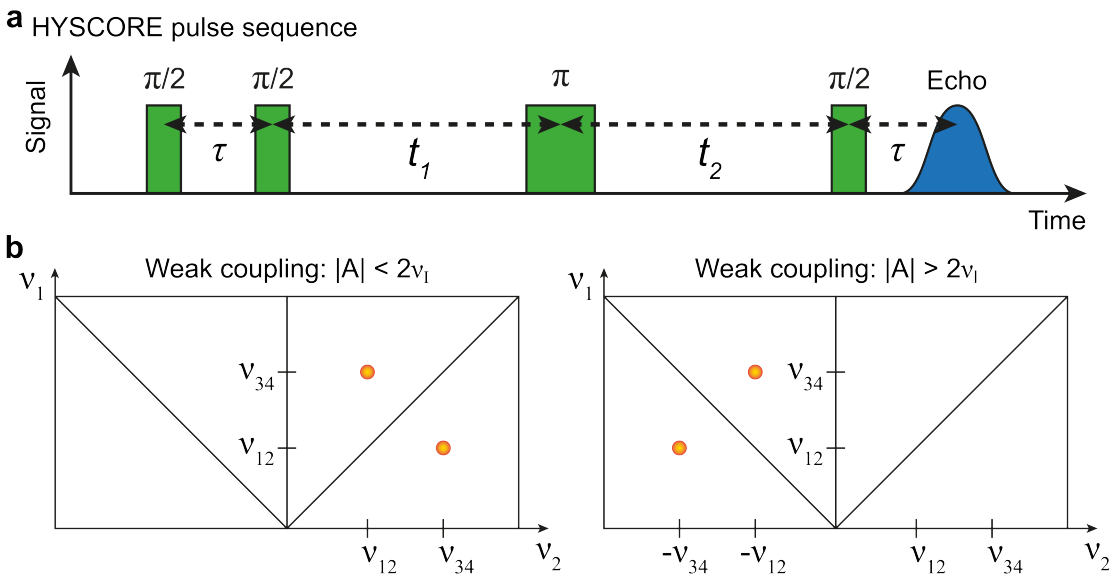


Figure 3.7: HYSCORE technique. (a) Pulse sequence for HYSCORE. The echo intensity is recorded while varying the two time intervals t_1 and t_2. The two-dimensional time-domain spectrum is converted into the frequency domain using a Fourier transformation. Hyperfine coupling parameters can be estimated from the relative distances between the peaks (ν_{12}, ν_{34}) and (ν_{34}, ν_{12}), which appear in different quadrants depending on the coupling regime. Adapted and modified from Ref. [308].

starts from the equilibrium with a polarisation along the z direction. Similar to the Hahn echo sequence, the first $\pi/2$-pulse rotate the spins to the xy plane, creating electron coherence terms in the density matrix. After a time period τ, the second $\pi/2$-pulse converts the electron coherence terms to nuclear polarisation and nuclear coherence terms in the density matrix. Subsequently, the nuclear spins precess at their respective nuclear Larmor frequencies (ν_{12} or ν_{34}). After a time-period t_1, a π-pulse is applied to interchange the nuclear spin phases between the two electron spin manifolds. And then the nuclear spins are allowed to freely evolve for another time-period t_2. During this time period, those nuclear spins with a frequency ν_{12} during t_1 now evolve at a frequency ν_{34}, and vice versa. Afterwards, a $\pi/2$-pulse converted the nuclear coherence terms back to electron coherence terms, which leads to a detectable echo signal. A two-dimensional time-domain HYSCORE spectrum is obtained by plotting the echo signal as a function of t_1 and t_2. This time-domain signal is transformed to the frequency domain using a fast Fourier

transformation (FFT). The two frequency axes, ν_1 and ν_2, correspond to t_1 and t_2, respectively. In the frequency-domain spectrum, peaks will appear at (ν_{12}, ν_{34}) and (ν_{34}, ν_{12}), and the hyperfine coupling parameters can be extracted from the relative distances between these peaks. The positions of these peaks depend on the coupling regime. We denote the magnitude of the hyperfine coupling and the nuclear Larmor frequency as A and ν_I, respectively. In the weak coupling regime ($|A| < 2\nu_I$) and the strong coupling regime ($|A| > 2\nu_I$), the relevant peaks (ν_{12}, ν_{34}) and (ν_{34}, ν_{12}) appear in the first and second quadrants, respectively. A detailed explanation of the HYSCORE mechanism can be found in Ref. [240, 306].

In this thesis, all EPR measurements were carried out using a Bruker EleXsys E580 (for X-band and Q-band) and E680 (for X-band). The sample temperature was controlled with an Oxford Instruments CF9350 cryostat and ITC503 temperature controller. We used the dielectric ring resonator Bruker ER4118X-MD5 and Bruker ER5106 QT-2W resonators for X-band (around 9.5 GHz) and Q-band (34 GHz) frequencies, respectively. The pulses in HYSCORE were controlled by the SpinJet AWG E5804200. The spectra were fitted using the EasySpin package [309].

3.2.2 Single-molecule transistor

A SMT, as the name implies, is a transistor miniaturised to the smallest feasible scale using a single molecule. In these devices, the molecule is situated between the source and drain electrodes, while a third electrode, known as a gate, modulates the current passing through the molecule. On the one hand, this concept could potentially allow the development of extremely small, dense, and fast electronic devices, such as nanometer-sized transistors, switches, and diodes, as demonstrated in literature [310]. On the other hand, SMTs also provide a unique platform for studying quantum phenomena and exploring the fundamental limits of electronic devices. It has been employed as a spectroscopic tool to investigate a broad range of molecular properties, such as transport properties of different charged

states, exchange couplings, vibrational modes, electron/nuclear spin coherence times, quantum interference effects, and Kondo physics in molecules [310–312]. This section provides a brief overview of the fundamental principles of a single-molecule transistor based on Ref. [311].

A single-molecule device is typically fabricated by placing, e.g. through depositing a single molecule into a nanometer-sized gap. This allows the molecule to bridge the source and drain electrode. Figure 3.8a illustrates the alignment of the chemical potentials of the electrodes and the molecule. If we assume a neutral molecule has N electrons, then $\mu_{N\rightarrow N+1}$ refers to the energy needed to add another electron to the neutral molecule. This energy considers the capacitive coupling between the molecule and surrounding electrodes, as well as the intrinsic molecular energy levels. The gap between $\mu_{N\rightarrow N+1}$ and $\mu_{N-1\rightarrow N}$ is called the addition energy, E_{add}. With zero bias, electron transport can only occur when the molecular level is in resonance with the chemical potential of the source and drain electrodes. In Figure 3.8b, no current flows through the junction. However, when a bias voltage V is applied, as depicted in Figure 3.8c, the chemical potential of the source and drain electrodes are shifted, allowing the energy level ε_0 to lie in between the bias window, thus enabling electron conduction. The condition when electron transport is suppressed is called Coulomb blockade. Figure 3.8d–e present the current–voltage characteristics for different bias voltages and different electronic couplings between the molecule and electrodes ($\Gamma_{\mathrm{S,D}}$). The coupling strength is related to the broadening of molecular levels as well as the overlap between these molecular levels and the energy levels of the electrodes [313]. Different coupling strengths can lead to distinct electron transport behaviours. We only consider the weak coupling regime here, which occurs in GNR-based SMTs that will be discussed in Chapter 6. In this scenario, an electron first hops from the source electrode to the molecule, and then hops to the drain electrode. Because of the electrons hops one by one, which is called sequential tunneling, the device is also known as single-electron transistor.

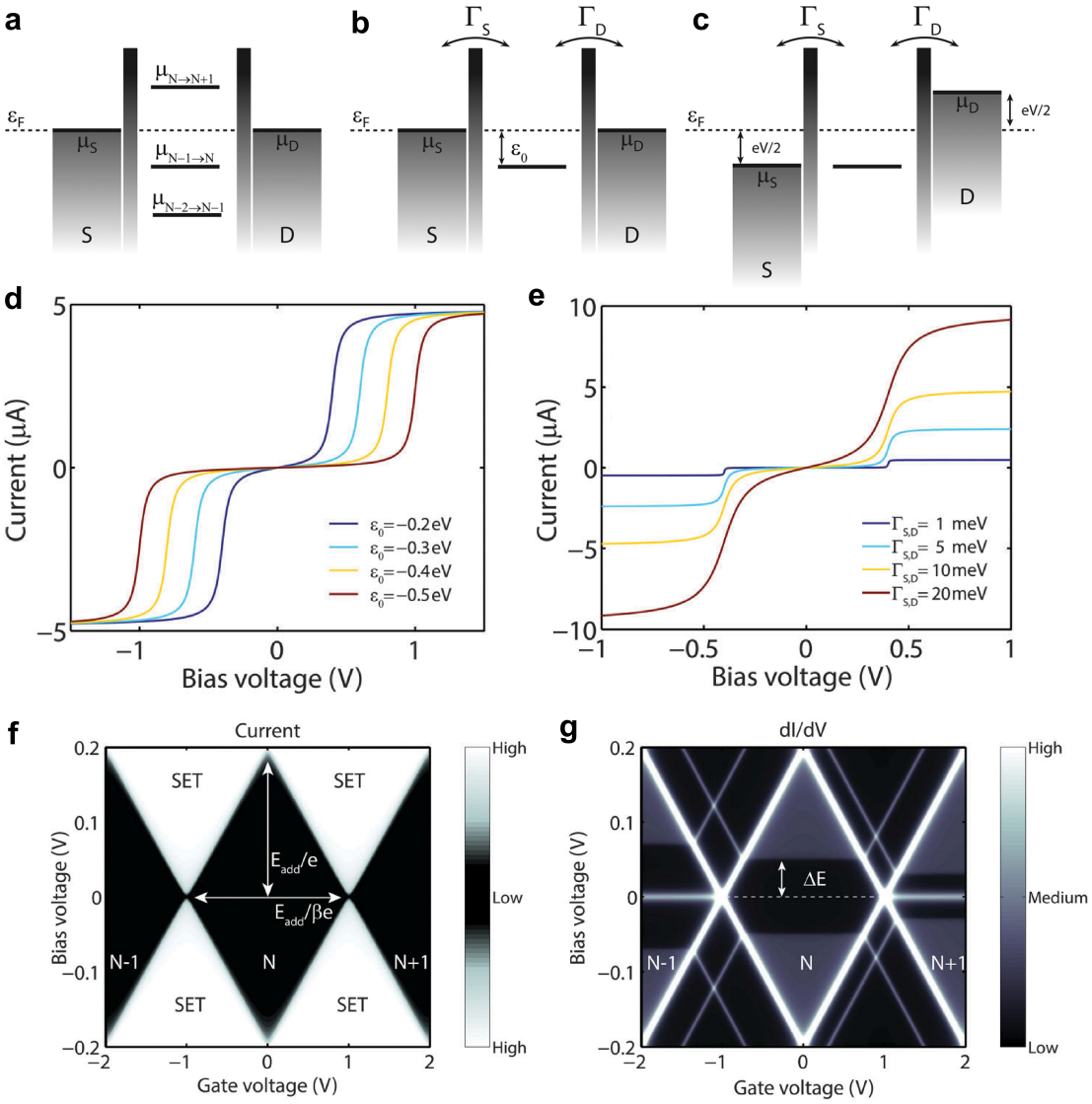


Figure 3.8: Charge transport through a single molecule. (a–c) Chemical-potential diagrams of a single-molecule transistor. The Fermi energy, and chemical potentials of the source (S) and drain (D) electrons are denoted as ε_{F}, μ_{S}, and μ_{D}, respectively. The number of electrons in the neutral molecule is represented by N. The energy required to add one more electron to the neutral molecule is denoted by $\mu_{N\to N+1}$. A single level, ε_0, is plotted between the source and drain in (b) and (c). The electronic coupling between the molecule and the source and drain are represented by Γ_{S} and Γ_{D}, respectively. In the equilibrium state in (b), no current can flow, unless a bias voltage V is applied, as in (c). (d) Current versus voltage for different ε_0 and a fixed $\Gamma_{\mathrm{S,D}}$ of 10 meV. (e) Current versus voltage for different $\Gamma_{\mathrm{S,D}}$ and a fixed ε_0 of −0.2 eV. (f) Current versus bias and gate voltage map. The current flow is blocked in the diamond-shaped black regions (Coulomb diamond). In the white regions, the blockade is lifted, and single-electron tunneling (SET) occurs. The shape of the Coulomb diamond is determined by E_{add}, the addition energy, and β, the gate-coupling parameter. Each Coulomb diamond corresponds to a fixed number of electrons. (g) Differential conductance map of (f). The thick boundaries of Coulomb diamonds correspond to resonant tunneling through molecular levels. The slanted lines in the SET region parallel to the Coulomb-diamond edges correspond to excited states. The horizontal lines inside Coulomb diamonds indicate inelastic cotunneling excitations, characterised by the energy of the excitation state ΔE. Adapted from Ref. [311].

So far, we only considered two electrodes. However, a third electrode, the gate electrode, can be added to regulate the energy levels of the molecule, as it can either attract or repel electrons when a positive or negative voltage is applied. Therefore, we gain an additional degree of freedom to control the relative position of the chemical potential of the molecule with respect to the chemical potentials of the source and drain electrodes. Figure 3.8f–g display the current map and differential conductance map versus bias voltage and gate voltage. These diagrams are referred to as stability diagrams. In Figure 3.8f, the black and white areas represent the Coulomb-blockade regime and the single-electron-transport regime, respectively. The Coulomb-blockade region has a diamond shape, often called the Coulomb diamond. Each Coulomb diamond contains a fixed number of electrons, allowing the investigation of the behaviours of different charged states of the molecule. In the differential conductance map (Figure 3.8g), the thick white lines (Coulomb-diamond edges) correspond to the resonance between the molecular level and the electrode energy levels. The thinner slanted lines, running parallel to the Coulomb-diamond edges, are attributed to electron transport involving the excited states of the molecule. Additionally, a horizontal line can be found inside the Coulomb diamond, which occurs because of inelastic cotunneling. It is important to mention that the stability diagrams shown here are very simplified. In real experiments, stability diagrams can be more sophisticated and involve a broader range of quantum phenomena. More details can be found in Ref. [310–315].

Figure 3.9a shows a schematic diagram of a typical single-molecule device fabricated using GNRs. A GNR bridges the electro-burned gap between two graphene leads of width d = 1–10 nm. These two graphene leads serve as source and drain electrodes, respectively, and each is connected to a gold pad. The gate electrode is beneath an n-doped Si wafer with an oxide layer. The GNR molecules are added to the device by drop casting from solutions, with a yield of approximately five out of every one hundred electro-burned gaps. All of these nanodevices are integrated

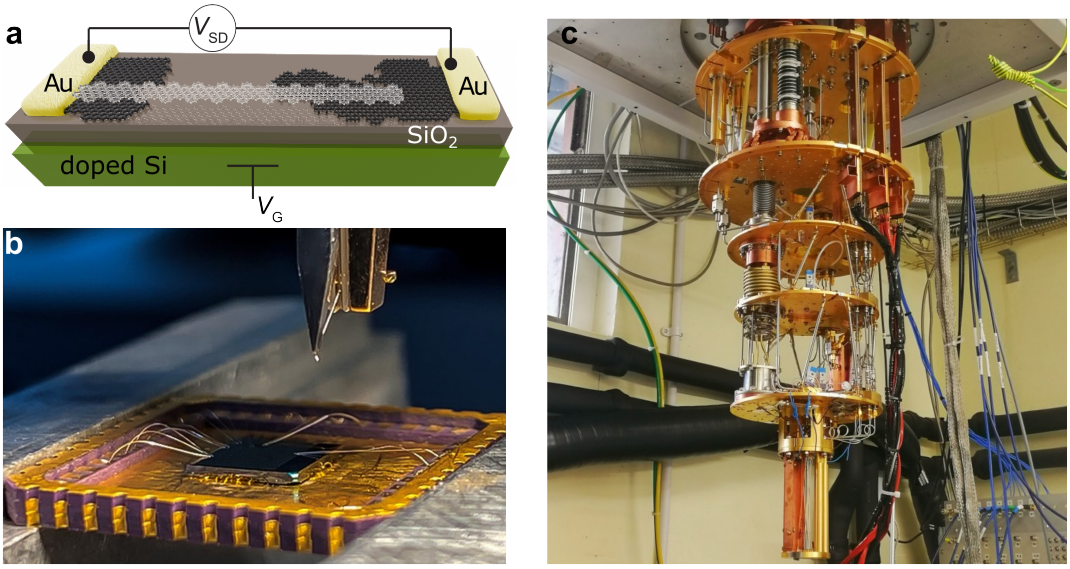


Figure 3.9: Single-molecule device and dilution fridge. (a) Schematic diagram of a single-molecule device, with a graphene nanoribbon bridging two graphene electrodes. (b) Chip with multiple nanodevices. (c) Dilution fridge for cryogenic measurements..

in one single chip, shown in Figure 3.9b. We typically carry out single-molecule transport measurements at cryogenic temperatures, so that many fine features of electron transport can be resolved. We used a dilution fridge (Figure 3.9c) to create a millikelvin-temperature environment. The nanofabricated chip is loaded into the fridge for subsequent measurements. The results of single-molecule transport measurements will be discussed in Section 6.2.

3.2.3 Optical spectroscopy

Photoluminescence (PL) and Raman spectroscopy are commonly employed tools for studying the optical properties of materials. This section will provide a brief overview of their principles.

3.2.3.1 Photoluminescence spectroscopy

Photoluminescence refers to the emission of light from a photo-excited state of a material. Typically, a laser excitation is applied to measure both absorption and emission. In Figure 3.10, we depicted the energy of the ground and excited states

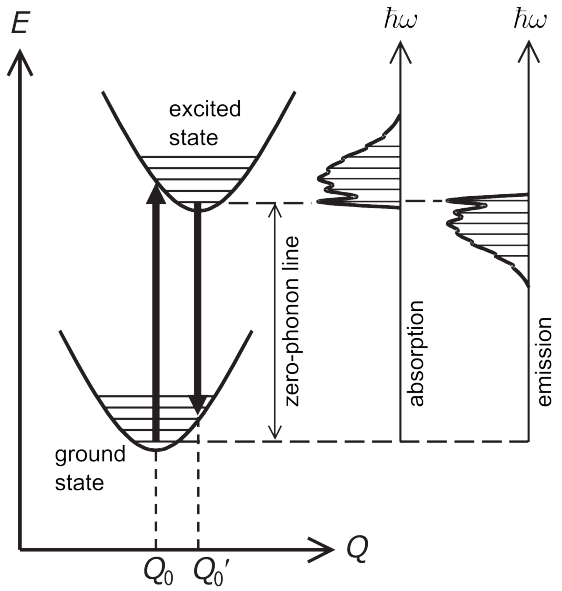


Figure 3.10: Optical absorption and emission between the electronic ground state and excited state. The two parabolas represent the energy of the ground and excited state as a function of the nuclear coordinates Q. The horizontal lines within the two parabolas indicate the vibrational levels. The general shape of the absorption and emission spectra are shown on the right-hand side of the figure. Adapted from Ref. [316].

as a function of the nuclear coordinates, with the approximation that they have a parabolic shape. In general, the nuclear coordinates in the equilibrium state (the minima of the parabola), marked as Q_0 and Q_0', are different in the electronic ground and excited states. The vibrational levels are represented by horizontal lines within each parabola. Upon absorption of a photon, the system changes from the lowest vibrational level of the ground state to the excited state. The system then relaxes to the lowest vibrational level of the excited state through non-radiative processes. After a certain period, the system returns to the ground state by emitting a photon, a process called photoluminescence. This photon emission is usually accompanied by phonons. The transition between the lowest vibrational level of the ground state to the lowest vibrational level of the excited state is called the zero-phonon line. The absorbed photon generally has a larger energy than the energy of zero-phonon line, whereas the emitted photon has less energy. A typical absorption spectrum and an emission spectrum are shown in Figure 3.10.

Quantitatively, the transition probability between two states is given by the matrix element of electric-dipole operator $\boldsymbol{\mu}_{\mathrm{e}}$. By using Born–Oppenheimer approximation, which says that the nuclei can be thought of being fixed when evaluating the electronic Schrödinger equation, the matrix element can be computed as follows [317]:

$$\langle \phi(q,Q)\chi(Q)|\boldsymbol{\mu}_{\mathrm{e}}|\phi'(q,Q)\chi'(Q)\rangle = \underbrace{\langle \phi(q,Q)|\boldsymbol{\mu}_{\mathrm{e}}|\phi'(q,Q)\rangle}_{\text{Orbital selection rule}} \underbrace{\langle \chi(Q)|\chi'(Q)\rangle}_{\text{Franck–Condon factor}} , \quad (3.71)$$

where ϕ and ϕ' are the electronic wavefunctions before and after transition, respectively, χ and χ' are the nuclear wavefunctions before and after the transition, respectively. The electronic coordinates and nuclear coordinates are denoted as q and Q, respectively. The first term in the right-hand side of Equation (3.71) is the electronic transition integral, which is governed by orbital selection rule. This integral can be expanded in a Taylor's series about the equilibrium nuclear coordinates Q_0 [317]:

$$\langle \phi(q,Q)|\boldsymbol{\mu}_{\mathrm{e}}|\phi'(q,Q)\rangle = \langle \phi(q,Q_0)|\boldsymbol{\mu}_{\mathrm{e}}|\phi'(q,Q_0)\rangle + \sum_i \left(\frac{\partial}{\partial Q_i}\langle \phi|\boldsymbol{\mu}_{\mathrm{e}}|\phi'\rangle\right)_{Q=Q_0} Q_i + \ldots \quad (3.72)$$

The electronic wavefunctions are generally assumed to be a slow varying function of the nuclear coordinates Q. Within Franck–Condon approximation, the nuclear coordinates Q in the electronic transition integral can be replaced by the equilibrium value Q_0 [317]. In other words, only the first term Equation (3.72) needs to be evaluated.

The second term in Equation (3.71) is the Franck–Condon factor that calculates the overlap integral between the vibrational wavefunctions before and after the electronic transition. Consequently, the relative intensities of different vibronic peaks in the optical spectra are entirely determined by the Franck–Condon factor [317]. Within the Franck–Condon approximation, the absorption and emission spectra, as shown in Figure 3.10, are strictly symmetrical with respect to the zero-phonon line. However, this is rarely the case in real situations, since the Franck–Condon

approximation often breaks down. In this case, one can resort to the Herzberg–Teller approach, which considers the first-order term in Equation (3.72) and deals with the Q dependence of electronic transition integral by calculating the variation of the electronic wavefunction $\phi(q, Q)$ with Q [317]. Since $\phi(q, Q)$ varies slowly with Q, the change of electronic wavefunction induced by Q can be treated as a perturbation. Since within the Herzberg–Teller approximation, only the first-order term in the Taylor's expansion in Equation (3.72) is needed, the Herzberg–Teller approximation can also be regarded as the first-order correction to the Franck–Condon approximation. More details can be found in Ref. [317].

3.2.3.2 Raman spectroscopy

Raman spectroscopy is a useful tool for extracting information about the vibrational modes of a material. Figure 3.11 illustrates the principles of Raman and Rayleigh scattering. When a laser illuminates the sample, the incident photon temporarily drives a transition from the ground state to a virtual excited state. The photon is then scattered through either the Rayleigh process or Raman process. In Rayleigh scattering, the photon's energy remains constant, whereas in Raman scattering, a vibrational excited state is involved. The Raman scattering is called anti-Stokes or Stokes Raman scattering depending on whether the scattered photon has a higher or lower energy than the incident photon. In Figure 3.11, we provide a typical example of the peaks resulting from these scattering processes. Typically, Rayleigh scattering dominates in a spectrum and exhibits a much larger intensity than Raman scattering. Therefore, the Rayleigh-scattering peak is not fully represented in the diagram. Moreover, Stokes Raman scattering has a larger intensity than anti-Stokes scattering. This is because the system generally starts from the vibrational ground state in the equilibrium state. In practice, when a sample is illuminated with a laser, both Raman scattering and photoluminescence can occur and can be detected. The critical distinction between them is the source of the scattered or

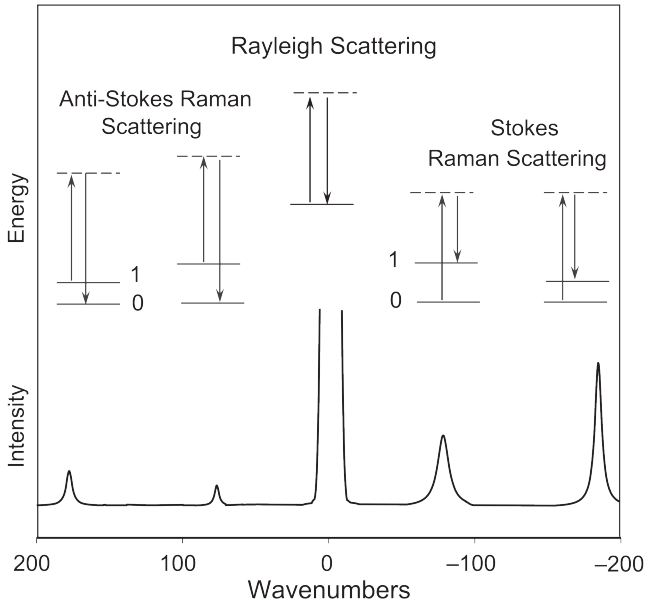


Figure 3.11: Rayleigh scattering and Raman scattering. The laser excitation and photon scattering processes are represented by upward and downward arrows, respectively. The dashed lines represent virtual states. The number 0 and 1 denote the vibrational ground and excited state, respectively. In Rayleigh scattering, the frequency of the scattered photon remains unchanged, whereas in anti-Stokes or Stokes Raman scattering the scattered photon has a larger or lower frequency, respectively. Adapted from Ref. [318].

emitted light: Raman scattering describes an inelastic interaction of the photon with the vibrational modes of the material, whereas photoluminescence results from electronic transitions occurring within the material. Moreover, not all the vibrational modes can be detected using Raman spectroscopy. The Raman scattering intensity can be described by [319]

$$\langle \chi_{\mathrm{i}} | \alpha_{pq} | \chi_{\mathrm{f}} \rangle, \quad p, q = x, y, z, \tag{3.73}$$

where χ_{i} and χ_{f} are the initial and final vibrational states in the Raman scattering process, respectively, α_{pq} is the scattering tensor, which is a second-order symmetric tensor. By using group-theory techniques, one can work out the Raman activities based on the symmetry of vibrational modes. A vibrational mode is Raman-active if it has even parity, i.e. having even symmetry upon inversion [319].

4

Topological States in GNRs

Contents

4.1 Introduction 111
4.2 Designing topologically nontrivial GNRs 113
4.2.1 Tuning the topology via unit-cell design 120
4.2.2 Tuning the topology via connection between unit cells . . 123
4.2.3 Topology at different energy gaps 127
4.3 Relationship between $\mathbb{Z}$ topology and Clar's sextet rule 131
4.3.1 Relationship between $\mathbb{Z}$ index and Wannier functions . . . 131
4.3.2 $\mathbb{Z}$ index, Wannier functions, and Clar's sextet rule 136
4.4 Topology in porphyrin nanoribbons 147
4.5 Dissipationless transport channels in beard–zigzag GNRs 155
4.6 Summary and outlook 161
4.7 Project overview 163

4.1 Introduction

Graphene nanoribbons (GNRs) have captured enormous attention from researchers because of their highly adjustable electronic properties. The quantum confinement in GNRs not only opens a band gap, making them ideal candidates for field-effect transistors [35–38], but also introduces an ample degree of freedom for novel GNR structures [33, 34, 64, 320]. Factors such as width, edge shape, and end termination

of GNRs can be rationally designed to control their electronic behaviours, positioning GNRs as promising candidates for the development of miniaturised, compact, and high-performance electronic devices.

In the current stage, there is still a lack of practical applications of GNRs. Large efforts have been made to find interesting electronic states and device functionalities. One of the most intriguing discoveries in recent years is the emergence of topological states in GNRs. Topology, a mathematical concept that has profoundly influenced the field of condensed-matter physics, has often been applied to investigate 2D and 3D systems. The concept of topology has led to the discovery of topological insulators and superconductors, which represents a significant advance in the fundamental understanding of electronic states of matter, and also opens up new avenues for technological developments [43, 321]. In recent years, topological phases have also been revealed in GNRs. Based on the band topology, GNRs can be classified into distinct phases. The topological phases have created pathways for the exploration of many exotic quantum phenomena. For example, the topological junction states can be harnessed to construct quantum spin chains [12], which hold potential for building quantum logic elements [268]. Furthermore, by coupling the topological junction states in GNRs to superconductors, it is possible to realise Majorana zero-modes [12, 58, 59], which could enable topological quantum computation, which is intrinsically fault-tolerant [322]. The localised nature of topological boundary states in GNRs also presents a chemically programmable route for applications in optoelectronics and single-photon sources [50, 51]. Moreover, for wide GNRs with width $\gtrapprox 10\,\mathrm{nm}$, which can be viewed as quasi-2D objects, the topological edge states could support dissipationless channels for charge transport [48, 187, 323].

In contrast to the topological phases in 2D or 3D that often need careful design of either the crystal structure, or the external electric or magnetic field [42, 44], the topological phases of GNRs essentially depend on the GNRs' lattice parameters, such

as width, edge shape, and end-termination type [12, 214]. Since the advent of bottom-up chemical synthesis of GNRs, it became possible to investigate electronic states in atomically precise GNRs. Up to now, the topological states have been demonstrated in multiple bottom-up synthesised GNRs [37, 59, 158, 221, 222, 224, 225].

This chapter is organised as follows. Firstly, we will examine several novel GNRs and showcase three approaches to tune their topological phases. These strategies encompass the modification of unit cells, the reconfiguration of connections between unit cells, and adjustment of electron-filling levels. Secondly, we will reveal the relationship between the topological phases, a concept in condensed-matter physics, of GNRs and Clar's sextet rule, an empirical rule in organic chemistry. It offers valuable insights for the chemical design of topologically nontrivial GNRs. Thirdly, we will broaden the scope of our topological phase calculations to encompass fused-porphyrin nanoribbons, thereby enriching the potential avenues for identifying topological states in other 1D systems. Finally, we will investigate the topological chiral edge states emerged in sublattice-imbalanced GNRs that are subjected to transverse electric fields.

4.2 Designing topologically nontrivial GNRs

So far, topological states have been observed in several GNRs [37, 59, 158, 221, 222, 224, 225]. These GNRs, however, were all synthesised on metal surfaces under ultra-high vacuum conditions. In order to fabricate devices from topological GNRs it is vital to be able to synthesise the GNRs in more facile environment. To offer more options and guidance for chemists when synthesising new topological GNRs, we investigated the topological phases in six novel GNRs and their derivatives. These six GNRs were designed by Prof. Xinliang Feng's group at TU Dresden. The structures of these six GNRs are shown in Figure 4.1, with the unit cell highlighted in red. We label them as **1**, **2**, **3**, **4**, **5**, and **6**. These labels will be used throughout

this thesis. All the ribbon edges are passivated by hydrogen atoms. Based on these unit cells, chemists can design the molecular precursors to synthesise these ribbons from bottom-up approach, hopefully also improve their stability in ambient conditions. Here, we aim to identify interesting topological phases and provide guidelines to design new ribbons via computational approaches.

At first, we calculated the band structures of the six GNRs using a nearest-neighbour tight-binding model and DFT. In the tight-binding model, we used the p_z-orbitals of carbon atoms as bases, and assumed the hopping integral between nearest neighbours to be $-2.7\,\mathrm{eV}$, which is close to the value determined from experiments and DFT calculations [65]. These parameters apply to all of the following tight-binding calculations unless otherwise specified. The DFT calculations were performed with SIESTA [299]. We employed the Perdew–Burke–Ernzerhof (PBE) generalised-gradient approximation (GGA) for the exchange-correlation functional [288]. Numerical atomic orbitals with double-ζ plus polarisation (DZP) were used as basis set. The energy shift of the localised basis was set to 100 meV. Core electrons were substituted by pseudopotentials that were downloaded from the online database [324]. Plane-wave energy cutoff was set to 400 Ry to ensure the fineness of the real-space grid. The Brillouin zone is sampled by a $21 \times 1 \times 1$ Monkhorst-Pack grid, where 21 means the number of k points along the periodic direction. A vacuum region of at least 20 Å is added in the non-periodic directions to prevent unwanted interactions. The structures were optimised until the maximum forces on the atoms is less than $0.01\,\mathrm{eV/Å}$. Convergence tests have been carried out for all the parameters mentioned above. This parameter set will be used for all the DFT calculations in this chapter unless otherwise specified.

As shown in Figure 4.1, band structures calculated from the tight-binding model and DFT are plotted relative to the Fermi level E_F in grey and black colours, respectively. The tight-binding model gives very close estimation to DFT in all cases. All of the six GNRs have a semiconducting gap. Therefore, it is valid to evaluate the

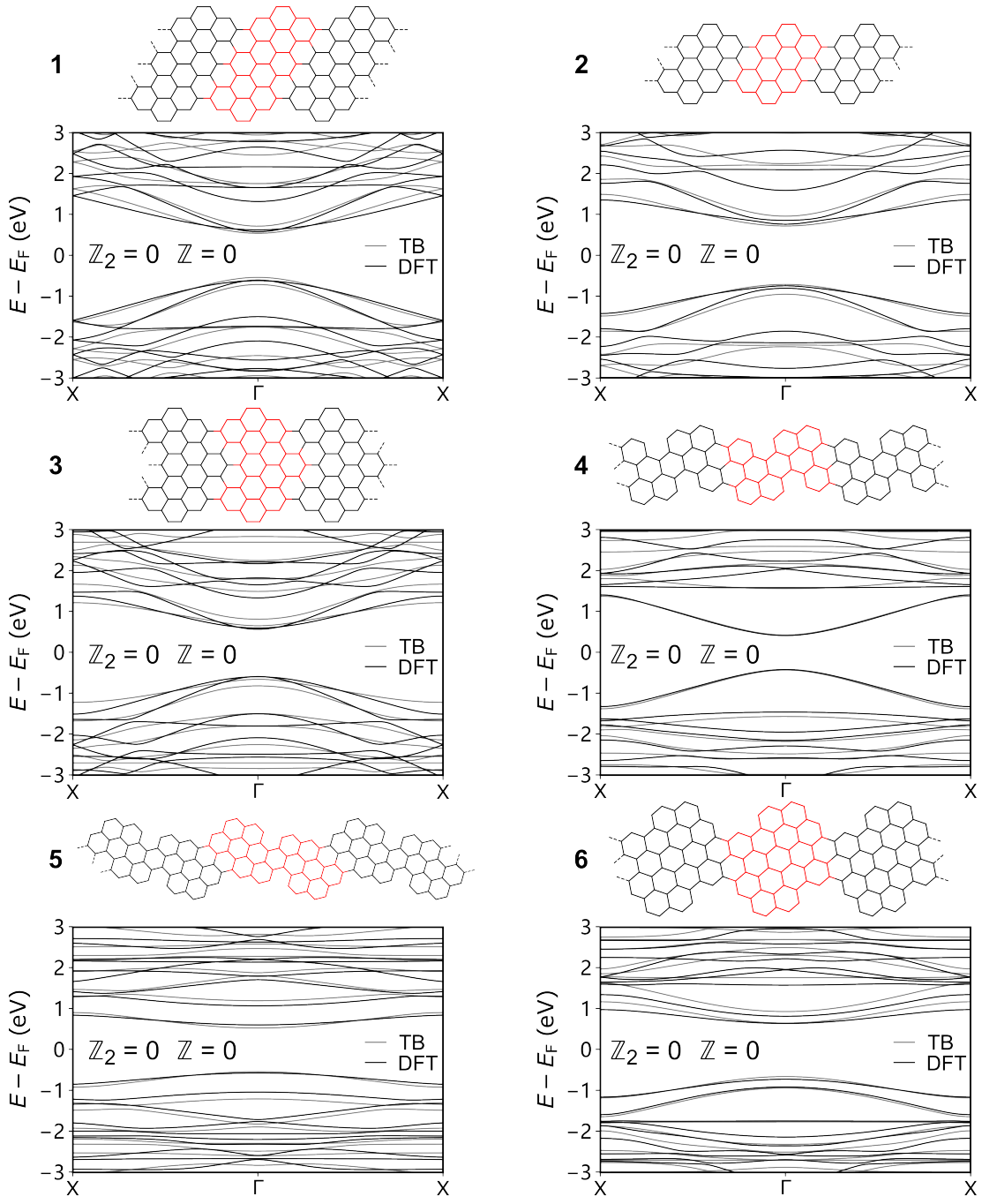


Figure 4.1: Topological classification of GNR **1**–**6**. The unit cells are highlighted in red. For each GNR, the band structures calculated from the tight-binding (TB) model and DFT are shown in grey and black, respectively. All GNRs shown here have $\mathbb{Z}_2 = 0$ and $\mathbb{Z} = 0$.

topological indices – $\mathbb{Z}_2$ and $\mathbb{Z}$ invariants – for the occupied bands of each ribbon, because topological phases are well-defined for gapped systems but not for metallic systems. The topological indices are calculated for the six ribbons by a numerical integration approach within the tight-binding formalism. All of the six ribbons have $\mathbb{Z}_2 = 0$ and $\mathbb{Z} = 0$. According to bulk–boundary correspondence, $\mathbb{Z}_2 = 0$ or 1 implies that the system has an even or odd number of boundary states, viz., end states for 1D system. The $\mathbb{Z}$ invariant tells the number of boundary states in the system. From the results, it can be concluded that all six GNRs are topologically trivial, and do not possess topological end states. The $\mathbb{Z}$ and $\mathbb{Z}_2$ indices are called invariants because they remain unchanged, even if the Hamiltonian undergoes perturbations, as long as the band gap does not close. Although the band gaps calculated from both the tight-binding model and DFT are known to lack sufficient accuracy compared with experimental data, the topological indices are not sensitive to modest changes in the band gap. Consequently, the topological classification presented here is valid.

To further validate the results, we calculated the LDOS at the end and in the bulk of an eight-unit finite GNR, i.e. an octamer, for each of the six GNRs. As demonstrated in Figure 4.2, the LDOS of the end cell and the bulk cell are depicted in teal and magenta, respectively. If a localised end state exists at a certain energy, the LDOS will be non-zero for the end cell but zero for the bulk cell. Such end states do not appear in any of the six GNRs, which is consistent with the prediction of topological indices.

Another method to determine the topological phase is through the examination of Wannier centres. This approach not only provides an alternative way of validating the topological invariants obtained from numerical integration, but it is also capable of calculating more complex systems that are challenging to calculate using the tight-binding model. In the following, we will use GNR **2** as an example to illustrate the process of characterising the topological phase in the Wannier-centres approach.

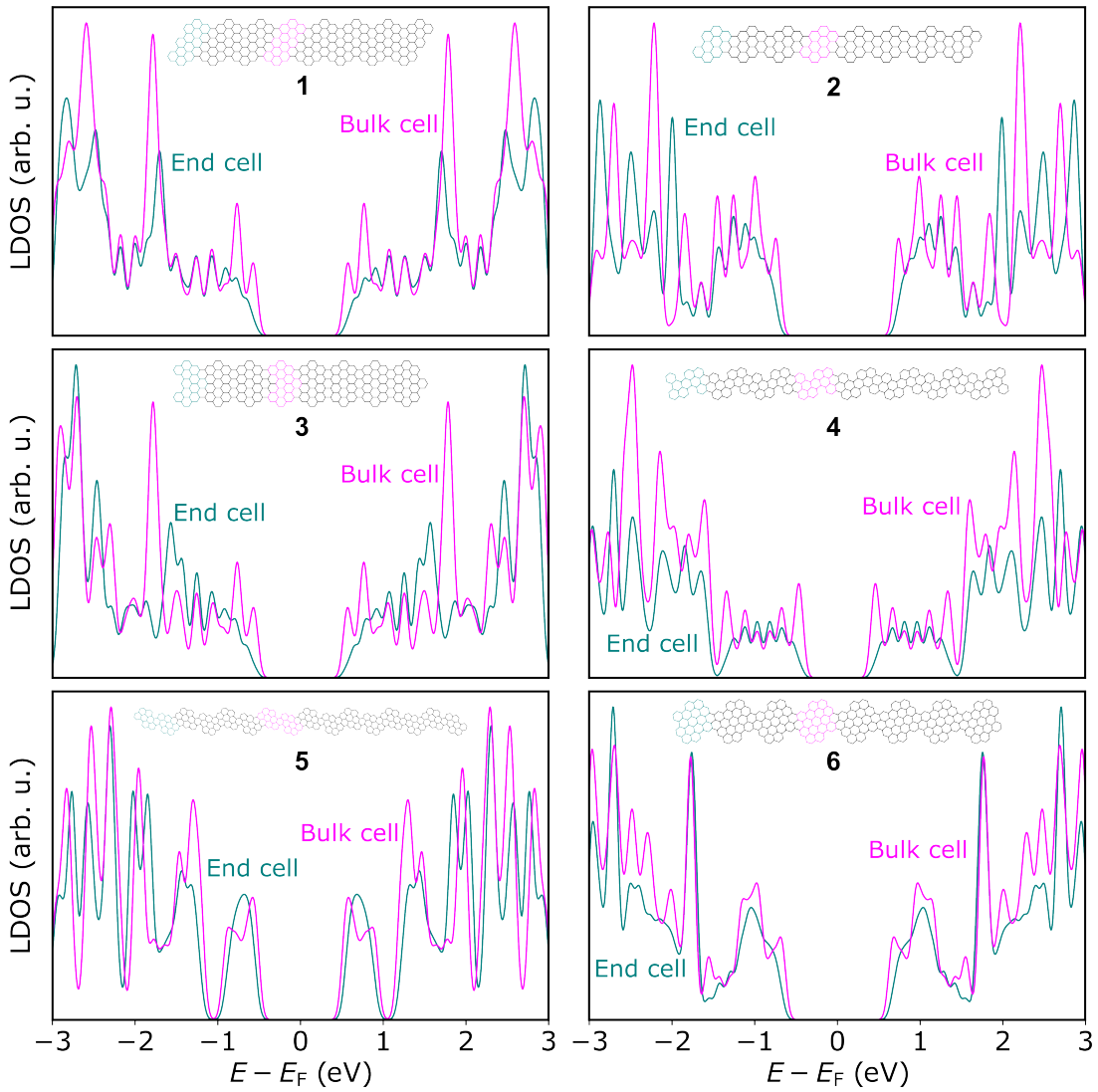


Figure 4.2: LDOS of GNR **1**–**6** at the bulk cell and the end cell. End states, whose LDOS is non-zero for end cell but zero for bulk cell, are absent in all GNRs.

Firstly, we calculated the band structure of GNR **2**. The left and middle panels of Figure 4.3 display the fat band structures, where the wavefunctions are projected on the carbon p_x- & p_y-orbitals (orange) and the p_z-orbitals (green), respectively. The width of a fat band scales with the projection weight. This allows us to identify the bands predominantly contributed by carbon p_z-orbitals. Such bands are referred to as p_z-bands or π-bands because the neighbouring carbon p_z-orbitals bond with each other via π-bonding. The lower-energy bands correspond to the sp^2-hybridised bonds, or called σ-bonds. These σ-bands are far away from the Fermi level and do

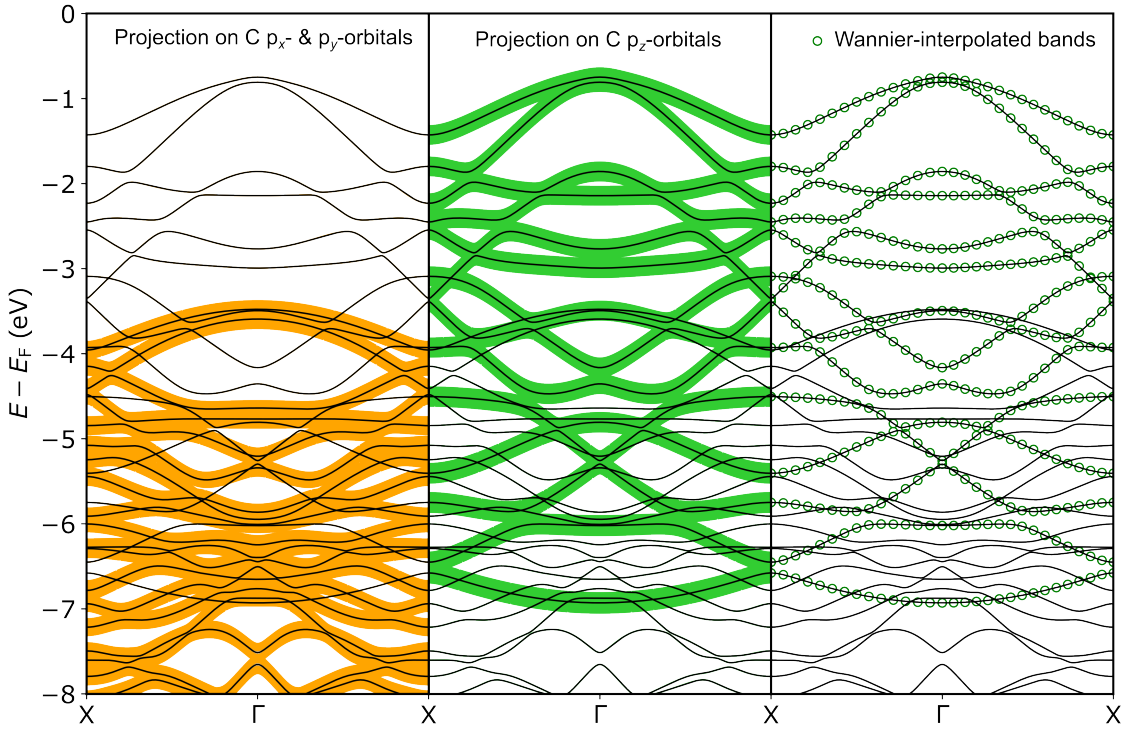


Figure 4.3: Fat bands and Wannier-interpolated bands of GNR **2**. The projection on carbon p_x- & p_y-orbitals of each bands are plotted in the left panel, while the middle panel shows the projection on p_z-orbitals. The Wannierisation was carried out for all occupied p_z-bands. The Wannier-interpolated bands are plotted in the right panel.

not contribute to the topological states. Hence, we chose only the occupied p_z-band manifold for Wannierisation, implemented with the Wannier90 package [303–305]. We plotted the Wannier-interpolated bands in the right panel of Figure 4.3, and they align well with the original p_z-bands. As the same time, we also obtained 14 maximally localised Wannier functions (MLWFs), illustrated in Figure 4.4. For the remainder of this thesis, when we refer to Wannier functions, we mean MLWFs unless otherwise specified. Note that in the Wannier90 calculation, the phases of Wannier functions can be arbitrary, and the red and blue colours in Figure 4.3 represent positive and negative amplitudes, respectively. The arbitrary phases lead to randomised red or blue colours in the upper part of the Wannier function isosurfaces. These colours do not carry significant physical meaning and should be disregarded. Instead, the centres of these Wannier functions, the Wannier centres, are the physical quantities that warrant attention. We represent the Wannier centres

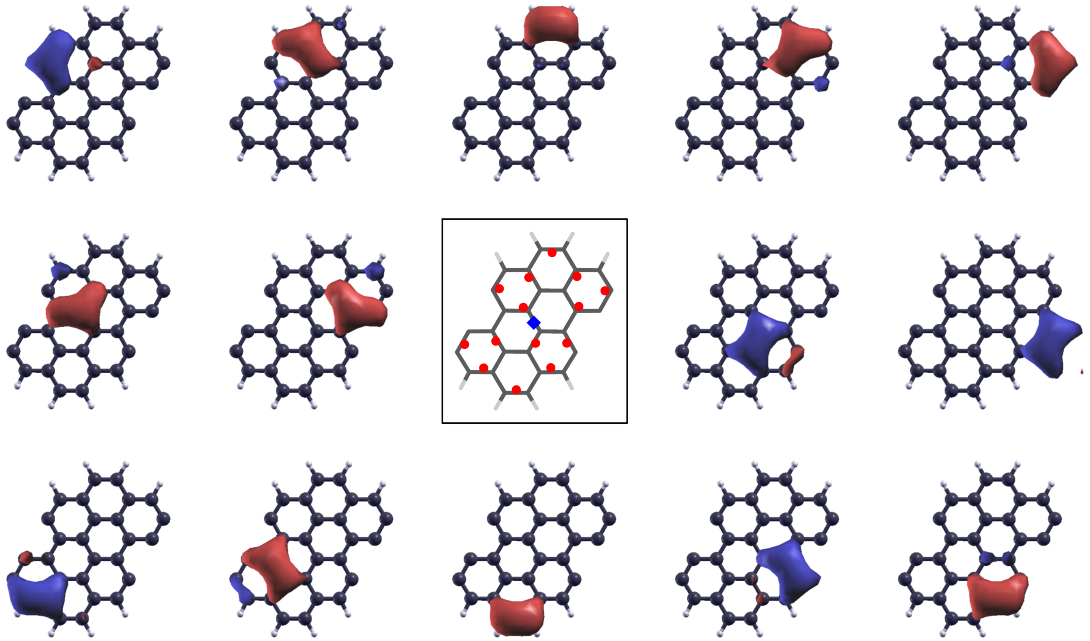


Figure 4.4: Maximally localised Wannier functions of GNR **2**. They are obtained from the Wannierisation of 14 occupied p_z-bands. The centres of the Wannier functions are represented by red dots in the central graph, and the sum of all Wannier centres is represented by the blue diamond. Isovalue was set to 0.1 for all Wannier functions.

as red dots in the central graph of Figure 4.4. The vector sum of the Wannier centres is calculated, and represented by a blue diamond, which appears in the centre of the unit cell. As discussed in Section 3.1.4, when the sum of Wannier centres is in the centre of unit cell, it corresponds to an intercellular Zak phase $\gamma = 0$ and $\mathbb{Z}_2 = 0$. Conversely, when it is at the unit-cell boundary, it corresponds to $\gamma = \pi$ and $\mathbb{Z}_2 = 1$. Therefore, for GNR **2**, the calculation results of Wannier centres substantiate the prior calculation of topological indices.

Furthermore, we calculated the Wannier centres for the other five GNRs. As shown in Figure 4.5, the sums of Wannier centres (blue diamonds) of all the ribbons are exactly in the centre of their respective unit cell, except for GNR **3**. For GNR **3**, the blue diamond is slightly offset from the unit-cell centre. This is because the unit cell of GNR **3** does not conform to inversion or mirror symmetry with respect to the vertical plane. Only when the unit cell of a 1D system respects inversion or

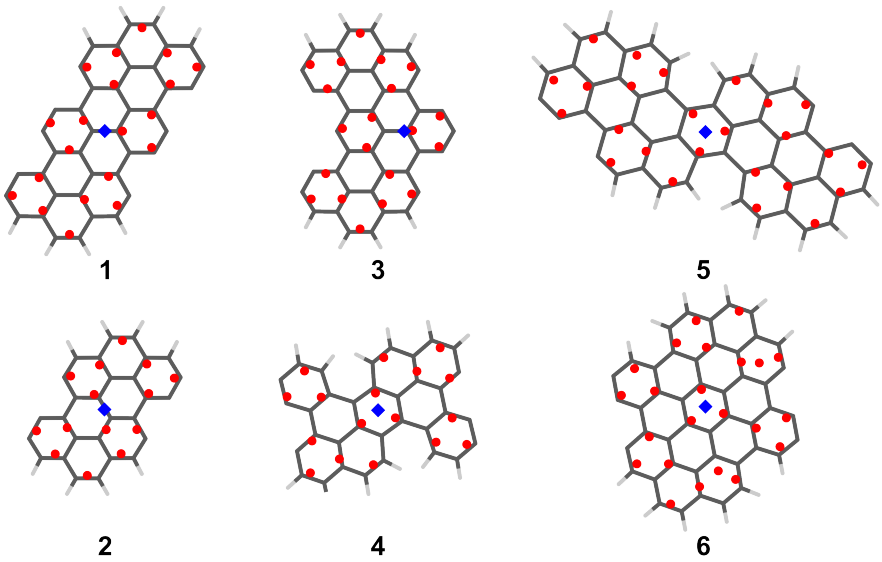


Figure 4.5: Wannier centres of GNR **1**–**6**. The Wannier centres for each GNR are represented by red dots. The sums of Wannier centres are represented by blue diamonds, and they are all in the centre of the respective unit cell, indicating trivial topology.

mirror symmetry, the $\mathbb{Z}_2$ invariant is strictly quantised to 0 or 1 and the sum of Wannier centres is located at either (up to a numerical error) the unit-cell centre or boundary. Nonetheless, if we overlook the minor offset, we can still consider the sum of Wannier centres for all six GNRs as being in the respective unit-cell centres.

In conclusion, we managed to calculate the topological indices, the LDOS, and the Wannier centres for all six GNRs. These results unequivocally tell us that these ribbons are topologically trivial. In the following three sections, we will investigate strategies to design topologically nontrivial GNRs based on these six structures.

4.2.1 Tuning the topology via unit-cell design

Previous studies have concluded that the topology of a GNR depends on its end termination [12, 212–214]. For GNRs with the same bulk structure, their topological phases can be different if they have different end terminations. Since the end termination of a GNR is essentially defined by its unit cell, we can get different topological phases by changing the unit cell while keeping the bulk structure the same. In this section, when we say different unit-cell design, we mean keeping the

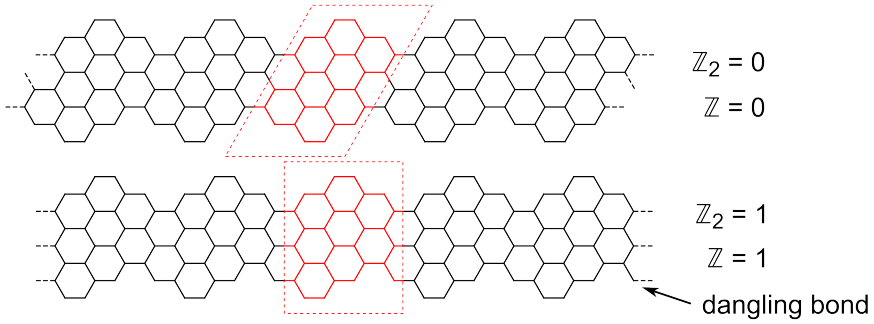


Figure 4.6: GNR **2** and a derivative of it with the same bulk structure but different end terminations. The first structure is topologically trivial, while the second structure is nontrivial. The unit cells for the two structures are highlighted in red. The second structure will have a dangling bond if the ribbon is truncated. Topological indices were calculated from the tight-binding model.

bulk of the ribbon the same but changing its unit cell and, accordingly, the end termination. In Figure 4.6, we show GNR **2** and a derivative of it that has the same bulk structure but a different unit cell and a different end termination. These two ribbons have different topological phases as determined from theoretical calculations. Although the second structure shown in Figure 4.6 is topologically nontrivial, we want to avoid this type of design because it has a dangling bond at the right end, and in practical synthesis, such dangling carbon atoms will form a methyl group and are excluded from the π-electron network. Thus, in the subsequent sections, we will avoid designing such unit cells that could result in dangling bonds at the termini.

In Figure 4.7 we show two examples of tuning the topological phases by changing the unit cell. As discussed earlier, GNRs **3** and **4** are topologically trivial. They both have $\mathbb{Z}_2 = 0$, $\mathbb{Z} = 0$. Their sums of Wannier centres, denoted by blue diamonds, are located at the centres of respective unit cell. By altering the unit-cell design, the sum of Wannier centres shifts to the unit-cell boundary in both cases. The topological indices ($\mathbb{Z}_2 = 1$, $\mathbb{Z} = 1$) also confirmed that GNR **3a** and **4a** are topologically nontrivial and they both possess one localised end state at zero energy. We then calculated the LDOS of an octamer of **3a** and **4a**. From the LDOS traces calculated at a fixed position (either at the end cell or the bulk cell), one can find,

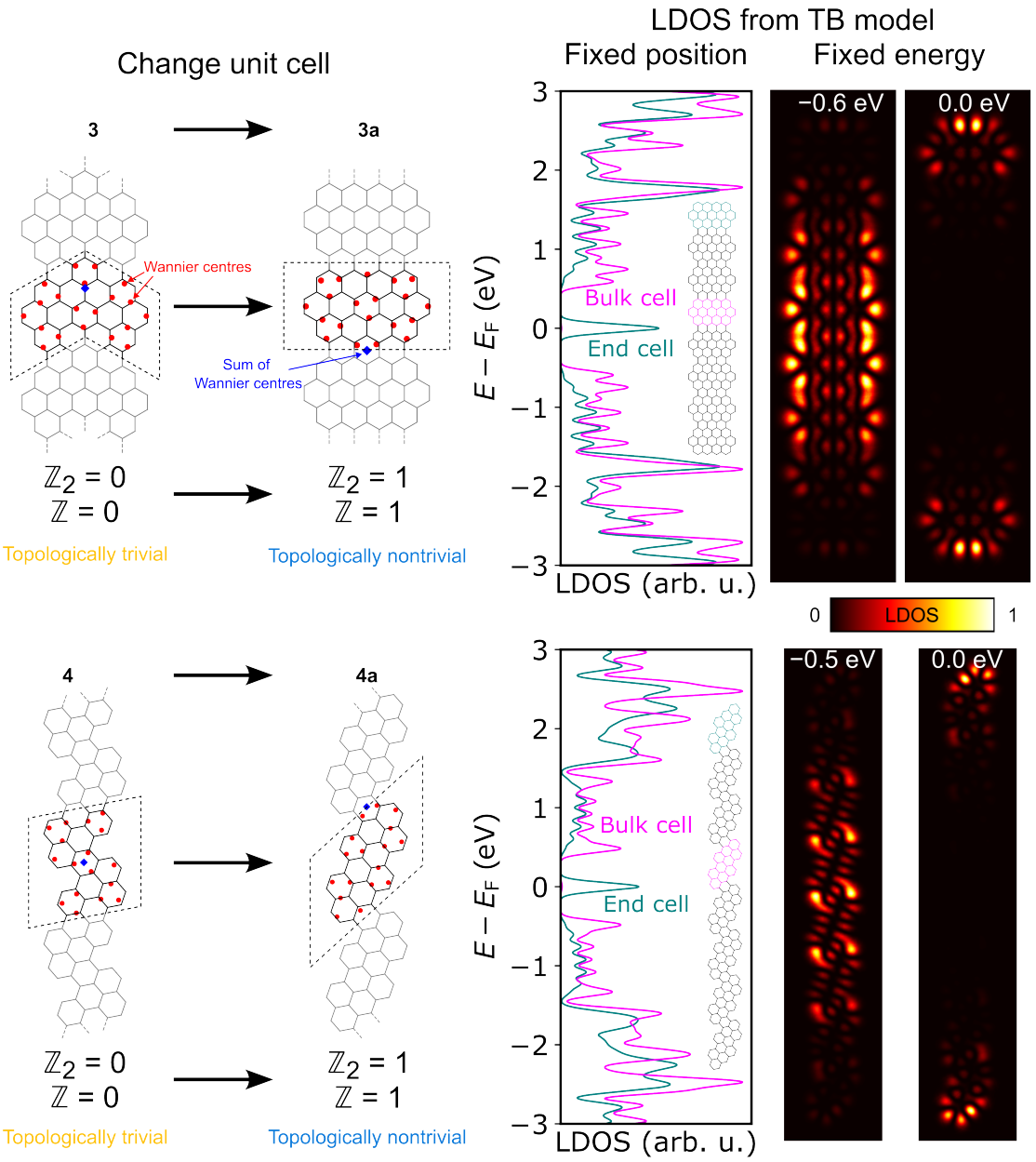


Figure 4.7: Tuning GNR topology by changing the unit cell. The GNRs **3** and **4** are topologically trivial, as confirmed by the calculation of the topological invariants ($\mathbb{Z}_2 = 0, \mathbb{Z} = 0$) and sum of Wannier centres (the blue diamonds located at the centre of the unit cell). By changing to a new unit cell, designated as **3a** and **4a**, the GNRs become topologically nontrivial ($\mathbb{Z}_2 = 1, \mathbb{Z} = 1$, sum of Wannier centres shifts to the unit-cell boundary). The topological invariants are calculated using the tight-binding model, and the Wannier centres were calculated by DFT, followed by Wannierisation. In the right panels, the LDOS is calculated for both fixed positions and fixed energies. In the fixed-position LDOS traces (with 0.05 eV Gaussian broadening), the two nontrivial GNRs **3a** and **4a** exhibit zero-energy states that are contributed solely by the end cells. These zero-energy states are visualised by LDOS maps integrated within a 0.1 eV window around 0.0 eV. For comparison, the bulk states just below the zero-energy states are displayed alongside. The LDOS maps were calculated at a height of 3 Å above the GNR planes.

at zero energy, a peak that is solely caused by the end cells. In other words, such topological end states emerge only when the bulk of the material is truncated. We also calculated the LDOS maps at fixed energies. To do this, we first construct the Bloch wavefunctions from the tight-binding calculation results by assuming the $2p_z$-orbitals of carbon atoms are Slater-type orbitals:

$$\psi_n(\boldsymbol{r}) = \sum_j C_j^n z \exp\left(-\zeta \left|\boldsymbol{r} - \boldsymbol{r}_n\right|\right), \tag{4.1}$$

where C_j^n is the eigenvector calculated from the tight-binding model following the steps introduced in Section 3.1.1. The coordinate along the perpendicular direction with respect to the GNR plane is denoted as z. The effective nuclear charge constant ζ was set to 1.625, an empirical value used in the literature [59]. Following that we compute the LDOS by summing up the charge density $|\psi_n(\boldsymbol{r})|^2$ at a fixed height z_0 in an energy interval $[E_1, E_2]$, we obtain

$$\text{LDOS}\left(x, y; z_0 \text{ fixed}\right) = \sum_n \left|\psi_n(x, y, z_0)\right|^2 \quad \text{for } n \text{ with } E_1 < E_n < E_2. \tag{4.2}$$

We calculated the LDOS maps of both the zero-energy localised end states and the bulk states right below the Fermi level. Note that the LDOS of a GNR at fixed positions and fixed energies simulate the STM measurement results of this GNR.

4.2.2 Tuning the topology via connection between unit cells

Topological phases can also be tuned by keeping the unit-cell geometry fixed while altering the connection between neighbouring unit cells. In chemical synthesis, this means keeping the shape of the molecular precursor, but changing the choice of atoms that are to be connected with the neighbours of this precursor during polymerisation. There have been previous experimental examples where the unit cell of two different GNRs share the same geometry but have different orientations. For instance, as shown in Figure 2.12a and Figure 2.12c, the 7-AGNR and (3,1) chiral-GNR were synthesised from two isomers of the dibromo-bianthryl (DBBA) molecule.

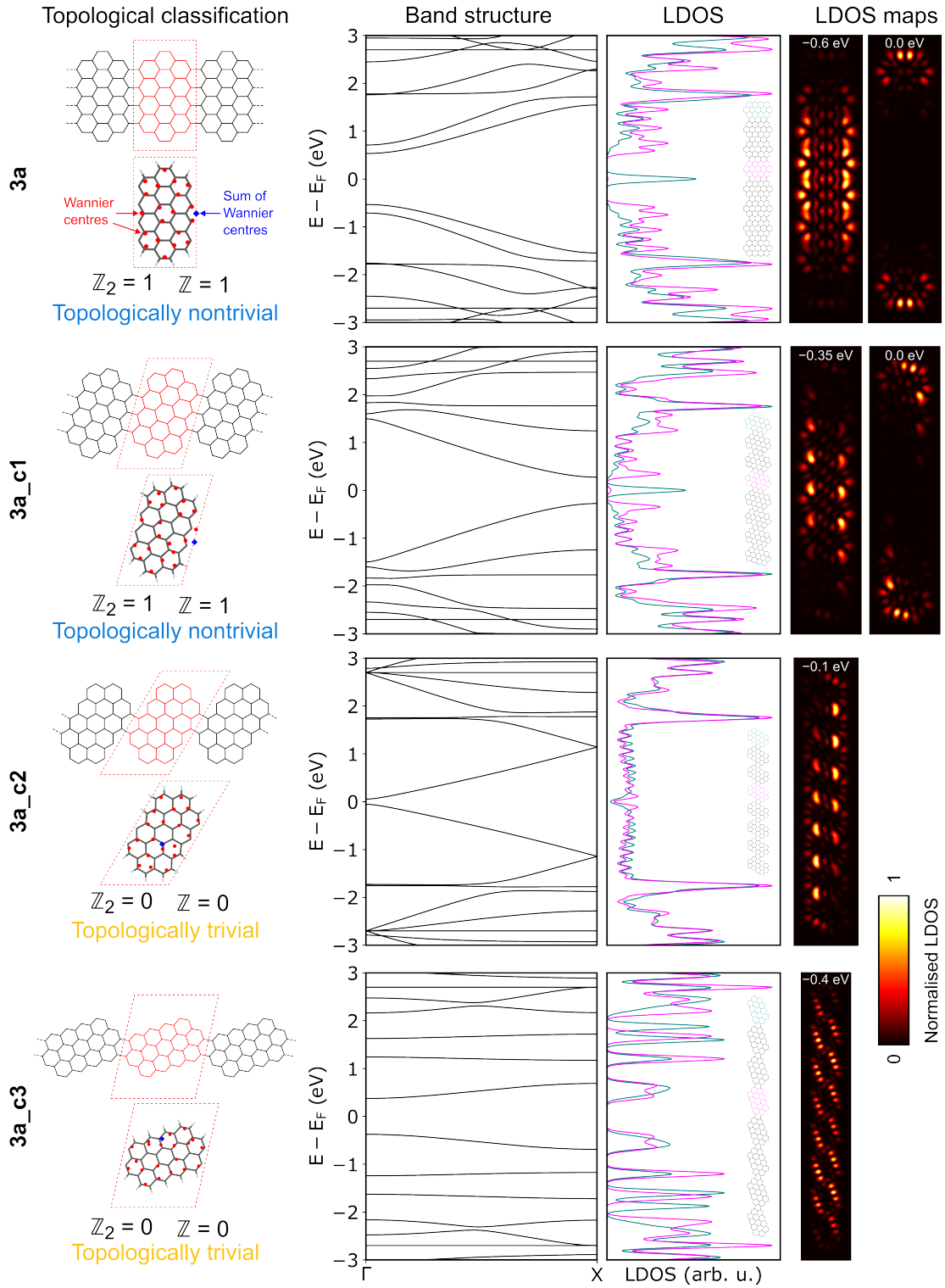


Figure 4.8: Tuning GNR topology by changing connection between unit cells. In each case, the repeating unit is highlighted in red and in dashed boxes. The sum of Wannier centres, $\mathbb{Z}_2$, and $\mathbb{Z}$ invariants are evaluated, classifying the GNRs into distinct topological phases. For topologically nontrivial GNRs, additional LDOS peaks, which are solely caused by end cells, emerge at zero energy, whereas no corresponding states can be found in the band structures at zero energy. No localised end states can be found in topologically trivial GNRs. The calculations procedures and corresponding parameters are same as those in Figure 4.7.

The connection between neighbouring unit cells was controlled by the position of two bromine atoms. Following a similar approach, we investigated the topological phases of GNRs with identical unit-cell geometries but different connections.

Taking the GNR **3a** as an example, we designed several GNRs that have the same unit-cell shape as **3a**, but with different connections (Figure 4.8). We labelled them as **3a__c1**, **3a__c2**, **3a__c3**, respectively. By calculating the topological invariants and Wannier centres, we found that **3a** and **3a__c1** are topologically nontrivial whereas **3a__c2** and **3a__c3** are topologically trivial. The sums of Wannier centres of **3a__c2** and **3a__c3** are slightly offset from their respective unit-cell centres. Such offsets are probably because the structures are not flat but twisted, since the hydrogen atoms of neighboring unit cells hinder each other in the spatial arrangements. As with the calculation results in Figure 4.7, we compared the LDOS at the end cell and bulk cell for these GNRs, and also depicted their LDOS maps in Figure 4.8. The localised end states at zero energy appear only in **3a** and **3a__c1**, but are absent in **3a__c2** and **3a__c3**. The zero-energy states have no corresponding bands in the band structure of infinite ribbons, and they are situated in the middle of the band gap. Based on the bulk–boundary correspondence, in-gap states emerge at the interface between two systems with distinct topological phases. The end of a 1D material can be regarded as the interface between the material and vacuum. Since vacuum is topologically trivial, the in-gap states of a topologically nontrivial GNRs will appear as end states. Therefore, they are also called in-gap end states.

Similarly, we designed five new GNRs based on the unit cell of **4a**, as shown in Figure 4.9. Among the six GNRs, **4a**, **4a__c1**, **4a__c3** and **4a__c4** are topologically nontrivial and exhibit zero-energy end states. The charge-density maps of the end states are presented in purple. In addition to these ribbons, we have designed more GNRs following similar principle and they can be found in Figure 8.2 in the Appendix. All these examples show that the topological phases can be tuned,

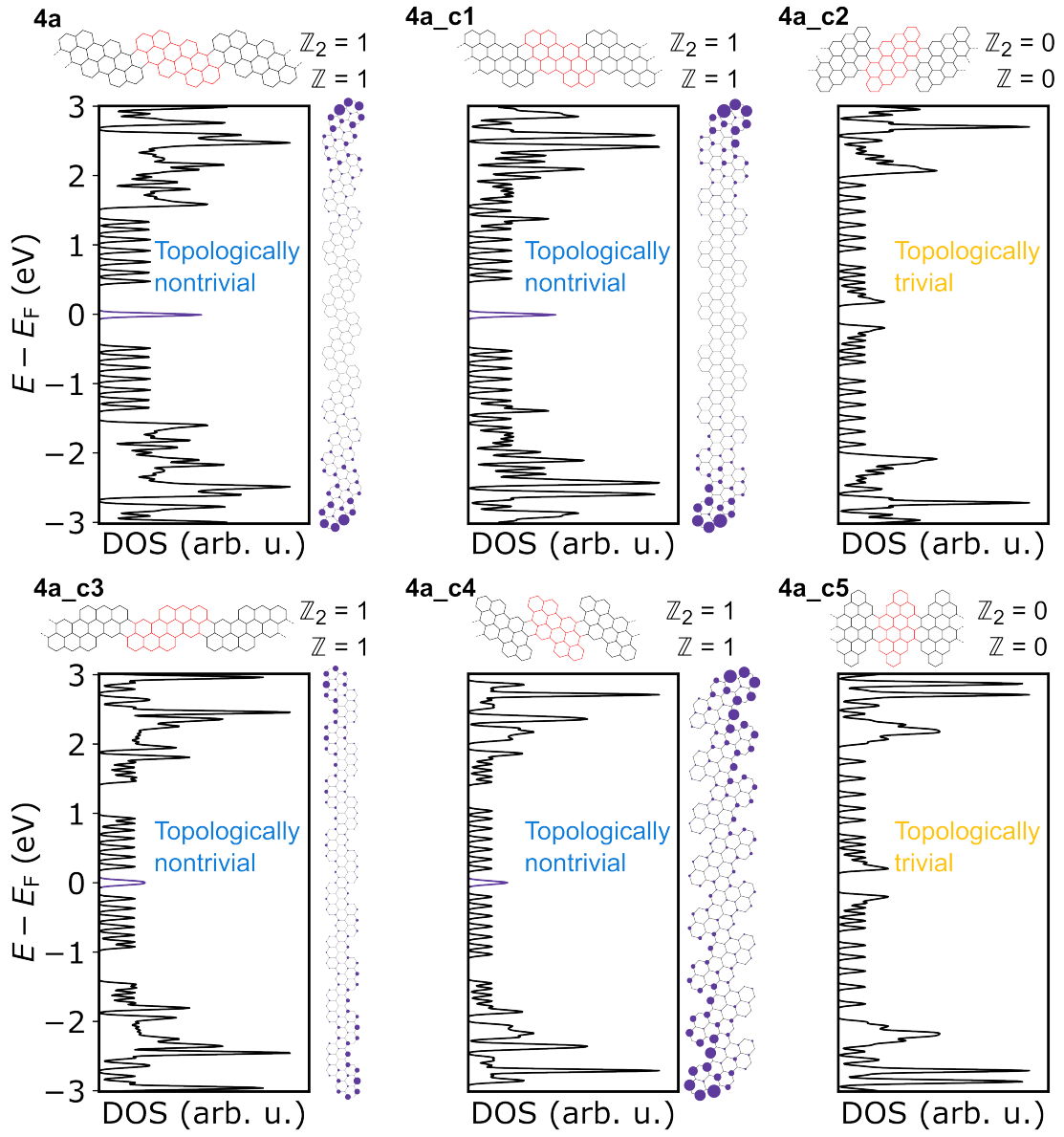


Figure 4.9: Distinct topological phases of GNR **4a** with different connections. Six variants of GNR **4a** are designed by changing the neighbouring-cell connections, labelled by **4a**, **4a_c1**, **4a_c2**, **4a_c3**, **4a_c4**, **4a_c5**, respectively. The repeating unit is highlighted in red. $\mathbb{Z}_2$ and $\mathbb{Z}$ are evaluated, classifying the GNRs into distinct topological phases. The densities of states (DOSs) were calculated for an octamer of each GNR with 0.02 eV Gaussian broadening. The topologically nontrivial GNRs **4a**, **4a_c1**, **4a_c3** and **4a_c4** possess zero-energy end-states where the topologically trivial GNRs **4a_c2** and **4a_c5** do not. The peaks of the end states are highlighted in purple in the DOS. The charge-density map of the end states are also depicted in purple and superimposed on the structural model of the octamers. The circle radius scales with the amplitude of charge density, and the amplitudes are normalised in each case.

swapping between trivial and nontrivial phases, by modifying the connection between unit cells, keeping the unit-cell shape unchanged.

4.2.3 Topology at different energy gaps

A GNR can have several energy gaps in its band structure, with each gap having different topological phase. For example, Rizzo et al. has demonstrated an example of GNR that has several topological end states at different energy gaps [221]. In STM, the ribbon can be doped with electrons or holes, enabling the investigation of electronic states away from the Fermi level. In this section, we will study the topological phases in different energy gaps of GNRs.

In Figure 4.10, we show three examples, which are selected for a detailed discussion because the energy gaps in these examples are relatively large so that the in-gap states can be clearly separated from other states. The first GNR, **1__c1**, has the same unit-cell shape as GNR **1** but the connection between the unit cells are different. The $\mathbb{Z}_2$ invariants at different energy gaps were evaluated from the tight-binding model. As the $\mathbb{Z}$ invariant requires chiral symmetry, the Fermion operator Q_k mentioned in Section 3.1.3 respects chiral symmetry only when there is an equal number of occupied and unoccupied states. When the energy bands are filled to other gaps than the band gap around the Fermi level, there will be unequal number of occupied and unoccupied states. Therefore, the $\mathbb{Z}$ invariant can only be evaluated at the Fermi level but not at other energy gaps. In Figure 4.10 we only show the $\mathbb{Z}_2$ indices, and the presence or absence of in-gap states is confirmed by the LDOS results. For GNR **1__c1**, there are no in-gap states at zero energy, but instead, two end states emerge at the energy gaps around $\pm 1.3\,\mathrm{eV}$. We only displayed the charge-density map at $-1.3\,\mathrm{eV}$. Similar calculations were carried out for GNR **2** and **3a__c3**. The results suggest that, when energy bands are occupied by electrons up to the energy gaps with $\mathbb{Z}_2 = 1$, the system will display topological end states. In Figure 4.11 we showcased more examples of GNRs with distinct topological phases

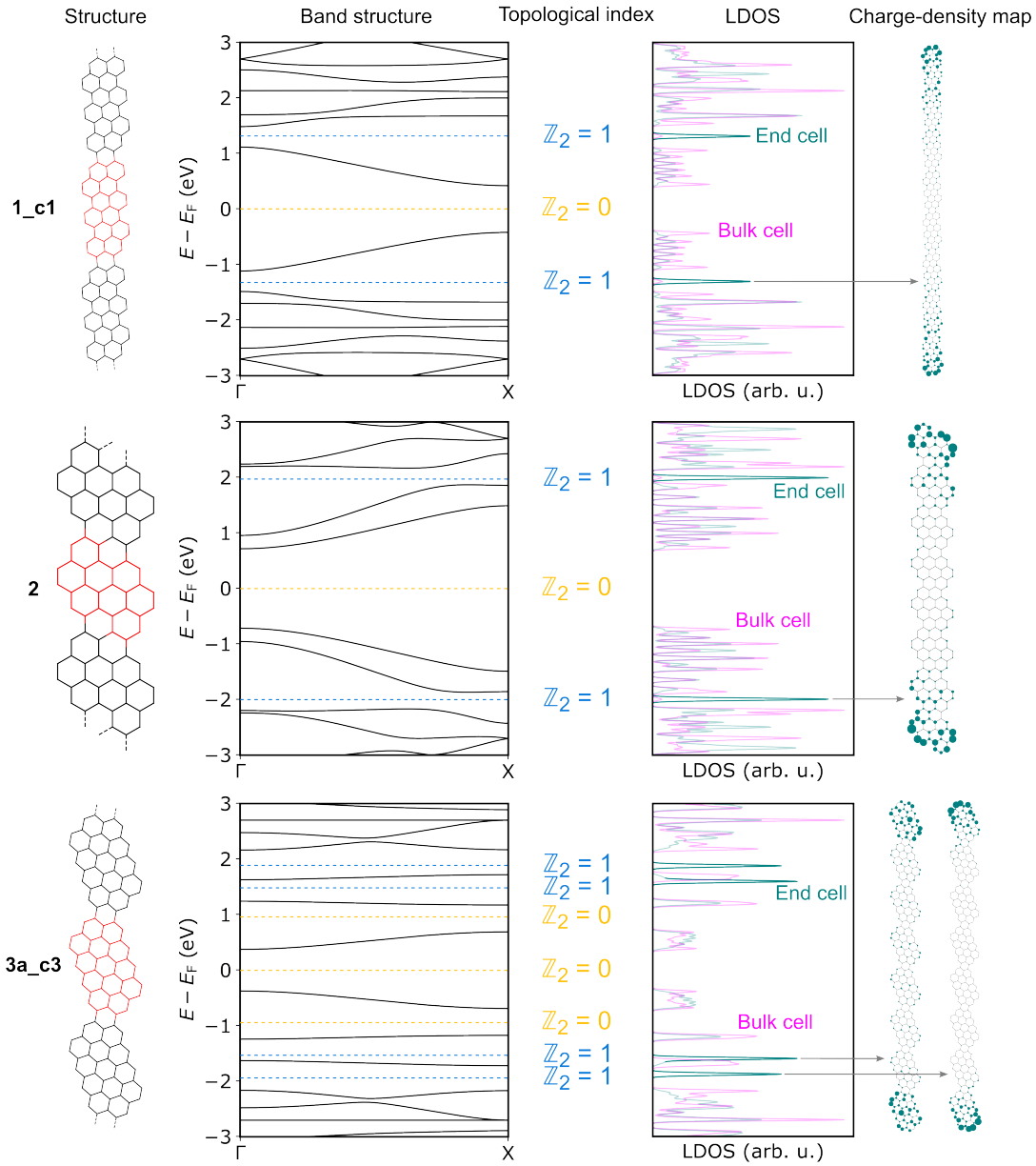


Figure 4.10: Distinct topological phases in different energy gaps. For each GNR, the repeating unit is highlighted in red. $\mathbb{Z}_2$ invariants are calculated for different energy gaps, indicating the topological phases when energy bands are filled by electrons up to the corresponding gaps. The local densities of states (LDOSs) for the end cell and bulk cell were calculated for the octamer of each GNR with 0.02 eV Gaussian broadening. For the gaps with $\mathbb{Z}_2 = 1$, localised end states that contributed solely by end cells emerge in the middle of the gap. The charge-density maps (teal colour) of the in-gap states are superimposed on the structural models. The circle radius scales with the amplitude of charge density, and the amplitudes were normalised in each case.

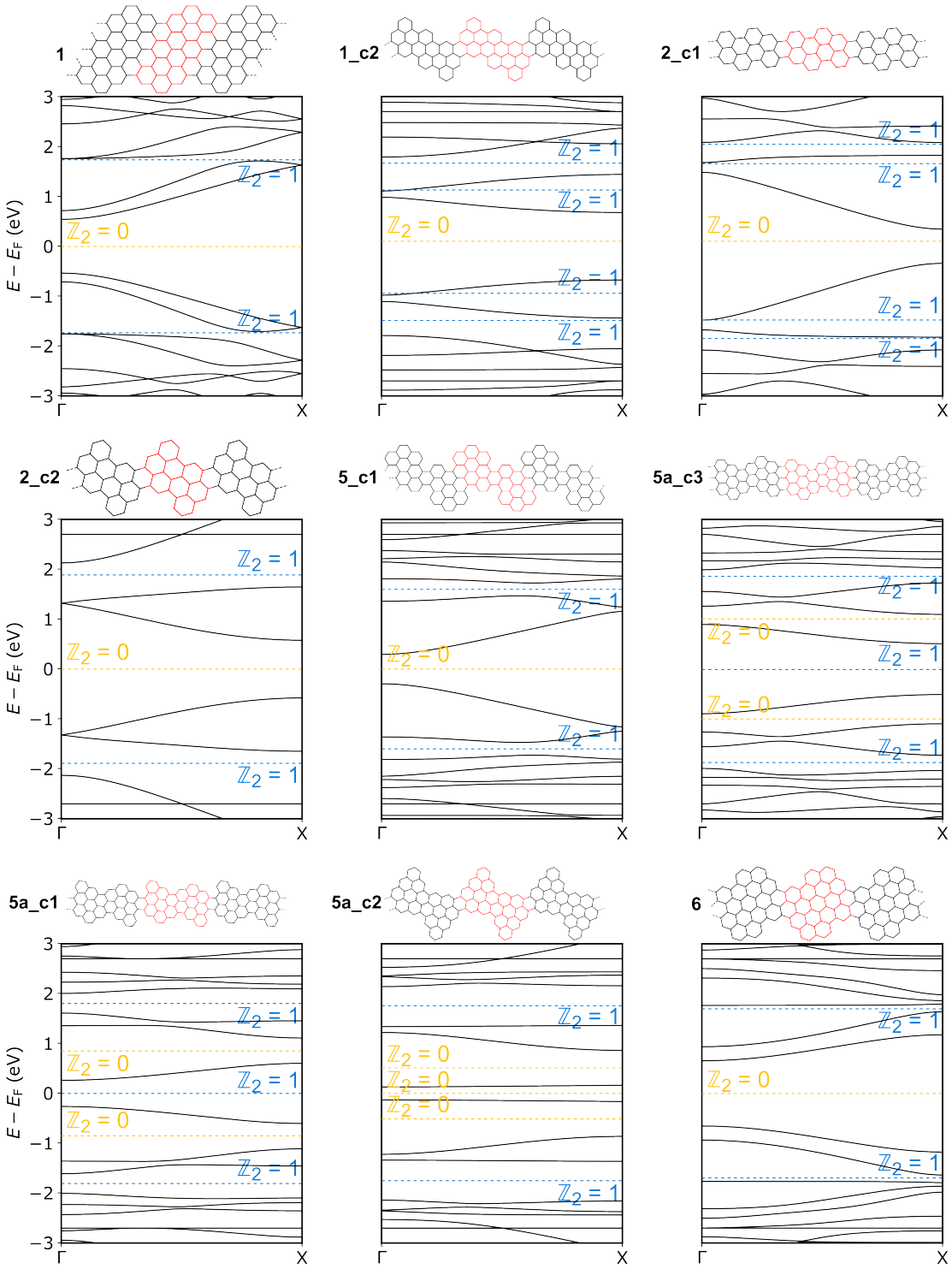


Figure 4.11: More examples of distinct topological phases in different energy gaps. The repeating unit of each GNR is highlighted in red. The $\mathbb{Z}_2$ invariants are evaluated for different energy gaps, indicating the topological phases when energy bands are filled by electrons up to the corresponding gaps.

in different energy gaps. These gaps are all close to the Fermi level and, therefore, become easily accessible by electron or hole doping in experiments.

To summarise, in this section we have explored three approaches to change the topological phases of GNRs. The GNRs shown here were all derived from six initial structures by either changing the unit cell, or changing the way unit cells are connected. This work provides a toolbox for chemists and is to assist the design of topologically nontrivial GNRs. Eventually, we comment on the robustness of the topological end states in GNRs. The topological phases of GNRs are protected by the spatial symmetries of the lattice. Any breaking of the spatial symmetries at the end unit cell of a GNR would change the topological end states [12]. Furthermore, the end states are also robust against local perturbations such as lattice distortions, which holds true especially for the mid-gap end states in a GNR with a large band gap [12]. Cao et al. showed that for a 7-AGNR, the end states survive from any local perturbation on the terminal carbon atoms with an integrated strength lower than 4 eV [12]. Moreover, Lin et al. showed that the topological end states of GNRs are robust when higher-order hoppings are included in the tight-binding model. Besides the theoretical works, there are also experimental studies testing the robustness of topological end states in GNRs. It was demonstrated that end states can be destroyed by oxidation [158], double-hydrogenation [220], Br-substitution [150], or by carbon vacancies in one of the termini [150]. The end state at the other terminus, however, still remains intact. In general, any defect or perturbation in the bulk that is far away from the terminations should not have a large effect on the topological end states.

4.3 Relationship between $\mathbb{Z}$ topology and Clar's sextet rule

4.3.1 Relationship between $\mathbb{Z}$ index and Wannier functions

We have mentioned that the $\mathbb{Z}$ index indicates the number of zero modes that a system has. We will elaborate further on this using a 7-AGNR as an example. As shown in Figure 4.12, we calculated the $\mathbb{Z}$ indices of three different unit cells of a 7-AGNR, denoted as 7-AGNR-z, 7-AGNR-z′, and 7-AGNR-b, respectively. The letters "z" and "b" stand for "zigzag" and "beard" termination, respectively. If we were to calculate the $\mathbb{Z}_2$ index for 7-AGNR-z and 7-AGNR-b, we would get zero for both cases. This is inadequate to determine whether the system has no end state or an even (more than one) number of end states. In such cases, one has to resort to the $\mathbb{Z}$ index, which tells the number of in-gap states. For each occupied energy level there will be an unoccupied counterpart. So the $\mathbb{Z}$ index actually tells the number of pairs of in-gap states. For 7-AGNR-z that has $\mathbb{Z} = 1$, there is one pair of in-gap states, whereas 7-AGNR-z′ and 7-AGNR-b both have $\mathbb{Z} = 2$, thus each having two pairs of in-gap states (Figure 4.12c). Figure 4.12.

Next we shall explain how the $\mathbb{Z}$ index is correlated with Wannier functions. As we have introduced in Section 2.2.2, Jiang et al. derived the formula that calculates $\mathbb{Z}$ index from Bloch functions:

$$\mathbb{Z} = -\frac{\mathrm{i}}{\pi} \sum_{n\in\mathrm{occ}} \mathrm{inter}\left(\int_{\mathrm{BZ}} \alpha_{nk}^{\dagger} \partial_k \alpha_{nk} - \beta_{nk}^{\dagger} \partial_k \beta_{nk} \right) \mathrm{d}k, \tag{4.3}$$

where "inter" means taking the intercellular part, α_{nk} and β_{nk} stand for the A sublattice part and B sublattice part of the Bloch wavefunction u_{nk}, "occ" means taking all the occupied bands. Guzmán et al. derived a similar formula as Equation (4.3), and in addition to that, they also formulated the equation in Wannier representation [325]. The transformation between Wannier functions and Bloch functions is given in Equation (3.49). Here we define the projection

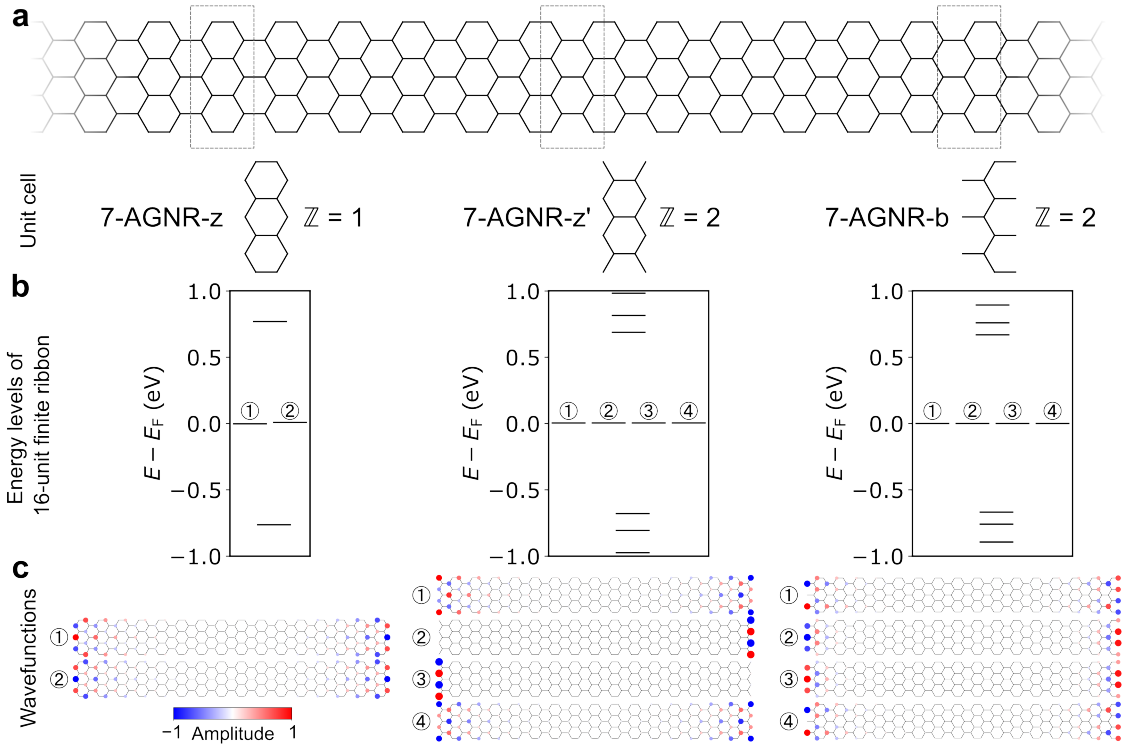


Figure 4.12: Three different unit cells of 7-AGNR with different $\mathbb{Z}$ indices. (a) Three unit cells of 7-AGNR, highlighted by dashed boxes and labelled as 7-AGNR-z, 7-AGNR-z′, and 7-AGNR-b, respectively. The $\mathbb{Z}$ indices are calculated for each unit cell. (b) Energy-levels diagrams calculated for a 16-unit finite ribbon for each unit cell. (c) Wavefunctions of zero energy states that are labelled in (b). The colour and radius of the circles in each lattice site scale with the wavefunction amplitudes, and the amplitudes are normalised in each case. All results were obtained from tight-binding calculations.

operators $\hat{P}^A$ and $\hat{P}^B$ which can project a wavefunction on the A and B sublattice, respectively. They satisfy the following relations:

$$\hat{P}^A u_{nk} = \alpha_{nk}, \quad \hat{P}^B u_{nk} = \beta_{nk}. \tag{4.4}$$

Subsequently, by making use of Equation (3.49) and Equation (4.4), and then substituting the Bloch functions in Equation (4.3) with Wannier functions w_{nR}, we arrive at [325]:

$$\mathbb{Z} = \frac{2\boldsymbol{\Pi} - \boldsymbol{p}}{\boldsymbol{a}}, \tag{4.5}$$

where $\boldsymbol{a}$ is the lattice translation vector, and $\boldsymbol{\Pi}$ and $\boldsymbol{p}$ are the chiral polarisation and geometrical polarisation vectors, respectively.

The chiral polarisation vector $\boldsymbol{\Pi}$ is defined as the difference between the expected value of the projected position operators of two sublattices over the Wannier functions of occupied states. It is written as:

$$\boldsymbol{\Pi} \equiv \sum_{n\epsilon \mathrm{occ}} \langle X^A \rangle_{nR} - \langle X^B \rangle_{nR}, \tag{4.6}$$

where $\langle X^{A,B} \rangle_{nR}$ is the average projected position of Wannier function w_{nR} on the sublattice A or B. It is defined as:

$$\langle X^\alpha \rangle_{nR} \equiv \langle w_{nR} | \hat{P}^\alpha \hat{X} \hat{P}^\alpha | w_{nR} \rangle, \quad \alpha = A, B \ , \tag{4.7}$$

where $\hat{X}$ is the position operator.

The geometrical polarisation vector $\boldsymbol{p}$ is defined as the difference between the geometrical positions of the atoms belonging to the two sublattices [325]. Since we are discussing a one-dimensional system, herein we only calculate the longitudinal direction along a ribbon, i.e. the x component:

$$\boldsymbol{p} = \sum_{i\epsilon A} x^i - \sum_{i\epsilon B} x^i, \tag{4.8}$$

where i is the atomic index. The physical meaning of $\boldsymbol{p}$ is the geometrical polarisation vector that points from the centre of mass of the B sublattice to that of the A sublattice. Considering that the Wannier function describes the charge distribution of an electron in a specific state in the crystal, the chiral polarisation vector $\boldsymbol{\Pi}$ can be understood as the polarisation of the charge distribution between the A and B sublattices.

In the following we will present an example of calculating $\mathbb{Z}$ index using Wannier functions. We choose the 7-AGNR-z unit cell. Similar to what we presented in Figure 4.3, we carried out the Wannierisation for all occupied p_z-bands. As shown in Figure 4.13a, the Wannier-interpolated bands (green circles) agree well with the p_z-bands (with large projection weight on p_z-orbitals, marked by green colour) in the original DFT-calculated band structure. Meanwhile, we also obtained seven

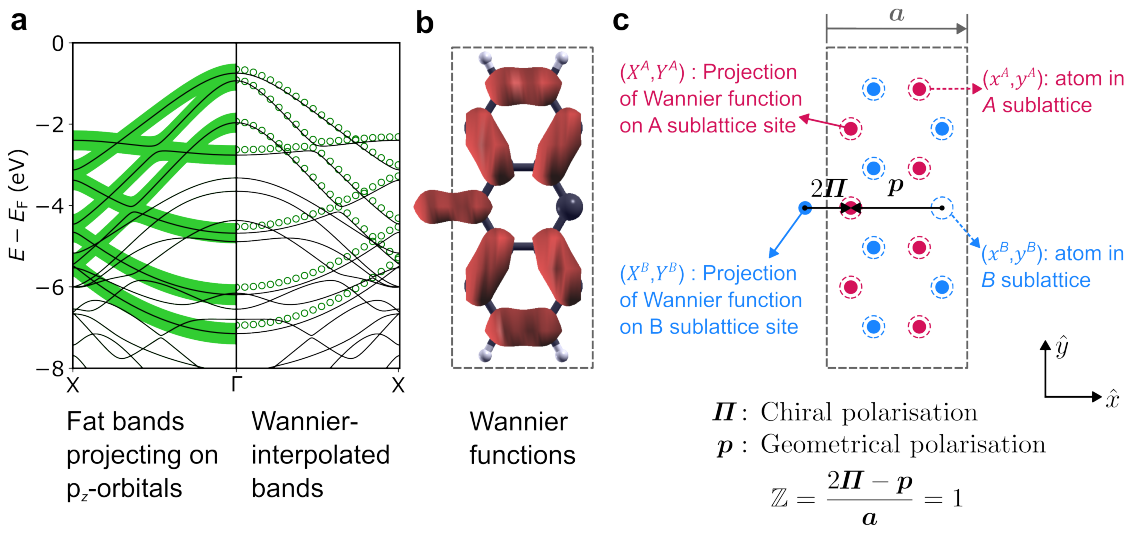


Figure 4.13: Wannier functions of a 7-AGNR. (a) Band structure calculated from DFT. The green bands superimposed on black solid lines are fat bands whose widths scale with the weight of the eigenstates' projection onto carbon p_z-orbitals. The seven occupied bands with large projection on p_z-orbitals are Wannierised, resulting in the Wannier-interpolated bands (green circles). (b) The seven Wannier functions obtained from Wanniersation, with isovalue of 0.18. The dashed box denotes the unit cell. (c) Projection of the Wannier functions onto the two sublattices. Atoms are represented by dashed circles. Red and blue colours are used to distinguish the two sublattices. The projections of the Wannier functions on the two sublattices are represented by red and blue solid dots, respectively. The lattice vector, twice of chiral polarisation vector, geometrical polarisation vector are represented by arrows, and labelled by $\boldsymbol{a}$, $2\boldsymbol{\Pi}$, $\boldsymbol{p}$, respectively. $\mathbb{Z}$ index was calculated below the diagram.

Wannier functions, which are superimposed on the same unit-cell structural model for simplicity (Figure 4.13b). As mentioned in Section 4.2, the Wannier functions calculated from Wannier90 have arbitrary phase factors. Here we manually adjusted the phases and showed the same colour in front side of the Wannier function isosurfaces to avoid confusion. In Figure 4.13c, we show the calculation of $\mathbb{Z}$ index pictorially. The projected positions of Wannier functions on the two sublattices are represented by red and blue solid dots, respectively, and their coordinates are labelled (X^A, Y^A) and (X^B, Y^B), respectively. The atom positions in the unit cell are represented by red and blue dashed circles. And the coordinates are labelled (x^A, y^A) and (x^B, y^B) for the two sublattices, respectively. The chiral and geometrical polarisation vectors can be computed according to the formula in

Equation (4.6) and Equation (4.8). They are depicted as arrows in the diagram. Using the results of $\boldsymbol{\Pi}$ and $\boldsymbol{p}$, we can determine the $\mathbb{Z}$ index, which equals to 1 and agrees with the numerical integration result shown in Figure 4.12.

We notice that in Figure 4.13 all the projected positions (X, Y) match the atom positions (x, y) in the unit cell except for one. This causes the vector $2\boldsymbol{\Pi}$ to differ from the vector $\boldsymbol{p}$ by a lattice vector $\boldsymbol{a}$. In other words, the $\mathbb{Z}$ index becomes nonzero when there is a Wannier function being equally divided by the unit-cell boundary. In fact, the $\mathbb{Z}$ index can also be expressed in a different way. In 2017, Rhim et al. justified the bulk–boundary correspondence in 1D inversion-symmetric topological insulators using the intercellular Zak phase γ^{inter} [208]. In Wannier representation, γ^{inter} can be expressed as:

$$\gamma^{\text{inter}} = \frac{2\pi}{e}\left(Q^{\text{R}\to\text{L}} - Q^{\text{L}\to\text{R}}\right) \bmod 2\pi, \tag{4.9}$$

where e is the electron charge. It is assumed that each Wannier function is normalised and hosts one electron charge. $Q^{\text{R}\to\text{L}}$ denotes the total charge weight in the left-hand side of a unit-cell interface contributed by all Wannier functions with their centres belonging to the right-hand side of the unit-cell interface, and vice versa for $Q^{\text{L}\to\text{R}}$. They can be understood as the exchange (right to left, or left to right) of Wannier functions with respect to a unit-cell boundary. Since the unit cells are periodic in a GNR, we can use any unit-cell boundary as a reference. For the case in Figure 4.13b, taking the left side of dashed box as reference, there is one Wannier function divided by the unit-cell boundary almost equally into two parts. Since each Wannier function hosts one electron, we can obtain $Q^{\text{R}\to\text{L}} \approx e/2$, and $Q^{\text{L}\to\text{R}} \approx 0$. Therefore we get $\gamma^{\text{inter}} = \pi$. Consequently, according to Equation (2.12), we have $\mathbb{Z}_2 = 1$, which agrees with the $\mathbb{Z}$ index. Inspired by the work of Rhim et al. [208], we can write the formula of the $\mathbb{Z}$ index in a similar way. Remember that, as introduced in Section 2.2.2, the $\mathbb{Z}$ index takes the difference between phase factors contributed

by the two sublattices, whereas the intercellular Zak phase sums them up. By making use of this difference we can derive an alternative formula of the $\mathbb{Z}$ index:

$$\mathbb{Z} = \frac{2}{e}\left(Q^{\mathrm{R}\to\mathrm{L}} + Q^{\mathrm{L}\to\mathrm{R}}\right). \tag{4.10}$$

It sums up the total exchange of Wannier function across a unit-cell boundary, by adding both the "right to left" and "left to right" components. Unlike γ^{inter} that is modulo 2π, $\mathbb{Z}$ calculated from Equation (4.10) can take any integer values.

In fact, in practical calculations, one does not need to evaluate Equation (4.7). That is because in such bipartite systems, the number of Wannier functions for occupied p_z-bands are half of the number of total atoms. When we calculate the maximally localised Wannier functions (MLWFs) with Wannier90, each MLWF is localised around two neighbouring A–B atoms. If this atom pair is cut by the unit-cell boundary, the corresponding Wannier function is often divided equally by the unit-cell boundary. Hence, we can use a less rigorous but more intuitive approach, which is determining the $\mathbb{Z}$ index by the number of Wannier functions cut by a unit-cell boundary. It is important to point out that here we represent the Wannier functions isosurfaces with an appropriate cutoff. The cutoff, or isovalue, should not be too low, otherwise the isosurface occupies a large space and could not show its localised nature.

4.3.2 $\mathbb{Z}$ index, Wannier functions, and Clar's sextet rule

Now we discuss the relationship between $\mathbb{Z}$ index, Wannier functions, and Clar's sextet rule. We will elucidate this relationship using the three different unit cells of a 7-AGNR that were used in Figure 4.12 as examples. As shown in Figure 4.14, firstly we can find that the previously mentioned rule to determine the $\mathbb{Z}$ index also applies for 7-AGNR-z′ and 7-AGNR-b, both of which have two Wannier functions cut by the unit-cell boundary and have $\mathbb{Z} = 2$. Since Wannier functions are periodic in real space, we can plot a Wannier function for any unit cell. We plotted the Wannier

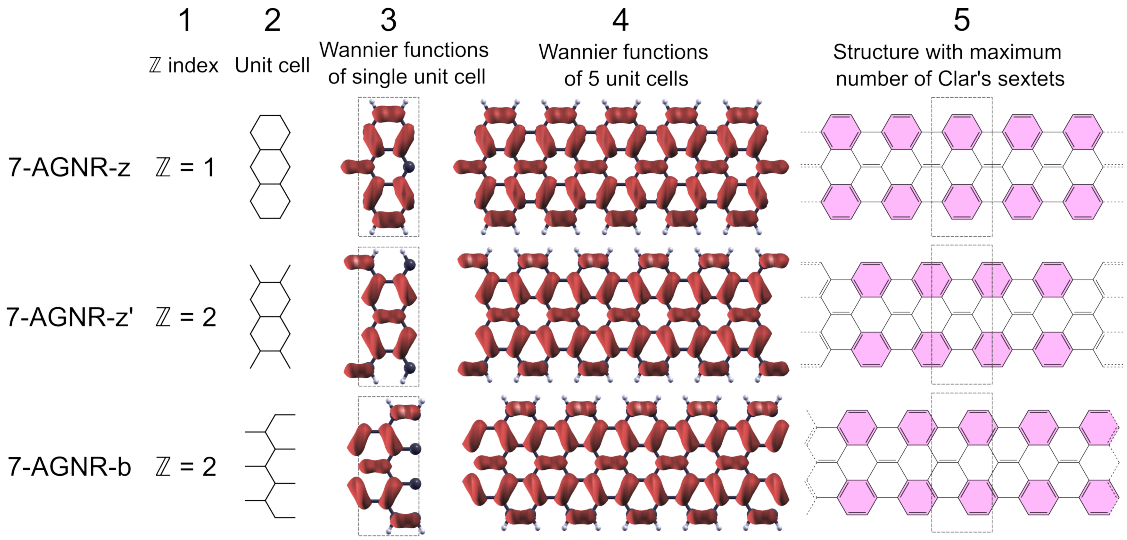


Figure 4.14: ℤ indices, Wannier functions, and Clar's sextets of different 7-AGNR unit cells. The Wannier functions calculated from occupied p_z-bands are displayed for three different unit cells of 7-AGNR. The isovalues of all Wannier functions were set to 0.18. For each case, the ℤ index is equal to the number of Wannier functions cut by the unit-cell boundary (dashed boxes in the third column). In the fourth column, the Wannier functions are plotted across five unit cells. In the fifth column, each structure is plotted with the maximum number of Clar's sextets (see text for explanation). The Clar's sextets are highlighted in pink colour. The position of each double bond in the fifth column corresponds to the position of a double bond in the fourth column.

functions for the three unit cells across five consecutive unit cells, as illustrated in Figure 4.14. Upon close observation, we notice that the Wannier functions are actually equivalent across the three cases. The Wannier functions in each case can be obtained from one another by a certain translation in the longitudinal direction. The configuration of these Wannier functions reminds us of the Clar's sextet rule. In organic chemistry, a polycyclic aromatic hydrocarbon (PAH) molecule can be viewed as a cluster of rings (or hexagons), where each ring is composed of six carbon atoms. Each of these carbon atoms contributes one p_z-electron to form a π-bond with its neighbour, collectively creating a π-cloud. While all C–C bonds are considered to be equivalent in a two-dimensional infinite graphene sheet, that is not the case in finite organic molecules. Since each carbon atom is connected with more than one neighbouring atoms, but only share one p_z-electron to form π-bond, not all the neighbouring pairs of carbon atoms can have a π-bond between

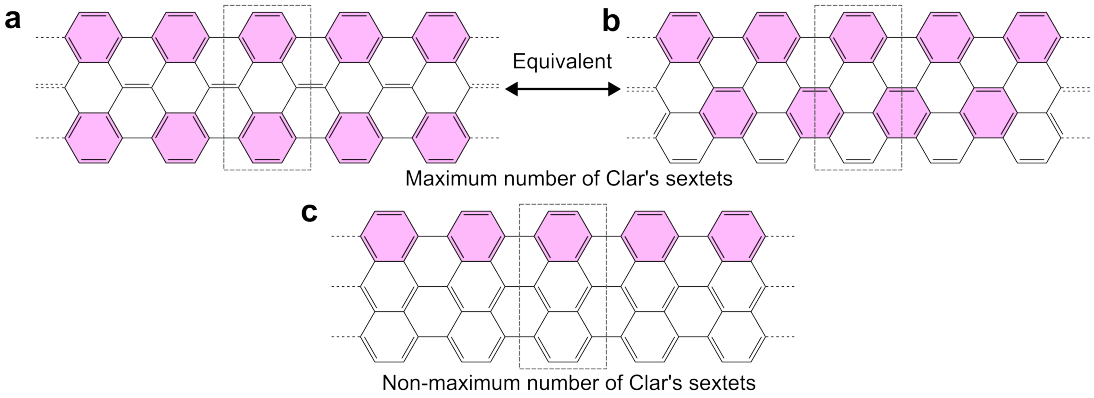


Figure 4.15: Structural models of 7-AGNR with maximal and non-maximal number of Clar's sextets. (a–b) Two equivalent representations of maximal number of Clar's sextets. (c) A representation with non-maximal number of Clar's sextets. Unit cells are enclosed in dashed boxes.

them. Therefore, there can be alternative ways of forming π-bonds between the carbon atoms in an aromatic molecule. The Clar's sextet rule postulate that the most stable form of a PAH is the one in which the greatest number of rings contain six π electrons – these rings are referred to as "Clar sextets". In other words, a PAH molecule is most stable if it has the maximum number of Clar's sextets.

We will explain this using the example of a 7-AGNR-z again. As shown in Figure 4.15, the Clar's sextet, represented by a ring with six alternating single and double bonds, is depicted in pink. The two structures in Figure 4.15a–b both have two Clar's sextets per unit cell, which is the maximum number of Clar's sextets that can be drawn, whereas the structure in Figure 4.15c only has one Clar's sextet per unit cell. The positions of the double bonds in the two structures in Figure 4.15a–b are actually identical. The only difference is that the same double bonds are considered as belonging to different hexagons. Now let us return to Figure 4.14. It is remarkable to see that the positions of the Wannier functions all coincide with the positions of double bonds in the structural models with the maximum number of Clar's sextets. Although there are alternative ways to draw Clar's sextets, the arrangement of the Wannier functions always corresponds to the arrangement of double bonds in a configuration with the maximum number of

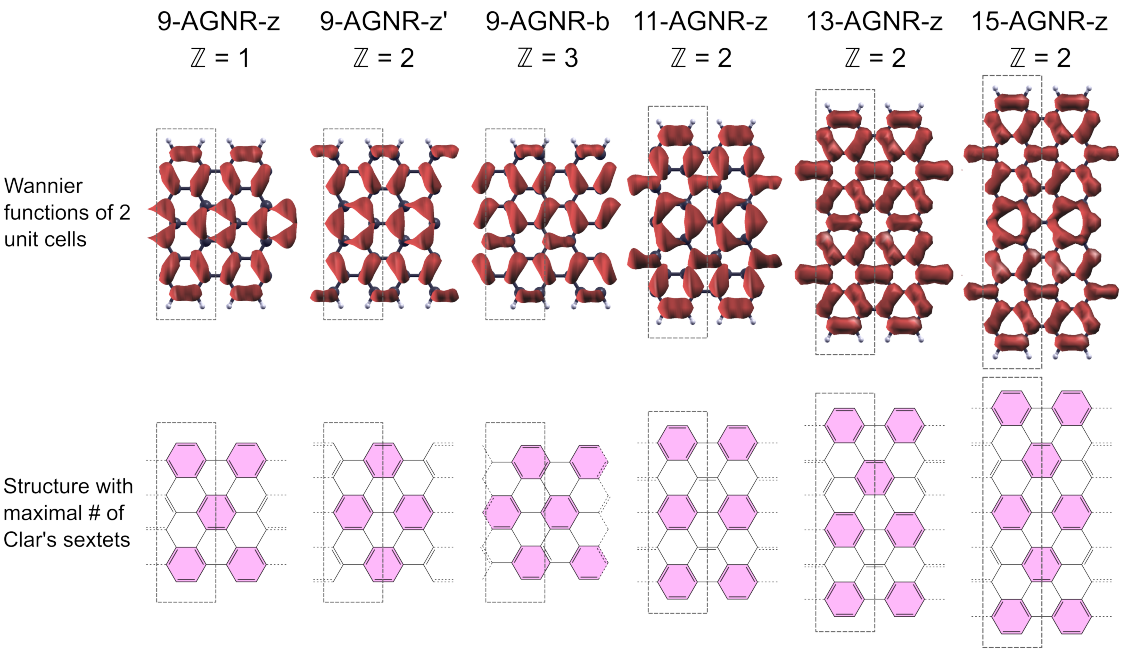


Figure 4.16: ℤ indices, Wannier functions, and Clar's sextets in other AGNR examples. For each case, the unit cell is enclosed by a dashed box, and the ℤ index equals to the number of Wannier functions cut by the unit-cell boundary. The positions of Wannier functions correspond to the positions of double bonds in the structural model with the maximum number of Clar's sextets. The isovalue of the Wannier functions were set to 0.18, 0.16, 0.24, 0.25 for 9-AGNRs, 11-AGNR, 13-AGNR, 15-AGNR, respectively.

Clar's sextets. Since the ℤ index is equal to the number of Wannier functions that are cut by a unit-cell boundary, now it can be stated that the ℤ index is equal to the number of double bonds that are cut by a unit-cell boundary in a structure with the maximum number of Clar's sextets. This relation is remarkable because it enables one to predict the ℤ index simply by drawing Clar's sextets!

We further verify this correspondence by calculating the Wannier functions of 9-AGNR with different unit cells, and other AGNRs with different width. As shown in Figure 4.16, we plotted the Wannier functions of 9-AGNR-z, 9-AGNR-z′, 9-AGNR-b, 11-AGNR-z, 13-AGNR-z, 15-AGNR-z. Appropriate isovalues were chosen in each case to show the positions of the localised Wannier functions while not making them overlap on each other. Then we mapped each Wannier function to a double bond in the structural model. All of these structural models have the maximum number of Clar's sextets. The relationship between Wannier functions

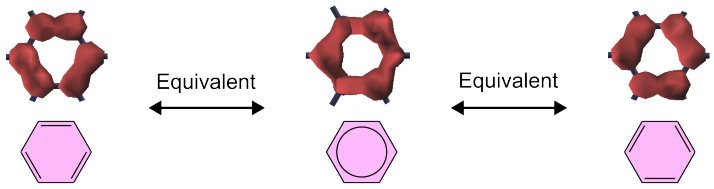


Figure 4.17: Three different configurations of Wannier functions that correspond to the same Clar's sextet.

and Clar's sextets also holds for these ribbons: For each of these GNRs, the $\mathbb{Z}$ index is equal to the number of Wannier functions that are cut by the unit-cell boundary, and is also equal to the number of double bonds that are cut by the unit-cell boundary in the configuration with maximal number of Clar's sextets.

There is a special case in Figure 4.16 that needs further scrutiny. In the case of 9-AGNR-z, the Wannier function in the middle is centred on carbon atoms rather than C–C bonds. As illustrated in Figure 4.17, we show that such an arrangement where three Wannier functions are localised on three carbon atoms in a hexagon (the middle one in Figure 4.17) is actually equivalent to the case where three Wannier functions are localised on three C–C bonds in a hexagon (the left and right one in Figure 4.17). In each case we drew the corresponding Clar's sextets below the Wannier functions. The Wannier functions in the middle case can be regarded as corresponding to a Clar's sextet represented by a ring in a hexagon. Therefore, for 9-AGNR-z, there is effectively only one Wannier function being equally cut by the unit-cell boundary. A more rigorous proof can be obtained by evaluating Equations (4.5) to (4.8), or Equation (4.10).

Having found the relationship between $\mathbb{Z}$ index, Wannier functions, and Clar's sextets, it becomes natural to predict the $\mathbb{Z}$ index directly from the Clar's sextet drawing. For a general GNR, we need to find a strategy to draw the maximum number of Clar's sextets. Speaking in the language of chemistry, we need to find the resonance structure with the maximum number of Clar's sextets, or, in other words, the Clar's formula of the structure. In Figure 4.18, we depicted the structural

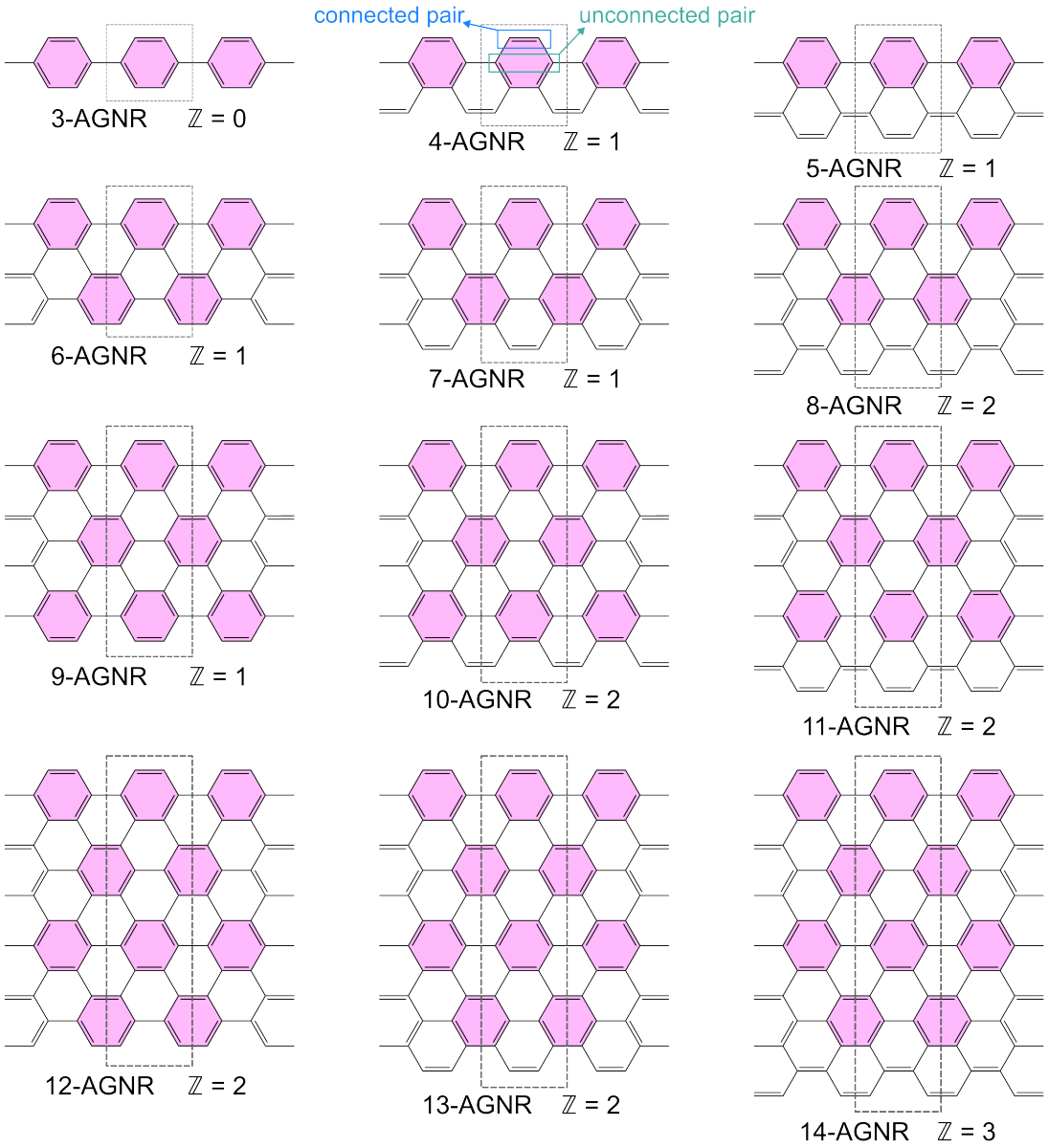


Figure 4.18: ℤ index and Clar's sextet of AGNRs. The structural models of AGNRs with width N_a = 3 – 14 are plotted with the maximum number of Clar's sextets. The ℤ indices were calculated from the tight-binding model and confirmed by DFT, except for 5,8,11,14-AGNR, for which ℤ indices can only be determined from DFT. In all cases the ℤ index matches the number of double bonds cut by the unit-cell (dashed boxes) boundary. The carbon atoms pairs inside the blue and green boxes marked in the 7-AGNR are called a "connected atoms pair"and a "unconnected atoms pair", respectively.

models of AGNRs with widths ranging from $N_a = 3$ to $N_a = 14$, each of them in the configuration that yields the maximum number of Clar's sextets. The unit cells are defined by the dashed boxes. By counting the number of double bonds cut by the unit-cell boundary, we can obtain the $\mathbb{Z}$ indices for these ribbons. Notably, all of them are in line with the $\mathbb{Z}$ indices obtained from theoretical calculations. The $\mathbb{Z}$ indices are shown below each structure in Figure 4.18. They were all calculated within the tight-binding formalism, except for 5,8,11,14-AGNR. The tight-binding model predicts a zero band gap for AGNRs with widths of $N_a = 3p + 2$, where p is a positive integer, leading to not well-defined $\mathbb{Z}$ indices. Therefore, for such AGNRs, the $\mathbb{Z}$ index can only be calculated from DFT plus Wannierisation. In fact, for the AGNRs with widths of $N_a = 3p + 2$, there is also an ambiguity about drawing double bonds in the configuration with the maximum number of Clar's sextets. In the following, we will resolve this ambiguity using 8-AGNR as an example.

In Figure 4.19a, we drew two representations of 8-AGNRs, both having the maximum number (two per unit cell) of Clar's sextets, but having different numbers of double bonds cut by the unit-cell boundary. The first configuration has one double bond cut by the unit-cell boundary, thus predicting $\mathbb{Z} = 1$, whereas the second configuration predicts $\mathbb{Z} = 2$. Therefore, we conducted a DFT calculation and then Wannierised the occupied p_z-bands. One one hand, we can obtain a strictly orthonormal Wannier basis that can be used for tight-binding calculations. Using the tight-binding Hamiltonian in the Wannier basis, we can then compute the $\mathbb{Z}$ index to be two from numerical integration. On the other hand, we obtain eight Wannier functions from the Wannierisation, which are presented in the bottom-right corner of Figure 4.19a. By examining this graph, we can identify two Wannier functions that are cut by the unit-cell boundary, which also predicts $\mathbb{Z} = 2$. We can then compare the band structures (Figure 4.19b) calculated from the tight-binding model and DFT. The tight-binding model assumes all the C–C bonds to be equivalent, leading to a zero band gap. In real structures, however, the C–C

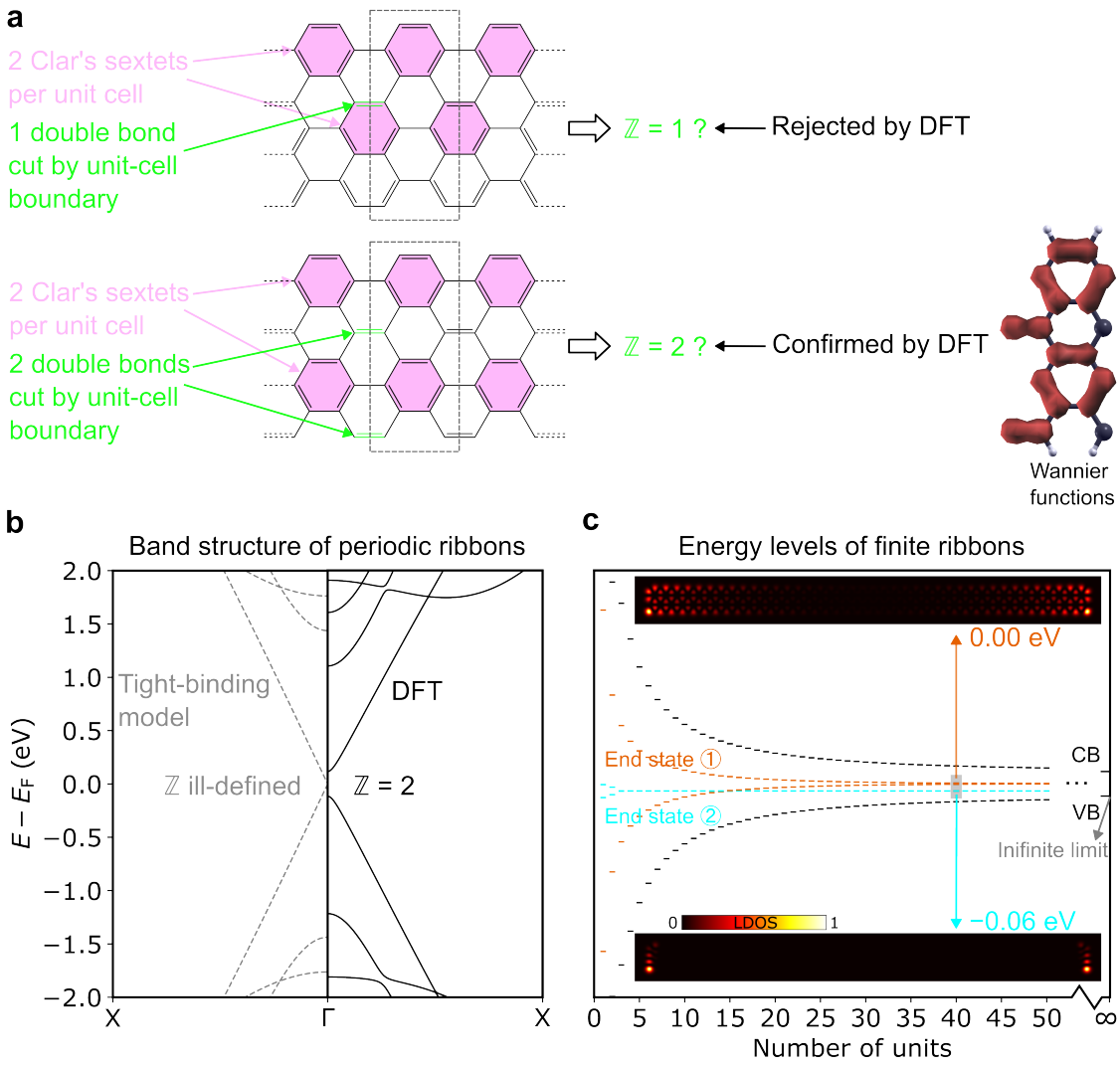


Figure 4.19: Ambiguity of topological phases in 8-AGNRs. (a) Two representations of 8-AGNRs, both having maximal (two per unit cell) numbers of Clar's sextets (pink), while having different numbers of double bonds cut by the unit-cell boundary (green). The two representations lead to different predictions of the ℤ index. DFT calculations confirmed that ℤ equals to 2 rather than 1. The Wannier functions (with isovalue of 0.26) match with the double bonds in the second representation. (b) Band structure of 8-AGNR calculated with the tight-binding model (left, grey) and DFT (right, black). The ℤ index can only be evaluated for DFT-calculated bands. (c) Energy levels of finite 8-AGNRs as a function of the number of units. The insets are the LDOS maps of the two end states for a 40-unit 8-AGNR. These two end states only emerge in finite 8-AGNRs. The LDOS maps were calculated at 3 Å above the GNR planes and integrated in a 0.02 eV energy window.

bonds at the edges are shorter than those in the bulk. This minor change opens a band gap in a 8-AGNR. Furthermore, in Figure 4.19c, we show the energy levels of finite 8-AGNRs as a function of the number of repeating units. While two energy levels (black lines) gradually converge to the infinite limit, i.e. the CB and VB, two pairs of in-gap states (brown and cyan lines) between them gradually converge to approximately zero energy. In finite ribbons, we found these in-gap states around zero energy, whereas we could not find any in-gap states in infinite ribbons. The presence of the two in-gap states validates the prediction of $\mathbb{Z} = 2$. Furthermore, we calculated the LDOS maps of the two in-gap states for a 40-unit 8-AGNR, shown as insets in Figure 4.19c. While both of the two in-gap states are localised at the two ends, the end state ① is less localised than the end state ②. Thus, the energy levels of the former converge slower than those of the latter.

Thus far, we have resolved the ambiguity of Clar's sextets and $\mathbb{Z}$ indices of AGNRs with width of $N_a = 3p + 2$. For this class of AGNRs, the $3p$ rows of carbon atoms will form p rows of Clar's sextets. The remaining two rows of carbon atoms are connected by horizontal π-bonds (like the second structure in Figure 4.19a), rather than slanted π-bonds (first structure in Figure 4.19a). By drawing Clar's sextets and double bonds following this rule, we predict the $\mathbb{Z}$ indices of 5,8,11,14-AGNR (Figure 4.18) and they are in line with the theoretical calculation results. In fact, there are already experimental characterisations that support our predictions. It was shown by STM measurements that 5-AGNRs have only one localised end state, which agrees with $\mathbb{Z} = 1$ [37, 108, 158].

Now we revisit Figure 4.18 and focus on the way to draw the maximum number of Clar's sextets in an AGNR. When N_a is increased by one or two, there will be one or two more rows of double bonds added, respectively. When N_a is increased by three, however, the three additional rows of carbon atoms form a row of Clar's sextets. And interestingly, in each AGNR the Clar's sextets are arranged in a hexagonal pattern. As depicted in Figure 4.20, imagine each Clar's sextet as a node, then these

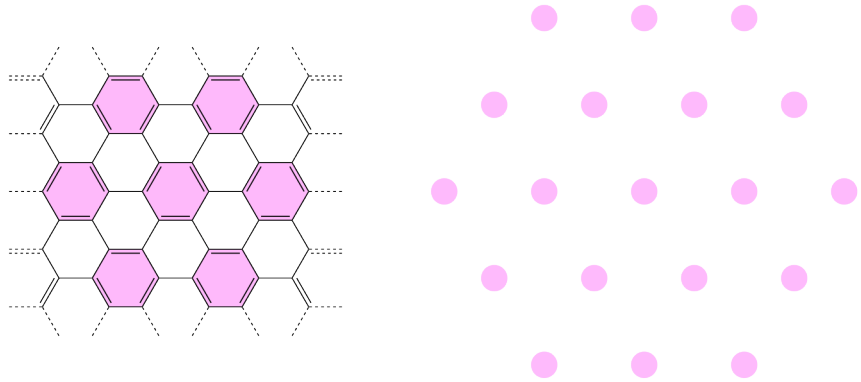


Figure 4.20: Pattern of the most densely packed Clar's sextets. The structural model in the left is drawn with the most densely packed Clar's sextets. By replacing each Clar's sextet with a dot, the arrangement of all Clar's sextets form a hexagonal pattern (right).

nodes form a hexagonal pattern. Each node touches six neighboring nodes, creating a densely packed structure. This arrangement is the most efficient packing of spheres with coplanar centres in a plane, and apparently, it is also the most densely packed configuration of Clar's sextets in a honeycomb lattice. This kind of pattern is also corroborated by DFT-calculation results reported by Wassmann et al. [326].

Next we define a "connected atoms pair" and a "unconnected atoms pair" in a unit cell, as shown in the blue and green boxes in Figure 4.18, respectively. The number of rows of "unconnected atoms pair" are denoted as N_{unco}, following the naming convention in Ref. [55]. Then we can deduce the number of double bonds cut by a unit-cell boundary, i.e. the $\mathbb{Z}$ index, from N_{a} and N_{unco}. For three types of termination, i.e. the zigzag-, zigzag'-, beard-type termination as illustrated in Figure 4.12, we can work out the following relationships:

$$\text{For zigzag termination:} \qquad \mathbb{Z} = \lfloor \frac{N_{\text{a}}+2}{6} \rfloor = N_{\text{unco}} - \lfloor \frac{N_{\text{a}}}{3} \rfloor \tag{4.11}$$

$$\text{For zigzag' termination:} \qquad \mathbb{Z} = \lfloor \frac{N_{\text{a}}+5}{6} \rfloor = N_{\text{unco}} - \lfloor \frac{N_{\text{a}}}{3} \rfloor \tag{4.12}$$

$$\text{For beard termination:} \qquad \mathbb{Z} = \lfloor \frac{N_{\text{a}}}{3} \rfloor = N_{\text{unco}} - \lfloor \frac{N_{\text{a}}}{3} \rfloor. \tag{4.13}$$

The relation $\mathbb{Z} = N_{\text{unco}} - \lfloor \frac{N_{\text{a}}}{3} \rfloor$ for AGNRs has been derived by Jiang et al. by analytically solving the Equation (4.3) in the tight-binding formalism [55]. Re-

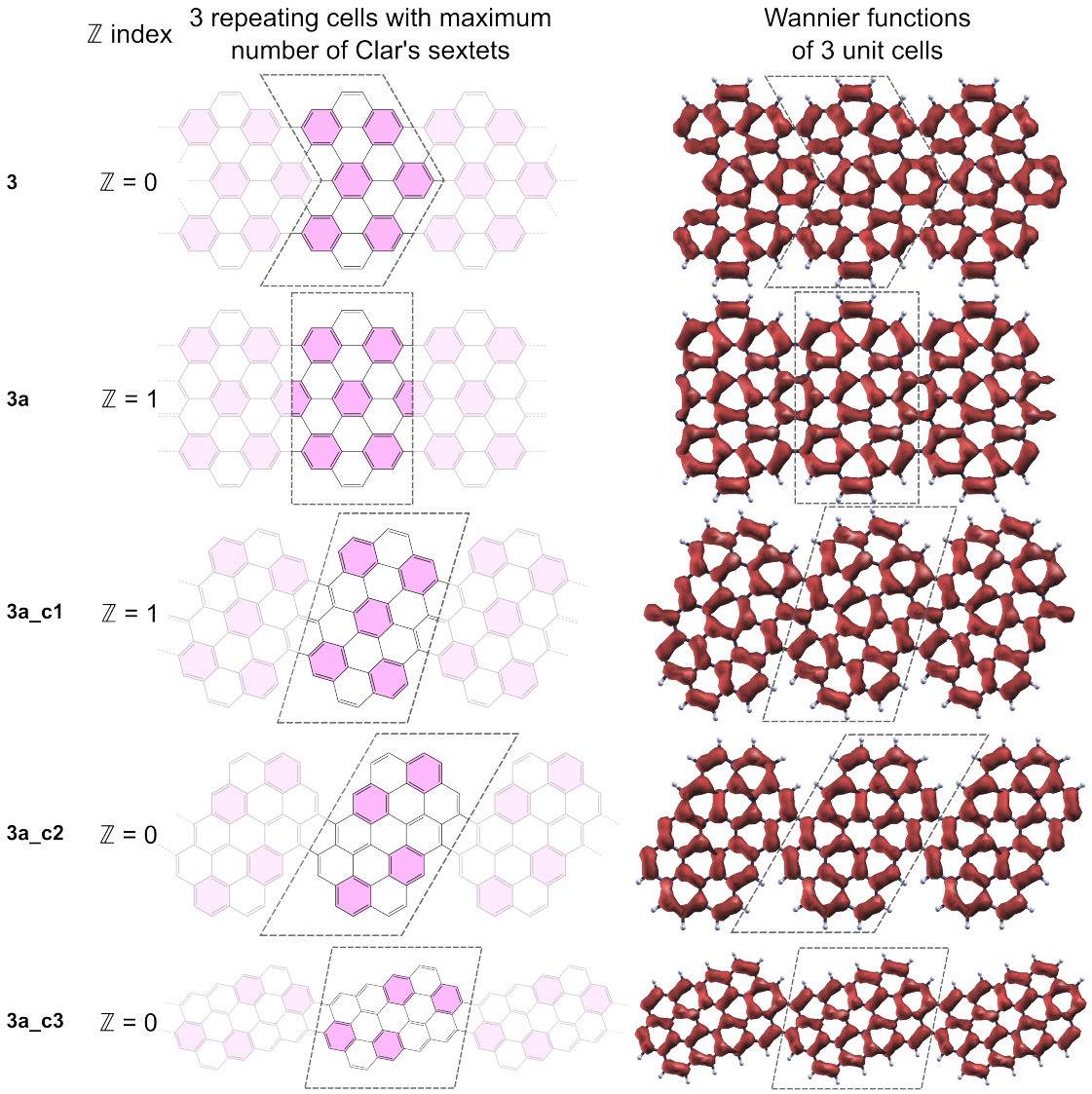


Figure 4.21: Relationship between ℤ indices, Wannier functions, and Clar's sextets of GNR **3** and its derivatives. GNR **3** and GNR **3a** have the same backbone structure but differ by their unit cell definition. **3a**, **3a_c1**, **3a_c2**, **3a_c3** have the same unit cells shape but different connections between neighbouring cells. For each structure, the ℤ index was calculated from the tight-binding model. Three repeating cells are drawn with the maximum number of Clar's sextets. The Wannier functions are calculated from DFT followed by Wannierisation. Isovalues of all the Wannier functions were set to 0.25. The double bonds in structural models in second column all match the Wannier functions in last column. The number of double bonds cut by a unit cell (dashed box) boundary agrees with the ℤ index.

markably, we have obtained the same formula from simply drawing Clar's sextets and counting double bonds.

Up to now, we have only discussed AGNRs. In order to verify the relationship between $\mathbb{Z}$ indices, Wannier functions, and Clar's sextets in other types of GNRs, we carried out calculations for GNR **3** and its derivatives. As shown in Figure 4.21, we calculated the $\mathbb{Z}$ indices from the tight-binding model for the **3a**, **3a_c1**, **3a_c2**, **3a_c3**. In the second column we plotted the structural models with the maximum number of Clar's sextets. The unit cells are highlighted as dashed boxes. The double bonds in the structural model of each case all match the positions of Wannier functions (last column in Figure 4.21) calculated from DFT followed by Wannierisation. And in each case the number of double bonds cut by a unit-cell boundary is also equal to the $\mathbb{Z}$ index. Hence, the relationship between $\mathbb{Z}$ indices, Wannier functions, and Clar's sextets is also supported by these examples.

To conclude, we have uncovered the correlation between the $\mathbb{Z}$ topology and the Clar's sextet rule. The former is a concept from condensed-matter physics and is calculated from the Hamiltonian of a GNR, whereas the latter is an empirical rule used in organic chemistry to determine the most stable form of a polycyclic aromatic hydrocarbon molecule. On the one hand, our discovery links seemingly disparate concepts from two fields, providing new insights into both the topology and the Clar's sextet rule. On the other hand, in light of the fact that the bottom-up chemical approach has recently become a mainstream method for synthesising atomically precise GNRs, our findings will offer valuable guidance for chemists aiming to design topologically interesting GNRs.

4.4 Topology in porphyrin nanoribbons

In this section, we will extend the exploration of topological phases from GNRs to other similar 1D structures. Porphyrin, an essential component of hemoglobin,

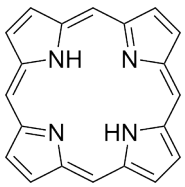


Figure 4.22: Structure of porphyrin.

is composed of four pyrrole units that are linked by four methine bridges. The structure of porphyrin is shown in Figure 4.22. The porphyrin molecule has a square planar conformation, and contains 18 delocalised π-electrons. It is an aromatic molecule based on the Hückel's rule. It has attracted vast interests from researchers because of its versatility. On the one hand, a porphyrin can host a large range of metals in its centre [327]. On the other hand, it can be used as a building block to synthesise larger molecules, such as porphyrin-based π-extended molecules [328, 329], nano-rings [330–332], chains [333, 334], covalent organic frameworks (COFs) [335], and hybrid structures with GNR segments [160, 259, 336, 337]. Among them, one particularly interesting one is the one-dimensional chain formed by triply fusing porphyrin monomers, because such a chain resembles a GNR [338, 339]. The band structures of such fused-porphyrin nanoribbons have been calculated before [340], however, the topological phases in such structures still remained unexplored. Therefore, in this section we will examine the topological phases in fused-porphyrin nanoribbons using same computational approach as we used for GNRs.

We used Zn-porphyrin as the basic component for a fused nanoribbon. The structural model is illustrated on the left of Figure 4.23, where the unit cell is highlighted by a dashed box. We calculated the fat bands and projected density of states (PDOS) for elements C, N, and Zn. The fat bands show the contribution of each type of orbital to each point in the band structure, and similarly, the PDOS traces also show the contribution of each type of orbital but make an average over the Brillouin zone. We omitted the orbitals that have insignificant contributions. In order to calculate topological phases, first we need a set of a p_z-like Wannier

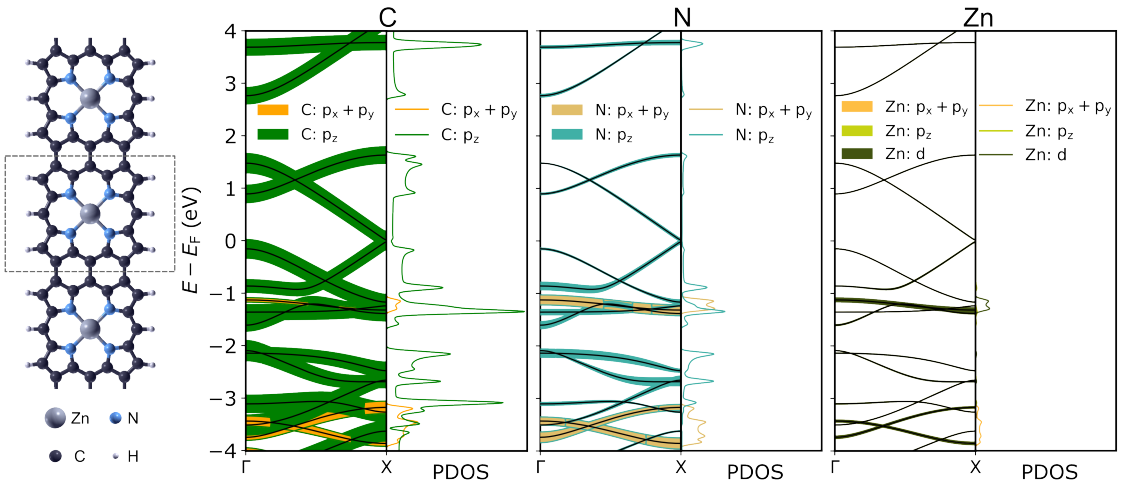


Figure 4.23: Fat bands and projected density of states of a fused Zn-porphyrin nanoribbon. The structural model is shown on the left, where the unit cell is highlighted by a dashed box. The three panels on the right show the DFT-calculated fat bands (left) and PDOS (right) for elements C, N, and Zn, respectively. A 0.03 eV Gaussian broadening was used for all PDOS traces.

basis. We extract the p_z-band manifold – the bands contributed by p_z-orbitals of C, N, and Zn – through Wannierisation. The obtained Wannier basis can be used for tight-binding calculations. Not only can the topological invariants be evaluated from the tight-binding model in Wannier basis, but also the calculation of truncated finite Zn-porphyrin nanoribbons become much faster.

Figure 4.24a presents the Wannier-interpolated bands. Based on DFT-calculated band structure, the ribbon is almost metallic, so that the topological index is ill-defined at the Fermi level. As an alternative, we evaluated the $\mathbb{Z}_2$ indices at two gaps that appear at around 2.0 eV and −1.8 eV, which have $\mathbb{Z}_2 = 1$ and $\mathbb{Z}_2 = 0$, respectively. As we mentioned in Section 4.2.3, the $\mathbb{Z}$ index can only be evaluated at the Fermi level for systems with chiral symmetry. Therefore, we cannot determine the exact number of topological end states from $\mathbb{Z}$, but only from calculating LDOS of finite Zn-porphyrin ribbons. We constructed the tight-binding Hamiltonian of an octamer of Zn-porphyrins using the Wannier basis, and then calculated the LDOS at the end and the bulk. As presented in Figure 4.24b, there are one end state and two end states emerging at the energy gap around 2.0 eV and −1.8 eV, respectively. The

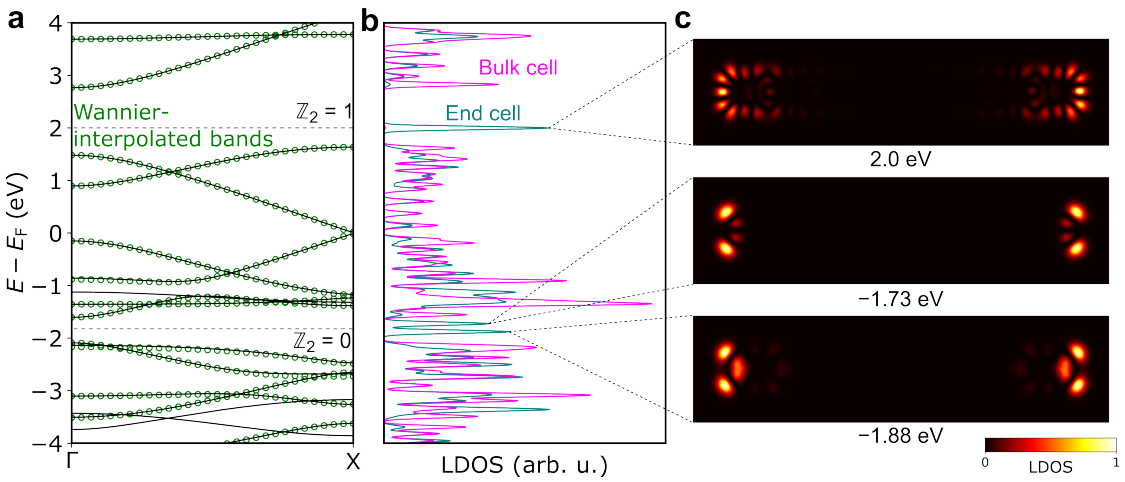


Figure 4.24: Three end states of a fused Zn-porphyrin nanoribbon. (a) DFT-calculated (black solid lines) and Wannier-interpolated (green empty circles) band structures. The $\mathbb{Z}_2$ invariants are evaluated for the two energy gaps. (b) LDOSs of the end cell (teal) and bulk cell (magenta) of an octamer, calculated using the Wannier basis. A 0.03 eV Gaussian broadening was used. There are three peaks that are solely caused by end cells, located at 2.0 eV, −1.73 eV, and −1.88 eV, respectively. (c) LDOS maps of the three localised end states, corresponding to the three marked peaks in (b), respectively. The LDOS maps were calculated at 3 Å above the porphyrin plane and integrated over 0.1 eV energy window.

LDOS maps for these three end states are depicted in Figure 4.24c. The number of end states in the two energy gaps agree with the parity of $\mathbb{Z}_2$ indices.

To further validate the results, we calculated the energy levels and wavefunctions of several finite Zn-porphyrin nanoribbons (monomer, dimer, trimer, tetramer, hexamer, and octamer) using DFT. Their energy levels are depicted in Figure 4.25a. The in-gap states are shown in magenta, and they do not have counterparts in the DOS of an infinite ribbon (Figure 4.25b). Strictly speaking, end states (or in-gap states) cannot be defined in a monomer as it is too short. Nevertheless, we highlight these two energy levels in magenta for the monomer in Figure 4.25a, since they are the states that will gradually converge to the end states as the ribbon becomes longer. Note that each end state actually consists of a pair of near-degenerate energy levels, which are similar to a pair of bonding and anti-bonding orbitals. When a ribbon is sufficiently long, the electrons at the two ends have almost zero coupling with each other, and thus the two levels become degenerate. On the contrary, for

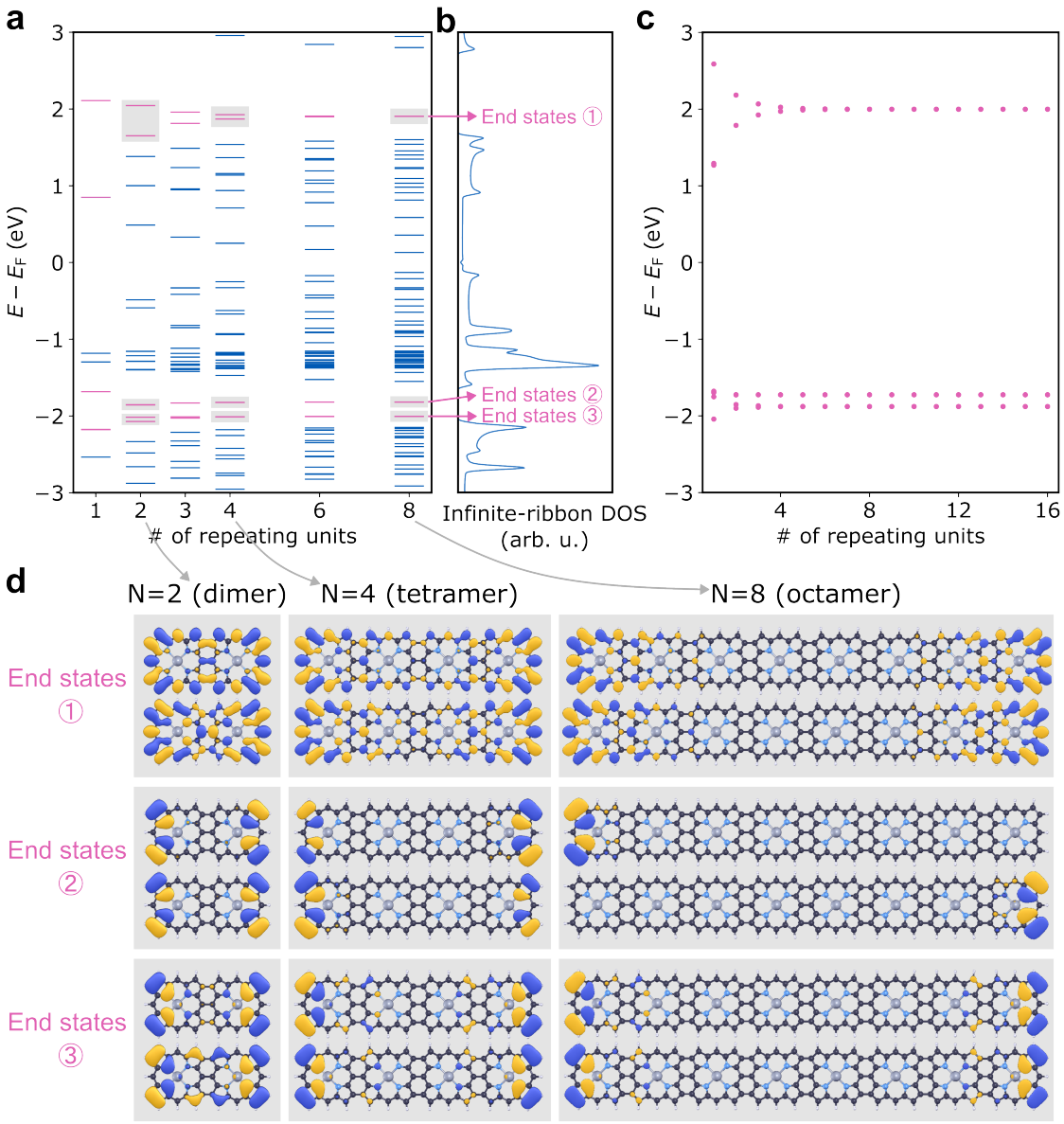


Figure 4.25: Energy levels and end states of finite Zn-porphyrin nanoribbons. (a) Energy levels of finite Zn-porphyrin nanoribbons with 1, 2, 3, 4, 6, and 8 units, calculated from DFT. (b) DOS of an infinite ribbon calculated with periodic boundary conditions. Three pairs of end states (magenta) emerge in finite ribbons and have no counterparts in the infinite ribbon. (c) Energy levels of the three pairs of end states calculated with the tight-binding model using Wannier basis. (d) Wavefunctions of the three pairs of end states of dimer, tetramer, and octamer, obtained from DFT calculation. The isolevel was set to 0.01 for all wavefunctions.

shorter ribbons, the two ends couple to each other, causing an energy splitting of the two levels. To better examine the convergence of the end states as ribbon increases in width, we calculated the energy levels of the three pairs of end states as a function of the number of repeating units with the tight-binding model using a Wannier basis (Figure 4.25c). They are in line with the DFT-calculated results except for the monomer. The end states at 2.0 eV converge at about five repeating units, while the two pairs of end states around −1.8 eV already converge at about two repeating units.

It is intriguing to see that topological phases also exist in fused porphyrin nanoribbons, although the Zn-porphyrin nanoribbon does not have chiral symmetry, and the $\mathbb{Z}$ indices cannot be evaluated. We can provide a possible explanation to the emergence of end states based on the SSH model, which possesses chiral symmetry. The porphyrin molecule is inversion-symmetric. The energy states around the gap at 2.0 eV have approximately mirror symmetry, occupying the left and right half of the porphyrin unit symmetrically, and therefore can be modelled as two charge centres A and B. When porphyrin units are fused to a ribbon, the B–A pairs across a unit-cell boundary couples stronger than a A–B pair within a unit cell. Hence, the electronic states around 2.0 eV can be modelled by a topologically nontrivial SSH chain.

Next we will provide a qualitative explanation to the emergence of two end states around −1.8 eV using a double-SSH model. The electronic states around −1.8 eV have approximately four-fold symmetry, with four charge centres locating at the four pyrrole units. When the porphyrin units are fused together, it can be regarded as two copies of topologically nontrivial SSH chain parallel to each other. The structural model of a double-SSH chain is depicted in Figure 4.26a. Each SSH chain has two sublattices: A and B. We used the nearest-neighbour tight-binding model to describe the system. The hopping between neighbouring unit cells, within the unit cell, and between chains are described by the hopping integrals v, w, and t, which are set to −2 eV, −1 eV, and −0.2 eV, respectively. These parameters describe a system with two weakly-coupled topologically nontrivial SSH chains.

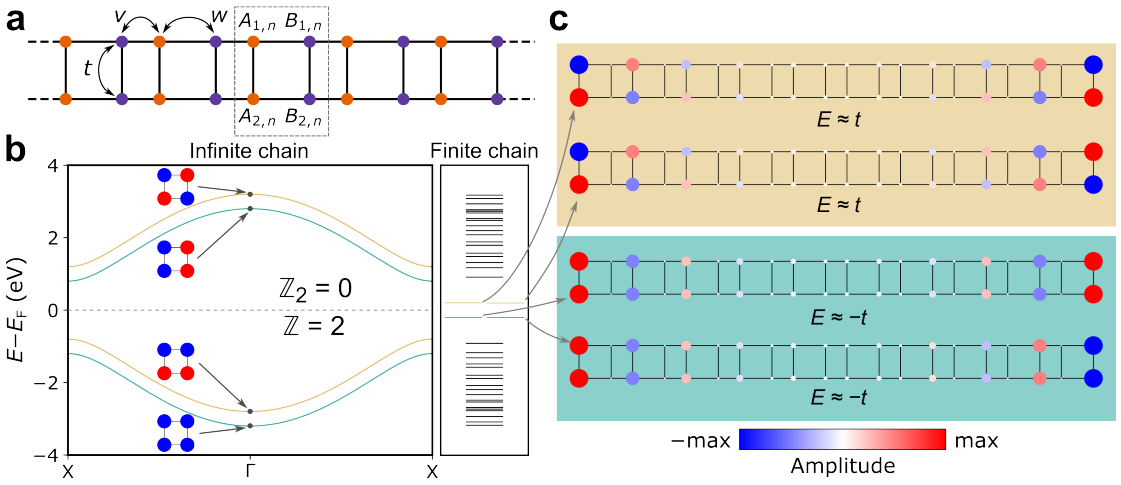


Figure 4.26: Double SSH-chain model. (a) Structural model of a double SSH-chain. Each SSH chain has two sublattices: A and B. The unit cell is defined by the dashed box. Nearest-neighbour hopping parameters for lattice sites within the same chain are denoted as v (for hopping between neighbouring unit cells) and w (for hopping within the unit cell). The interchain hopping parameter is denoted as t. (b) Band structure for an infinite chain and energy levels of a finite chain with ten units. The hopping parameters v, w, and t were set to -2 eV, -1 eV, and -0.2 eV, respectively. The wavefunctions of the four bands at the Γ point are drawn and indicated by arrows. The red and blue colours represent positive and negative amplitudes, respectively. The four bands are classified into two groups based on whether the wavefunctions have symmetric (turquoise) or antisymmetric (tan) coupling between the two SSH-chains. For the two occupied bands $\mathbb{Z}_2$ is 0 and $\mathbb{Z}$ is 2, and this result matches the emergence of two pairs of in-gap states in the ten-unit finite chain. (c) Wavefunctions of the two pairs of end states. The amplitudes were normalised in each case. All the results were calculated from the tight-binding model.

The band structure of this system is shown in Figure 4.26b. The wavefunctions for each band at the Γ point are drawn and indicated by arrows. The states of the two occupied bands are coupled symmetrically between A (left) and B (right) sublattices, while those of the two unoccupied bands are coupled antisymmetrically between A and B sublattices. The four bands can also be classified into two groups according to whether the wavefunctions of these bands display a symmetric or an antisymmetric coupling between the two chains. Based on this criterion, we colour the two band groups in turquoise and tan colour for symmetrical and antisymmetrical coupling between the two chains, respectively. For example, as shown in Figure 4.26b, for the wavefunctions of the two turquoise bands at the Γ point, the wavefunction amplitudes of the upper chain (top) and the lower chain (bottom) have the same

sign (both blue or both red). On the contrary, for the wavefunctions of the two tan bands at the Γ point, the wavefunction amplitudes of the upper chain and the lower chain have opposite signs (one is red while the other one is blue).

The $\mathbb{Z}_2$ index and the $\mathbb{Z}$ index for the two occupied bands were found to be 0 and 2, respectively. This result implies that there should be two in-gap end states around the Fermi level. The existence of in-gap states is validated by plotting the energy levels of a ten-unit finite chain, shown next to the band structure in Figure 4.26b. There are two pairs of degenerate states showing up at $E \approx \pm t$, respectively. We presented the wavefunctions of these four energy levels in Figure 4.26c. The two states shown in the tan box are related to the two energy bands shown in tan colour (Figure 4.26b). For these two states, the two chains are antisymmetrically coupled. In contrast to that, the two states shown in the turquoise box are related to the two energy bands shown in turquoise colour (Figure 4.26b). For these two states, the two chains are symmetrically coupled.

Now we can compare these four wavefunctions in Figure 4.26c with the wavefunctions of end states ② and end states ③ in Figure 4.25d. The fused porphyrin nanoribbon contains two chains of pyrroles. Similar to the two localised end states shown in the tan box in Figure 4.26c, the two chains of pyrroles in the two wavefunctions of end states ② are antisymmetrically coupled. On the contrary, similar to the two localised end states shown in the turquoise box in Figure 4.26c, the two chains of pyrroles in the two wavefunctions of end states ③ are symmetrically coupled. Moreover, there is also a small energy splitting between ② and ③ in Figure 4.25a, which is similar to the case of double-SSH model, where there is an energy splitting of $2t$ between the two end states (Figure 4.26b). Although the end states ② and ③ of the Zn-porphyrin nanoribbon that we discussed before do not appear around the Fermi level, our double-SSH model is able to give a qualitative explanation to the emergence of topological states in fused Zn-porphyrin nanoribbons. Lastly, we point out that the topological states in fused porphyrin nanoribbons

result purely from the coupling between the carbon and nitrogen atoms. As we can see in Figure 4.25d, the wavefunctions of the topological end states are mainly distributed over carbon and nitrogen atoms, while having minimal contribution from the Zn atoms. The same topological states also appear in fused porphyrin nanoribbons with other metal centres, or those ribbons without metal centres.

4.5 Dissipationless transport channels in beard–zigzag GNRs

In the previous sections, we focused on the topological end states in GNRs. As discussed in Section 2.1.2, the edge states supported by certain GNRs can also be understood in the theoretical framework of topology [87, 89]. When a GNR becomes wider, the lateral wavenumber becomes a good quantum number. The Hamiltonian can then be parameterised by $k_\parallel$ and $k_\perp$, the wavenumber parallel and perpendicular to the edge, respectively. For each $k_\parallel$, the Zak phase and the winding number can be calculated for the Hamiltonian $H(k_\perp; k_\parallel \text{ fixed})$. The result will determine whether the system has zero-energy edge states at this $k_\parallel$ wavevector. The boundary states in this case are edge states, rather than end states, since the Zak phase is obtained by integration over the transverse wavevector $k_\perp$ rather than over the longitudinal wavevector $k_\parallel$. By calculating the Zak phase for all $k_\parallel$, we can determine the range of $k_\parallel$ where zero-energy flat bands exist, which correspond to edge states. In Section 2.1.2.2, we furthermore discussed that edge states exist in zigzag, beard, chiral, and also in other types of edges that have zigzag segments. Beard–zigzag GNRs, which have one zigzag and one beard edge, also support a zero-energy flat band, which spans in the whole Brillouin zone. Many of the intriguing properties and promising applications of edge states have already been reviewed in Section 2.1.2. In this section, we will propose a strategy to realise dissipationless transport channels in beard–zigzag GNRs.

Dissipationless transport of charge carriers is key to reduce heat dissipation in electronic chips. The search for energy-efficient materials and architectures is urged by needs of modern electronics. The two well-known strategies to realise dissipationless transport are either through superconductivity or the chiral transport channels in quantum Hall effect. Their real applications are limited, however, by the requirements of extremely low temperatures or strong magnetic fields [167, 341]. Topological materials have been widely explored to achieve dissipationless transport. However, the zero-energy flat bands in beard–zigzag GNRs cannot be directly used for charge transport because of its null electron group velocity. Researchers have extensively explored approaches to modify the band structure of GNRs in order to manipulate the electronic properties. One important way is to apply a transverse electric field. For instance, transverse electric fields can be utilised to achieve half-metallicity [9], tune topological phases [215], or induce Dirac fermions [342] in GNRs. Inspired by these studies, we also consider to apply transverse electric fields to the beard–zigzag GNRs in theoretical models, and we demonstrate that chiral dissipationless transport channels will appear in such systems.

In Figure 4.27, we show the calculation results of a beard–zigzag GNR with width N_r = 51, labelled as 51-BZGNR. We calculated the band structure and wavefunctions of the ribbon with different magnitudes of transverse electric fields using both the tight-binding model and DFT. The structure used for tight-binding calculations is shown in Figure 4.27a. Zoomed views of the zigzag and beard edges are presented in the insets. The unit cell of 51-BZGNR is highlighted in cyan colour. There is a sublattice imbalance in the unit cell. The A and B sublattices have 26 and 25 carbon atoms, respectively. Structures with sublattice imbalance possess non-zero chiral charges and always host flat bands at zero energy [325]. Using the tight-binding model, we calculated the band structures with transverse electric fields of 0, 0.015, and 0.04 V/Å. For each case we also calculated the wavefunctions at three k points near the K point. At zero electric field (Figure 4.27b), there is a

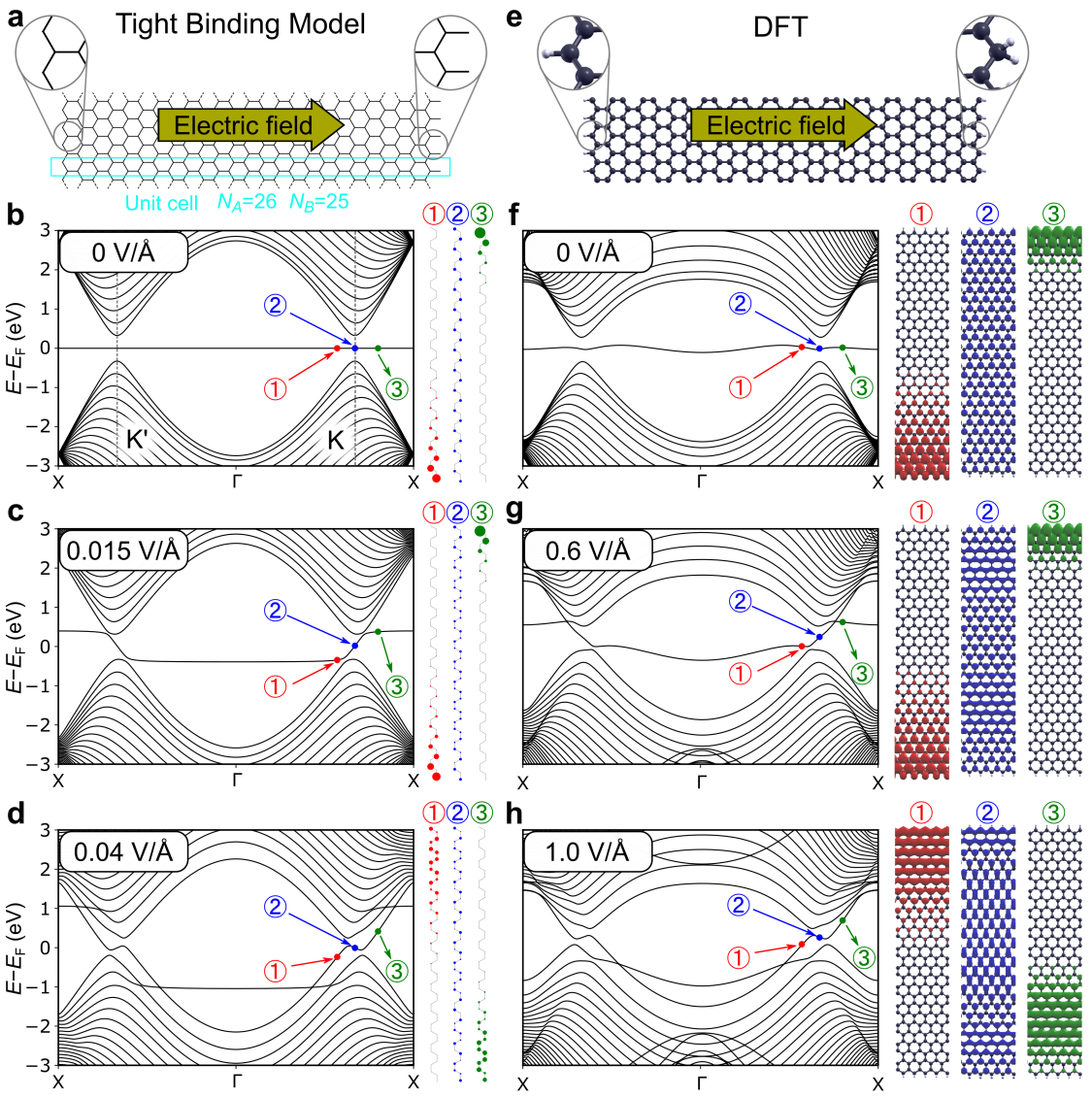


Figure 4.27: Chiral dissipationless modes in beard–zigzag GNRs with transverse electric fields. The left and right hand side show the results calculated from (a–d) the tight-binding model and (e–h) DFT, respectively. The difference in the electric fields used in the tight-binding model and DFT is explained in the main text. (a,e) Structure of a beard–zigzag GNR. Zoomed views of the zigzag and beard edges are shown in circles. The unit cell is highlighted in a cyan box. The numbers of atoms in the A sublattice (N_A) and the B sublattice (N_B) are 26 and 25, respectively. (b,f) Band structures without electric field, exhibiting a flat band at zero energy. The wavefunctions at three k points (denoted by red, blue, and green colours, respectively) around the K point are displayed aside the band structure. (c,g) Band structures with a small transverse electric field (0.015 V/Å in the tight-binding model and 0.6 V/Å in DFT). The flat band is turned into a dispersive band, which has opposite group velocities at K and K′ points. (d,h) Band structures with a larger transverse electric field (0.04 V/Å in the tight-binding model and 1.0 V/Å in DFT). The linear dispersion at Dirac points changes to a cubic dispersion. In all of the wavefunctions obtained from the tight-binding model, the radius of the circle at each lattice site scales with the wavefunction amplitude, and the amplitude was normalised in each case. The wavefunctions obtained from DFT are shown in five unit cells, with isovalue set to 0.02 for all cases.

flat band at zero energy, denoted as ZEB. At 0.015 V/Å (Figure 4.27c), the ZEB at K and K′ points exhibits a linear dispersion. The slopes are equal in magnitude but have opposite signs at the K and K′ points. This means that the ZEB has opposite group velocities at the K and K′ points. Thus they can function as chiral transport channels. The K and K′ points are not only far enough from each other, but also far from the time-reversal invariant points (the Γ and X points), so that charge carriers with opposite transport directions will not be easily mixed. In other words, elastic backscattering of charge carriers will be suppressed in the absence of short range scatterers, such as armchair-edge segment, that can cause intervalley mixing. This suppression is, in a way, similar to that in the quantum valley Hall regime and in topological kink states [48, 99, 343]. Contrary to the quantum valley Hall regime [48, 99], the charge transport here does not necessarily stick to the edges, but spans over the whole ribbon, as shown in the wavefunction depicted in blue in Figure 4.27c. Likewise, this system has no domain walls as required for topological kink states [343]. In addition, the charge current is valley-polarised so that the ribbon can work as a perfect valley filter [98]. Upon further increasing the electric field to 0.04 V/Å (Figure 4.27d), the linear dispersion changes to cubic-like dispersion, which is a very unusual behaviour that rarely appears in materials.

All of our calculations carried out with the tight-binding model are validated using DFT, as shown in Figure 4.27e–h. The structure used for DFT calculations is slightly different from that for the tight-binding calculations. This is because if such ribbon is to be synthesised, the beard edge will most likely become a zigzag edge decorated with methyl groups that are sp^3-hybridised, and the C–C single bonds formed at the beard edge do not contribute to the π-electron band. Therefore, the beard–zigzag model does not accurately describe such a ribbon with methyl groups. The beard–zigzag structure, however, can be realised by modifying a ZGNR with asymmetric hydrogenation at two edges. In this case, one row of carbon atoms can be excluded from the π-network by double hydrogenation of one side

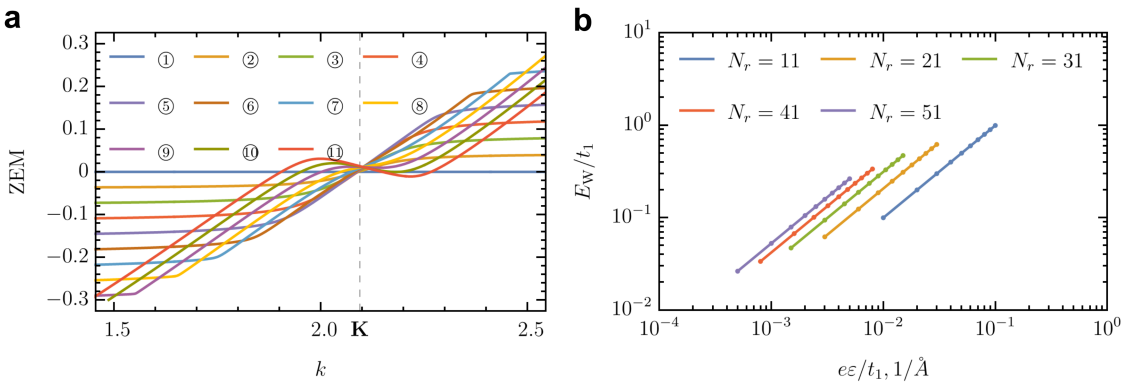


Figure 4.28: Dependence of the ZEB on electric field and ribbon width. (a) Evolution of the ZEB of a 51-BZGNR in transverse electric fields from $e\varepsilon/t_1$=0.0 to 0.015 Å^{-1} in steps of 0.0015 Å^{-1}, marked with ①–⑪, respectively. (b) The bandwidth of the ZEB (E_w/t_1) as a function of the transverse electric field $e\varepsilon/t_1$ for HBGNR with widths N_r=11,21,31,41,51. The results were calculated by Dr. Vasil Saroka in a collaboration.

of the ribbon, while a single hydrogenation is used on the other side. We used a ZGNR with width N_r = 52 and a double hydrogenation at one zigzag edge, as shown in Figure 4.27e. The calculations were implemented in SIESTA. A static transverse electric field was simulated by adding a sawtooth-like potential along the transverse direction of the ribbon. Sufficient vacuum distance (at least 20 Å) was added along the transverse direction to prevent interactions between replicas of the ribbon. All the important features that are obtained by the tight-binding calculations, such as a linear dispersion or cubic dispersion at Dirac points, are almost perfectly reproduced by DFT. The only discrepancy is that the critical electric field to achieve gapless modes with linear dispersion around Dirac points is increased by one order of magnitude in the DFT calculations compared with the tight-binding results, which can be attributed to the screening effect caused by electric polarisation of the metallic ribbon [344].

We also investigated how the ZEB depends on the electric field and on the ribbon width. Figure 4.28a presents the evolution of the ZEB of a 51-BZGNR as the in-plane transverse electric field $e\varepsilon/t_1$ increases from 0.0 to 0.015 Å^{-1} in steps of 0.0015 Å^{-1}. Here we use the symbol t_1 to denote the nearest-neighbour hopping parameter in the tight-binding model. The electric field ε is measured in

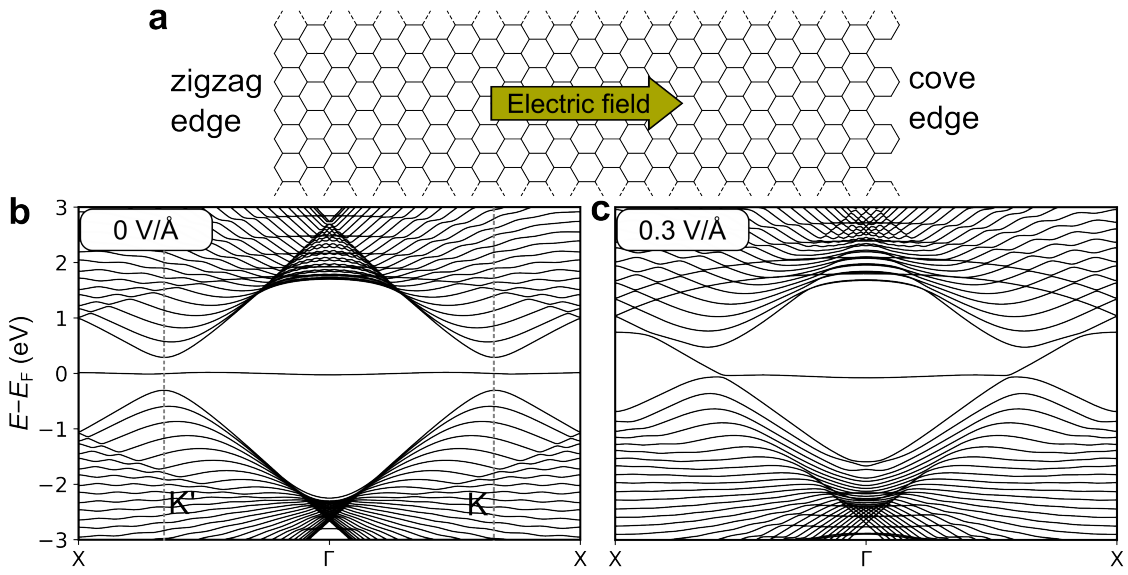


Figure 4.29: Chiral dissipationless modes in cove–zigzag GNRs with a transverse electric field. (a) Structure of the cove–zigzag GNR. Band structures with (b) zero and (c) 0.3 V/Å transverse electric field were calculated using DFT. The zero-energy flat band is turned into linearly dispersive band upon adding the electric field. Similar to Figure 4.27, this dispersive band has opposite group velocities at the K and K′ points.

units of t_1/e. As the electric field increases, the ZEB changes gradually from a flat band to a linear band, then to a cubic band around the K point. Figure 4.28b shows the bandwidth of the ZEB as a function of the transverse electric field for ribbons with widths $N_r = 11, 21, 31, 41, 51$. The bandwidth of the ZEB is a linear function of the electric field. For wider ribbons, a lower critical field is required to induce a linear dispersion of the ZEB.

We, furthermore, explored such chiral gapless transport channels in GNRs with other edge shapes. The essential requirement for the flat band is a sublattice imbalance in the unit cell. Moreover, in order to create chiral transport channels that are immune to backscattering in the absence of intervalley mixing, we need to find a GNR where the two Dirac valleys are separated, like in the beard–zigzag GNR. Based on these criteria, we designed a cove–zigzag GNR, as shown in Figure 4.29a. It also has a flat band at zero energy across the Brillouin zone (Figure 4.29b). When applying a transverse electric field (Figure 4.29c), this flat band becomes dispersive

and has opposite group velocities at the K and K′ points, which is similar to the results shown in Figure 4.27 for beard–zigzag GNRs.

To conclude, our calculations have proven a novel way to achieve chiral dissipationless transport channels in GNRs. Such channels can not only be realised in beard–zigzag GNRs, but also in other sublattice-imbalanced and valley-separated GNRs like cove–zigzag GNRs.

4.6 Summary and outlook

In this chapter, we discussed the topological phases of GNRs and other similar 1D structures. The ultimate goal was to find interesting topological states that can be applied in novel functional devices. In Section 4.2, we investigated three strategies to tune the topological phase of a GNR. Based on these strategies, we designed a large number of GNRs by modifying six initial structures. These results are to enrich the toolbox for chemists to design topologically nontrivial GNRs, especially those that can survive in more facile environments and make device fabrication more accessible. In Section 4.3, we uncovered the relationship between the $\mathbb{Z}$ topology in GNRs and the empirical Clar's sextet rule that has been widely known in the field of organic chemistry. The result has deepened the understanding of topological phases in GNRs, and also suggests a simple way to predict the topological phases by drawing Clar's sextets. There are still many open questions on this topic. For example, the correlation between $\mathbb{Z}$ index and the maximum number of Clar's sextets still lacks a rigorous mathematical proof. We can provide a possible perspective that might help to solve this problem. The problem of drawing double bonds in a GNR unit cell is mathematically equivalent to finding a set of non-adjacent edges in a undirected graph that describes the connections between atoms in the GNR: this graph is constructed by replacing every atom with a vertex and every bond with an edge. The $\mathbb{Z}$ index is calculated from a tight-binding Hamiltonian matrix, which is

proportional to the adjacency matrix of the aforementioned graph. Therefore, it is possible to view this problem from the perspective of graph theory. In addition, for GNRs with a large and irregular unit cell, it can be very difficult to find the configuration with the maximum number of Clar's sextets. This problem is also called the Clar's problem, which has been proven to be NP-hard computationally for general two-connected plane graphs [345]. There have been various algorithms designed to solve the Clar's problem [345–347]. Nonetheless, the GNRs currently synthesised from bottom-up approach usually have a relatively small unit cell, so it is still possible to find the maximum number of Clar's sextets for these GNRs by hand. Finally, we point out that, although the topological phase of a GNR can be accurately predicted by the tight-binding model or spin-restricted DFT, we have ignored the spin degree of freedom in this chapter. The zero-energy topological states are often spin-polarised when considering the spin degree of freedom. In the next chapter, we will reveal the spin-polarisation of the topological states by carrying out spin-unrestricted DFT calculations.

In Section 4.4, we extended the exploration of topological phases to other one-dimensional systems, such as fused-porphyrin nanoribbons. The synthesis of fused-porphyrin nanoribbons has been demonstrated long time ago [338, 339]. Now, with high-resolution STM, these topological states should readily be verified. The porphyrins can also be doped with heteroatoms to make the topological states shift towards the Fermi level [348], so that the states can be more easily characterised in experiments. Recently, there have also been studies on nanoribbons fused from various molecules with nonhexagonal rings [349–351]. It is still an open question whether topological phases exist in such nanoribbons.

In Section 4.5, we explored the dissipationless transport channels that can be realised in beard–zigzag GNRs in transverse electric fields. The origin of zero-energy flat bands in beard–zigzag GNRs can also be related to the concept of topology. We demonstrated that, by making use of transverse electric fields, we can realise

transport channels in beard–zigzag GNRs similar to the valley-polarised states in the quantum valley Hall effect [48, 99]. Other sublattice-imbalanced and valley-separated GNRs, such as some cove–zigzag GNRs, could also support such chiral transport channels. It is important to remark that the effect we proposed here may better be experimentally verified in wide rather than narrow GNRs, since strong quantum confinement and electron–electron interactions in narrow GNRs could result in magnetic instabilities, leading to spin-polarised states. Moreover, our work could also bring new perspectives on dissipationless transport channels in other fields than condensed matter, such as photonics [201, 352], microwave metamaterials [353], or nanomechanical metamaterials [354]. For example, Plotnik et al. have observed zero-energy modes in photonic honeycomb lattices with beard–zigzag edges [352]. An experimental verification of our proposal should also be feasible in photonic systems.

4.7 Project overview

The six initial structures **1**–**6** were designed by Prof. Xinliang Feng's group from TU Dresden. Dr. Ming-Yee Tsang and Dr. Xuelin Yao provided valuable discussions on the study of the relationship between $\mathbb{Z}$ topology and Clar's sextet rule. The studies on dissipationless transport channels in beard–zigzag GNRs were carried out in collaboration with Dr. Vasil Saroka. I carried out all the theoretical calculations presented in this chapter except for the results in Figure 4.28.

5

Spin States and Quantum Coherence in GNRs

Contents

5.1 Introduction 165
5.2 Spin states and topological phase 166
5.3 Spin states from functionalisation groups 177
5.3.1 Cyano functionalisation 178
5.3.2 Vanadyl-porphyrin functionalisation 187
5.4 Summary and outlook 194
5.5 Project overview 195

5.1 Introduction

In the previous chapter we explored the topological states in GNRs. The DFT calculations, however, were carried out using spin-unrestricted methods, as this simplification speeds up the computations without affecting the determination of topological phases. This chapter delves into the spin states that emerge in certain GNRs. These spin states in GNRs exhibit appealing quantum properties that could be harnessed for applications in quantum information technologies, spintronics, quantum sensing, optoelectronics and more, as we reviewed in Section 2.3. To date,

there have been experimental demonstrations of magnetic zigzag edge states [103, 104], spin chains [56, 57], single-spin manipulation [258, 355], and induced metallicity from coupled spin states [257, 356] based on various bottom-up synthesised GNRs. These GNRs, however, were synthesised and characterised in an ultra-high vacuum, which is impractical for device fabrication. In this chapter, we will concentrate on solution-processable GNRs.

Spin states in GNRs can either originate from unpaired electrons within the GNR itself, or from external functionalisation groups. First, this chapter will discuss the inherent spin-polarised states in finite GNRs that are related to the topological states from the last chapter. Two instances of this, the peri-tetracene molecule and a type of 8-GNR, have been successfully synthesised in the solution phase by Prof. Jishan Wu's group from NUS and Dr. Xuelin Yao, respectively. Second, we will investigate the spin-polarised states in two functionalised cove-edge GNRs. The first one is functionalised by cyano groups, and the ribbon is expected to be an antiferromagnetic spin chain. The second one is functionalised by vanadyl-porphyrin groups, which paves the way to combine various spin species in GNRs. By using EPR spectroscopy, we addressed several unexplored questions regarding functionalised GNRs: 1) the existence of defects in bottom-up synthesised GNRs in solution phase; 2) the potential enhancement of the quantum coherence time of spin states in GNRs solutions compared with GNRs powders; 3) the possibility of spin injection into the GNR backbone from vanadyl-porphyrin side groups; 4) the changes in the spin dynamics of these grafted vanadyl-porphyrins.

5.2 Spin states and topological phase

There are various ways to create spin-polarised states in GNRs, which were discussed in Section 2.3.3. We showed that a spin chain can be constructed from topological junction states. In the previous chapter, we primarily used the tight-binding model

and spin-restricted DFT to calculate the topological phases, where the spin degree of freedom was completely absent. In fact, the topological end states or junction states in GNRs are spin-polarised when considering the electron–electron Coulomb repulsion [159, 217–219]. For instance, taking a ribbon with $\mathbb{Z} = 1$ as an example, using a single-particle approximation in DFT, it has a gapped bulk band structure and a pair of in-gap states close to zero energy. These in-gap states are localised at the two ends. We define the wavefunctions of the localised states at the left end and the right end as ψ_{L} and ψ_{R}, respectively. The in-gap states are a pair of bonding (ψ_-) and antibonding (ψ_+) orbitals originating from the hybridisation of ψ_{L} and ψ_{R} [159]:

$$\psi_\pm = \frac{1}{\sqrt{2}} \left(\psi_{\mathrm{L}} \pm \psi_{\mathrm{R}} \right). \tag{5.1}$$

The orbitals ψ_- and ψ_+ represent the HOMO and LUMO for a finite ribbon, respectively. Each of these can accommodate two electrons. The energy splitting δ between the HOMO and LUMO is determined by the matrix element between ψ_{L} and ψ_{R} [159]:

$$\delta = 2\langle \psi_{\mathrm{L}} | H | \psi_{\mathrm{R}} \rangle. \tag{5.2}$$

For ribbons that are sufficiently long, δ will be negligible, meaning the two energy levels are near-degenerate at zero energy.

In real system, the ground states are governed not only by the hybridisation of orbitals, but also by the electrostatic Coulomb repulsion. The hybridisation between ψ_{L} and ψ_{R} tends to form a non-magnetic closed-shell[1] state. The energy reduction associated with the hybridisation of the orbitals is called the hybridisation energy. In contrast, Coulomb repulsion favours the formation of an open-shell[2] magnetic state with unpaired spins in singly occupied molecular orbitals (SOMOs) [253]. For topological states, the more localised they are, the stronger the Coulomb

[1] Closed-shell systems are those molecules where all electrons are paired up in the valence shell.

[2] Open-shell systems are those molecules where at least one electron is unpaired in the valence shell.

repulsion. When the Coulomb repulsion energy outweighs the hybridisation energy, the topological states transform into a pair of spin-split states, where the electrons are no longer paired [158, 159, 218].

In Section 4.2, we designed many new GNRs with topological end states. The spin degree of freedom, however, was ignored. This section will verify the spin polarisation of the topological states that we discussed in the previous chapter. Taking GNR **4a** as an example, its $\mathbb{Z}$ index equals 1 (see Figure 4.7), and thus it has one pair of localised end states. We performed calculations on finite oligomers with one to eight units of GNR **4a** using spin-unrestricted DFT. The termini and edges of these molecules are all passivated by hydrogen atoms. These calculations were implemented in SIESTA, with most parameters similar to those used in Section 4.2. For each molecule, we considered two initial spin configurations: atoms with odd and even indices having opposite spins (antiferromagnetic state, or AFM), or all atoms having the same spins (ferromagnetic, or FM). A vacuum length of at least 20 Å was added along both the transverse and the longitudinal direction of the ribbon in order to suppress interactions between replicas of the ribbon. The Monkhorst-Pack grid was changed to $1 \times 1 \times 1$ for the simulation of finite oligomers.

In Figure 5.1a, we compare the single-point energy of the finite ribbons in AFM and FM states, and the non-polarised state obtained from spin-restricted DFT calculations. The energies of the monomer and dimer of GNR **4a** are the same in spin-unrestricted or spin-restricted calculations. In contrast, for ribbons with more than three units, the AFM and FM states have lower energy than the non-polarised state, and the AFM state is always the ground state. We computed the energy gap between the AFM and FM states, and plotted the energy gaps as a function of the number of units in Figure 5.1b. The energy gaps for ribbons with more than three units can be well fitted with an exponential decay function. This can be explained by the dependence of exchange coupling on the distance. The energy gap between the AFM and FM states is proportional to the effective exchange-coupling

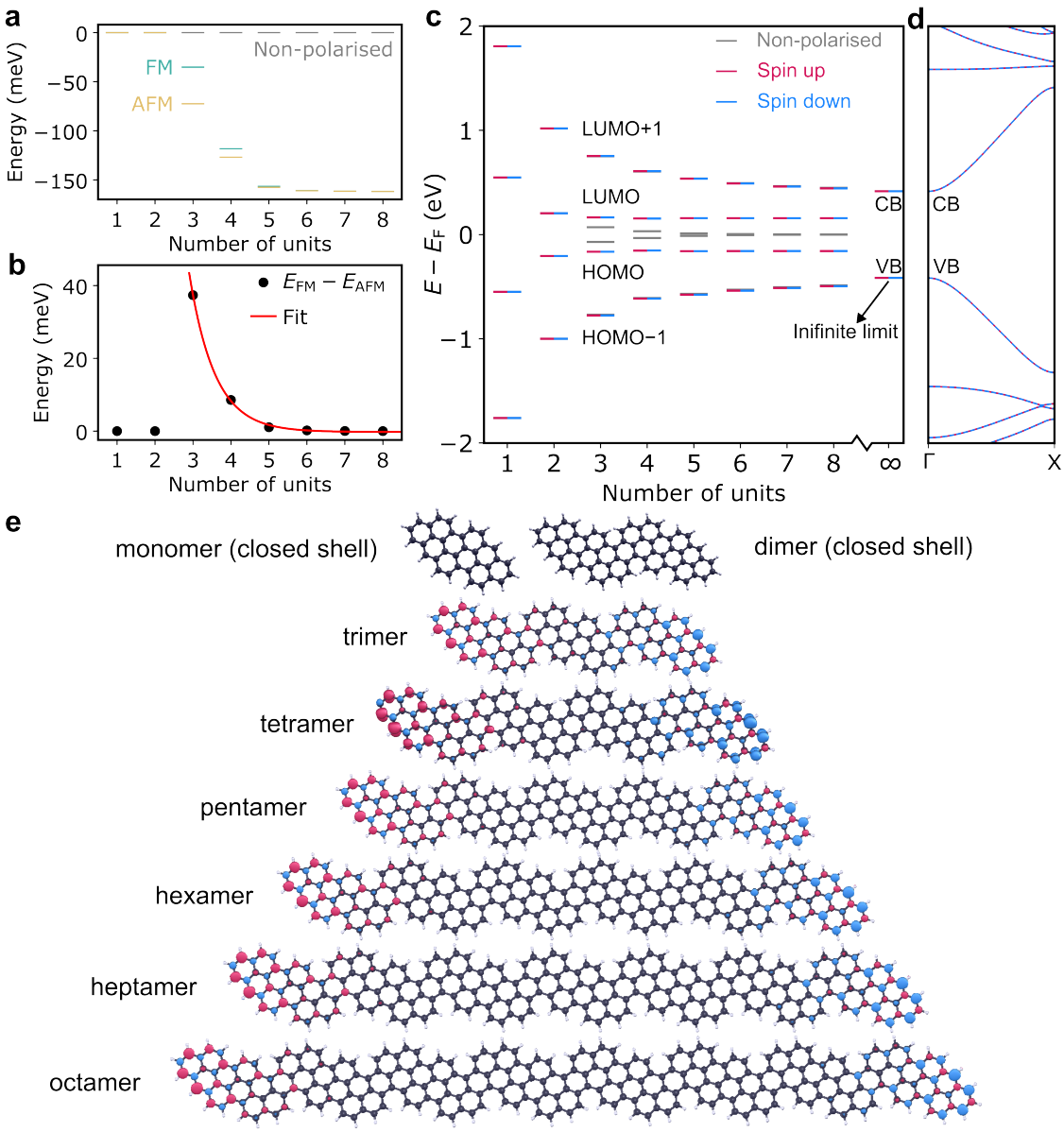


Figure 5.1: Spin-polarised topological end states in GNR **4a**. (a) Energy of antiferromagnetic (AFM, tan colour), ferromagnetic (FM, turquoise colour), and non-polarised (grey colour) state of finite GNR **4a** with varying number of units. The non-polarised state is used as reference. (b) Energy difference between the FM state and the AFM state as a function of number of units. For more than two units, the data is fitted with an exponential decay. (c) Frontier energy levels of finite GNR **4a** in non-polarised state (grey) and AFM state (red and blue). In the AFM state, the spin-up and spin-down energy levels are plotted in red and blue, respectively. The HOMO−1 and LUMO+1 of finite ribbons gradually converge to the valence band and the conduction band in the infinite limit, whereas HOMO and LUMO are the topological end states that exist only in finite ribbons, but not in infinite ribbons. The HOMO–LUMO gap converges to zero in non-polarised calculation, but converges to 0.31 eV for spin-polarised calculation with AFM configuration. (d) Band structure of GNR **4a** with periodic boundary conditions. All the spin-up (red) and spin-down (blue) bands are degenerate. (e) Spin-density isosurfaces of the AFM state of finite ribbons. The monomer and dimer are in closed-shell form, while the others have spin-polarised end states. The isovalues were set to 0.002 for all cases. Red and blue colour represent spin up and spin down, respectively. All calculations were carried out with DFT.

strength between the spin states at the two ends. The exchange-coupling strength between two electron spins is determined by the overlap between the two spin orbitals. Since atomic orbitals decay exponentially in space, the overlap between the two spin orbitals at the two ends also decays exponentially as the ribbon becomes longer. Therefore, the exchange-coupling strength also exhibits an exponential decay as the number of units increases.

To examine the change of the energy levels of topological end states in spin-unrestricted calculations, we plotted the frontier energy levels of the finite ribbons in the non-polarised state and the AFM ground state. In the AFM state, all the spin-up and spin-down levels are degenerate. The energy levels of the HOMO−1 and LUMO+1 of finite ribbons in the AFM state are nearly identical to those in the non-polarised state. Moreover, they gradually converge to the VB and CB in the infinite limit as the ribbon gets longer. The HOMO and LUMO of finite ribbons are topological in-gap states that do not have counterparts in the band structure of the infinite ribbon (Figure 5.1d). Such topological in-gap states are localised end states that only appear in a finite ribbon but not in an infinite ribbon. In a spin-non-polarised calculation, the HOMO and LUMO gradually converge to zero energy as the ribbon gets longer, whereas in the spin-polarised AFM state, the HOMO–LUMO gap converges to a finite value of about 0.31 eV. We displayed the spin-density isosurfaces of these finite ribbons in Figure 5.1e. Apart from the monomer and dimer that are in the closed-shell form, all the longer ribbons are in the singly-occupied spin-split form in the ground state, with the spin-polarised states at the two ends antiferromagnetically coupled to each other. Our results are in line with other reports of spin-polarised topological states of GNRs in literature [154, 158, 218]. In shorter ribbons, the orbitals at the two ends have a large overlap with each other, leading to a significant energy reduction by forming singly-occupied closed-shell orbitals. As the ribbons get longer, the Coulomb repulsion energy surpasses the hybridisation energy, hence the states at

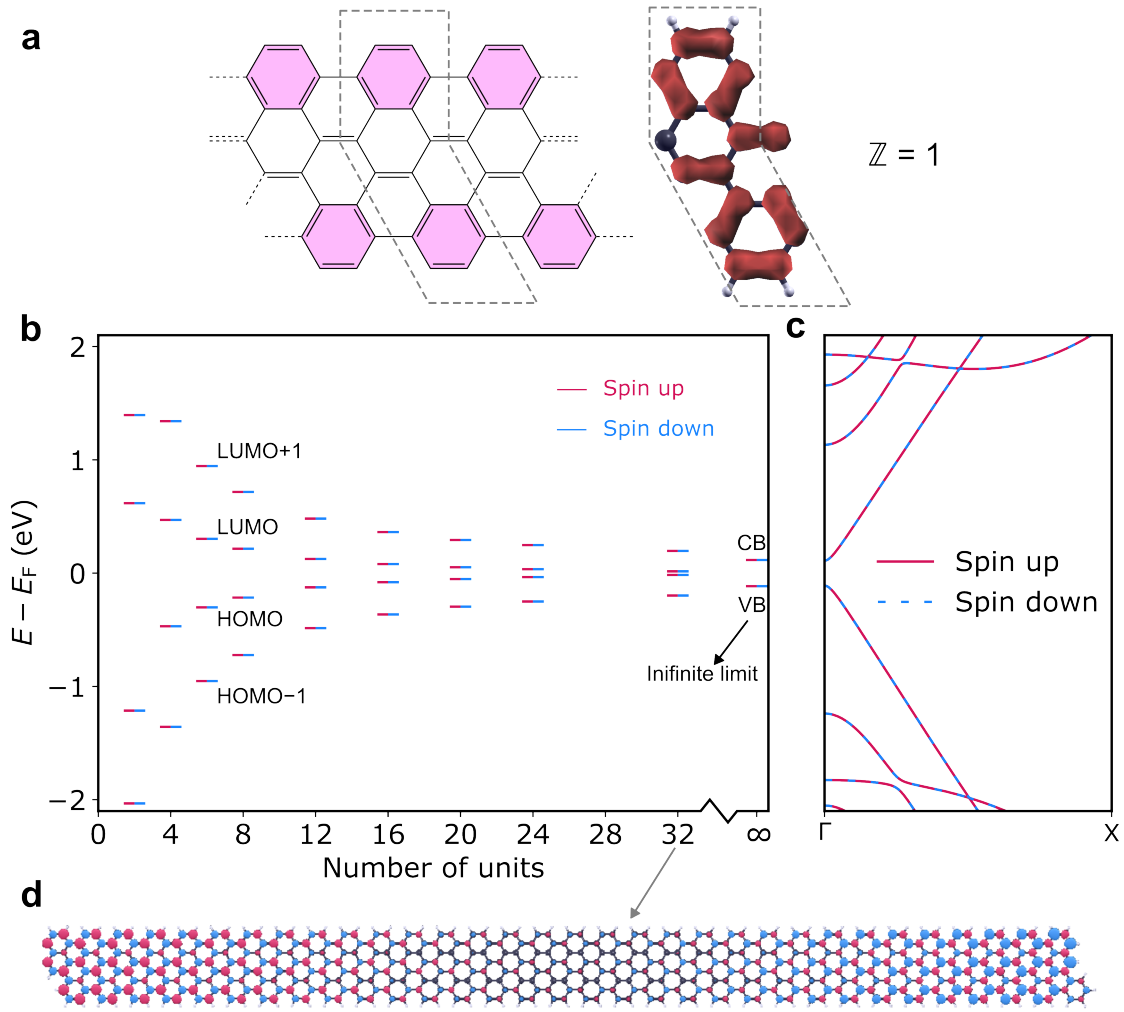


Figure 5.2: Spin-polarised topological end states in 8-AGNR. (a) Structural model and Wannier functions of the 8-AGNR. The maximal possible number of Clar's sextets (pink hexagons) are shown in the structural model. The dashed box denotes the unit cell. The eight Wannier functions calculated from p_z-type occupied bands are displayed within the same unit cell. There is one Wannier function cut by the unit-cell boundary, in line with $\mathbb{Z} = 1$. (b) Frontier energy levels of finite 8-AGNRs in the ground state calculated from spin-unrestricted DFT. The spin-up and spin-down energy levels are represented by red and blue lines, respectively. The HOMO−1 and LUMO+1 gradually converge to valence band and conduction band in the infinite limit, whereas the HOMO and LUMO are the topological end states that exist only in finite ribbons and they gradually converge to zero energy. (c) Band structure of an infinite 8-AGNR. All spin-up (red) and spin-down (blue) bands are degenerate. (d) Spin-polarised end states of a finite 8-AGNR with 32 units.

the two ends become degenerate singly-occupied states. The effective exchange coupling, which is proportional to the singlet–triplet energy gap, becomes weaker for longer ribbons as the two ends are more spatially separated.

So far, GNR **4a** is only studied theoretically but has not been synthesised

yet. Next, we will present another example, a type of 8-AGNR, which has been successfully synthesised recently by my colleague Dr. Xuelin Yao. Figure 5.2a displays the structural model of an 8-AGNR with maximal Clar's sextets, whose configuration is consistent with the one shown in Figure 4.19. The Wannier functions calculated from all occupied p_z-bands align with the double bonds in the structural model. There is one Wannier function cut by the unit-cell boundary, which is in line with $\mathbb{Z} = 1$. In Figure 5.2b, we present the frontier energy levels[3] of a finite 8-AGNR with varying number of repeating units. Similar to GNR **4a**, the HOMO−1 and LUMO+1 of finite 8-AGNRs gradually converge to the valence band (VB) and conduction band (CB), respectively. The in-gap states, HOMO and LUMO, in an 8-AGNR, however, exhibit a much smaller energy splitting than in GNR **4a**. Moreover, the energy levels of finite 8-AGNRs converge much slower with increasing length compared with GNR **4a**. This is because of the smaller band gap of 8-AGNR. Meanwhile, the spin-polarised topological end states are relatively more delocalised even in very long ribbons, as can be seen from Figure 5.2d.

In fact, the spin-polarised end states can be related to the topology of GNRs from another perspective. As discussed in Section 4.3, the number of zero-energy modes, or the $\mathbb{Z}$ index of a GNR, corresponds to the number of double bonds cut by a unit-cell boundary in the structural representation with the maximum number of Clar's sextets. In organic chemistry, the Clar's sextet rule is commonly used to determine the stability of different resonance forms of an aromatic molecule. For some aromatic molecules, the most stable form, i.e. the one with the greatest number of Clar's sextets, may host unpaired electrons. This rule can also be applied to a finite GNR. First, we draw maximal Clar's sextets in a GNR. Upon truncation of the GNR, the carbon atoms that have double-bond connections across the unit-cell boundary, which otherwise would have been connected to other carbon atoms in an infinite ribbon, are now singly passivated by hydrogen atoms. Consequently,

[3]Frontier energy levels mean those energy levels close to the Fermi level.

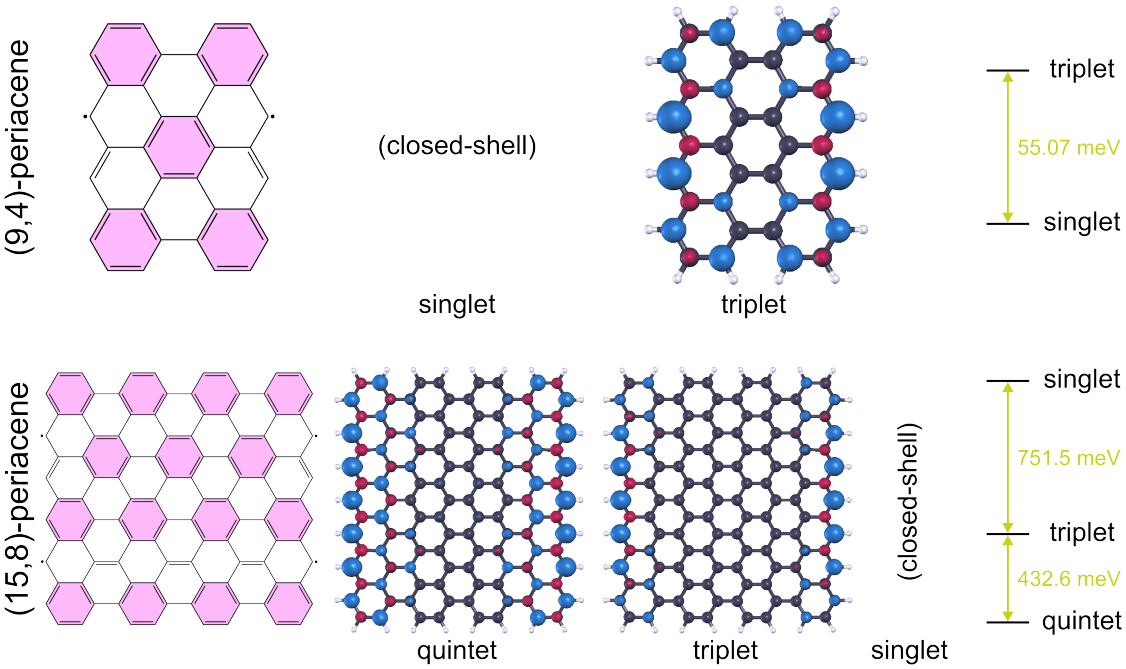


Figure 5.3: Clar's sextet rule and spin polarised states in periacenes. In the configuration with the maximum number of Clar's sextets, the (9,4)-periacene and (15,8)-periacene have two and four radicals, respectively. The (9,4)-periacene has a singlet ground state, while the (15,8)-periacene has a quintet ground state. The spin-density maps and energy values were calculated from DFT. Isovalues were set to 0.004 for all spin density plots. Red and blue colours represent α and β spins, respectively.

a $2p_z$-electron is left unpaired in each of these carbon atoms, and the GNR thus hosts spin-polarised states at its two ends. Consequently, the $\mathbb{Z}$ index is equal to the pair of radicals at the GNR termini.

We used two periacenes as examples, shown in Figure 5.3. In organic chemistry, an acene is a type of polycyclic aromatic hydrocarbon formed by linearly fusing benzene rings. A periacene is composed of a series of acenes that are fused along the direction perpendicular to each acene. Periacenes can be regarded as very short AGNRs. We label a periacene using the notation (N_a, N_z), where N_a and N_z are the number of rows of carbon atoms counted along the zigzag and the armchair directions, respectively. The two periacenes in Figure 5.3 are labelled as (9,4)-periacene and (15,8)-periacene, which can be viewed as a short 9-AGNR and a short 15-AGNR, respectively. The (9,4)-periacene has five Clar's sextets in maximum, and two radicals are left at the two zigzag edges. The (15,8)-periacene

has 15 Clar's sextets in maximum, and four radicals at the two zigzag edges. As calculated in Section 4.3, the $\mathbb{Z}$ indices of 9-AGNR and 15-AGNR are 1 and 2, respectively. Therefore, in both cases, the number of pairs of radicals at the termini is consistent with the $\mathbb{Z}$ index. This becomes more apparent if one compares the Clar's sextets in Figure 5.3 and those in Figure 4.18.

Although we can determine the number of radicals in a finite GNR molecule, we cannot determine the real spin multiplicity of the ground state of this molecule, as we need to consider the size of the molecule and the interaction between the radicals. We calculated the single-point energies of two periacenes with different spin multiplicities using ORCA. We employed the B3LYP exchange–correlation functional and 6-31G** basis set. For (9,4)-periacene, the ground state is a closed-shell singlet, and the first excited state is an open-shell triplet. This is likely because that the two radicals are too close in (9,4)-periacene and hybridise with each other, resulting in a closed-shell ground state. In contrast, the (15,8)-periacene has a quintet ground state, which agrees with the existence of four unpaired electrons at the zigzag edges.

So far, we have demonstrated the spin-polarisation of topological end states. It is important to clarify that, however, in short and narrow GNRs, the accurate prediction of the spin multiplicities of the ground state can be excessively challenging. This is because of the enhanced electron–electron interactions in confined systems, especially in ribbons with multiple radicals. In such situations, other advanced computational methods, such as density matrix renormalisation groups (DMRG) [357], complete active space self-consistent fields (CASSCF) [358], multireference configuration interactions (MRCI) [359], and coupled cluster methods [359] can offer more accurate estimations than the density-functional approximations. These methods, however, are beyond the scope of this thesis. Hence we will not give a detailed discussion of them here.

Lastly, it is important to mention that the two examples we have computationally studied above have been successfully synthesised and shown to be stable under

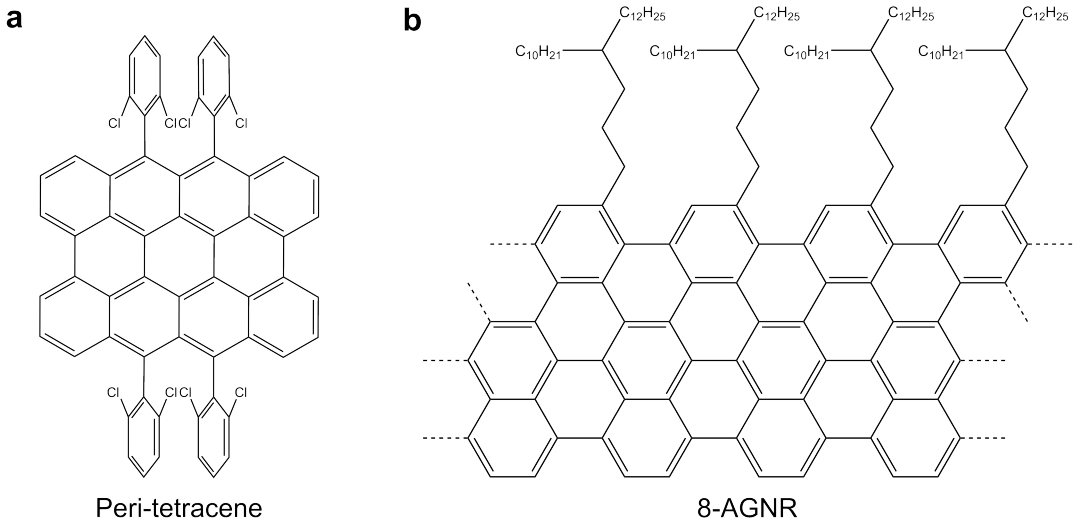


Figure 5.4: Peri-tetracene (by Prof. Jishan Wu's group) and 8-AGNR (by Dr. Xuelin Yao) synthesised in solution phase. The side groups prevent the molecules from aggregation, and thus make them processable in solutions.

ambient conditions. The (9,4)-periacene, also known as peri-tetracene (Figure 5.4a), has been independently synthesised by two of our collaborating groups (Prof. Jishan Wu group [360] and Prof. Xinliang Feng group [361]). The side groups added to the zigzag edges can effectively protect the radicals from oxidation. My colleague, Dr. Federico Lombardi, has experimentally studied its magnetic properties. The peri-tetracene molecule has a thermally accessible triplet[4], which allows EPR transitions. Figure 5.5b shows the CW EPR spectra of peri-tetracene samples in solid state (black), dOTP solution (pink), and CS_2 solution (green). The dashed line is a simulation obtained through the EasySpin package [309]. The splittings are caused by the hyperfine interactions with the surrounding hydrogen nuclei in the molecule. In the solid (powder) state, the spectrum has a broader linewidth that covers the fine features. The spin–lattice relaxation time T_1 (Figure 5.5c) and spin coherence time T_m (Figure 5.5d) of peri-tetracene were measured in different matrices using pulsed EPR at X-band frequency. In dOTP matrix, T_1 reaches

[4]The experimental value of the single-triplet gap of peri-tetracene molecule was determined to be about 104 meV, larger than the calculated value of 55 meV. Considering a Boltzmann distribution, about 1.74% of the molecules are in a triplet state at room temperature.

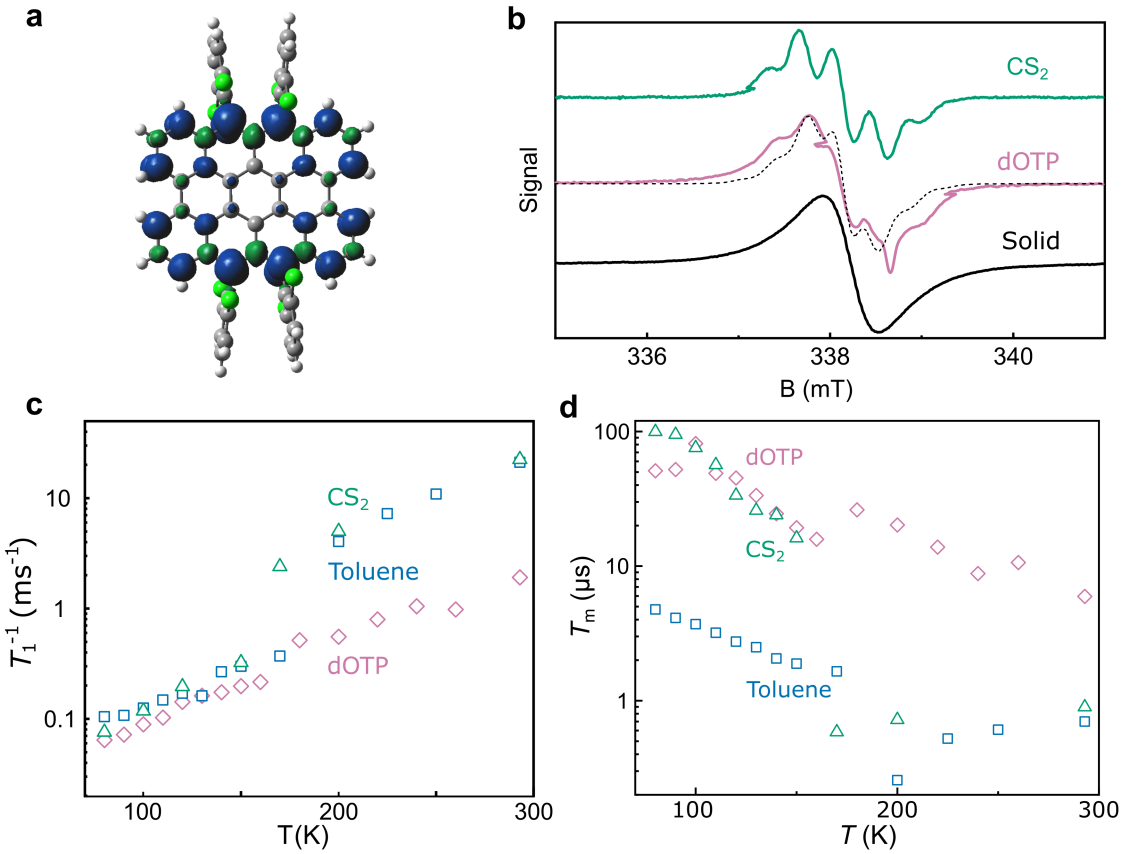


Figure 5.5: EPR spectra, spin–lattice relaxation time, and spin coherence time of peri-tetracene molecule. (a) Spin density isosurface of triplet state of peri-tetracene. Blue and green colours represent spin-up and spin-down, respectively. The isovalue was set to 0.002. (b) EPR spectra of peri-tetracene samples in solid state (black), dOTP matrix (pink), and CS_2 matrix (green). The dashed line is a simulation obtained through the EasySpin package. (c) Spin–lattice relaxation rate versus temperature for peri-tetracene samples in CS_2 (green), toluene (blue), and dOTP (pink) solutions. (d) Spin coherence time versus temperature for peri-tetracene samples in CS_2 (green), toluene (blue), and dOTP (pink) matrices. Experiments and simulation were implemented by Dr. Federico Lombardi.

0.6–15 ms for T>80 K. Remarkably, even in the presence of external hyperfine bath, the spin coherence time T_m reaches 100 µs at 80 K in CS_2 solution, which is higher than theoretically predicted lower limit (80 µs) of spin coherence time in carbon nanostructures [45]. These results reveal the great potential of carbon nanostructures as quantum units. The observed T_m can be further improved by chemical engineering of the nuclear bath, dynamic decoupling, or by investigating single molecules rather than an ensemble.

A type of 8-AGNR has also been synthesised in the solution phase by another colleague, Dr. Xuelin Yao. The structure is shown in Figure 5.4b. The long alkyl chains attached to the edges can prevent the aggregation of the ribbons. The experimental characterisation of this ribbon is currently in progress.

5.3 Spin states from functionalisation groups

Thanks to the bottom-up synthesis technique, GNRs can be decorated with various side groups, thus endowing the GNRs with different properties and functionalities. In this section, we will investigate two side-functionalised cove-edge GNRs with different spin-bearing side groups. Furthermore, they both have the same bulky side groups that make them soluble in multiple solvents. We first calculated the spin density distribution of these GNRs with DFT, implemented in SIESTA, and then measured their spin dynamics using EPR spectroscopy.

All EPR measurements were carried out using a Bruker EleXsys E580 (for X-band and Q-band) and E680 (for X-band). The samples were put in a quartz tube with a 3 mm outer diameter. For solution samples, we tested different solvents such as toluene, 2-Methyltetrahydrofuran (2MTHF), chloroform, and tetralin. The GNRs have higher solubility in tetralin, so we chose tetralin as solvent to prepare all the solution samples. The sample temperature was controlled with an Oxford Instruments CF9350 cryostat and ITC503 temperature controller. We used the dielectric ring resonator Bruker ER4118X-MD5 and Bruker ER5106 QT-2W resonators for X-band (around 9.5 GHz) and Q-band (34 GHz) frequencies, respectively. The field-swept spectra and the phase-memory time T_m were measured using the Hahn-echo pulse sequence ($\pi/2$–τ–π–τ–echo). The dephasing of spins is a result of multiple processes, including the intrinsic spin–spin relaxation time, also known as spin coherence time, as well as other factors like instantaneous diffusion caused by the pulses. Therefore, the measured T_m is only a lower limit of the real

spin coherence time. Nonetheless, we sometimes still use T_{m} to represent the spin coherence time. The spin–lattice relaxation time T_1 was measured using the picket-fence recovery pulse sequence, where a train of 28 π-pulses with a 96 ns interval were applied for randomising the spins. The $\pi/2$ pulse and π pulse durations were set to 24 ns and 48 ns, respectively, for all measurements except for HYSCORE. The pulse lengths in HYSCORE were different as the pulse amplitudes were modulated by the SpinJet AWG E5804200. The spectra were fitted using the EasySpin package [309].

5.3.1 Cyano functionalisation

The cyano-functionalised cove-GNRs, labelled as GNR-CN, is shown in Figure 5.6a. There is one unpaired electron in each CN group. The bulky groups, depicted in orange, were obtained by anthracenes modified with *N*-octadecylmaleimide, and will be referred to as AOM groups in the following. We calculated the spin-density distribution of GNR-CN using spin-unrestricted DFT implemented in SIESTA. To simplify the calculation, the bulky groups were removed. Because of steric hindrance, the bulky groups in neighboring unit cells are more likely to align at opposite edges during cyclisation. Therefore, we used a supercell, containing two unit cells with CN groups attached to opposite edges as the repeating unit in DFT calculation. After geometrical optimisation, we calculated the single-point energies of GNR-CN with two different initial spin configurations. One is the antiferromagnetic configuration, where all the atoms with odd indices are initialised to spin-up and all the atoms with even indices are initialised to spin-down. The other is the ferromagnetic configuration, with all the atoms initialised to spin-up. These two spin settings result in different spin polarisations in CN groups. In the first case the spins localised at the CN groups are antiferromagnetically coupled across the ribbon, and ferromagnetically coupled along the same edge, as shown in Figure 5.6b. In the second case, all the spins of the CN groups are aligned ferromagnetically. The configuration with antiferromagnetic alignment is 17.73 meV lower in energy per

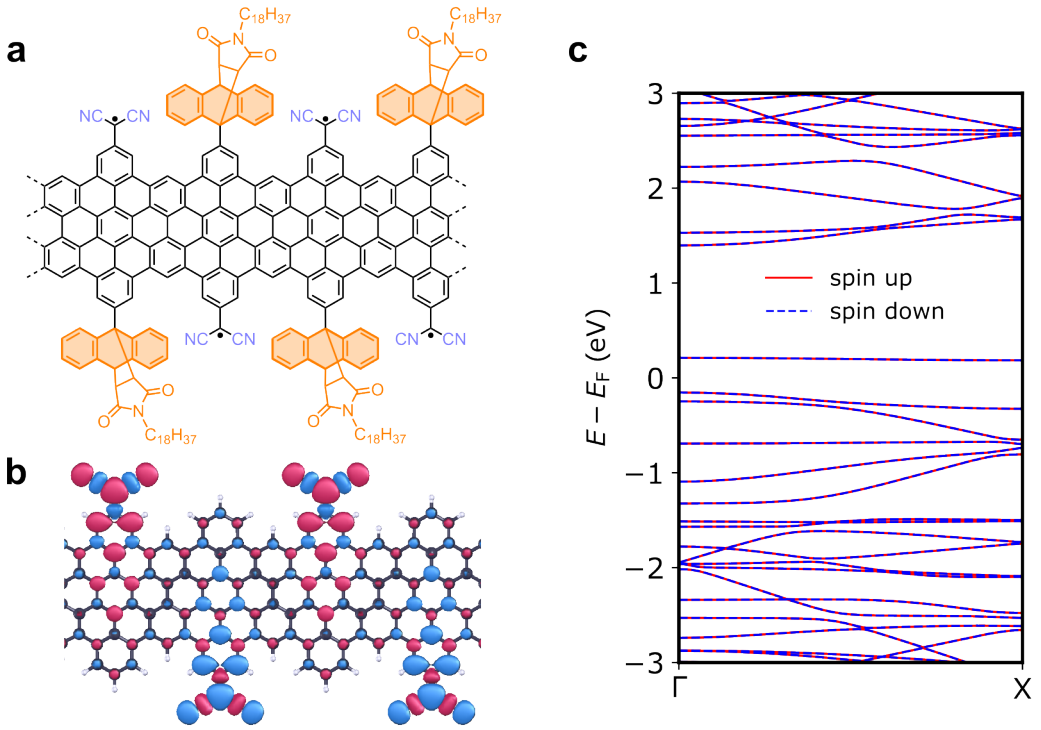


Figure 5.6: Spin density and band structure of GNR-CN. (a) Structure of GNR-CN (synthesised by Dr. Xuelin Yao). The cyano groups and bulky groups that help increase solubility are shown in light purple and orange, respectively. (b) DFT-calculated spin-density isosurface, with an isovalue of 0.001. Red and blue colours represent spin up and spin down, respectively. (c) DFT-calculated band structure of GNR-CN. The energy bands for spin up and spin down are plotted as red solid and blue dashed lines, respectively. They are degenerate in the AFM ground state.

unit cell than the ferromagnetically aligned configuration, and, therefore, DFT predicts that the GNR-CN ribbon is an antiferromagnetic spin chain in the ground state. We also plotted the band structure of GNR-CN in the ground state, as shown in Figure 5.6c, where all the spin-up bands and spin-down bands are degenerate.

The calculation results shown in Figure 5.6 are based on the structure of GNR-CN without any imperfections or irregularities. These, however, cannot be guaranteed by current solution-phase synthesis techniques. After conducting pulsed-EPR characterisations, we can compare the spectra, spin–lattice relaxation times T_1, and spin coherence times T_m of GNR-CN and a similar GNR where the $-(CN)_2$ groups are replaced with bromine atoms, denoted as GNR-Br. The structures of GNR-Br and GNR-CN are shown in Figure 5.7a. The GNR-Br should not have

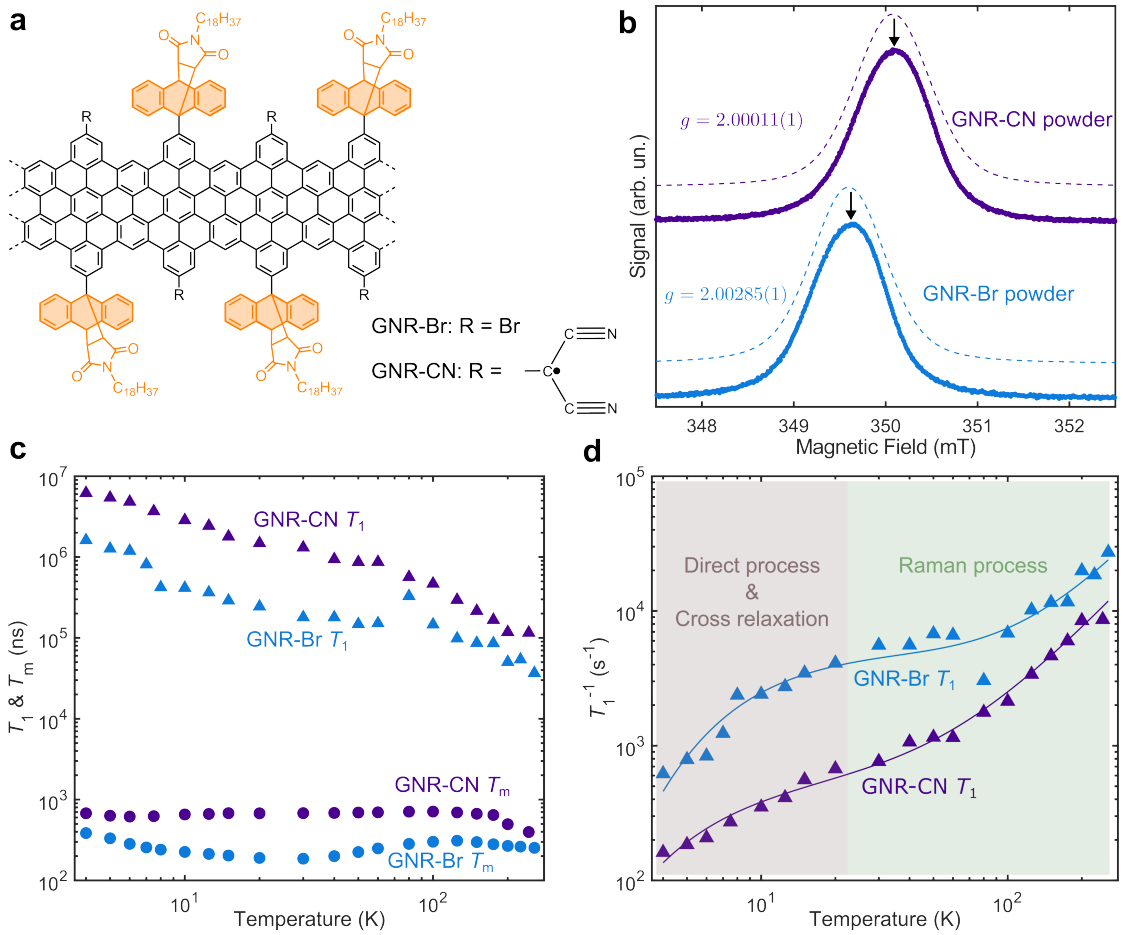


Figure 5.7: EPR Spectra, T_1, and T_m of GNR-CN and GNR-Br powder samples. (a) Structural models of GNR-Br and GNR-CN. (b) EDFS spectra of GNR-Br (blue) and GNR-CN (purple) powder samples measured at X-band frequency. Dashed lines are fits to the spectra. (c) T_1 (triangles) and T_m (dots) of GNR-Br (blue) and GNR-CN (purple) samples versus temperature, measured at the magnetic fields marked by arrows in (b). (d) Inverse of T_1 of GNR-Br (blue) and GNR-CN (purple) versus temperature. The solid lines are fits to the data. The spin–lattice relaxation is dominated by a direct process and a cross-relaxation mechanism at lower temperatures, while dominated by a Raman process at higher temperatures.

spin polarised states if the lattice structure is perfect. The spectrum of GNR-Br, however, displays a strong peak, which can only be attributed to defects. Such defects likely stem from the imperfect reactions during the cyclodehydrogenation step [362, 363]. The g-factors were obtained by fitting the EDFS spectra using the Matlab package EasySpin [309]. A Voigt line broadening is used in the fitting. The peak-to-peak line widths[5] for the Gaussian and Lorentzian components are

[5]Peak-to-peak represents the horizontal distance between the minimum and the maximum of a

0.678(6) and 0.182(5), respectively, for the GNR-CN sample, and 0.647(6) and 0.197(4), respectively, for the GNR-Br sample. The lineshapes of two samples are quite close to each other. Moreover, the g-factors of the two samples are both close to that of a free electron, which is typical for organic radicals [240]. The small difference between the g-factors of GNR-CN and GNR-Br can be attributed to the different chemical environments of the spin centres.

We measured the spin–lattice relaxation time with the picket-fence pulse sequence, which can eliminate the effects of spectral diffusion, a stochastic process of resonance-frequency changes due to random flip-flops of nearby nuclear or electron spins [240]. After we obtained the echo signal $Y(t)$ as a function of the time interval t, we fit it with a bi-exponential model:

$$Y(t) = A_1 \exp\left(-\frac{t}{T_1}\right) + A_2 \exp\left(-\frac{t}{T_{\text{fast}}}\right), \tag{5.3}$$

where A_1 and A_2 are coefficients, and T_{fast} describes a fast relaxation process that is usually attributed to instantaneous diffusion, a process that describes the change of the resonance frequency of the observed spin when a neighbouring spin, to which the observed spin is dipole-coupled, is flipped by the second pulse [240]. In Figure 5.7c, we plot the T_1 times of GNR-CN and GNR-Br for different temperatures. The T_1 times of GNR-CN are several times higher than those of GNR-Br. Note that as the EPR signal from GNR-Br originates entirely from defects, the signal from GNR-CN is likely a result of both defects in the GNR backbone and spin states in the CN side groups. It is difficult to distinguish them as they have similar g-factors and show similar spin dynamics. There are several possible reasons for the discrepancy between the T_1 times of GNR-CN and GNR-Br. The first possible reason is that the spin states of the defects in the GNR backbone are more delocalised than those of the CN appendages. Larger delocalisations are known to cause a lower T_1 [244].

first-derivative lineshape.

A second possible explanation is that the concentration of unpaired spins in GNR-Br is higher than that in GNR-CN. As will be shown later when the spin–lattice relaxation mechanisms are fitted (Table 5.1), cross relaxation is significantly stronger in GNR-Br, which is related to a larger density of spin clusters. Furthermore, it is also likely that the discrepancy stems from different experimental conditions. Although the spectrometer, the resonator, and the measurement procedures were kept the same, the coupling of the resonator may slightly differ as it is very difficult to keep it the same for the different samples. A different coupling may result in a different efficiency of the nutation pulse, and therefore results in a different concentrations of excited spins. In order to clarify the underlying reasons, additional studies need to be carried out. For example, a comparison between the spin density of CN spin states and defect spin states can be carried out by performing DFT calculations. The spin relaxation times of these two kinds of spin species can be directly calculated through theoretical approaches. Additional comparative measurements can be performed after quantifying the concentration of unpaired spins in the samples. Moreover, a more rigorous experimental control is required to rule out the influence of varying instrumental conditions.

The phase-memory time T_m is extracted by fitting the echo signal as a function of time interval τ using a mono-exponential model:

$$Y(t) = A\exp\left(-\frac{2\tau}{T_\mathrm{m}}\right), \tag{5.4}$$

The factor of 2 comes from the fact that 2τ measures the time interval between the $\pi/2$ pulse and the echo in a Hahn-echo sequence. The dephasing of spins is affected by multiple factors. The dephasing rate can be expressed by the following equation [364]:

$$\frac{1}{T_\mathrm{m}} = \frac{1}{2T_1} + \frac{1}{T_\mathrm{ee}} + \frac{1}{T_\mathrm{en}}, \tag{5.5}$$

where T_ee and T_en describe the dephasing arising from electron–electron spin

Table 5.1: Fit parameters of spin–lattice relaxation mechanisms for GNR-Br and GNR-CN powder samples.

Sample	$A_{\mathrm{dir}}\,(\mathrm{K^{-1}s^{-1}})$	$A_{\mathrm{cro}}\,(\mathrm{s^{-1}})$	$\Delta_{\mathrm{ST}}\,(\mathrm{K})$	$A_{\mathrm{Ram}}\,(\mathrm{s^{-1}})$	$\theta_{\mathrm{D}}\,(\mathrm{K})$
GNR-Br	0.1156	1.12×10^4	12.63	9.63×10^4	216.1
GNR-CN	12.34	842.7	8.53	3.06×10^4	195.4

coupling and electron–nuclear spin coupling, respectively. In our case, T_1 is much longer than T_{m}, thus it is unlikely to be the main limiting factor of T_{m}. The phase-memory time T_{m} is largely influenced by the π-stacking of GNRs in the powder state [63]. We also notice that there is a discrepancy between the T_{m} times of GNR-CN and GNR-Br. This could possibly be explained by the fact that the spin states in CN groups are farther from the bulky groups compared with the defects in the GNR backbone, and are thus less affected by the nuclear spins of hydrogens in bulky AOM groups, which could lead to a lower T_{m} [244].

We fitted the inverse of T_1 against the temperature for the two samples. This unravels the mechanisms for spin–lattice relaxation. We included three terms – direct process, cross relaxation, and Raman process – in the model, and produced a rather good fit to the data, as shown in Figure 5.7d. The model is written as:

$$\frac{1}{T_1} = A_{\mathrm{dir}} T + A_{\mathrm{cro}} \frac{1}{1 + \exp\left(\frac{\Delta_{\mathrm{ST}}}{kT}\right)} + A_{\mathrm{Ram}} \left(\frac{T}{\theta_{\mathrm{D}}}\right)^9 \int_0^{\theta_{\mathrm{D}}/T} \frac{x^8 \mathrm{e}^x}{(\mathrm{e}^x - 1)^2}\,\mathrm{d}x, \qquad (5.6)$$

where A_{dir}, A_{cro}, and A_{Ram} are the coefficients of each term. The Boltzmann constant is denoted as k. The parameters are summarised in Table 5.1.

The direct process describes the transfer between the spin-flip energy and a lattice-phonon energy. This leads to a linear dependence between $1/T_1$ and temperature, and usually dominates the spin–lattice relaxation at temperatures below 20 K. Cross relaxation typically arises in amorphous solids with a high concentration of paramagnetic centres, where not only individual spin centres exist, but also pairs or larger clusters of spin centres [365–368]. Pairs of $S = 1/2$ spin centres will be in either singlet or triplet state, with energy splitting Δ_{ST}. Cross

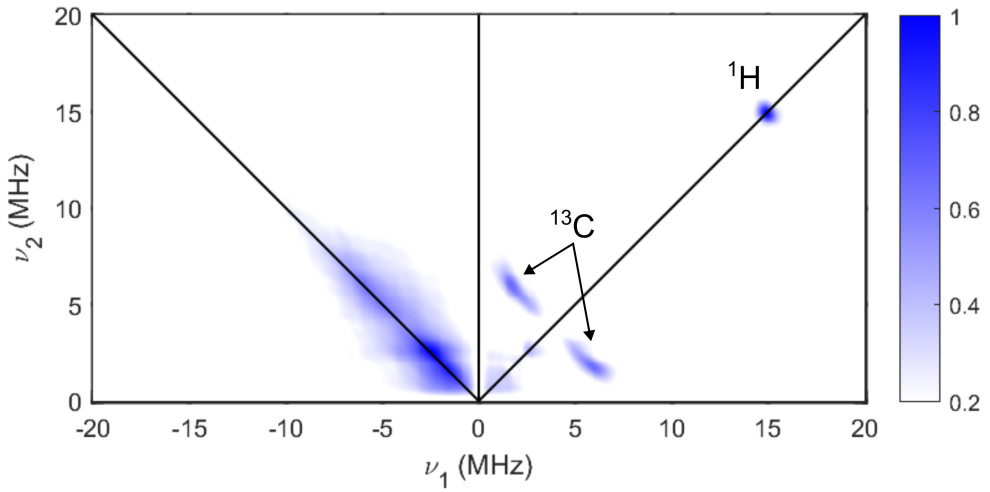


Figure 5.8: HYSCORE spectrum of GNR-CN power sample. Peaks resulting from hyperfine interactions with ^{13}C and ^{1}H nuclei are labelled in the graph.

relaxation refers to a simultaneous process in which the spin state of a single radical undergoes a downward transition while there is an accompanying upward transition within the triplet state of a pair [365, 369]. Under these circumstances, the system displays a bi-exponential relaxation pattern with two rate constants. As shown in Figure 5.7d, both the direct process and cross relaxation dominate the spin–lattice relaxation at temperatures below 20 K. We found that the coefficient of the cross-relaxation process is more than 10 times larger in GNR-Br than in GNR-CN. This observation is probably related to a larger concentration of clusters of unpaired spins in the GNR-Br sample. There is no rigorous control over the concentration of unpaired electrons during the synthesis. Therefore, it may vary for different batches of samples. In addition, a more efficient cross-relaxation process in GNR-Br is also likely a reason for its lower T_1 times compared with GNR-CN. At higher temperatures, the two-phonon Raman process takes the leading role. This process involves a virtual excited state with an energy below the Debye temperature, denoted as θ_{D}. It is important to note that the parameter values in Table 5.1 should be interpreted with caution. There are multiple reasons for this. Firstly, the number of data points is limited. Secondly, it is difficult to disentangle the different influence factors using a single bi-exponential fitting. For instance, there are likely

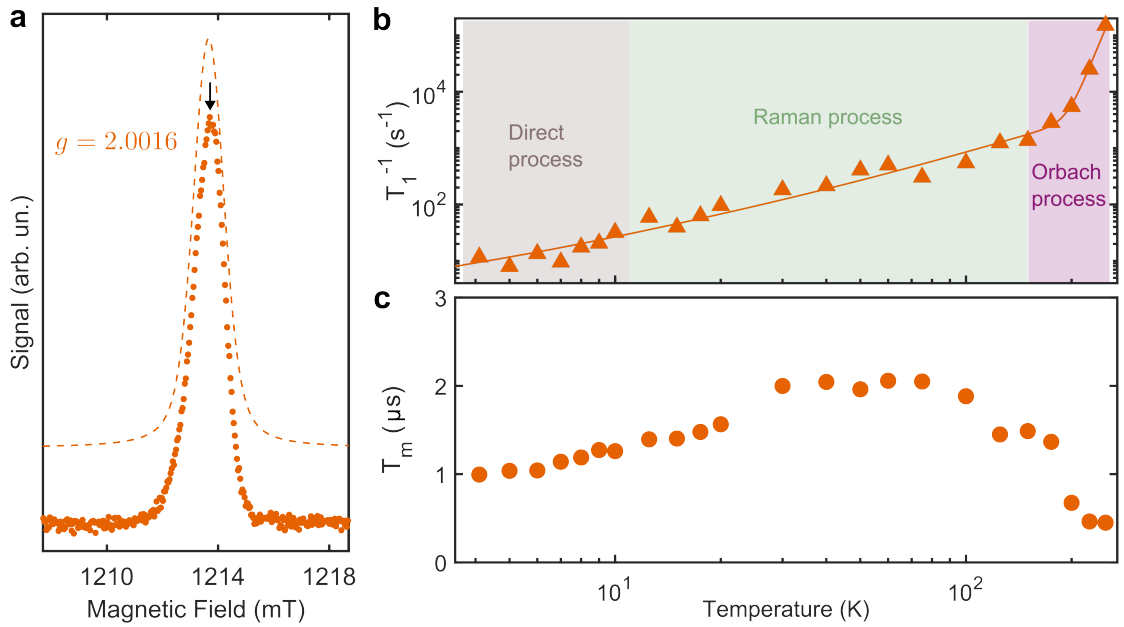


Figure 5.9: EPR spectrum, T_1, and T_m of a GNR-CN solution sample. (a) EDFS spectrum measured at Q-band frequency. The dashed line is the simulated spectrum. (b) Inverse of T_1 versus temperature. T_1 is measured at the magnetic field marked by the arrow in (a). The solid line is a fit to the data. The spin–lattice relaxation is dominated by a direct process, a Raman process, and then an Orbach process as temperature increases from 4 K to room temperature. Colour regions correspond to temperature ranges with different dominant relaxation mechanisms. (c) T_m versus temperature.

more than one spin species in GNR-CN samples. The powder samples also have pairs or clusters of spin centres. Additionally, the pulses can induce instantaneous diffusion. All these factors can contribute to a relaxation rate constant. Therefore, it is challenging to extract the intrinsic T_1 with high precision.

We concluded before that the EPR signal from GNR-CN is likely a result of both defects and the spin states in CN groups. In order to make sure if the spin states in CN groups exist in the sample, we attempted to measure the hyperfine interaction parameters using the HYSCORE technique. If spin states do exist in the CN side groups, they will interact with the nuclear spins of nitrogens and we can extract the hyperfine interaction parameters from a HYSCORE spectrum. As shown in Figure 5.8, the peaks due to ^{13}C and ^{1}H nuclei are clearly visible in the first quadrant. The hyperfine coupling with ^{14}N nuclei, if present, should be in the strong coupling regime, resulting in symmetrical peaks with respect to the diagonal line in

Table 5.2: Fit parameters of spin–lattice relaxation mechanisms for a GNR-CN solution (tetralin) sample.

Sample	$A_{\mathrm{dir}}\,(\mathrm{K^{-1}s^{-1}})$	$A_{\mathrm{Ram}}\,(\mathrm{s^{-1}})$	$\theta_{\mathrm{D}}\,(\mathrm{K})$	$A_{\mathrm{Orb}}\,(\mathrm{K^{-3}s^{-1}})$	$\Delta_{\mathrm{Orb}}\,(\mathrm{K})$
GNR-CN solution	2.257	330.1	27.08	27.86	4108

the second quadrant. However, we can only find a wide peak around the diagonal line in the second quadrant, which is attributed to artifacts caused by imperfect pulses. It is possible that the ^{14}N peaks are completely obscured by these artifacts.

We also prepared a GNR-CN solution sample using tetralin as solvent, and then measured the spectrum and spin dynamics at Q-band frequency. As shown in Figure 5.9a, the g-factor is closer to the value of a free electron compared with that of the powder sample. The inverse of T_1 versus temperature was fitted using the following model:

$$\frac{1}{T_1} = A_{\mathrm{dir}}T + A_{\mathrm{Ram}}\left(\frac{T}{\theta_{\mathrm{D}}}\right)^9 \int_0^{\theta_{\mathrm{D}}/T} \frac{x^8 \mathrm{e}^x}{(\mathrm{e}^x - 1)^2}\,\mathrm{d}x + A_{\mathrm{Orb}}\frac{\Delta_{\mathrm{Orb}}^3}{\mathrm{e}^{\Delta_{\mathrm{Orb}}/kT} - 1}. \tag{5.7}$$

In this model, cross relaxation is absent due to the separation of the ribbons in solution. For higher temperature above 200 K, the rapid decrease of T_1 prompts us to include the Orbach processs in the model. The Orbach process describes a two-phonon relaxation process. It, however, involves an actual, rather than virtual, excited state of the molecule. The energy of this excited state is denoted as Δ_{Orb}. The coefficient of the Orbach process is denotes as A_{Orb} in Equation (5.7). Table 5.2 summarises the parameters obtained from fitting the relaxation mechanisms of the spin states in the GNR-CN solution sample.

The T_{m} of the GNR-CN solution sample displays an unusual behaviour. It firstly increases with temperature for $T < 30\,\mathrm{K}$, and then decreases for $T > 100\,\mathrm{K}$. A similar behaviour was observed in other molecular samples in the literature, where the increase of T_{m} at low temperatures was explained by the quantum tunneling rotation of methyl groups [239, 370, 371]. The quantum tunneling rotation averages out the hyperfine coupling with the three protons in a methyl group, thus eliminating

their influence on decoherence [239]. This mechanism may also be present in our samples. However, the methyl groups only exist in the alkyl chains in our samples. We speculate that quantum tunneling rotation of CN groups might also have a similar effect as the methyl groups. The quantum tunneling rotation of protons in methyl groups, however, is a rotation of only 120°, whereas the quantum tunneling rotation of two CN groups is a rotation of 180°. The CN groups are also significantly heavier than hydrogen atoms. Therefore, the quantum tunneling rotation will happen less likely for CN groups than for methyl groups. We do not see the effect of a quantum tunneling rotation in powder samples, where decoherence is dominated by π-stacking of the nanoribbons.

Although the T_1 and T_m of GNR-CN solution samples are longer than those of powder samples, they are not directly comparable since they were measured at different frequencies. In the next section, we will make a more rigorous comparison of powder and solution samples of GNR-VO, and see the enhancement of spin coherence time upon dissolving the GNRs.

5.3.2 Vanadyl-porphyrin functionalisation

The vanadyl-porphyrin functionalised GNR has the same backbone structure and bulky groups as GNR-CN, with only the cyano groups replaced by vanadyl-porphyrins. We calculated the spin density and band structure (Figure 5.10). Similar to GNR-CN, the nearest VO groups across opposite edge can have either antiferromagnetic or ferromagnetic coupling to each other. Single-point DFT calculations reveal that these two configurations have nearly identical energy, suggesting negligible interactions between spin states in different porphyrin sites. The spin-density map here might not reflect the real situation, as not all the unit cells necessarily have porphyrins grafted on the edges.

We measured the spectra and spin dynamics of GNR-VO samples under three conditions: powder sample at X-band, powder sample at Q-band, and solution

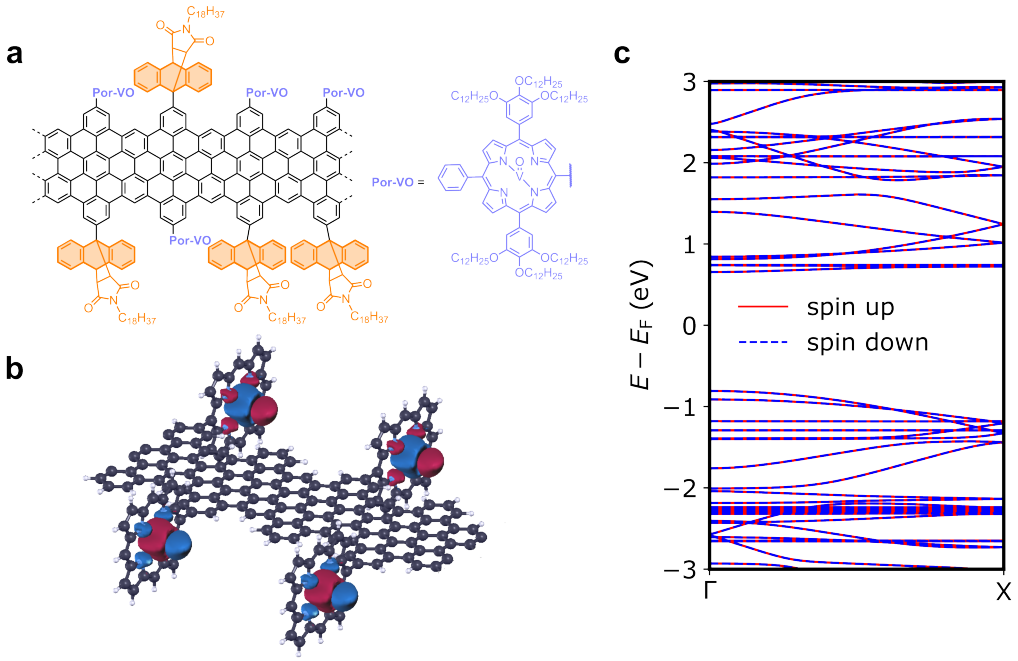


Figure 5.10: Structure and spin density of GNR-VO. (a) Structure of GNR-VO (synthesised by Dr. Xuelin Yao and Dr. Dimitris Alexandropoulos). The porphyrin groups and bulky groups that help increase solubility are shown in light purple and orange colours, respectively. (b) DFT-calculated spin density isosurface, with isovalue of 0.001. Red and blue colours represent spin up and spin down, respectively. (c) DFT-calculated band structure of GNR-VO. The energy bands for spin up and spin down are plotted in red solid and blue dashed lines, respectively.

sample at Q-band. We simulated the spectra using the EasySpin package [309], as indicated by the dashed lines in Figure 5.11a. By analysing the spectra, two spin species can be identified. One spin species has a g-factor of 1.99912(4), a typical value for carbon radicals. The calculation results shown in Figure 5.10b indicate that the VO spin states are very localised at the porphyrin groups. Almost no spin density is injected to the GNR backbone. Therefore, the spin states with g-factor of 1.99912(4) are most likely to be caused by defects in the GNR backbone, denoted as GNR state in the following. The other one is related to the vanadyl groups, named as VO state in the following. Because ^{51}V has a nuclear spin of $I = 7/2$, the VO state leads to an eight-fold $(2I + 1)$ splitting in the EPR spectrum. The eight-fold splitting in Figure 5.11a is less clear than that in Figure 5.13a. An explanation for this observation is that there is a large amount of defects in the GNR-VO sample,

Table 5.3: Simulation parameters for GNR-VO powder spectrum.

	Parameter	Fit Result
VO state	$g_\parallel$, $g_\perp$	1.98085(7), 1.95797(18)
	$A_\parallel$, $A_\perp$	165.78(19) MHz, 475.79(62) MHz
	weight	83.84(0)%
GNR state	g_{iso}	1.99912(4)
	weight	16.16(24)%

and these defects result in a GNR state peak with a very large intensity making the peaks of VO state less obvious. In Table 5.3, we list the simulation parameters for the GNR-VO powder spectrum. The simulation of other batches of samples yields similar results. The g-tensor and hyperfine tensor of the VO state are both fitted using axial symmetry, i.e. $g_x = g_y = g_\perp$, $g_z = g_\parallel$, and same applies to A. In contrast, the g-tensor of the GNR state is isotropic, denoted as g_{iso}. Although the g-factor of graphene was demonstrated to be anisotropic [372], we do not see any anisotropy of the g-factor of the GNR state by fitting the spectrum. The major reason is that all the GNRs are randomly oriented in our sample, therefore the g-anisotropy becomes averaged out. It is possible to observe the effect of g-anisotropy of spins in GNRs at higher frequencies when the GNR spins are coupled to other types of spin species attached to the GNR edge [62].

We furthermore characterised the hyperfine coupling of GNR spins and VO spins using HYSCORE. As shown in Figure 5.12, the peaks resulting from hyperfine coupling between electrons spins and nuclear spins from ^{13}C and ^{1}H nuclei are identified in the first quadrant. For the VO state, the electrons spins also have a strong coupling to the ^{14}N nuclei. Since the nucleus of ^{14}N has spin $I = 1$, both single-quantum transition ($\Delta m_I = \pm 1$) and double-quantum transition ($\Delta m_I = \pm 2$) are present in the HYSCORE spectrum.

The T_1 and T_{m} times were measured using the same pulse sequences as for GNR-CN. All of the T_{m} were obtained by fitting the Hahn-echo decay with a

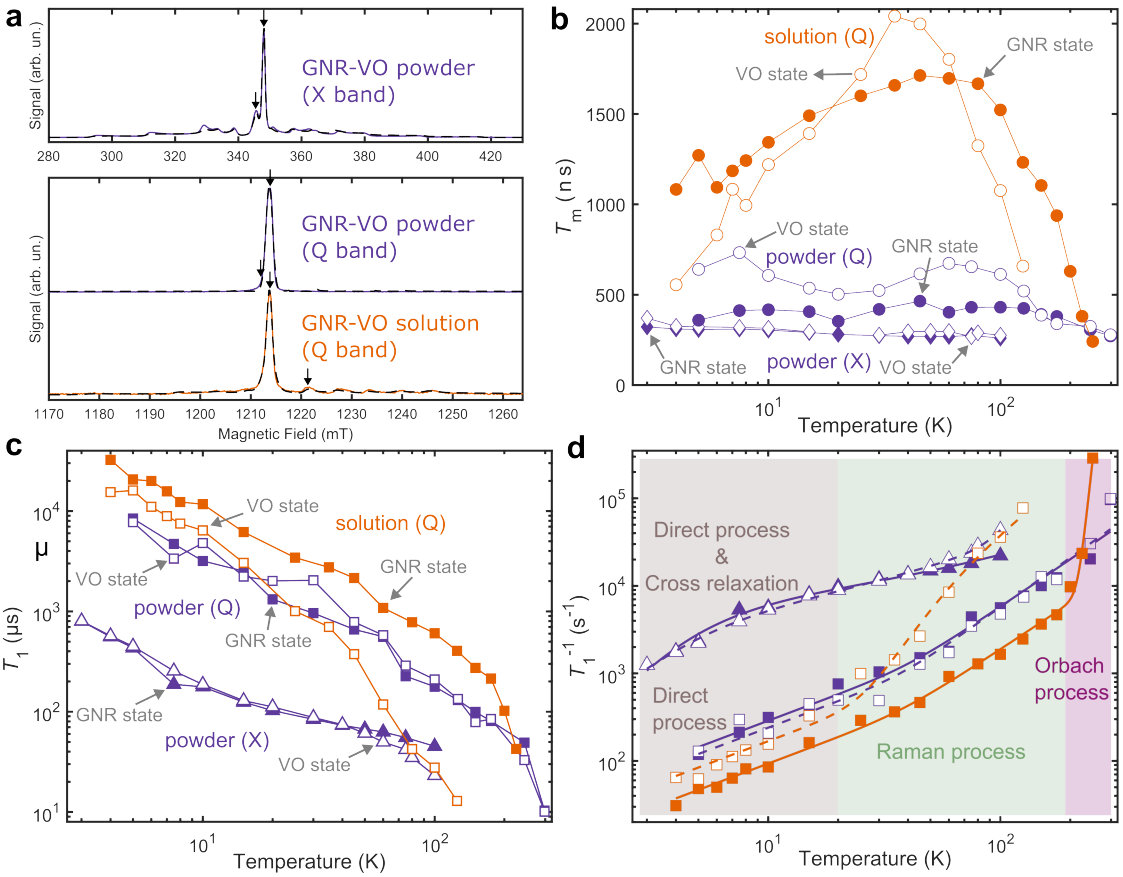


Figure 5.11: EPR spectra, T_1, T_m of GNR-VO powder and solution samples. (a) The EDFS spectra of a GNR-VO powder (dark purple) sample measured at X-band and Q-band frequencies, and GNR-VO solution (orange) sample measured at Q-band frequency. The black dashed lines are simulated spectra. The solution is prepared using tetralin as solvent. The arrows denote the locations at which the T_1 and T_m were measured. The spectra have contributions from spin states in the GNR backbone (GNR state) and in the vanadyl porphyrins (VO state). (b) Spin coherence time T_m of the GNR state (filled markers) and the VO state (empty markers) of a powder sample at X-band (purple diamonds), a powder sample at Q-band (purple circles), a solution sample at Q-band (orange circles). Solid lines are guides to the eyes. (c) Spin–lattice relaxation time T_1 of the GNR state (filled markers) and the VO state (empty markers) of powder sample at X-band (purple triangles), powder sample at Q-band (purple squares), solution sample at Q-band (orange squares). Solid lines are guides to the eyes. (d) Inverse of T_1 of the GNR state (filled markers) and the VO state (empty markers) of powder sample at X-band (purple diamonds), powder sample at Q-band (purple circles), solution sample at Q-band (orange circles). Solid lines (for the GNR state) and dashed lines (for the VO state) are fits to the data using models that will be explained in the main text. Different background colours correspond to the temperature ranges with different dominant relaxation mechanisms. At temperatures below 20 K, direct process and cross-relaxation mechanisms are used for the powder sample at X-band, while only the direct process is used for Q-band data. At intermediate temperatures, the Raman process is dominant in all cases. The Orbach process is used only for solution samples above 200 K.

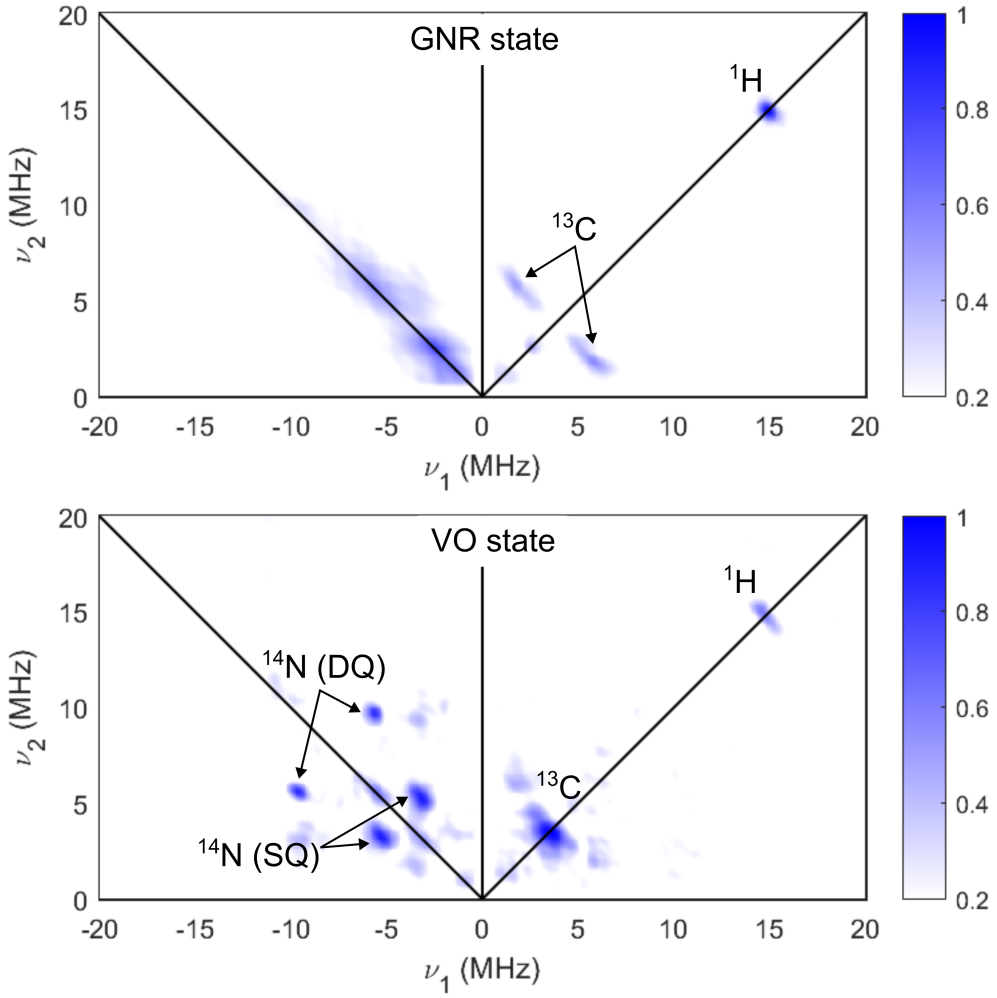


Figure 5.12: HYSCORE spectra of the GNR state and the VO state of GNR-VO. The former was measured for a powder sample, whereas the latter was measured for a solution sample. The peaks resulting from hyperfine interactions with ^{13}C, ^{1}H, and ^{14}N nuclei are labelled in the graph. SQ and DQ stand for single-quantum and double-quantum transitions, respectively.

mono-exponential model. All the T_1 were obtained by fitting the saturation recovery data with a bi-exponential model, except for the VO state of the solution sample measured at Q-band, for which a mono-exponential model produces a better fit. This can be possibly related to the low grafting ratio of porphyrins in GNR-VO. The fast relaxation channel in a bi-exponential model is mainly mediated by instantaneous diffusion, where an observed spin is affected by flipped spins nearby. In the solution sample, each ribbon is separated from other ribbons. Furthermore, because of a possible low grafting ratio, each porphyrin is likely to be separated

Table 5.4: Fit parameters of spin–lattice relaxation mechanisms for GNR-VO samples, including powder sample measured at X- and Q-band, and solution (tetralin) sample measured at Q-band.

	condition	$A_{\mathrm{dir}}\,(\mathrm{K^{-1}s^{-1}})$	$A_{\mathrm{cro}}\,(\mathrm{s^{-1}})$	$\Delta_{\mathrm{ST}}\,(\mathrm{K})$	$A_{\mathrm{Ram}}\,(\mathrm{s^{-1}})$	$\theta_{\mathrm{D}}\,(\mathrm{K})$	$A_{\mathrm{Orb}}\,(\mathrm{K^{-3}s^{-1}})$	$\Delta_{\mathrm{Orb}}\,(\mathrm{K})$
GNR state	powder (X)	149.1	1.64×10^4	9.67	–	–	–	–
	powder (Q)	28.83	–	–	1.20×10^5	210.6	–	–
	solution (Q)	9.342	–	–	3.13×10^4	192.3	4.90×10^4	6113
VO state	powder (X)	224.6	1.04×10^4	9.32	3.69×10^5	199.6	–	–
	powder (Q)	24.01	–	–	1.29×10^5	206	–	–
	solution (Q)	16.82	–	–	1.41×10^6	207	–	–

far from other porphyrins within the ribbon. Therefore, in the GNR-VO solution sample, a porphyrin is relatively isolated from other porphyrins. Consequently, the instantaneous diffusion is insignificant due to the large distance between VO spins, and thus no fast relaxation channel exist for the VO spins.

By comparing T_{m} (Figure 5.11b) and T_1 (Figure 5.11c) of the powder sample and the solution sample, we find that T_1 is more sensitive to frequency change whereas T_{m} is more sensitive to the π-stacking of the ribbons. The frequency dependence of T_1 has been studied both theoretically and experimentally before [308, 373]. The spin–lattice relaxation time is roughly proportional to the square root of the microwave frequency, $\sqrt{\nu}$ [373]. In comparison, T_{m} is more influenced by spin–spin coupling and nuclear spin diffusion. The elimination of π-stacking of ribbons in the solution sample significantly enhances T_{m}, reaching 1.5–2.0 µs at around 40 K. Above 200 K, T_{m} of both spin species in the solution sample is affected by the increased molecular motion and softening of the glassy matrix, and thus decreases to a similar level as in the powder sample.

We, furthermore, fitted the spin–lattice relaxation rate, $1/T_1$, versus temperature using the models mentioned in the last section. A summary of the fit parameters can be found in Table 5.4. The Raman process dominates the spin–lattice relaxation between 20 K and 200 K, while for temperatures exceeding 200 K, the Orbach process takes precedence. For temperatures below 20 K, the direct process is

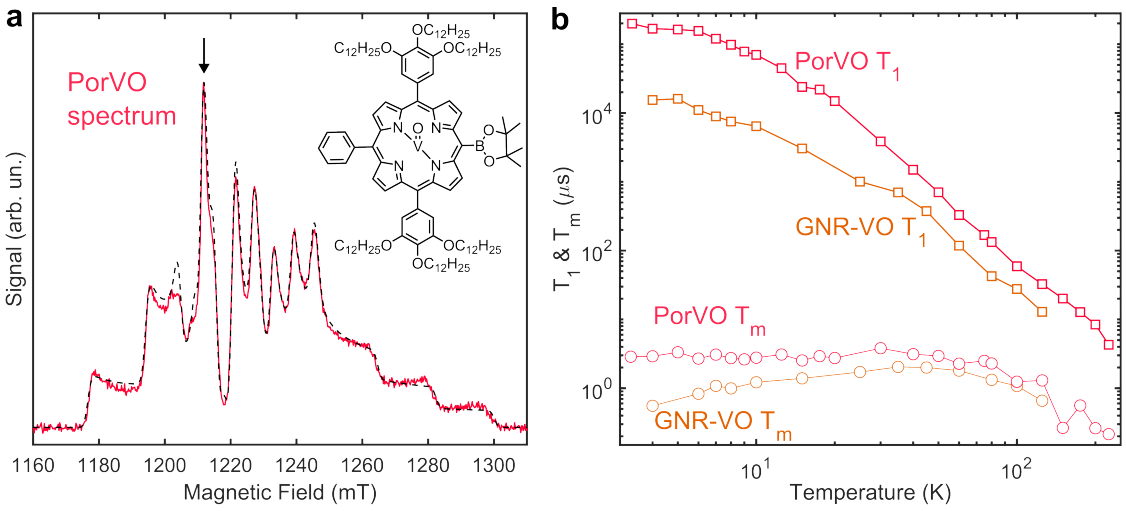


Figure 5.13: Comparison of T_1 and T_m of the VO states in GNR-VO and vanadyl porphyrin. (a) The EDFS spectrum (red solid line) of vanadyl porphyrin (PorVO) sample dissolved in tetralin. The black dashed line is the simulated spectrum. The structure of PorVO is shown in the inset. The arrow denotes the fields at which T_1 and T_m were measured. (b) The T_1 (squares) and T_m (circles) of GNR-VO (orange) and PorVO (red) samples. The solid lines are guides to the eyes.

evident for all samples. Cross relaxation is only observable in the powder sample measured at X-band frequency, but not at Q-band frequency. This could be attributed to the overwhelming influence of the direct process at Q-band frequency, which is proportional to B^4, thereby rendering the cross-relaxation process less noticeable [240].

Finally, we compare the spin dynamics of the VO state in GNR-VO with that in the vanadyl-porphyrin precursor, denoted as PorVO. Figure 5.13a shows the spectrum of the vanadyl porphyrin that was used to synthesise GNR-VO. The dashed line is the simulated spectrum. The T_1 and T_m are extracted from bi-exponential and mono-exponential fitting, respectively. It can be found that both T_1 and T_m of PorVO are longer than those of VO state of GNR-VO for all temperatures. The lower T_1 of VO spins in GNR-VO is likely because the spin–lattice relaxation of these VO spins is affected not only by the vibration of porphyrin, but also by the vibration of the GNR backbone. The lower T_m of VO spins in GNR-VO is probably because of the interactions between different porphyrin side groups within the GNR,

or interaction between the porphyrin side groups and the GNR state.

5.4 Summary and outlook

In summary, we have studied two kinds of spin states in GNRs using both computational and experimental approaches. Specifically, we focused on the spin state in GNRs that can be synthesised in ambient conditions rather than ultra-high vacuum conditions that were conventionally used in literature. The quantum properties of the spin states in such GNRs can be experimentally characterised by EPR, which is difficult to access by the conventionally more often used STM.

In the first section, we discussed the spin polarisation of topological end states. It is supplementary to the investigation of topological phases in Chapter 4. In Section 2.2 we revealed the relationship between $\mathbb{Z}$ topological index and Clar's sextet rule. The Clar's sextet rule is widely used in the field of organic chemistry to check the stability of different resonance structures of an aromatic molecule. Some aromatic molecules have unpaired electrons in their most stable resonance forms. In this chapter, we have shown that the $\mathbb{Z}$ topological index can be related to the number of unpaired electrons in a finite GNRs. We also gave two examples, peri-tetracene and 8-AGNR, which have recently been synthesised in the solution phase. The next step in this field will be incorporating these spin states in GNRs in real devices and studying them in more facile conditions.

In the second section, we studied the spin states in functionalised cove-edge GNRs using pulsed EPR techniques. Our results suggest that the cove-edge GNRs contain defects, which produce EPR signals and interfere with the study of the interesting spin states. At the moment we are unable to determine the level of defects in the sample, because we only have a very limited amount of sample, which could not be weighed accurately with the given instruments. The synthesis route needs to be optimised in the future to suppress these defects. We also proved that

the spin coherence time can be significantly increased by dissolving GNRs with bulky side groups in solutions, where the π-stacking of ribbons is eliminated. The results also imply that the coherence time can be even longer if one builds a GNR-based single-molecule device, where both π-stacking and surrounding nuclear spin bath are removed. For the GNR-VO sample, DFT calculation results suggest that the spin states in vanadyl-porphyrin are very localised and not likely to be injected to the GNR backbone. Nonetheless, our study opens the possibility of integrating multiple spin species in GNRs using a bottom-up synthesis approach. These spin species can work as qubits and can be addressed at different frequencies[371]. In addition, we also proved that the spin–lattice relaxation time and spin coherence time of vanadyl spin will be reduced after connecting the vanadyl porphyrin to GNR backbone. The result provides valuable information for designing quantum devices based on GNRs in the future. Finally, we also analysed the spin–lattice relaxation mechanisms and the possible factors that influence the spin coherence time. We have briefly mentioned the role of phonon modes in Raman process and Orbach process. The quantum nature of the phonons, however, can not be revealed from EPR measurements. In next chapter, we will delve into the vibrational states of GNRs and present the experimental observation of discretised phonon excitations in single-molecule transport measurements and optical characterisations.

5.5 Project overview

The peri-tetracene molecule in Figure 5.4a was synthesised by Prof. Jishan Wu's group from the National University of Singapore. The 8-AGNR in Figure 5.4b and GNR-CN in Section 5.3.1 was synthesised by Dr. Xuelin Yao. The GNR-VO in Section 5.3.2 was synthesised by Dr. Xuelin Yao and Dr. Dimitris Alexandropoulos. Dr. Michael Slota and Dr. William Myers gave me training on the EPR spectrometer. I conducted all the EPR measurements and data analysis. Karen Yan assisted me

with the measurements of GNR-VO. I carried out all the theoretical calculations presented in this chapter.

6

Interplay between Electronic States and Phonons in GNRs

Contents

6.1 Introduction 197
6.2 Manifestation of vibrational states in single-molecule transport 199
6.2.1 Comparison of GNRs with different solubilities 199
6.2.2 Signature of vibrational modes in stability diagrams . . . 202
6.3 Manifestation of vibrational states in optical spectra . 208
6.3.1 Band structure analysis 209
6.3.2 Vibrational and optical properties 214
6.4 Summary and outlook 224
6.5 Project overview 226

6.1 Introduction

Vibrational modes of GNRs carry fingerprint information about the structures of the GNRs. The vibrational properties of the two most basic GNRs, armchair and zigzag GNRs, have been extensively calculated [270, 271, 292]. These properties are often revealed in Raman spectra [273, 293, 374, 375], providing a crucial characterisation of GNRs' structures [106, 272, 276]. In fact, lattice vibrations of GNRs affect many

properties, such as spin relaxation, electron transport, and optical transitions. In the previous chapter, we analysed the spin–lattice relaxation of spin states in GNRs. Some relaxation mechanisms, such as Raman processes or Orbach processes, are assisted by the GNR's lattice vibrations. The quantum behaviour of vibrational modes, however, are not directly observable in EPR measurements. In this chapter, we will examine the manifestations of the vibrational states of GNRs in two realms, single-molecule transport and optical measurements, where we will see the quantum behaviours of phonons. We carried out theoretical calculations of vibrational modes of GNRs, which provide a solid support for understanding the experimental results.

In this chapter, the GNRs used in experiments are the cove-edge GNRs with bulky side groups that are the same as those investigated in Section 5.3. Traditionally, such cove-edge GNRs were often grafted with long alkyl chains at the edges [125, 376]. Although these ribbons are processable in a liquid phase, they are very prone to aggregation, making the quantum states in an individual ribbon inaccessible. Here, we demonstrate a new generation of soluble GNRs by using bulkier side groups. The stable solution of such GNRs has enabled the fabrication of single-molecule devices. Very clean features of vibrational levels were resolved from quantum transport measurement. The transport measurement results lay the foundation of utilising soluble GNRs in next-generation electronic devices with high compactness and performance. Furthermore, in soluble GNRs, we discovered a boost of photoluminescence quantum yield compared with those with poor solubility. The calculations of vibrational modes play a crucial role in elucidating the optical spectra and unraveling the electron–phonon coupling. In the following, we will delve into the specifics of these key manifestations of vibrational states in single-molecule transport and optical measurements.

6.2 Manifestation of vibrational states in single-molecule transport

6.2.1 Comparison of GNRs with different solubilities

As we have shown in this work, GNRs possess a plethora of intriguing electronics states. To exploit the topological and spin phenomena in quantum electron transport, a high-quality single-electron transistor with a certain level of cleanliness is necessary, so that the electronic states of a single molecule can be accessed. Although the bottom-up synthetic approach is able to produce various GNRs with a large degree of control over their structures, the integration of bottom-up synthesised GNRs into electronic nanodevices is still in its infancy. Traditional GNRs tend to agglomerate and form carpets, which are not conducive to fabricating single-molecule devices. In this chapter, we will demonstrate a strategy to achieve exceptional electronic cleanliness through the debundling[1] of GNRs produced by the chemical design of side groups.

Cove-edge GNRs can be functionalised with two different types of side groups, which are shown in Figure 6.1a. The first type is the more conventionally used long alkyl chains. Such GNRs, labelled as GNR-alkyl, have poor solubility in solvents. The second type is a newly designed three-dimensional bulky side group, with a diameter of about 0.5 nm, significantly larger than the distance between layers of π-stacked graphite (0.3 nm). This bulky group, labelled as AOM, is a cycloadduct synthesised from the Diels–Alder reaction of anthracene with *N*-octadecylmaleimide. The AOM bulky group was also used in GNR-Br, GNR-VO, and GNR-CN that we discussed in Chapter 5. The grafting ratio of AOM groups is estimated to be about 77%, with the remaining side groups being unreacted anthracenes. We label this type of ribbon as GNR-AOM for simplicity. Note that these side groups have neutral

[1] Debundling means separating and dispersing aggregated bundles of nanoribbons into individual, isolated nanoribbons.

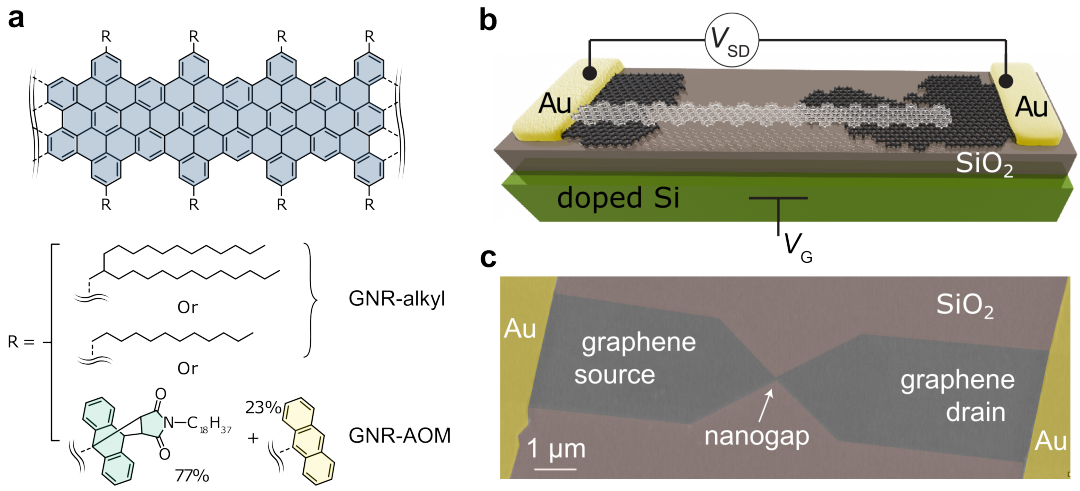


Figure 6.1: Structure of cove-edge GNRs and single-molecule device. (a) Structures of the cove-edge GNRs with different side chains. The side chains on the top are alkyl chains, while those at the bottom are the bulky (AOM) groups that can hinder π-stacking of ribbons. These two kinds of GNRs are labelled as GNR-alkyl and GNR-AOM, respectively. For GNR-AOM, the grafting ratio of AOM groups and anthracene groups are 77% and 23%, respectively. The GNRs were synthesised by Dr. Wenhui Niu et al. (b) Device geometry used for quantum-transport measurements. A GNR bridges two graphene electrodes. The side groups are omitted for clarity. A bias voltage (V_{SD}) is added between the source and drain electrodes. A 300 nm SiO_2 layer on an n-doped Si wafer is used as the gate electrode. (c) Scanning electron microscope image of the device, with false colours. Experimental data were provided by Dr. Wenhui Niu, Dr. Simen Sopp, Dr. Alessandro Lodi, and Dr. Alex Gee [38].

charges and are singly connected with the backbone through covalent bonds. They only influence solubility and have negligible impact on the electronic properties.

Single-electron devices using GNR-alkyl and GNR-AOM are fabricated to demonstrate the effect of debundling on the electron transport in quantum electronics. Figure 6.1b illustrates a schematic diagram of the device, and Figure 6.1c is scanning electron microscopy (SEM) image of it. A GNR bridges the electro-burned gap between two graphene leads of width d = 1–10 nm. These two graphene leads serve as source and drain electrodes, respectively, and each one is connected to a gold pad. The gate electrode can either be an n-doped Si wafer with an oxide layer, or a Pd electrode etched into undoped Si and covered by HfO_2. We only show the former one in Figure 6.1. The GNR molecules are added to the device by drop casting from solutions, with a yield of approximately five out of every

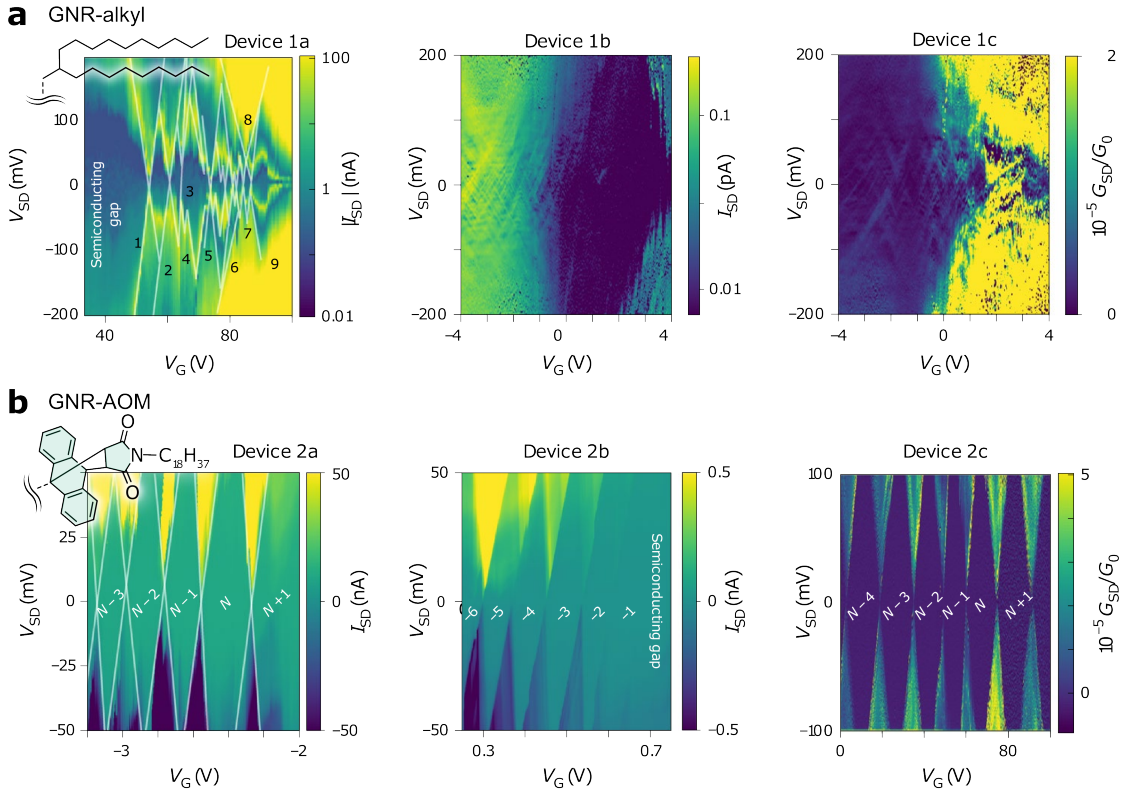


Figure 6.2: Stability diagrams of the devices fabricated using (a) GNR-alkyl and (b) GNR-AOM. Three devices were measured for each kind of GNR. We plotted either the source–drain current (I_{SD}) or the differential conductance (G_{SD}) (in units of the conductance quantum G_0) versus the source–drain bias voltage V_{SD} and gate voltage V_G. All measurements were carried out at temperatures below 500 mK. Coulomb diamonds, where possible, are labelled with an arbitrary number of electrons N. Experimental data were provided by Dr. Simen Sopp, Dr. Alessandro Lodi, and Dr. Alex Gee [38].

one hundred electro-burned gaps. A successful deposition of GNR molecules on an electro-burned gap can be confirmed by a sharp increase in tunnelling current compared with that before the molecule deposition.

We measured three devices for both GNR-alkyl and GNR-AOM. As shown in Figure 6.2, the stability diagram of GNR-alkyl device features a wide region of suppressed conductance, corresponding to the HOMO–LUMO gap. Multiple overlapping Coulomb diamonds of different sizes also appear (Figure 6.2a), which can be attributed to multiple nanoribbons bridging the nanogap, with each nanoribbon having different electrostatic couplings with surrounding electrodes. Furthermore, excited states are indistinguishable inside the diamonds. In stark contrast, the

single-electron transistors (SETs) fabricated from GNR-AOM exhibit exceptionally clean conduction features. The Coulomb diamonds have sharp edges, identical slopes and sizes, and display clear periodicity (Figure 6.2b). These features indicate the presence of a single nanoribbon in the nanogap for each device.

6.2.2 Signature of vibrational modes in stability diagrams

In addition, excited states appear as sharp lines inside the sequential tunneling region, running parallel to the Coulomb edges. This becomes more obvious when zooming in on a diamond. For instance, in Figure 6.3b, we present a high-resolution Coulomb diamond measured from device 2c. Equidistant lines parallel to the Coulomb diamond edge can be identified. These are typical features of vibrational excitations [377–379]. Conductance peaks originating from spin excitations would split in a magnetic field [380], while lead states are characterised by differential conductance peaks running non-parallel to the Coulomb diamond edges and exhibiting periodic patterns of positive and negative values [381]. Hence, excitations due to spin or lead can be ruled out. The evenly spaced conductance peaks observed in our experiments, which are parallel to the Coulomb diamond edge and insensitive to magnetic fields, can be unequivocally attributed to vibrational states.

Furthermore, we observed that in almost all Coulomb diamonds the conductance close to zero bias is suppressed compared with those at slightly higher bias. This is a feature of Franck–Condon blockade, which means that the electron transmission is suppressed at low bias when phonon-assisted transport is not available. According to the Franck–Condon principle, the transition probability is proportional to the square of the overlap of the vibrational wavefunctions (or nuclear coordinates) before and after electron tunnelling. Electron tunnelling is more probable to happen when this overlap is large. In other words, electrons are most probably transmitted when the changes in nuclear positions are minimal. Usually, a molecule has different equilibrium nuclear configurations in neutral and charged states,

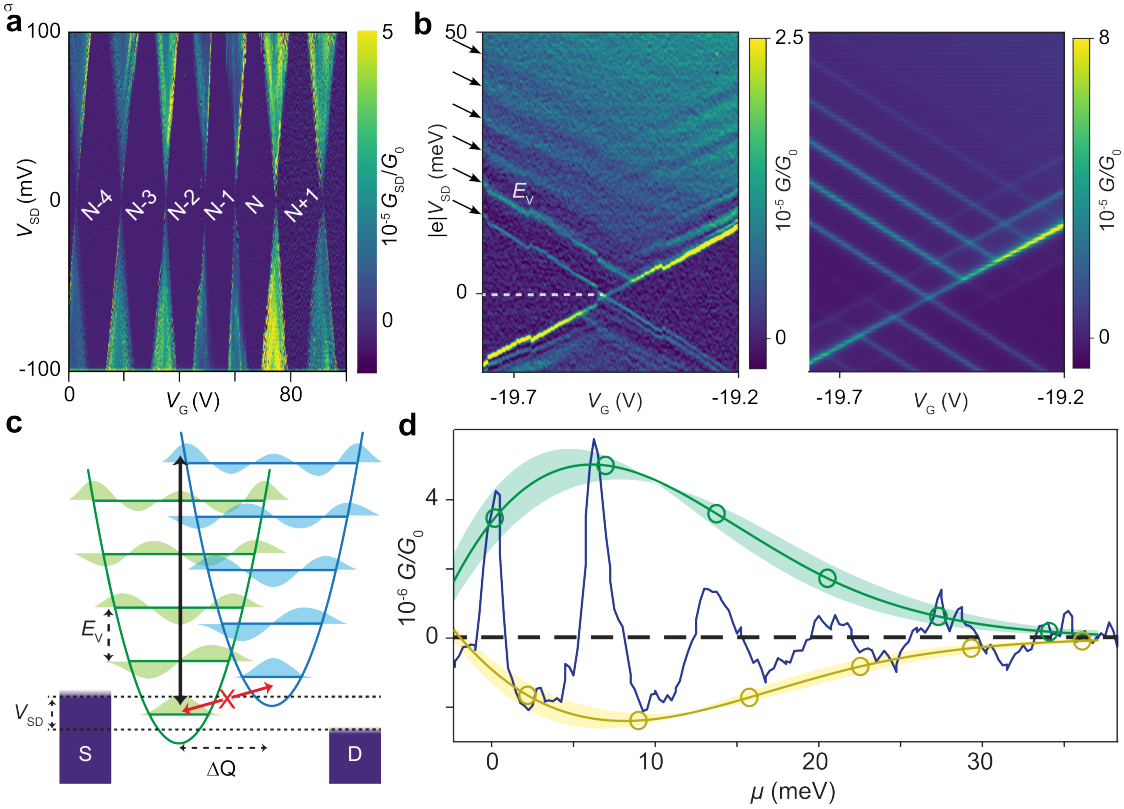


Figure 6.3: Signatures of electron–phonon coupling in single-molecule measurements on GNR-AOM. (a) Stability diagram of device 2c, the same as that shown in Figure 6.2b. (b) Differential conductance G versus source–drain voltage V_{SD} and gate voltage V_G with higher resolution (left) and a simulation using a quantum rate-equation model (right). G_0 is the conductance quantum. The excited states are indicated by arrows. The vertical distance between the equidistant lines corresponds to the quantisation energy E_v. The measurements were carried out at $T = 20\,\text{mK}$. (c) Schematic diagram of the Franck–Condon blockade for electron transport in single-molecule devices. Two adjacent charge states (green and blue) have different equilibrium coordinates, represented by a horizontal shift ΔQ. The transitions between ground states are suppressed while ground-to-excited-states transitions are possible at high bias voltages. (d) Conductance peaks as a function of the chemical potential μ (blue line). The green and yellow lines and circles are the maxima and minima simulated using the Franck–Condon model, with shaded areas indicating confidence intervals. Experimental data were provided by Dr. Simen Sopp, Dr. Alessandro Lodi, and Dr. Alex Gee. Simulations were conducted by Dr. Simen Sopp [38].

which means the nuclear coordinates of the vibrational ground state of neutral and charged molecule have a very small overlap. In contrast to that, the ground state of the neutral molecule might have a larger overlap with a vibrational excited state of the charged molecule. Considering that electron tunneling happens on a significantly faster timescale than the movement of nuclear positions, the electron

tends to hop to the vibrational excited state of the molecule by emitting a phonon, rather than hop to the vibrational ground state of the molecule. Figure 6.3c illustrates the Franck–Condon blockade using a schematic diagram, where two different charged states are represented by two parabolas[2], and different vibrational levels are represented by shaded wavy lines.

In practice, electron transmission may involve multiple vibrational levels, i.e. multiple number of phonon excitations. Quantitatively, the maximum of differential conductance peaks can be described by the following equation:

$$G_n^{\max} \propto \frac{\mathrm{e}^{-\lambda}\lambda^n}{n!}, \tag{6.1}$$

where n is the phonon quantum number, and λ is the electron–phonon coupling parameter. This equation can determine the probability of how much each vibrational level is involved in electron transport. By using this equation, we obtained an excellent fit for both the stability diagram (Figure 6.3b) and the conductance peaks at a fixed gate voltage (Figure 6.3d). The vertical distance between the parallel equidistant lines in Figure 6.3b represents the energy of the associated vibrational mode, $E_\mathrm{v} = \hbar\omega$, where ω is the vibrational frequency. From the fitting we determined that the phonon energy E_v is approximately $7.0 \pm 0.2\,\mathrm{meV}$. When an additional bias voltage eV_SD matches integer multiples of the vibrational energy, i.e. $n\hbar\omega$, the electron will jump to the molecule from the source electrode, accompanied by a transition from the vibrational ground state to the n-th excited state. In other words, electron tunneling is assisted by the emission of n phonons. According to Equation (6.1), the number of emitted phonons follows a Poisson distribution. The parameter λ represents the average number of phonons emitted during electron transport. In some literature it is called the Huang–Rhys factor[3]. A larger λ indicates a stronger electron–phonon coupling of a vibrational mode and more

[2]Each parabola stands for the energy of the molecule as a function of nuclear coordinates.

[3]The Huang–Rhys factor λ is related to the reorganisation energy E_reog by $E_\mathrm{reog} = \lambda\hbar\omega$. In some other convention the symbol λ is used to represent the reorganisation energy [382].

phonons emitted during electron transport. In our case, the simulation yields $\lambda = 1.5 \pm 0.2$, which validates the theoretical prediction of strong electron–phonon coupling in GNRs [383].

We further investigated the vibrational mode that was involved in the single-molecule transport measurement using DFT calculations. Given that the ribbons are typically around 100 nm long, we calculated the phonon dispersion of the ribbon with periodic boundary conditions. We carried out these calculations with SIESTA [299], using PBE-GGA exchange–correlation functional [288] and DZP numerical atomic basis. Sufficient vacuum distance was added along the non-periodic directions to avoid unwanted interactions. The k sampling was set to $50 \times 1 \times 1$ and mesh cutoff was set to 800 Ry to ensure better convergence. Tighter force convergence criteria were used for the structural optimisation before carrying out the phonon calculation. The structure was relaxed until the maximum atomic force was below 0.004 eV/Å. The phonon dispersion relation was calculated with a $3 \times 1 \times 1$ supercell, where 3 represents the number of unit cells along the longitudinal direction. Since the real structure is very bulky, we had to simplify the structure for calculations. We attempted different simplification protocols, i.e. either replacing all the side groups with hydrogens, or replacing them with anthracene groups. In Figure 6.4, we present the phonon dispersion of a bare cove-edge GNR without any functionalisation groups (left) and a cove-edge GNR with anthracene side groups (right). For the anthracene-functionalised GNR, we identified a transverse bending mode (TBM) with 6.92 meV at the Γ point, which is in excellent agreement with the observed vibrational state in our experiments. Upon removal of the anthracene side groups, the energy of TBM reduces to 5.44 meV. We also showed the vector representation of TBM in Figure 6.4. The results suggest that the presence of side groups restricts the bending of the backbone, leading to a smaller amplitude and a higher energy of the bending mode.

In the real structure, the side groups are a mixture of anthracene and AOM groups. For the calculation shown in Figure 6.4, we replaced all the side groups

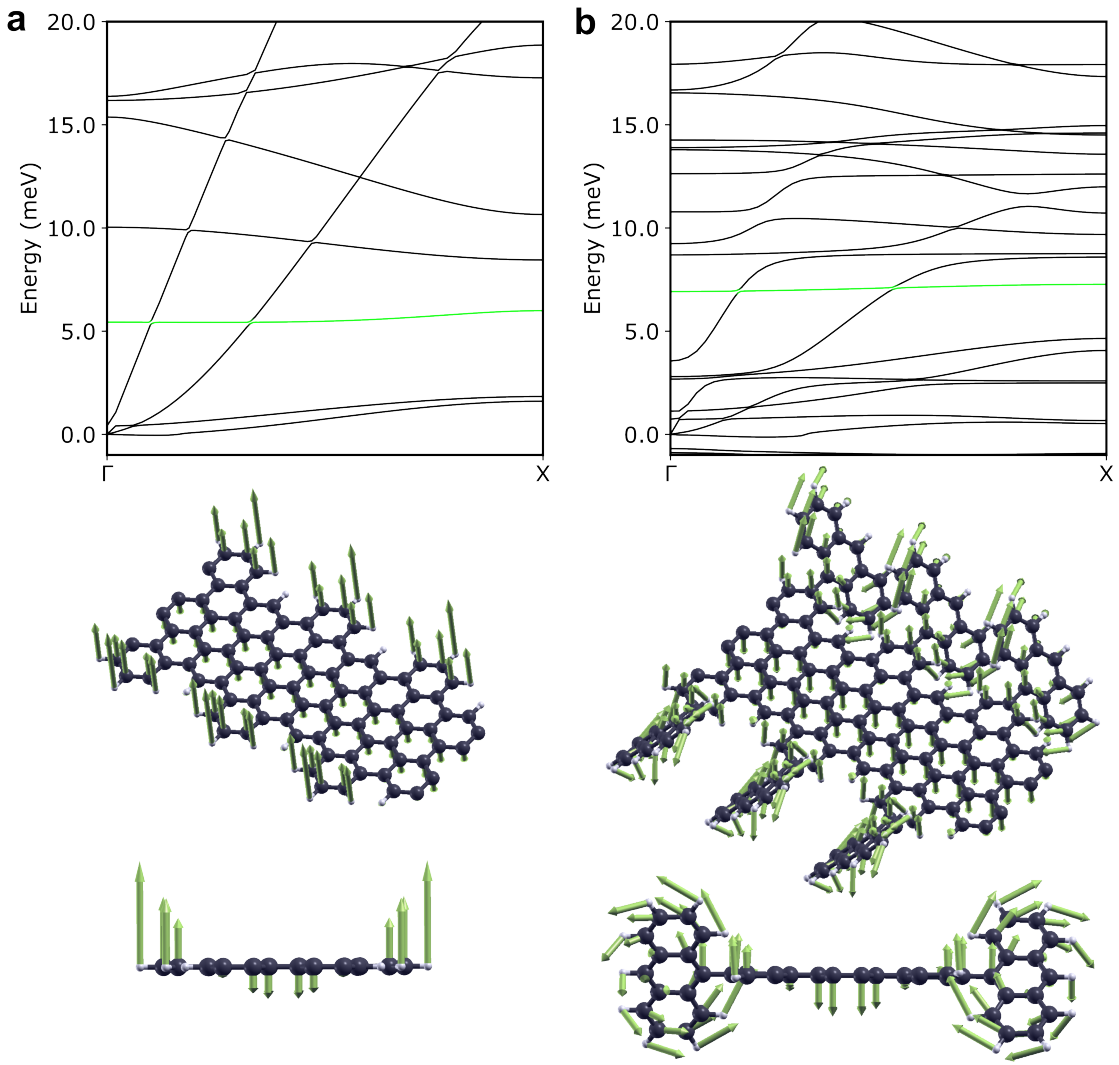


Figure 6.4: Transverse bending mode (TBM) of cove-edge GNR (a) without functionalisation groups and (b) with anthracene side groups. Phonon dispersion for each structure is plotted on the top, with the TBM highlighted in green. The vector representations of the TBMs are shown at the bottom.

with anthracene groups. Since the anthracenes are connected with the backbone through single bonds, they can be easily rotated. In the previous calculation, the anthracene groups on opposite sides of the ribbon had different orientations. We attempted another initial configuration, in which the anthracene groups at opposite sides had the same orientation, and repeated the structural relaxation and phonon calculations. The results are presented in Figure 6.5a, where the TBM has an energy of 7.48 meV. We also attempted to use the AOM side groups directly in

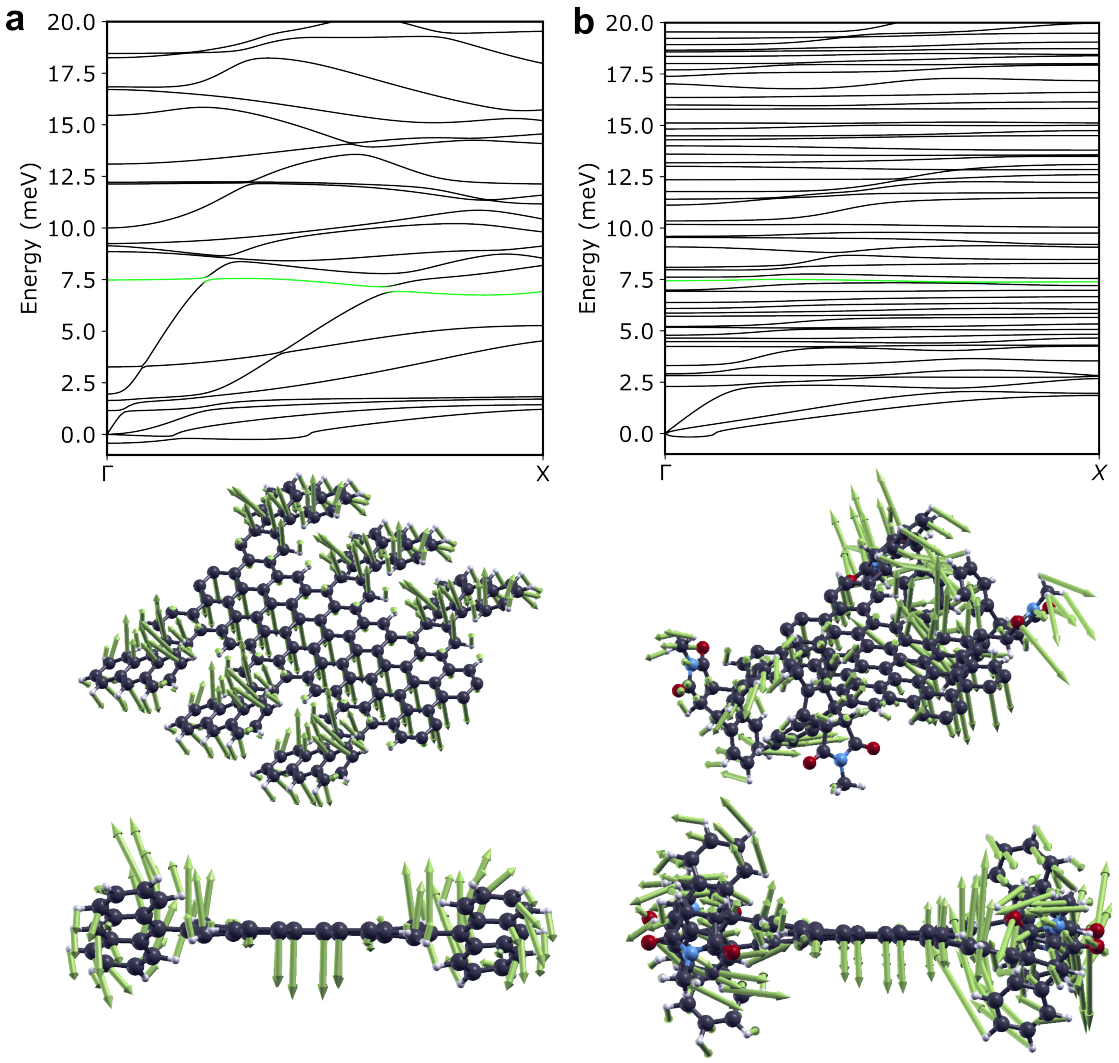


Figure 6.5: Transverse bending mode (TBM) of cove-edge GNR with different side groups. (a) Phonon dispersion (top) and vector representation of the TBM (bottom) of the cove-edge GNR grafted with anthracene groups that have the same orientations on opposite sides. (a) Phonon dispersion (top) and vector representation of the TBM (bottom) of the cove-edge GNR with AOM groups, where the alkyl chains are replaced with hydrogens. The TBMs are highlighted in green in both phonon dispersion plots.

the calculation, with the hope of achieving better agreement with the experimental result. The actual structure of AOM group is shown in Figure 6.1a, where there is a long alkyl chain. In our calculation we removed the alkyl chain and replaced it with a hydrogen. Although this structure is closer to the real situation, the calculation is very computationally demanding. Because of the steric hindrance between AOM groups in adjacent unit cells, the AOM groups cannot be simply translated to the

next unit cell but have to be rotated. Consequently, we had to use a supercell consisting of two unit cells as the repeating unit in the DFT calculation. For such a large unit cell, the k-sampling and mesh cutoff had to be decreased to $11 \times 1 \times 1$ and 200 Ry, respectively. The supercell parameter used in the phonon calculation was also reduced to $1 \times 1 \times 1$. The phonon dispersion and TBM are shown in Figure 6.5b. The phonon dispersion becomes very dense due to the contribution of the vibration modes of the side groups. The energy of the TBM is 7.44 meV for the ribbon with AOM groups. These results still align with the experimental observations.

To conclude, we have demonstrated the superiority of soluble GNRs in fabricating single-molecule devices. Most importantly, we are able to reveal the quantum nature of phonons from quantum-transport measurements. The emission of phonons are clearly observed from the discretised vibrational excited states in stability diagrams. We confirmed the strong electron–phonon coupling of transverse bending mode in cove-edge GNRs. As we will see in the next section, the transverse bending mode also plays a role in optical transitions in cove-edge GNRs.

6.3 Manifestation of vibrational states in optical spectra

The solubilisation of GNRs is beneficial not only for the fabrication of single-molecule devices, but also for achieving high photoluminescence (PL) yield. The PLQE of conventional carbon nanomaterials is often limited by disorder, inter-ribbon interactions, and non-radiative dark states [384]. For example, a single suspended CNT can have a 7% PLQE [385]. Bundles of CNTs, however, have a very low yield around 1–2% when dispersed in solvents [386–388]. Although the use of surfactants can increase the PLQE of CNTs to 20% [389], they are detrimental to the intrinsic electronic properties of CNTs [390, 391]. These issues can be resolved by synthesising molecular GNRs using a bottom-up approach. The bulky side groups can effectively suppress π-stacking and inter-ribbon interactions, without

harming the π-conjugation of the ribbon backbone. In this section, we will present our recent studies on the optical characterisations of the two GNRs used in the last section: GNR-alkyl and GNR-AOM. In the soluble GNR-AOM sample, we discovered a bright fluorescence. Assisted by DFT calculations, we identified the signatures of electron–phonon coupling from experimental features. The optical measurements were conducted by Bernd Sturdza from the Department of Physics in Oxford. The samples were prepared by Dr. Wenhui Niu, Dr. Ji Ma from TU Dresden, and Dr. Xuelin Yao from my group.

6.3.1 Band structure analysis

The band structure of GNR-AOM was calculated with SIESTA using the parameters described at the beginning of Section 4.2. Similar to the calculation in the last section, we used a supercell for the band structure calculation because of the steric hindrance between the bulky groups. The alkyl chains attached to AOM groups were also removed to simplify the calculation. Figure 6.6b–c display the band structure and PDOS of GNR-AOM, respectively. The frontier bands mainly stem from the ribbon backbone, whereas the energy levels of the side groups are far from the Fermi level and thus do not interfere with the optical transitions, which involve only the two highest valence bands and the two lowest conduction bands. We labelled four interband transitions in Figure 6.6b, where the number 1 denotes the valence or conduction band that is closest to the Fermi level, and the number 2 denotes the valence or conduction band that is second closest to the Fermi level. According to the theoretical studies of Villegas et al., the transitions E_{11} and E_{22} are forbidden, while the two allowed transitions E_{12} and E_{21} actually arise from a combination of the transitions between the two highest valence bands and the two lowest conduction bands [53]. We label the transitions here and will reveal them in the experimental results later. Although the band structure calculated from DFT is not as accurate

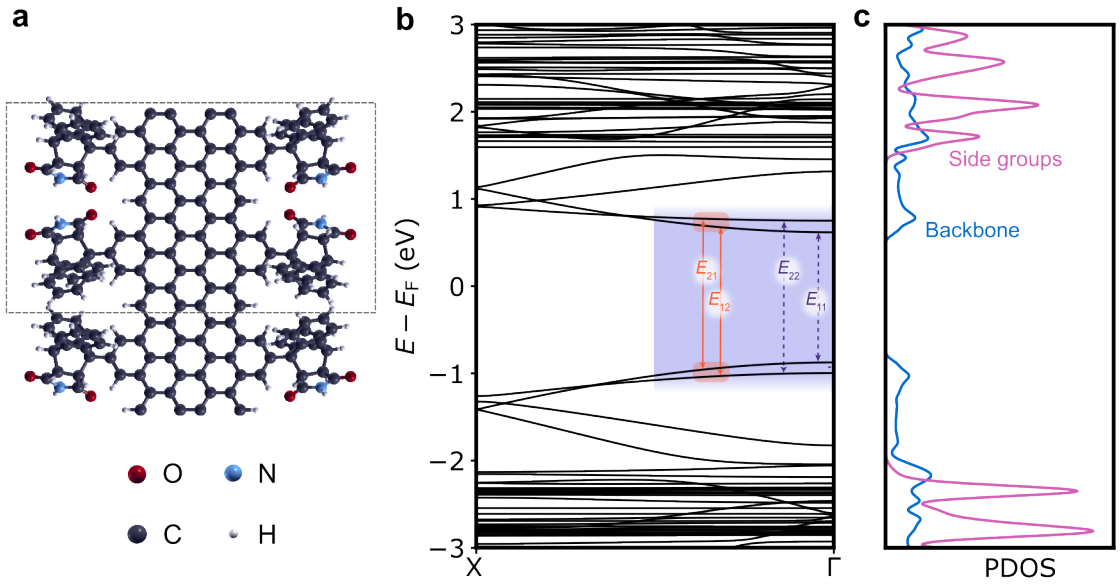


Figure 6.6: Band structure and projected DOS of GNR-AOM. (a) Structure of GNR-AOM. The unit cell used for DFT calculations is highlighted in the dashed box. (b) Band structure of GNR-AOM. The forbidden (E_{11} and E_{22}) and allowed (E_{12} and E_{21}) optical transitions are highlighted in purple and orange, respectively. (c) Projected DOS (PDOS) of GNR-AOM showing contributions of the backbone (blue) and side groups (magenta). A 0.05 eV Gaussian broadening was used for the PDOS.

as that from GW approximation, our band structure is qualitatively very similar to that from GW-calculation [53] and can still be used to analyse the optical spectra.

In Figure 6.7, we compare the band structures of graphene, a (6,6) CNT, a 6-ZGNR, and a cove-edge GNR, and illustrate the brightening mechanism of photoluminescence in GNR-AOM. The band structures of graphene and (6,6) CNT were calculated from the tight-binding model since it is accurate enough for our analysis here. We had to calculate the band structure of the 6-ZGNR using DFT, as the tight-binding model predicts a false zero band gap. The CNT can be obtained by rolling up a piece of graphene, and as a consequence, the Brillouin zone changes from 2D to 1D. The wavevector remains continuous along the longitudinal direction, but becomes discrete along the transverse (circumferential) direction. This is also true for the GNRs. Therefore, we represent the Brillouin zones of the CNT and GNRs as discrete lines in reciprocal space. In Figure 6.7, we colour the band structures based on the projection weight of the CNT/GNR states onto graphene

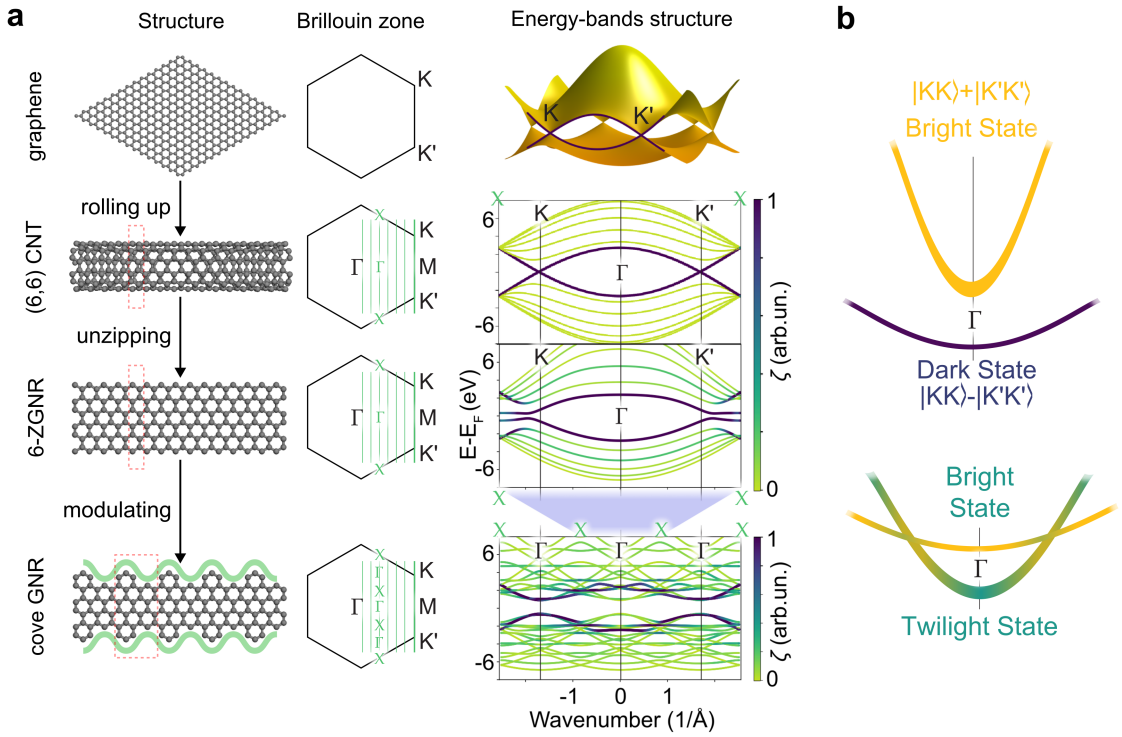


Figure 6.7: Valley mixing and twilight states. (a) The structure (first column), Brillouin zone (second column), and energy-band structures (third column) of graphene, a (6,6) CNT, a 6-ZGNR, and a cove-edge GNR. The red dashed boxes represent the unit cells. The first Brillouin zone of graphene is a hexagon, while that of the CNT and the GNRs are lines, with discretised wavevectors (green lines) along the lateral direction. The energy bands of the CNT and the GNRs are coloured based on their projection weight ζ onto the graphene states along the ticker green lines (in the second column) that pass through K–M–K′. (b) Twilight states resulting from valley mixing. The linear combinations of K valleys lead to either bright or dark states in the (6,6) CNT or 6-ZGNR. The valley mixing in cove-edge GNRs yields a twilight state in addition to the bright state. The twilight state will be explained later in the following subsection.

states, i.e. $\|\langle\Psi_{nk}^{\text{graphene}}|\Psi_{nk}^{\text{CNT/GNR}}\rangle\|$. Using the zone-folding approximation explained in Section 2.1.1, we analyse how the band structures of the CNT and GNRs are derived from that of graphene. The band structure of the (6,6) CNT in Figure 6.7 is coloured based on the projection along the k path that passes through K–M–K′, represented by a thicker green line. We can see that the valence band and the conduction band of the CNT are highlighted by projecting the CNT bands onto the graphene bands along that k path. In Figure 6.8, we project the CNT states onto graphene states ($\|\langle\Psi_{nk}^{\text{graphene}}|\Psi_{nk}^{\text{CNT}}\rangle\|$) along all the discrete k lines, where each k line corresponds to a subband in the band structure. The whole band structure

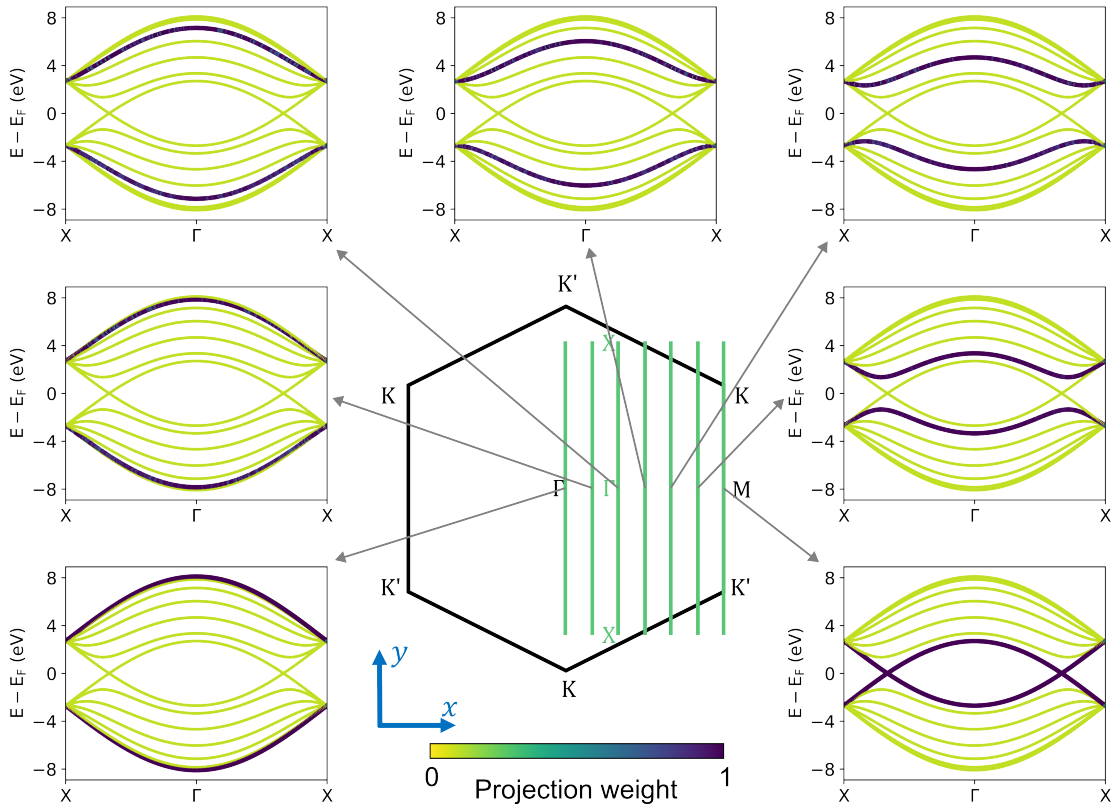


Figure 6.8: Band unfolding of a (6,6) carbon nanotube. The nanotube's wavevector is continuous along the y direction, but discrete along the x direction. Each green line in the reciprocal lattice represents a first Brillouin zone. The band structures are coloured based on the projection weight of carbon nanotube states onto the graphene states along these k lines. The band structure of the carbon nanotube can be regarded as folded graphene bands. The two K valleys remain separate in the carbon nanotube.

of the CNT can be perfectly reproduced by folding the graphene bands along these k lines. The two K valleys are separate in the (6,6) CNT. Because of conservation of momentum, PL is only allowed for states with zero net angular momentum. In such CNTs with separate K points, the linear combinations of these valleys give rise to a dark valley doublet state and two coupled singlets, only one of which is bright.

The unzipping of a CNT produces a zigzag GNR. In Figure 6.7, we use a 6-ZGNR as an example. Its K valleys are in the same positions as the (6,6) CNT. The bands around the K valleys, however, are modified due to the presence of two edges. The cove edge can be regarded as a spatially modulated zigzag edge, obtained by periodically removing carbon atoms. This modification results in a

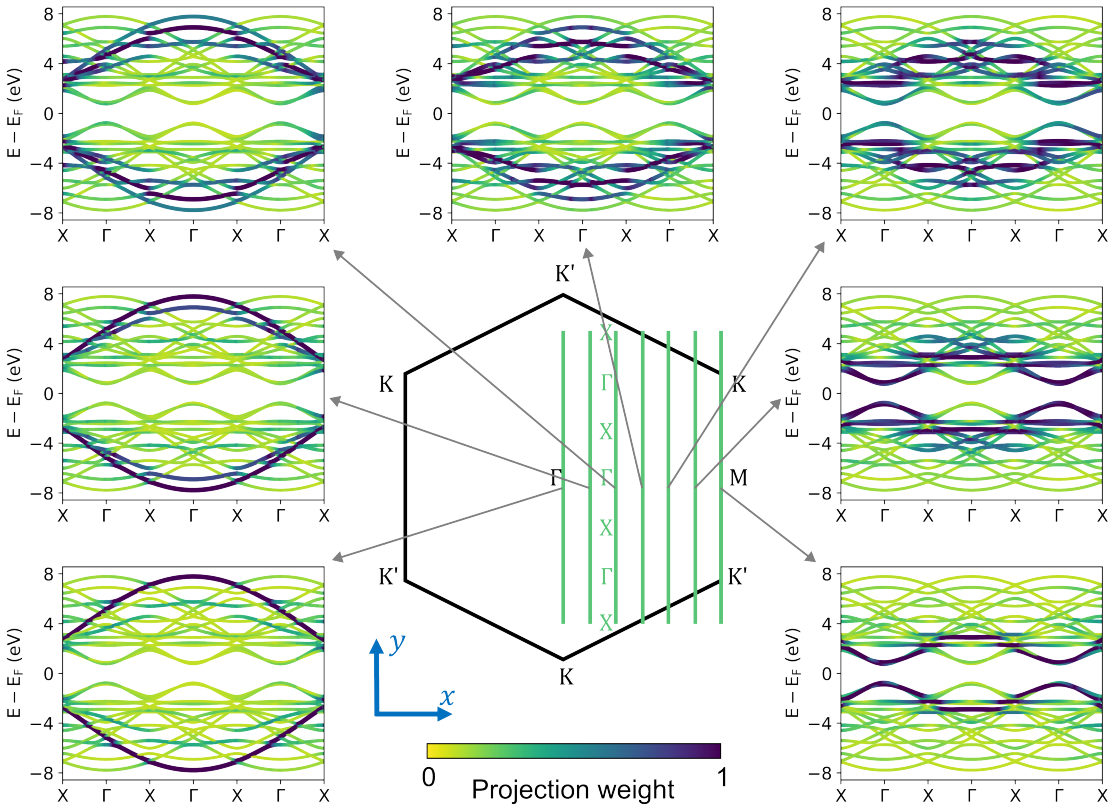


Figure 6.9: Band unfolding of a cove-edge GNR. The green lines are the same as those in Figure 6.8, except that each green line here is an extended Brillouin zone that is three times longer than the first Brillouin zone of the cove-edge GNR. The band structures are coloured based on the projection weight of the GNR states onto graphene states along these k lines. The graphene states at the two K valleys are both folded to the Γ point.

cove-edge GNR with a unit cell three times longer than that of the 6-ZGNR, as indicated by red boxes in Figure 6.7a. Consequently, the first Brillouin zone of the cove-edge GNR is one third of that of 6-ZGNR, and can be obtained by triply folding the latter. The zone-folding process is illustrated in Figure 6.7a, from which we can see that both K valleys are folded to the Γ point. Meanwhile, unlike in CNTs or ZGNRs, the transverse wavenumber is not a good quantum number in the cove-edge GNR, since the translational symmetry in the lateral direction is not well defined. Nevertheless, we still choose the same discrete k lines and plot the projected band structures of the cove-edge GNR for comparison with those of the (6,6) CNT. As depicted in Figure 6.9, the two highest occupied bands and two lowest unoccupied bands, which are responsible for the optical transitions, are

highlighted by projecting the GNR bands onto graphene bands along the k path passing through the two K valleys. In other words, by structuring a 2D graphene into a 1D cove-edge GNR, the original graphene bands around the Dirac cone will change into the frontier bands around the Γ point in the cove-edge GNR. The states at the two K valleys are completely mixed at the Γ point. As we will see in the next subsection, the states mixing will effectively brighten the dark excitons.

6.3.2 Vibrational and optical properties

The influence of side chains in optical spectra was investigated by measuring the absorption and PL of GNR-alkyl and GNR-AOM samples. The structures of GNR-alkyl and GNR-AOM are displayed in Figure 6.10a. GNR-AOM can dissolve in chloroform and form a stable solution, whereas GNR-alkyl forms a dispersion and precipitates within 30 min. Figure 6.10b shows that the absorption spectrum of GNR-alkyl displays a single broad peak, whereas GNR-AOM shows three peaks at 2.29 eV, 2.49 eV, and 2.63 eV, as well as another narrow feature at 2.09 eV. As for the PL spectra, GNR-alkyl does not show any response in chloroform solution. When embedded in a thin film of ethylene-vinyl acetate (EVA) polymer matrix, however, GNR-alkyl exhibits a weak PL response with five sharp peaks and a wider peak at 1.85 eV. The five sharp peaks are attributed to the D and G Raman signals. Therefore, only the peak at 1.85 eV is the real PL response. In contrast to that, GNR-AOM has a strong PL emission both in chloroform solution and when embedded in a polymer matrix. The PL spectra display a narrow peak at 2.09 eV and a broad peak at 1.90 eV. These peaks are not attributable to the Raman response because their positions do not match any possible Raman-active modes. The red-shift of the wide peak in PL spectrum of GNR-alkyl compared with that of GNR-AOM can be assigned to excimer emission from bundles of GNRs [392]. In fact, the PL intensity of GNR-AOM is much stronger than that of GNR-alkyl by two to three orders of magnitude (Figure 6.10c). The Raman peaks are thus hidden from the strong PL

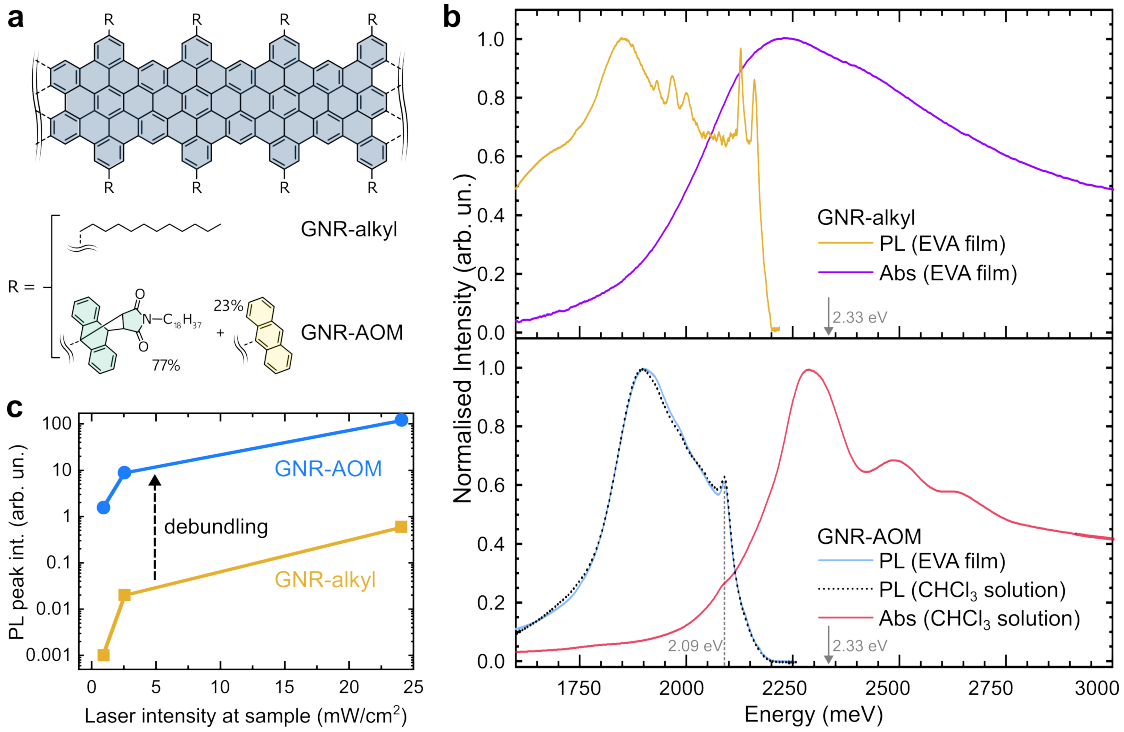


Figure 6.10: Photoluminescence (PL) and absorption (Abs) spectra of GNR-alkyl and GNR-AOM. (a) Structures of GNR-alkyl and GNR-AOM, same as those in Figure 6.1. (b) Normalised PL and absorption spectra of GNR-alkyl and GNR-AOM samples. The PL spectra were measured with 2.33 eV laser excitation. The chloroform solution of GNR-AOM has a concentration of 0.05 mg/ml. (c) PL peak intensity of GNR-alkyl and GNR-AOM samples at different laser intensities. The y-axis is displayed logarithmically for clarity. Measurements were conducted by Bernd Sturdza in a collaboration.

signal. We performed PLQE measurements on the GNR-AOM solution sample in an integrating sphere as detailed in Ref. [393]. The PLQE η can be calculated using

$$\eta = \frac{E_\mathrm{i} - (1 - A) \cdot E_\mathrm{o}}{E_\mathrm{e} \cdot A}, \tag{6.2}$$

where E_i is the area under the emission profile with the sample in the laser line, A is the fraction of laser light absorbed upon one pass through the sample, E_o is the area under the emission profile with the sample out of the laser line, and E_e is the area under the laser excitation curve with empty integrating sphere. The PL signal is fitted and then integrated between 550 nm and 950 nm. The PLQE of the GNR-AOM solution sample reaches 6.4±0.2% at room temperature and further increases to 7.7% upon cooling down to around 60 K, revealing the drastic influence

of debundling via bulky side groups. GNR-alkyl has a low PLQE mainly because of enhanced non-radiative recombinations of electron–hole pairs when inter-ribbon interactions are strong in the aggregates, whereas GNR-AOM has exceptionally good solubility and thus does not suffer from this issue. In the following, we will only analyse the optical spectra of GNR-AOM.

In order to interpret the features present in the absorption and PL spectra, we calculated the phonon modes of cove-edge GNRs. Phonon modes with even symmetry upon inversion can be detected by Raman spectroscopy. The Raman spectrum of GNR-AOM is shown in Figure 6.11. We simulated the Raman spectrum with Quantum Espresso [297] using LDA functional [287] and norm-conserving pseudopotentials. Since the simulation is very computationally demanding, we removed all the side groups for the Raman simulation. The structure was first optimised until the maximum force is below 4×10^{-5} au. The plane-wave energy cutoff was set to 70 Ry. We computed the Raman intensities by adopting the second-order response approach as proposed by Lazzeri et al. [294]. Although the peaks are shifted to higher energies, we can still assign the major peaks in the Raman spectrum to corresponding phonon modes, including shear mode, radial breathing-like mode (RBLM), 2RBLM (the second overtone of RBLM), D mode, and G mode. The vector representations of the low energy modes are shown in Figure 6.11 next to the simulated spectrum. In Section 6.2.2, we calculated the phonon dispersion of the cove-edge GNR with anthracene side groups. From this calculation result we identified the shear mode, RBLM, and 2RBLM. The energies of these modes are in much better agreement with the experimental values.

Next, we will investigate the origin of the peaks present in the absorption and PL spectrum. Upon measuring at lower temperatures, the spectra exhibit more pronounced features. Figure 6.12 shows the optical spectra of GNR-AOM at 77 K. Both the absorption and the PL spectrum display a peak at 2.09 eV. Since E_{11}

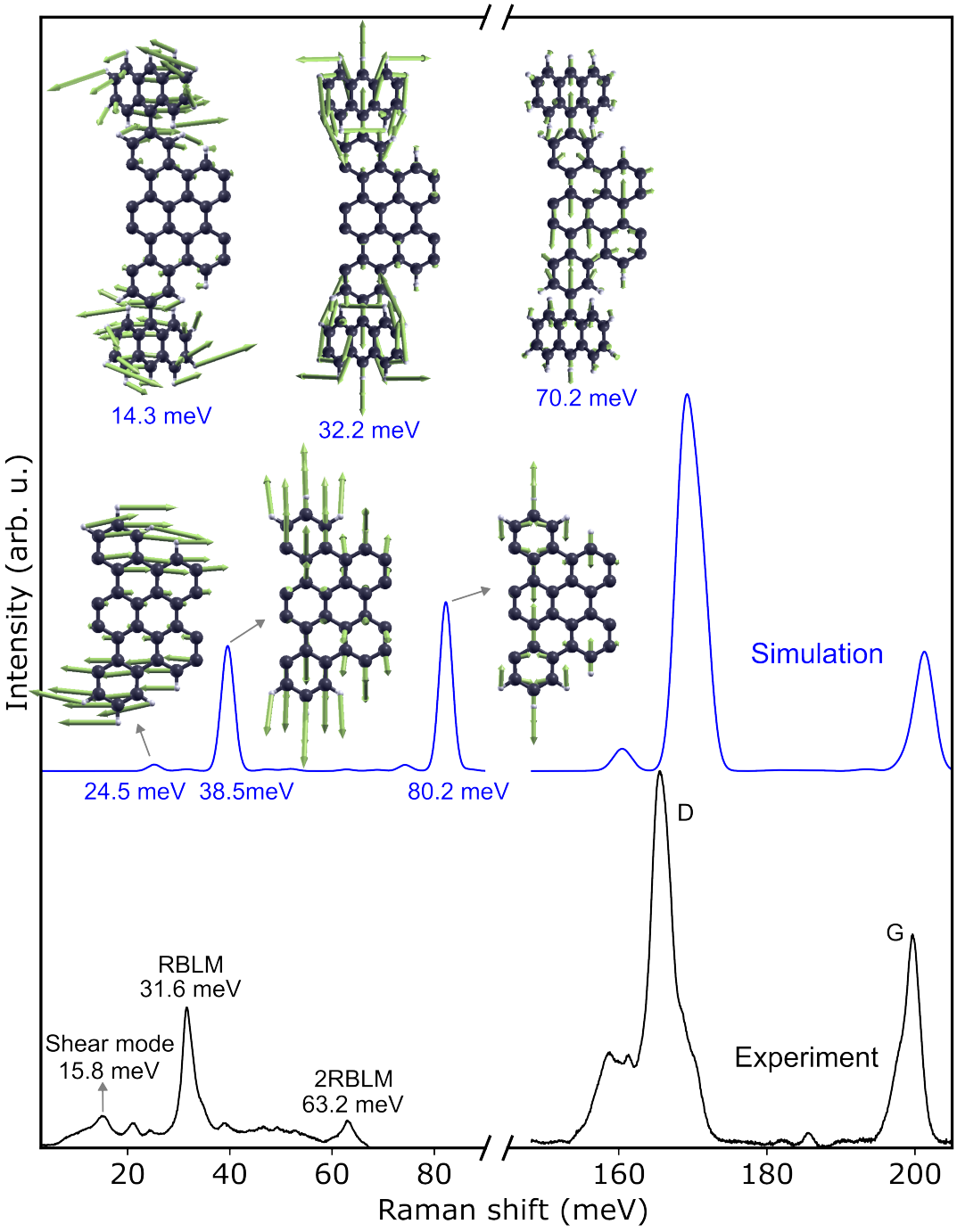


Figure 6.11: Raman spectrum of GNR-AOM. The experimental (black) and DFT-simulated (blue) spectra are shown at the bottom and on the top, respectively. The simulated spectrum was calculated for the cove-edge GNR without side groups. Vibrational modes for the peaks in the low energy regime (shear mode, RBLM, and 2RBLM) are illustrated as insets next to the simulated spectrum. These modes of the ribbon with anthracene side groups (insets on the top) have closer energies to the peaks in the experimental data. Measurements were conducted by Bernd Sturdza in a collaboration.

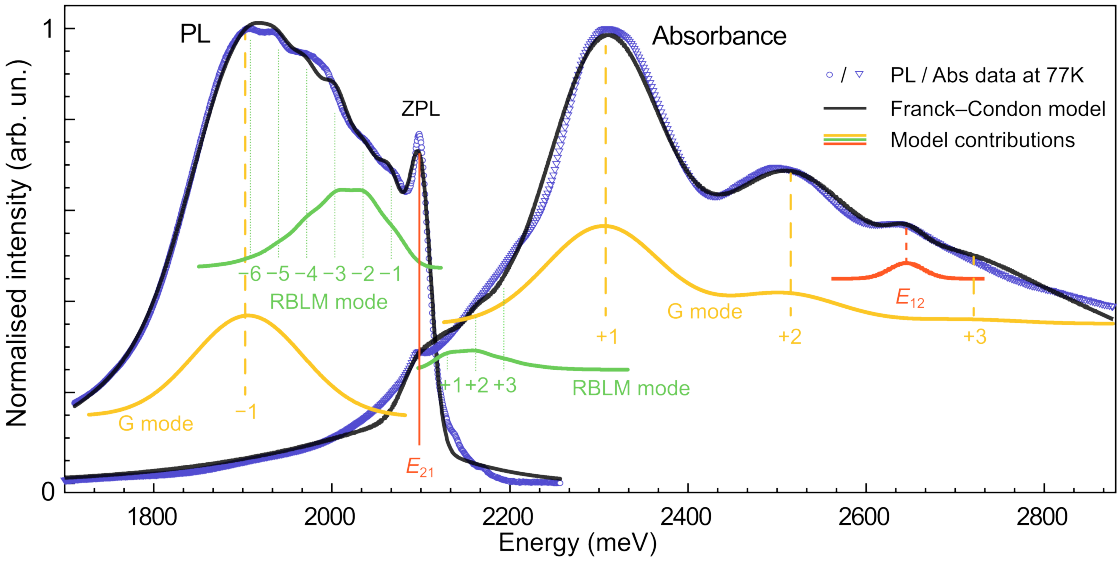


Figure 6.12: Photoluminescence and absorption spectra of GNR-AOM fitted with the Franck–Condon model. The measurements were taken on a thin film sample at 77 K. The spectra were fitted with the Franck–Condon model considering RBLM (green) and G mode (golden) phonons. The zero-phonon line (ZPL) and the smaller peak attributed to E_{12} transition are plotted in red. Measurements were conducted by Bernd Sturdza in a collaboration.

corresponds to a forbidden transition, we assign the feature at 2.09 eV to the zero-phonon line (ZPL) of the transition between first valence band and the second conduction band, corresponding to E_{21}. In addition, the PL spectrum has a series of peaks with a periodicity of about 30 meV, which matches the energy of RBLM. We fitted the PL and absorption spectra using the Franck–Condon model that includes both the RBLM and G phonons. The modelling can reproduce the main features of the spectra very well. The additional peak in the absorption spectrum at 2.63 eV cannot be fitted by the model. We speculate that this peak results from the 1-G side band of the second allowed interband transition E_{12}. In this way, the separation between the two allowed transitions is $\Delta E = E_{12} - E_{21} = 330$ meV, which approximately agrees with the DFT result (280 meV).

The fact that the PL and absorption spectra are not symmetric about the ZPL suggests that the Franck–Condon principle is not the only mechanism of electron–phonon coupling present in the system. We computed the Debye–Waller

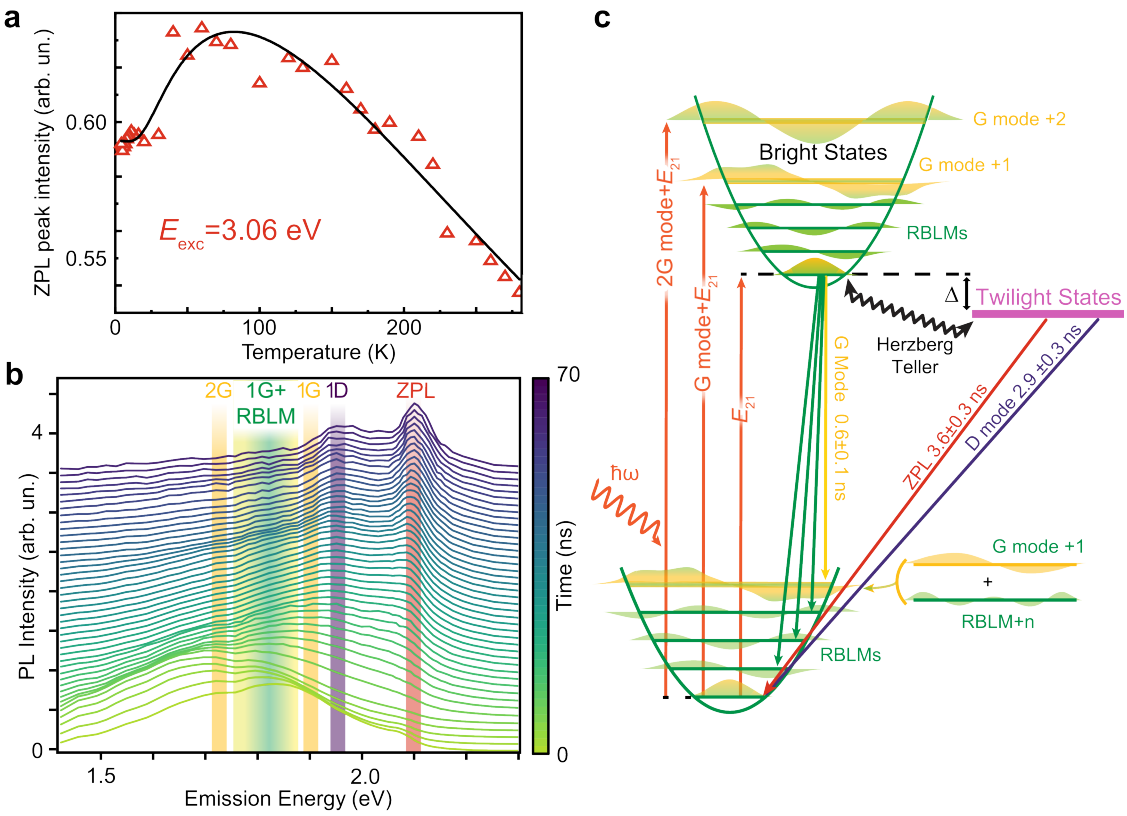


Figure 6.13: Electron–phonon coupling in optical transitions, temperature dependence and temporal evolution of PL. (a) The ZPL peak intensity as a function of temperature. The measurement was conducted with a laser excitation energy of E_{exc} = 3.06 eV. The solid line is a fit that is explained in the main text. (b) Temporal evolution of the PL spectrum. (c) Schematic diagram of optical transitions for GNR-AOM. The RBLMs and G modes are depicted in green and gold, respectively. The Franck–Condon coupling between bright states and phonon modes results in the features in optical spectra. The dark states are brightened by Herzberg–Tell coupling, leading to twilight states (magenta). Measurements were conducted by Bernd Sturdza in a collaboration.

factor α, which determines the intensity of the zero-phonon transition, and obtained 0.06 ± 0.01 and 0.010 ± 0.003 for PL and absorbance at 77 K, respectively. This discrepancy indicates that both Franck–Condon coupling and Herzberg–Teller coupling are present [394]. The Herzberg–Teller coupling becomes relevant when the assumption of adiabatic electronic transition breaks down. In the adiabatic approximation, it is assumed that electronic motion happens instantaneously when compared with nuclear motion because electrons move much faster than nuclei. The Franck–Condon approximation assumes that an electronic transition happens with the nuclear configuration being “frozen”. The electronic transition probability is

governed by the matrix element of the dipole moment, also called the electronic transition integral (Equation (3.72)). When expanding the electronic transition integral into Taylor's series with respect to nuclear coordinates, the Franck–Condon approximation only takes the zeroth-order term, whereas the Herzberg–Teller approximation also includes the first-order term. Therefore, the Herzberg–Teller coupling can be regarded as a first-order correction to the Franck–Condon coupling.

The temperature dependence of the PL emission provides more information about the excitonic structures. Figure 6.13a presents the ZPL peak intensity as a function of temperature, showing a maximum at around 75 K. This implies the existence of a lower dark excitonic state below the lowest bright exciton state, with an energy splitting Δ [53, 395, 396]. We fitted the data using the following equation, which similar to the one Mortimer et al. used to describe the ZPL peak intensity of CNTs [397]:

$$I \propto \frac{1}{\left(T^2 + T_0^2\right)^{1/4}} \cdot \frac{m + \mathrm{e}^{-\Delta/kT}}{1 + \mathrm{e}^{-\Delta/kT}}, \tag{6.3}$$

where T_0 is a temperature-independent Lorentzian broadening term, equal to 19.7 ± 1.5 meV. The energy splitting between the dark and bright excitonic state, Δ, is about 6 ± 1 meV, which is in line with that for CNTs [398]. This suggests that GNRs have excitonic structures similar to those in CNTs. The main difference lies in the spectral weight of the dark state, $m = 0.68 \pm 0.04$, which is about four times higher than that in CNTs [397]. This leads to a higher PLQE in GNRs compared with CNTs despite the presence of the dark excitonic state. Hence, we term the brightened dark states as twilight states, as illustrated in Figure 6.13c. In CNTs, because of selection rules of separate K and K′ valleys, multiple dark excitonic states exist so that the PL yield is low. We attribute the brightening in our cove-edge GNRs to the breaking of selection rules of K and K′ valleys in cove-edge GNRs because of valley mixing.

We also investigated the internal processes of PL emission by performing time-resolved PL measurements. Figure 6.13b shows how the emission evolves with time. The initial emission is a very bright cascade from the bright states, a process that is mediated by Franck–Condon coupling to RBLM and G phonons. On a longer timescale, the emission is dominated by the twilight states assisted by Herzberg–Teller coupling. The presence of the D mode was detected in time-resolved measurements, but not in the previous continuous wave measurements, indicating a weaker coupling between the electronic states and the D phonons. The decay mechanisms are depicted in detail in Figure 6.13c.

The previous assignment of PL peaks is also validated by photoluminescence excitation (PLE) spectroscopy measurements (Figure 6.14). Figure 6.14a shows the PLE map of a GNR-AOM solution sample, where the strongest emitting peak is the 1G side-band of the allowed transition E_{21}, i.e. $E_{21} + 1\mathrm{G}$. We compared the vertical line cuts of Figure 6.14a at 1.9 eV (ZPL−1G) and 2.09 eV (ZPL), respectively, with the absorption spectrum in Figure 6.14b. In general, the positions of the PLE peaks match the absorption data very well, which gives additional support to our previous assignment of the peaks in the PL spectrum. The slight shift between the PLE data and the absorption data between 2.2 eV and 2.3 eV is caused by the long pass filter used in the experiment. In Figure 6.14c we show a vertically normalised map of Figure 6.14a, highlighting the variation of intensities of the $E_{21} + 2\mathrm{G}$ peak and the $E_{12} + 1\mathrm{G}$ peak relative to the $E_{21} + 1\mathrm{G}$ peak. The $E_{12} + 1\mathrm{G}$ peak around 2.6 eV in the PLE spectrum is significantly larger than that in the absorption spectrum, and its intensity further increases as the emission energy increases towards the ZPL energy. This result confirms the assignment of this peak as the second interband transition.

In Figure 6.14c, we indicate the position of the $E_{21} + 1\mathrm{G}$ peak at different emission energies using a red line. We also show this trace in Figure 6.14d with a higher resolution, from which we find that the $E_{21} + 1\mathrm{G}$ peak position shifts by the energy of a RBLM phonon (31.6 meV) when the emission energy increases across

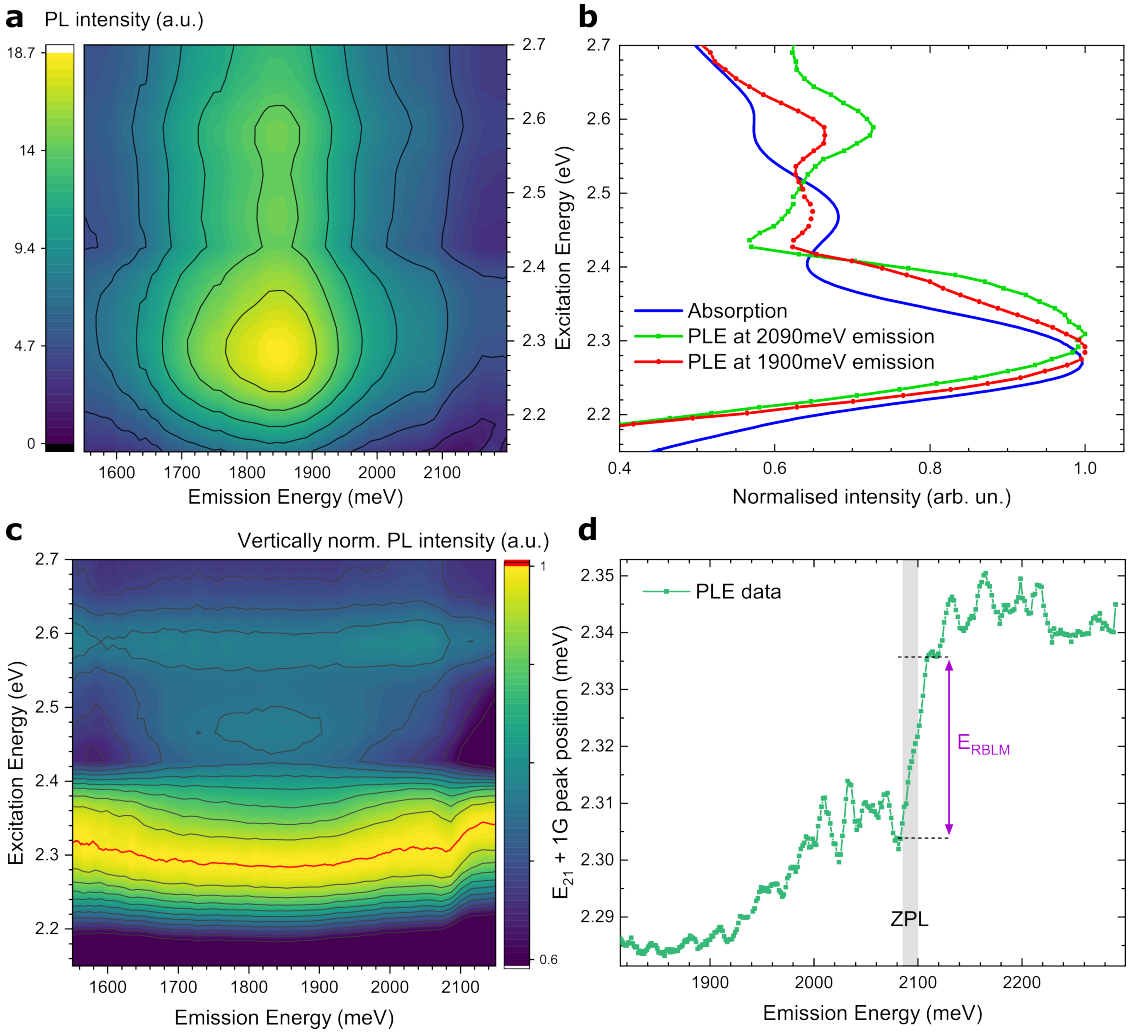


Figure 6.14: Photoluminescence excitation (PLE) spectra of GNR-AOM. (a) PLE map of a chloroform solution sample (0.05 mg/ml) of GNR-AOM, excited with a white light source. (b) Comparison between PLE spectra at 1.9 eV (red) and 2.09 eV (green) emission and the absorption spectrum (blue). (c) Normalised PLE map along the excitation energy axis. (d) Excitation position of the $E_{21} + 1\text{G}$ peak for different emission energies. Measurements were conducted by Bernd Sturdza in a collaboration.

the ZPL line. In other words, at emission energies below the ZPL, the E_{21} transition plus the creation of one G phonon is the dominant mechanism for absorption and emission. For emission energies higher than the ZPL, the absorption that involves both an RBLM phonon and G phonon leads to the strongest ZPL emission. This is because phonons need to be annihilated in order to achieve emission energies higher than the ZPL energy. Since D and G phonons have significantly higher energies and are irrelevant here, a large amount of RBLM phonons will be required for PL

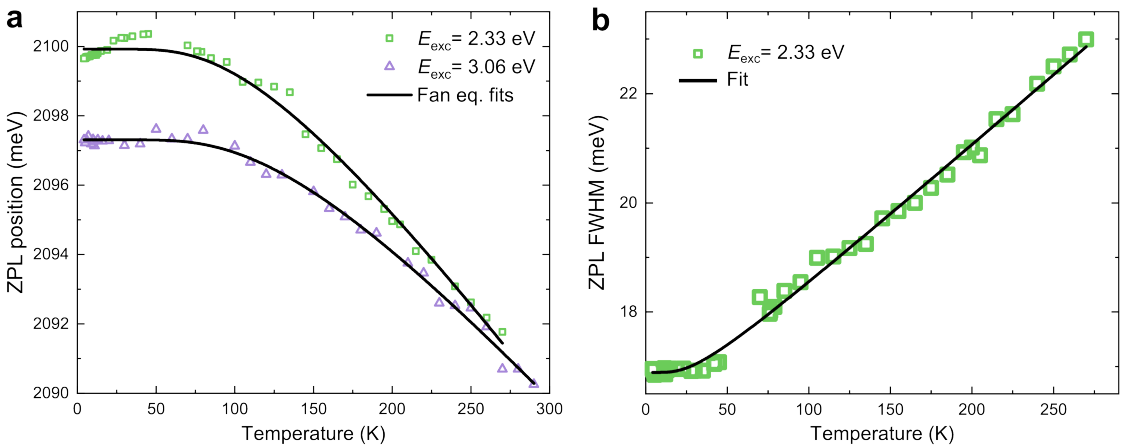


Figure 6.15: Temperature dependence of the zero-phonon line (ZPL) position and the ZPL FWHM. (a) ZPL position as a function of temperature. The measurements were taken with two excitation energies: 2.33 eV (green) and 3.06 eV (violet). The data were fitted with the Fan equation. (b) The full width at half maximum (FWHM) of the ZPL as a function of temperature, measured with $E_{\mathrm{exc}} = 2.33\,\mathrm{eV}$. The solid line is a fit that is explained in the main text. Measurements were conducted by Bernd Sturdza in a collaboration.

emission at energies higher than the ZPL energy. Therefore, the excitation energy is increased by E_{RBLM} for emission energies larger than E_{ZPL}.

Finally, we investigated the influence of electron–phonon coupling on the position and linewidth of the ZPL. Figure 6.15a shows the ZPL position as a function of temperature, measured at two different excitation energies. The trend can be accurately fit with the Fan equation [399, 400]:

$$E_{\mathrm{g}}(T) = E_{\mathrm{g}}(0) - \frac{A}{\mathrm{e}^{E_{\mathrm{ph}}/kT} - 1}, \tag{6.4}$$

where A is the Fan parameter and E_{ph} represents the energy of the phonon mode which drives the thermal shift of the energy band gap. From the fit, we obtain $E_{\mathrm{ph}} = 30 \pm 2\,\mathrm{meV}$ and $E_{\mathrm{ph}} = 35 \pm 2\,\mathrm{meV}$ for the 2.33 eV and 3.06 eV excitations, respectively, which are very close to the RBLM phonon energy (32.2 meV). The temperature dependence of the full width at half maximum (FWHM) of the ZPL is shown in Figure 6.15b. The line broadening can be well described by the following relation [401]:

$$\Gamma(T) = \Gamma_0 + \Gamma_{\mathrm{ph}} = \Gamma_0 + \frac{\gamma}{\mathrm{e}^{E_{\mathrm{ph}}/kT} - 1}, \tag{6.5}$$

where Γ_0 denotes a temperature-independent inhomogeneous broadening term induced by scattering on termini and defects [402], and Γ_{ph} is a homogeneous broadening term related to phonon scattering [403, 404]. The exciton–phonon coupling strength is represented by γ. From the fit, we obtain that $\Gamma_0 = 16.89 \pm 0.03\,\mathrm{meV}$, $E_{\mathrm{ph}} = 7.1 \pm 0.7\,\mathrm{meV}$, and $\gamma = 2.1 \pm 0.3\,\mathrm{meV}$. It is noteworthy that the phonon energy matches well with the transverse bending mode (TBM) that was detected by single-molecule transport measurements as discussed in Section 6.2. The same phonon mode is involved in two different physical processes. For the ZPL broadening, an exciton is created when the molecule absorbs a photon. This exciton is then scattered to a different energy level by the TBM phonon. The energy of the emitted photon during the recombination of the electron–hole pair is thus changed, leading to a broadening of the PL lineshape [401]. On the contrary, in electron transport, which is governed by the Franck–Condon principle, the electron hopping between the electrode and the molecule is more probable if it is accompanied by a transition of the molecule from the vibrational ground state to a vibrational excited state, i.e. emitting a certain number of phonons. The electron–phonon coupling parameter λ in Equation (6.1) quantifies the average number of phonons that are emitted during the electronic transition. It is remarkable that we can see the effect of the same phonon mode (TBM) in two completely different characterisations. Our GNRs thus will be an outstanding platform to study the interplay between electronic states and phonons.

6.4 Summary and outlook

In summary, we have revealed the manifestations of vibrational states of GNRs in both single-molecule transport and optical spectroscopy. In particular, we demonstrated the quantum nature of the vibrational modes, and the role of phonons in electron transport and optical transitions. In both experiments, we compared

the conventional cove-edge GNRs with alkyl side-chains (GNR-alkyl) and a novel version with bulky side groups (GNR-AOM). The latter offers exceptional solubility, which enables us to resolve fine features of electron–phonon coupling in experiments that would have been impossible with conventional insoluble GNRs.

In single-molecule transport measurements, the stability diagram of GNR-AOM exhibits extremely clean features that are much superior to previous GNR-devices [35, 36]. The periodic parallel lines in the sequential tunneling regime are a signature of electron transport in a single GNR assisted by transverse-bending-mode phonons. The conductance peaks arising from vibrational states can be well reproduced by the Franck–Condon model. Our results validated previous theoretical predictions of strong electron–phonon couplings in GNRs [383]. The exploitation of solubilising side groups in GNR-AOM avoids the use of surfactants that could be detrimental to the electronic properties [390, 391]. The chemical tunability of the structure of GNRs also opens ample opportunities for further improving their carrier mobility and conductance. In addition, as the quantum states can be clearly resolved in single-molecule devices, it becomes possible to study the interplay between electron spins, phonons, photons, and topological states in a single GNR.

By conducting optical characterisations, we demonstrated that the solubilisation leads to a boost of two to three orders of magnitude of the photoluminescence quantum efficiency compared with the insoluble GNRs, reaching 6.4% at room temperature. Although a higher PLQE of 9.1% was recently reported for another type of soluble GNRs with bulky side groups [405], the optical spectra of those GNRs remain broad and featureless, a sign of exciton delocalisation over multiple ribbons. In contrast, the absorption and PL spectra of our samples have clear features that can be well reproduced by the Franck–Condon model including RBLM and G mode phonons. We furthermore carried out DFT calculations for identifying the phonon modes and simulating the Raman spectrum. The major peaks in Raman spectrum of GNR-AOM are assigned to the shear mode, RBLM, 2RBLM, G, and

D mode. The roles of the phonon modes in PL emission were further uncovered by temperature-dependence and temporal evolution measurements. In cove-edge GNRs, the two K valleys are completely mixed, which breaks down the selection rule of K valleys and results in brightened dark states. A dark excitonic state exists at about 6 meV below the bright E_{21} excitonic state. This dark state is relatively brightened compared with those similar dark states in CNTs, therefore we call it the twilight state. Moreover, the zero-phonon line can be clearly identified in the spectra. We revealed that the shift and broadening of the ZPL are a result of coupling to RBLM and the TBM, respectively. Our results demonstrate the great potential of using soluble GNRs as bright optical emitters. We provided a direct insight into the internal mechanisms of the optical processes mediated by electron–phonon coupling in GNRs, offering guidance to further tuning of the optical properties by bottom-up chemical design. These results have broad implications for future research and applications, including optoelectronics [406–408], bio-imaging [408, 409], and quantum technologies [410–412].

6.5 Project overview

The GNR samples in the Section 6.2 were synthesised by Dr. Wenhui Niu, Dr. Akimitsu Narita, Dr. Yiyong Mai, Dr. Junzhi Liu. The single-molecule devices were fabricated by Dr. Alessandro Lodi, Dr. Alex Gee, Dr. Pascal Gehring, Dr. Chit Siong Lau, Dr. Jan Mol, Dr. Tian Pei. The electron transport measurements were performed by Dr. Simen Sopp, Dr. Alessandro Lodi, Dr. Alex Gee, Dr. Tian Pei, Dr. Jonathan Nägele. In Section 6.3, the GNR-AOM samples were synthesised by Dr. Wenhui Niu and Dr. Ji Ma. The GNR-alkyl samples were synthesised by Dr. Xuelin Yao. The optical measurements were performed by Bernd Sturdza. I carried out all the theoretical calculations presented in this chapter.

7
Conclusions

Carbon has been considered a prime candidate for quantum systems since decades. On the other hand, it is only now, with the advent of molecularly-made carbon nanostructures, shaped with atomic precision, that this prediction can become a reality. This thesis opens up long awaited connections between the expectations of theoretical physics, and the experimental possibilities actually available to us. We have shown how the quantum topological states, spin states, and vibrational states in GNRs can be engineered via structural design for applications in next-generation quantum devices. We not only designed new structures that may inspire chemists, but also examined several novel GNRs synthesised by chemists from both our group and collaborating groups, using various theoretical and experimental techniques.

After discussing an overview of the whole research area (Chapter 2), and providing the fundamentals of the methods that we use (Chapter 3), in Chapter 4, we focused on a better understanding of the topological phases in GNRs and offering guide for synthetic design. Furthermore, we aimed at expanding the exploration of the topological phases and making them more experimentally accessible. This will allow the topological states to be studied by other experimental techniques such as EPR spectroscopy, and in single-electron transistors. Moreover, our results also have

implications for designing new functional materials by exploiting the topological states. In Section 4.2, we started from six novel GNR structures and investigated three strategies to tune their topological phases. The first way was to change the unit cell design while keeping the GNR's edge shape. The second way was to keep the unit cell shape but alter the connection bonds between adjacent unit cells. From the synthetic point of view, this means keeping the monomer shape the same while changing the position of linker atoms. While both the first and second approaches require structural modifications, the third approach retains the structure the same, but tunes the level of electron filling. In practical this can be done by either tuning the sample bias in STM, or by tuning the gate voltage in a single-molecule transistor. We examined a large number of novel GNR designs based on these three approaches, hopefully providing a larger toolbox to design topological phases in more facile environments. In Section 4.3, we discussed the relationship between the topological index $\mathbb{Z}$ and the Clar's sextet rule. Previous studies have demonstrated the different formulation of the $\mathbb{Z}$ index in Bloch and Wannier representation. We further linked the Wannier representation of $\mathbb{Z}$ topology with the Clar's formula, revealing that the $\mathbb{Z}$ index can be obtained from counting the number of double bonds cut by a unit-cell boundary in the configuration with the maximum number of Clar's sextets. Our finding bridges the two seemingly completely unrelated concepts in physics and chemistry. It will not only deepen the understanding of topological phases of GNRs, but also offer a simple way to predict the topological phases by drawing Clar's sextets. In Section 4.4, we studied the topological phases in fused porphyrin nanoribbons, which have not been explored yet, although these ribbons have been synthesised long ago. By inspecting the two energy gaps around the Fermi level, we proved that three topological end states can be found in a fused porphyrin nanoribbon. The zinc-porphyrin nanoribbon that we calculated has a near-zero band gap, implying that we can induce a transition between a metallic phase and a topologically nontrivial phase by adjusting the Fermi level. Furthermore, the results

suggest that the topologically nontrivial phase can not only be found in GNRs, but also in other 1D conjugated systems. Finally, in Section 4.5, we investigated a type of sublattice-imbalanced GNRs, which possess a zero-energy flat band with topological origin. We proposed a way to realise dissipationless electron transport by applying a transverse electric field in such GNRs. Our model can not only be applied to GNRs, but also to other systems with a honeycomb lattice, like photonics [201, 352], nanomechanical metamaterials [354], and microwave metamaterials [353].

Chapter 5 is dedicated to the spin states in GNRs. In Section 5.2, we demonstrated the spin polarisation of topological end states that we had calculated in Chapter 4, in which the spin degree of freedom was ignored. By further extending our discovery of the relationship between the $\mathbb{Z}$ topology and the Clar's sextet rule, we showed that the topological index $\mathbb{Z}$ is directly related to the number of unpaired electrons in a finite GNR. Although calculations of the ground states of such confined systems require more advanced computational techniques, our simple prediction provides a starting point for exploring spin-polarised states in GNRs. In addition, I have predicted the presence of spin-polarised states in two GNRs recently synthesised by my collaborators. In Section 5.3, we characterised the spin dynamics in two functionalised cove-edge GNRs using EPR spectroscopy. We clarified several questions that were unclear before. Firstly, we found that defects are relatively common in solution-synthesised GNRs. They may strongly affect the analysis of the interesting spin states that we introduced from external functionalisation groups. To reduce the number of defects, the chemical synthesis of such GNRs needs to be improved in the future. Secondly, we validated that solubilisation of GNRs leads to a significant increase of the spin coherence time. This suggests that GNRs can be promising qubits for quantum information applications. Thirdly, our results on GNR-VO samples indicate that the spin states in vanadyl-porphyrin are very localised. Although the signal from the GNR backbone is likely a result of defects, we proved the successful integration of porphyrin units in GNRs, paving the way

for future work on assembling different qubits in a single GNR. In addition, we showed that the spin–lattice relaxation time and spin coherence time are reduced by grafting the vanadyl porphyrin to GNR backbone.

In Chapter 6, we show numerical calculation results on the vibrational states of cove-edge GNRs, which are manifested both in single-molecule transport measurements and optical measurements. We used similar solubilising side groups as we described in Chapter 5, showing their significance in resolving the quantum states in experiments. In Section 6.2, we present the quantum transport measurements of two types of GNRs, the insoluble GNR-alkyl and the soluble GNR-AOM. The latter exhibits exceptionally clean features in the stability diagram, from which we obtained important information on electron–phonon coupling in electron transport. The vibrational levels in the experimental dataset matches with the transverse bending mode from my numerical calculation. The conductance peaks are also well described by a Franck–Condon model fitting. Our study opens exciting possibilities of studying the interplay between spins, phonons, photons, and topological states in a single GNR. In Section 6.3, we report the optical characterisations of the same GNRs that we used for single-molecule tranport measurements. The GNR-AOM shows bright photoluminescence in both film and solution samples, with a high PLQE of 6.4% at room temperature, a result of both the special backbone structure and solubilising side groups. The cove-edge GNRs mix the K valleys and show different behaviours as the CNTs that are more dominated by dark states. Meanwhile the bulky side groups can significantly suppress the exciton transfer between ribbons. Hence, we obtained a brightened dark states, labelled as twilight states, below the lowest bright excitonic states. The clear features in the absorption and photoluminescence spectra of GNR-AOM can be reproduced by the Franck–Condon model with large confidence. The RBLM and G-mode phonons are the dominant vibrational states that are involved in the optical transistions.

Additionally, we showed that the position and the linewidth of the ZPL can be modified by coupling with the RBLM and transverse bending mode, respectively.

We expect the results of this thesis to profoundly affect the study of carbon nanomaterials in all possible directions of interest. The theoretical tools developed here allow examining topological phases in one-dimensional systems, a study which has only began in recent years, and can now complement more established work on the topological phases in higher dimensionalities. Not only do these results provide new insights for the fundamental understanding of the electronic states in GNRs, but they also pave the way for exploring nontrivial topologies in other one-dimensional materials, such as poly-porphyrins, and can be extended to poly-radical chains, and whole new classes of aromatic compounds. Moreover, these tools can now be expanded to theoretically characterise the interaction of these graphene systems with substrates, and in particular with superconductors, where Majorana fermion states are expected to appear. Spurred by this, our group has already measured the effect of superconducting electrodes, and other groups are racing towards the same goal [413]. Moreover, our results are not just influencing physicists, but chemists, too. It is thrilling that chemists in our group and elsewhere could pick up on the ideas introduced theoretically, and already start working on the synthesis of novel systems with improved properties. The development of a connection between topology and quite old rules of synthetic organic chemistry is particularly powerful: it can provide a rule of thumb that is widely available and easily employed by chemists, even without detailed knowledge of topological states. From the experimental point of view, our results affect most forms of investigation of carbon systems: electron transport, optical emission and absorption, and magnetism. The investigation of the quantum magnetic properties can open up the path to novel systems based on graphene nanoribbons, where quantum spins can be arranged periodically on the edges by using coordination chemistry, instead of just organic radicals. Conceptually, this is a huge first step forward: the metals

can now be used to introduce additional elements in the spin Hamiltonian, such as spin–orbit coupling, so as to alter the topology using an additional parameter, or to create different types of Majorana fermions. It will be interesting to understand how topologically nontrivial states interact with localised metal centres. Moreover, there is still little understanding on the theory of how multiple localised spins interact simultaneously with one single electronic transport channel, as produced in our experimental systems. This and other challenges are now being picked up by a new DPhil student in my group. Our use of multiple techniques, combined with a common theoretical background, has also allowed unravelling a unifying picture. We could show how the same quantised vibrational mode affects the behaviour in conditions that are usually very different: characteristic electron–phonon effects could be identified in millikelvin transport spectroscopy as well as visible optical transitions, with the same transverse bending mode playing a key role. This result can now be used, in perspective, to enhance even further the emission properties, or to alter the electronic transmission through nanoscale devices.

In essence, the results of this thesis show which are the fundamental ingredients, and the main characteristic parameters that can be used to engineer the quantum states of GNRs, such as the electronic, topological, spin, and vibrational degree of freedom. We think this level of tunability of the quantum states will offer unprecedented possibilities for the creation of applicative systems. The most immediate ones that come to mind are spin qubits with ultra-long coherence times, systems where multiple quantum units are connected to the same electron transport channel which can be organised in a scaled-up architecture, in multiple nanoscale chips on a surface. The possibility of having a very large electron–phonon coupling is encouraging for sensing applications, as carbon nanotubes also produce good sensors, although they suffer from poly-dispersity. The surprising brightening-up of the emission properties also indicates that these are excellent photon emitters, which can be used in optoelectronics. We can expect GNRs to play a central role

in the development of next-generation devices across a wide range of scientific and technological domains. In electronics, we know that TSMC has already set up a research group for the development of low-consumption electronics based on GNRs, and previous results from our group show that single-electron behaviour can be retained up to room temperature.

8
Appendix

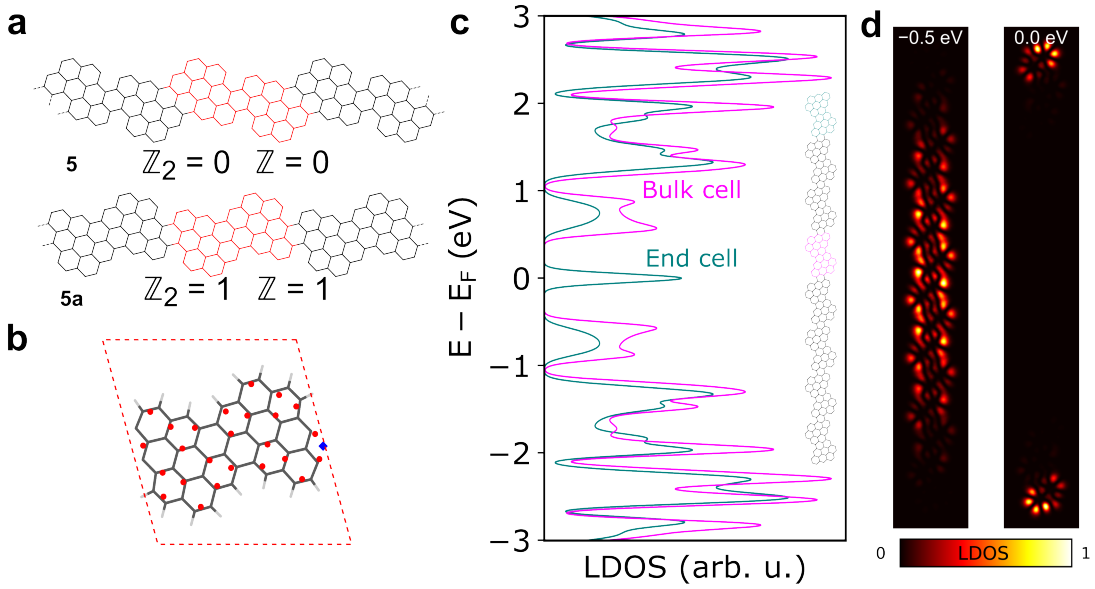


Figure 8.1: Nontrivial topology in an alternative unit cell of GNR **5**. (a) The alternative unit cell **5a** has nontrivial topology ($\mathbb{Z}_2 = 1, \mathbb{Z} = 1$), compared with the trivial GNR **5** ($\mathbb{Z}_2 = 0, \mathbb{Z} = 0$). (b) The Wannier centres (red dots) and their vector sum (blue diamond) are superimposed on the unit cell of **5a**. The sum of Wannier centres is at the unit cell boundary, indicating nontrivial topology. (c) The LDOS is calculated for bulk cell (magenta) and end cell (teal) of a **5a** octamer with 0.05 eV Gaussian broadening. (d) The LDOS map of **5a** octamer is simulated at −0.6 eV (bulk states) and 0.0 eV (end states) using the tight-binding model. The LDOS is calculated at 3 Å above the GNR plane, and integrated in a 0.1 eV energy window.

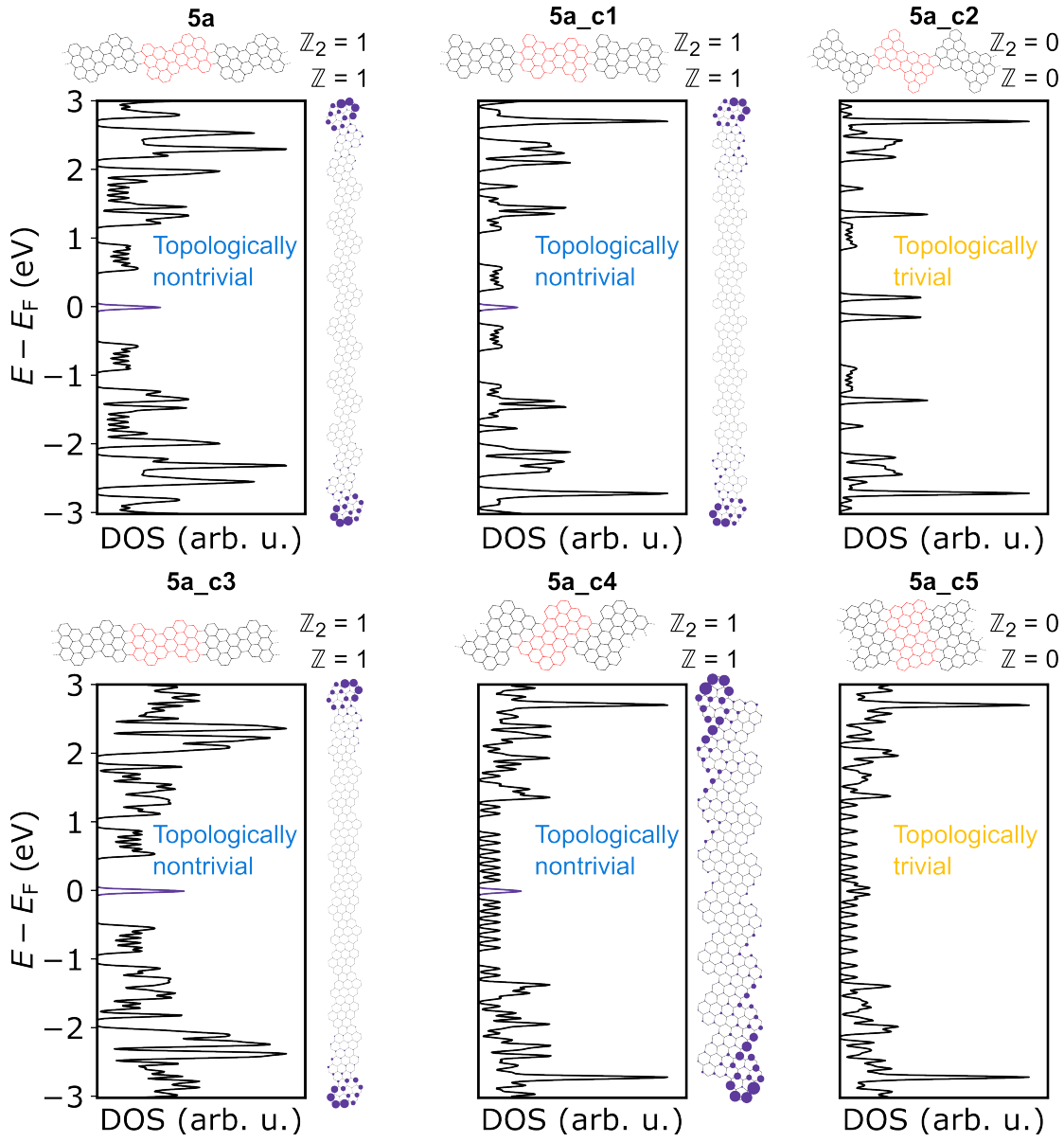


Figure 8.2: Distinct topological phases of GNR **5a** with different connections. Six variants of GNR **5a** are designed by changing the neighbouring-cell connections, labelled by **5a**, **5a_c1**, **5a_c2**, **5a_c3**, **5a_c4**, **5a_c5**, respectively. Repeating units are highlighted in red. $\mathbb{Z}_2$ and $\mathbb{Z}$ are evaluated and they classify the GNRs into distinct topological phases. DOSs are calculated for octamer of each GNRs with 0.02 eV Gaussian broadening. The topologically nontrivial GNRs **5a**, **5a_c1**, **5a_c3** and **5a_c4** possess zero-energy end states while topologically trivial GNRs **5a_c2** and **5a_c5** don't. The end states are highlighted in purple in the DOS. The charge-density map of end states are also plotted in purple and superimposed on the structural model of the octamers. The circle size scales with the amplitude of charge density, and the amplitudes are normalised in each case.

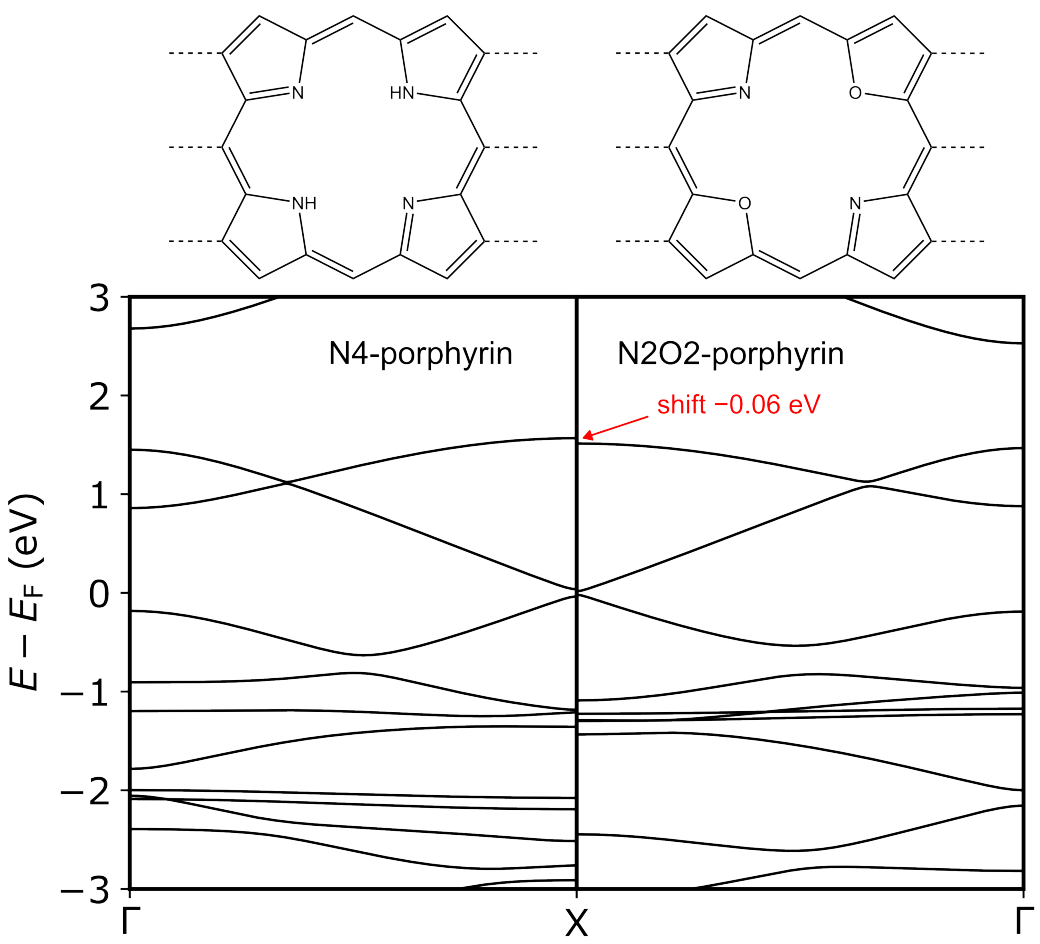


Figure 8.3: Band structures of fused nanoribbons from pristine porphyrin and N2O2-porphyrin. Two of the nitrogens are replaced with oxygens. The band structure looks similar but is shifted downward by −0.06 eV.

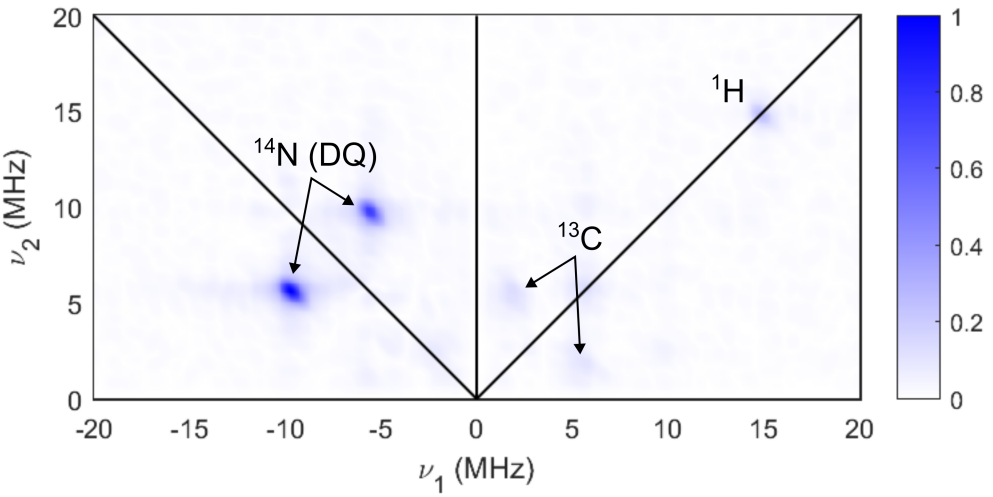


Figure 8.4: HYSCORE spectra of VO state of GNR-VO powder sample. The peaks that result from the hyperfine interactions with ^{13}C, ^{1}H, and ^{14}N nuclei are labelled in the graph. DQ stands for double-quantum transition.

Acronyms

1D one-dimensional. 12, 29, 42–44, 46, 48, 53, 62, 83–85, 89, 113, 116, 119, 125, 135, 147, 161, 210, 214, 229

2D two-dimensional. 17, 18, 37, 38, 40, 46, 112, 210, 214

2DEG two-dimensional electron gas. 33, 35

2MTHF 2-Methyltetrahydrofuran. 177

2PPE two-photon photoemission. 30

3D three-dimensional. 40, 46, 112

AFM atomic force microscopy. 21

AGNR armchair graphene nanoribbon. 9, 12–15, 24–26, 28–31, 45–48, 50–52, 64–66, 68, 87, 123, 130, 131, 133, 136, 138–140, 142, 144, 145, 147, 172–174, 177, 194, 195

BBC bulk–boundary correspondence. 38

CB conduction band. 144, 170, 172

CNT carbon nanotube. 3, 12, 21, 60, 208, 210–213, 220, 226, 230

CPI chiral-phase index. 46–48

CVD chemical-vapor deposition. 3

CW continuous-wave. 90, 93

DFT density-functional theory. 6, 14–16, 18, 20, 21, 31, 46, 47, 49, 64, 68, 77, 78, 81–83, 87, 88, 114, 116, 122, 133, 142, 145, 147, 149, 150, 152, 156, 158, 159, 162, 165, 167, 168, 177–179, 182, 187, 195, 205, 208–210, 218, 225

DOS density of states. 14, 22, 50, 150

EDFS echo-detected field-swept. 98, 180

EPR electron paramagnetic resonance. 5, 6, 56, 60, 89–94, 97, 98, 101, 166, 175, 177, 179, 181, 185, 188, 194, 195, 198, 227, 229

EVA ethylene-vinyl acetate. 214

FET field-effect transistor. 3, 23, 65

FFT fast Fourier transformation. 100

FWHM full width at half maximum. 223

GGA generalised-gradient approximation. 80, 205

GNR graphene nanoribbon. 1–7, 9–13, 15–21, 23–33, 41, 42, 44–46, 48, 50, 52, 53, 55, 59–69, 75, 80–84, 102, 104, 111–114, 116, 117, 119–121, 123, 125, 127, 130, 135, 140, 147, 148, 155, 156, 160–163, 165–168, 170–174, 177–179, 181, 183, 187–189, 193–195, 197–201, 205, 208–214, 216, 220, 224–233

HF Hatree–Fock. 78

HOMO highest occupied molecular orbital. 30, 167, 170, 172

HREELS high-resolution electron-energy-loss spectroscopy. 30

HYSCORE hyperfine sublevel correlation spectroscopy. 99–101, 178, 185, 189

LCM longitudinal compressive mode. 68

LDA local-density approximation. 14, 16, 80, 216

LDOS local density of states. 21, 22, 27, 31, 50, 116, 120, 121, 123, 125, 127, 144, 149, 150

LSDA local spin-density approximation. 14, 19, 80

LUMO lowest unoccupied molecular orbital. 30, 167, 170, 172

MLWF maximally localised Wannier function. 89, 118, 136

PAH polycyclic aromatic hydrocarbon. 137, 138

PBC periodic boundary condition. 29

PBE Perdew–Burke–Ernzerhof. 19, 205

PDOS projected density of states. 148, 209

PL photoluminescence. 208, 212, 214–216, 218–222, 224–226

PLE photoluminescence excitation. 221

PLQE photoluminescence quantum efficiency. 5, 208, 215, 216, 220, 225, 230

QAH quantum anomalous Hall. 41

QH quantum Hall. 33, 35, 38, 41

QSH quantum spin Hall. 17, 40, 41

QVH quantum valley Hall. 41

RBLM radial breathing-like mode. 67, 68, 216, 218, 221–223, 225, 226, 230, 231

SEM scanning electron microscopy. 200

SET single-electron transistor. 202

SLM shear-like mode. 68

SMT single-molecule transistor. 5, 101, 102

SOC spin–orbit coupling. 17, 39–41, 58, 59

SOMO singly occupied molecular orbital. 167

SSH Su–Schrieffer–Heeger. 42–44, 50, 53, 152, 154

STM scanning tunneling microscope. 5, 21, 25, 30–32, 51–54, 123, 144, 162, 194, 228

STS scanning tunneling spectroscopy. 21, 30, 64

TB tight-binding. 6

TBM transverse bending mode. 205, 206, 224, 226

TRS time reversal symmetry. 37, 38, 40, 41

UHV ultra-high vacuum. 21

VB valence band. 144, 170, 172

XC exchange-correlation. 79–81

ZGNR zigzag graphene nanoribbon. 9, 12, 14–17, 19–24, 26, 61, 66, 68, 158, 159, 210, 212, 213

ZPL zero-phonon line. 218, 220–224, 226, 231

Glossary

Chiral symmetry In condensed matter physics, chiral symmetry refers to a particular type of symmetry within the Hamiltonian describing the system. If the Hamiltonian of a system commutes with the chiral operator, the system is said to have chiral symmetry. In graphene, the chiral symmetry is equivalent to sublattice symmetry. 17, 18, 86

GW approximation GW approximation is a perturbative computational approach that combines the quasiparticle concept of many-body physics with the density functional theory (DFT) approach used in Kohn-Sham DFT. It accounts for the fact that the electron excitations are not just due to the external potential of the atomic nuclei but also due to the Coulomb interactions between electrons. The method is named after the contributions of the Green's function (G) and the screened Coulomb interaction (W). The GW method provides a better description of the electronic band gap and other electronic properties than the DFT approach, however, it is more computationally demanding than DFT. ix, 16, 22, 32, 210

Kohn–Sham DFT Kohn–Sham density functional theory (DFT) is a computational method used to study the electronic structure of molecules and solids. It is based on the idea that the total energy of a system can be expressed as a functional of the electron density. This means that the energy of a system can be calculated by knowing the distribution of electrons in the system. It reduces the problem into a set of non-interacting electrons that each move

in an effective potential, which is a combination of the external potential from the atomic nuclei and an effective potential that takes into account the electron-electron interactions. This approach is very computationally efficient, as it does not require solving the Schrödinger equation for each electron separately, but instead treats the electrons as a single effective potential. 15, 31

Majorana fermion Majorana fermions are particles that are their own antiparticles. They are neutral and do not carry any electric charge. They are a type of solution to the Dirac equation and were first proposed by the Italian theoretical physicist Ettore Majorana in 1937. While Majorana fermions are yet to be definitively observed as elementary particles in nature, there is significant interest in them in condensed matter physics, especially in the context of topological superconductors. In these systems, Majorana bound states can emerge as quasiparticle excitations, and they have potential applications in fault-tolerant topological quantum computing due to their non-abelian anyonic statistics. . 231

NP-hard NP-hardness, or non-deterministic polynomial-time hardness, refers to a class of problems in computational complexity theory. These problems are "at least as hard as the hardest problems in NP". Here, "NP" stands for "nondeterministic polynomial time", which is a class of problems for which solutions can be verified in polynomial time, though they may not necessarily be found in polynomial time. A problem is considered NP-hard if an algorithm for solving it can be translated into one for solving any problem in NP. This means that an NP-hard problem is at least as hard as any problem in NP, but could potentially be harder. 162

Quantum tunneling rotation Quantum tunneling is a quantum mechanical phenomenon where particles, such as electrons, can pass through potential barriers that classical physics suggests they shouldn't be able to pass through. For a classical rotation to happen, a chemical group needs to surmount an energy barrier. Taking a methyl group as an example, if it is rotate by 120° along the axis of symmetry, it changes to a different configuration with degenerate energy. The classical rotation can only happen if the group can pass over a energy barrier. However, quantum tunneling rotation refers to the process where the three hydrogen atoms in a methyl group can "tunnel" through potential energy barriers to undergo a rotation, effectively switching their positions. This rotation is not a classical rotation but a quantum mechanical process, where the hydrogens appear to move through energy barriers rather than over them. . 186

Type-I heterojunctions Type-I heterojunctions occur when the band gap energy of one material is smaller than that of the other material. The typical feature is straddling alignment of band edges. The conduction band minimum of one material is lower than the other material while the valence band maximum is higher than the other material. This will lead to the confinement of both electrons and holes in the same region, thus facilitate the strong electron-hole recombination at the interface, which can result in efficient generation of photocurrent and emission of light. 27

Type-II heterojunctions Type-II heterojunctions occur when the bands of one material is shifted relative to that of the other material. In this case, the band edges align in a staggered configuration. Both the conduction band minimum and valence band maximum of one material is lower than that of the other material, creating a potential energy barrier that separates the electrons and holes at the interface. This creates a built-in electric field in the interface and

facilitate the separation of electron-hole pairs. Type II heterojunctions are often used in photovoltaic devices and other electronic applications due to their ability to separate and transport charge carriers efficiently. 27

Acknowledgements

This thesis would not have been possible without the help and support from many people.

First, I would like to express my deep gratitudes to my supervisor Prof. Lapo Bogani. Thank you for creating a group with such friendly atmosphere where I can always find support in both academics and life. You have given me many essential advice and information in my research projects. Your guidance has inspired my exploration of many interesting things in both theory and experiments. You are also a great mentor that can always provide mental support and encouragement in the challenging moments, especially at the beginning of the COVID pandemic.

I thank the European Research Council (ERC) for the financial support throughout the four years, without which I would not be able to pursue my DPhil degree at Oxford. I am also grateful to the Trinity college for providing a supportive community. Especially, I thank the college for the graduate scholarship and writing-up grant that I have received.

I would also like to acknowledge the use of the University of Oxford Advanced Research Computing (ARC) facility in carrying out many of the calculations in this thesis. The ARC support team is always helpful when I encounter problems in using the computing services.

I would like to thank the all the collaborators who have contributed to the work included in this thesis: Dr. Ji Ma and Prof. Xinliang Feng from TU Dresden; Dr. Vasil Saroka from University of Rome Tor Vergata; Bernd Sturdza and Prof. Robin Nicholas from Department of Physics in Oxford. Thank you all for sharing your expertise in the collaboration. I also appreciate the help from Dr. William Myers. You are always ready to help me out from the troubles, and I have learned many knowledge from you about EPR.

I owe my profound gratitude to all the members in my group for the support and accompany throughout my DPhil journey. I thank Michael for patiently teaching me EPR techniques and helping me with data analysis, English writing. I would also like to thank Alessandro. You have given me so many insightful suggestions on various things, including transport, Python, and DFT. I thank Ming-Yee for always pointing out my inefficient code and give me smarter solutions. In particular, a big thank you to Michael and Ming-Yee, for all the time and efforts you have

spent on proofreading my thesis. I would also like to thank Xuelin and Dimitris for not only providing samples, but also sharing knowledge of chemistry with me. I will always remember the amazing cakes made by Dimitris. I also want to thank Alex for sharing your passion, as well as lots of knowledge ranging from transport measurements to proper British English. I thank Karen Yan for the time we did the EPR measurements together. I would also like to thank Simen, Iago, Federico, Arthur, Zhixin, Hewen, Chen, Matthew, James, Zhijie, Ramon, and Yongxiang for the friendship and accompany.

Finally, I want to thank my family for your love and support. You are always there to back me up. Also thank you to Xueyi Zeng, you had accompanied me throughout all the happy occasions and difficult times.

References

[1] K. S. Novoselov, A. K. Geim, S. V. Morozov, D. Jiang, Y. Zhang, S. V. Dubonos, I. V. Grigorieva, and A. A. Firsov. "Electric field effect in atomically thin carbon films". In: *Science* 306.5696 (2004), pp. 666–9. doi:10/bcqksc.

[2] Akanksha R. Urade, Indranil Lahiri, and K. S. Suresh. "Graphene Properties, Synthesis and Applications: A Review". In: *JOM* 75.3 (2023), pp. 614–630. doi:10/gsj5d8.

[3] E. W. Hill, A. Vijayaragahvan, and K. Novoselov. "Graphene Sensors". In: *Ieee Sensors Journal* 11.12 (2011), pp. 3161–3170. doi:10/dq499m.

[4] C. X. Guo, G. H. Guai, and C. M. Li. "Graphene Based Materials: Enhancing Solar Energy Harvesting". In: *Advanced Energy Materials* 1.3 (2011), pp. 448–452. doi:10/cvk54h.

[5] R. Raccichini, A. Varzi, S. Passerini, and B. Scrosati. "The role of graphene for electrochemical energy storage". In: *Nat Mater* 14.3 (2015), pp. 271–9. doi:10/gmzpjr.

[6] F. Bonaccorso, Z. Sun, T. Hasan, and A. C. Ferrari. "Graphene photonics and optoelectronics". In: *Nature Photonics* 4.9 (2010), pp. 611–622. doi:10/dtxkpd.

[7] D. Pesin and A. H. MacDonald. "Spintronics and pseudospintronics in graphene and topological insulators". In: *Nat Mater* 11.5 (2012), pp. 409–16. doi:10/gjp244.

[8] K. Nakada, M. Fujita, G. Dresselhaus, and M. S. Dresselhaus. "Edge state in graphene ribbons: Nanometer size effect and edge shape dependence". In: *Phys Rev B Condens Matter* 54.24 (1996), pp. 17954–17961. doi:10/bwr2tz.

[9] Y. W. Son, M. L. Cohen, and S. G. Louie. "Half-metallic graphene nanoribbons". In: *Nature* 444.7117 (2006), pp. 347–9. doi:10/cmcsvp.

[10] W. Y. Kim and K. S. Kim. "Prediction of very large values of magnetoresistance in a graphene nanoribbon device". In: *Nature Nanotechnology* 3.7 (2008), pp. 408–412. doi:10/bzmgc4.

[11] Z. F. Wang, S. Jin, and F. Liu. "Spatially separated spin carriers in spin-semiconducting graphene nanoribbons". In: *Phys Rev Lett* 111.9 (2013), p. 096803. doi:10/f5hc7m.

[12] T. Cao, F. Zhao, and S. G. Louie. "Topological Phases in Graphene Nanoribbons: Junction States, Spin Centers, and Quantum Spin Chains". In: *Phys Rev Lett* 119.7 (2017), p. 076401. doi:10/gbzfz7.

[13] L. Jiao, L. Zhang, X. Wang, G. Diankov, and H. Dai. "Narrow graphene nanoribbons from carbon nanotubes". In: *Nature* 458.7240 (2009), pp. 877–80. doi:10/djgbb2.

[14] D. V. Kosynkin, A. L. Higginbotham, A. Sinitskii, J. R. Lomeda, A. Dimiev, B. K. Price, and J. M. Tour. "Longitudinal unzipping of carbon nanotubes to form graphene nanoribbons". In: *Nature* 458.7240 (2009), pp. 872–6. doi:10/dqrt4s.

[15] A. G. Cano-Marquez, F. J. Rodriguez-Macias, J. Campos-Delgado, C. G. Espinosa-Gonzalez, F. Tristan-Lopez, D. Ramirez-Gonzalez, D. A. Cullen, D. J. Smith, M. Terrones, and Y. I. Vega-Cantu. "Ex-MWNTs: graphene sheets and ribbons produced by lithium intercalation and exfoliation of carbon nanotubes". In: *Nano Lett* 9.4 (2009), pp. 1527–33. doi:10/drhk7k.

[16] U. K. Parashar, S. Bhandari, R. K. Srivastava, D. Jariwala, and A. Srivastava. "Single step synthesis of graphene nanoribbons by catalyst particle size dependent cutting of multiwalled carbon nanotubes". In: *Nanoscale* 3.9 (2011), pp. 3876–82. doi:10/d47prj.

[17] Ana Laura Elías, Andrés R Botello-Méndez, David Meneses-Rodríguez, Viviana Jehová González, Daniel Ramírez-González, Lijie Ci, Emilio Munoz-Sandoval, Pulickel M Ajayan, Humberto Terrones, and Mauricio Terrones. "Longitudinal cutting of pure and doped carbon nanotubes to form graphitic nanoribbons using metal clusters as nanoscalpels". In: *Nano letters* 10.2 (2009), pp. 366–372. doi:10/cksjfs.

[18] J. Bai, X. Duan, and Y. Huang. "Rational fabrication of graphene nanoribbons using a nanowire etch mask". In: *Nano Lett* 9.5 (2009), pp. 2083–7. doi:10/d3spph.

[19] L. Tapaszto, G. Dobrik, P. Lambin, and L. P. Biro. "Tailoring the atomic structure of graphene nanoribbons by scanning tunnelling microscope lithography". In: *Nat Nanotechnol* 3.7 (2008), pp. 397–401. doi:10/cftrt3.

[20] L. Ci, Z. P. Xu, L. L. Wang, W. Gao, F. Ding, K. F. Kelly, B. I. Yakobson, and P. M. Ajayan. "Controlled Nanocutting of Graphene". In: *Nano Research* 1.2 (2008), pp. 116–122. doi:10/bwgxqf.

[21] S. S. Datta, D. R. Strachan, S. M. Khamis, and A. T. Johnson. "Crystallographic etching of few-layer graphene". In: *Nano Lett* 8.7 (2008), pp. 1912–5. doi:10/bhd274.

[22] L. C. Campos, V. R. Manfrinato, J. D. Sanchez-Yamagishi, J. Kong, and P. Jarillo-Herrero. "Anisotropic etching and nanoribbon formation in single-layer graphene". In: *Nano Lett* 9.7 (2009), pp. 2600–4. doi:10/fmdgtr.

[23] L. J. Ci, L. Song, D. Jariwala, A. L. Elias, W. Gao, M. Terrones, and P. M. Ajayan. "Graphene Shape Control by Multistage Cutting and Transfer". In: *Advanced Materials* 21.44 (2009), pp. 4487–+. doi:10/bpz58p.

[24] X. Li, X. Wang, L. Zhang, S. Lee, and H. Dai. "Chemically derived, ultrasmooth graphene nanoribbon semiconductors". In: *Science* 319.5867 (2008), pp. 1229–32. doi:10/ccbnxq.

[25] Z. S. Wu, W. C. Ren, L. B. Gao, B. L. Liu, J. P. Zhao, and H. M. Cheng. "Efficient Synthesis of Graphene Nanoribbons Sonochemically Cut from Graphene Sheets". In: *Nano Research* 3.1 (2010), pp. 16–22. doi:10/b4n8kn.

[26] J. Campos-Delgado, J. M. Romo-Herrera, X. Jia, D. A. Cullen, H. Muramatsu, Y. A. Kim, T. Hayashi, Z. Ren, D. J. Smith, Y. Okuno, T. Ohba, H. Kanoh, K. Kaneko, M. Endo, H. Terrones, M. S. Dresselhaus, and M. Terrones. "Bulk production of a new form of sp(2) carbon: crystalline graphene nanoribbons". In: *Nano Lett* 8.9 (2008), pp. 2773–8. doi:10/cd7pck.

[27] I. Martin-Fernandez, D. Wang, and Y. Zhang. "Direct growth of graphene nanoribbons for large-scale device fabrication". In: *Nano Lett* 12.12 (2012), pp. 6175–9. doi:10/f4fhdb.

[28] A. N. Sokolov, F. L. Yap, N. Liu, K. Kim, L. Ci, O. B. Johnson, H. Wang, M. Vosgueritchian, A. L. Koh, J. Chen, J. Park, and Z. Bao. "Direct growth of aligned graphitic nanoribbons from a DNA template by chemical vapour deposition". In: *Nat Commun* 4.1 (2013), p. 2402. doi:10/gbdk67.

[29] D. Wang, H. Tian, Y. Yang, D. Xie, T. L. Ren, and Y. Zhang. "Scalable and direct growth of graphene micro ribbons on dielectric substrates". In: *Sci Rep* 3 (2013), p. 1348. doi:10/gbcr7m.

[30] M. Sprinkle, M. Ruan, Y. Hu, J. Hankinson, M. Rubio-Roy, B. Zhang, X. Wu, C. Berger, and W. A. de Heer. "Scalable templated growth of graphene nanoribbons on SiC". In: *Nat Nanotechnol* 5.10 (2010), pp. 727–31. doi:10/c9zzrh.

[31] A. Narita, X. Feng, and K. Mullen. "Bottom-up synthesis of chemically precise graphene nanoribbons". In: *Chem Rec* 15.1 (2015), pp. 295–309. doi:10/f2wd5n.

[32] Xiao-Ye Wang, Akimitsu Narita, and Klaus Müllen. "Precision synthesis versus bulk-scale fabrication of graphenes". In: *Nature Reviews Chemistry* 2.1 (2017), p. 0100. doi:10/gc93mr.

[33] A. Narita, Z. Chen, Q. Chen, and K. Mullen. "Solution and on-surface synthesis of structurally defined graphene nanoribbons as a new family of semiconductors". In: *Chem Sci* 10.4 (2019), pp. 964–975. doi:10/gkb8dq.

[34] Y. Yano, N. Mitoma, H. Ito, and K. Itami. "A Quest for Structurally Uniform Graphene Nanoribbons: Synthesis, Properties, and Applications". In: *J Org Chem* 85.1 (2020), pp. 4–33. doi:10/gkb8hb.

[35] L. Martini, Z. P. Chen, N. Mishra, G. B. Barin, P. Fantuzzi, P. Ruffieux, R. Fasel, X. L. Feng, A. Narita, C. Coletti, K. Mullen, and A. Candini. "Structure-dependent electrical properties of graphene nanoribbon devices with graphene electrodes". In: *Carbon* 146 (2019), pp. 36–43. doi:10/grtt75.

[36] M. El Abbassi, M. L. Perrin, G. B. Barin, S. Sangtarash, J. Overbeck, O. Braun, C. J. Lambert, Q. Sun, T. Prechtl, A. Narita, K. Mullen, P. Ruffieux, H. Sadeghi, R. Fasel, and M. Calame. "Controlled Quantum Dot Formation in Atomically Engineered Graphene Nanoribbon Field-Effect Transistors". In: *ACS Nano* 14.5 (2020), pp. 5754–5762. doi:10/gkb9wz.

[37] M. J. J. Mangnus, F. R. Fischer, M. F. Crommie, I. Swart, and P. H. Jacobse. "Charge transport in topological graphene nanoribbons and nanoribbon heterostructures". In: *Physical Review B* 105.11 (2022), p. 115424. doi:10/grtt3t.

[38] W. Niu, S. Sopp, A. Lodi, A. Gee, F. Kong, T. Pei, P. Gehring, J. Nagele, C. S. Lau, J. Ma, J. Liu, A. Narita, J. Mol, M. Burghard, K. Mullen, Y. Mai, X. Feng, and L. Bogani. "Exceptionally clean single-electron transistors from solutions of molecular graphene nanoribbons". In: *Nat Mater* 22.2 (2023), pp. 180–185. doi:10/grtt48.

[39] J. M. Marmolejo-Tejada and J. Velasco-Medina. "Review on graphene nanoribbon devices for logic applications". In: *Microelectronics Journal* 48 (2016), pp. 18–38. doi:10/gf9rdq.

[40] Sanna Lone, Anil Bhardwaj, Amit Kant Pandit, Sumeet Gupta, and Shubham Mahajan. "A Review of Graphene Nanoribbon Field-Effect Transistor Structures". In: *Journal of Electronic Materials* 50.6 (2021), pp. 3169–3186. doi:10/gsj524.

[41] B. Trauzettel, D. V. Bulaev, D. Loss, and G. Burkard. "Spin qubits in graphene quantum dots". In: *Nature Physics* 3.3 (2007), pp. 192–196. doi:10/dr3mrx.

[42] Shun-Qing Shen. *Topological insulators*. Vol. 174. Springer, 2012.

[43] M. Z. Hasan and C. L. Kane. "Colloquium: Topological insulators". In: *Reviews of Modern Physics* 82.4 (2010), pp. 3045–3067. doi:10/fckvfn.

[44] A. Bansil, H. Lin, and T. Das. "Colloquium: Topological band theory". In: *Reviews of Modern Physics* 88.2 (2016), p. 021004. doi:10/gcpdbv.

[45] J. Fischer, B. Trauzettel, and D. Loss. "Hyperfine interaction and electron-spin decoherence in graphene and carbon nanotube quantum dots". In: *Physical Review B* 80.15 (2009), p. 155401. doi:10/c4x3hg.

[46] J. W. Bai, R. Cheng, F. X. Xiu, L. Liao, M. S. Wang, A. Shailos, K. L. Wang, Y. Huang, and X. F. Duan. "Very large magnetoresistance in graphene nanoribbons". In: *Nature Nanotechnology* 5.9 (2010), pp. 655–659. doi:10/dvgqnd.

[47] J. Guo, D. Gunlycke, and C. T. White. "Field effect on spin-polarized transport in graphene nanoribbons". In: *Applied Physics Letters* 92.16 (2008), p. 163109. doi:10/bnptw7.

[48] Z. H. Qiao, S. A. Yang, B. Wang, Y. G. Yao, and Q. Niu. "Spin-polarized and valley helical edge modes in graphene nanoribbons". In: *Physical Review B* 84.3 (2011), p. 035431. doi:10/c7855x.

[49] X. Wu, R. Wang, N. Liu, H. Zou, B. Shao, L. Shao, and C. Yam. "Controlling the emission frequency of graphene nanoribbon emitters based on spatially excited topological boundary states". In: *Phys Chem Chem Phys* 22.16 (2020), pp. 8277–8283. doi:10/gkb8v4.

[50] C. Ma, Z. Xiao, A. A. Puretzky, H. Wang, A. Mohsin, J. Huang, L. Liang, Y. Luo, B. J. Lawrie, G. Gu, W. Lu, K. Hong, J. Bernholc, and A. P. Li. "Engineering Edge States of Graphene Nanoribbons for Narrow-Band Photoluminescence". In: *ACS Nano* 14.4 (2020), pp. 5090–5098. doi:10/gkb98w.

[51] Song Jiang, Tomáš Neuman, Alex Boeglin, Fabrice Scheurer, and Guillaume Schull. "Topologically localized excitons in single graphene nanoribbons". In: *Science* 379.6636 (2023), pp. 1049–1054. doi:10/gss4td.

[52] Liangbo Liang and Vincent Meunier. "Atomically Precise Graphene Nanoribbon Heterojunctions for Excitonic Solar Cells". In: *The Journal of Physical Chemistry C* 119.1 (2015), pp. 775–783. doi:10/grwkf3.

[53] C. E. Villegas, P. B. Mendonca, and A. R. Rocha. "Optical spectrum of bottom-up graphene nanoribbons: towards efficient atom-thick excitonic solar cells". In: *Sci Rep* 4.1 (2014), p. 6579. doi:10/gkb8k3.

[54] S. Osella, A. Narita, M. G. Schwab, Y. Hernandez, X. Feng, K. Mullen, and D. Beljonne. "Graphene nanoribbons as low band gap donor materials for organic photovoltaics: quantum chemical aided design". In: *ACS Nano* 6.6 (2012), pp. 5539–48. doi:10/ghb4rf.

[55] J. Jiang and S. G. Louie. "Topology Classification using Chiral Symmetry and Spin Correlations in Graphene Nanoribbons". In: *Nano Lett* 21.1 (2021), pp. 197–202. doi:10/gkb9j3.

[56] E. C. H. Wen, P. H. Jacobse, J. Jiang, Z. Wang, R. D. McCurdy, S. G. Louie, M. F. Crommie, and F. R. Fischer. "Magnetic Interactions in Substitutional Core-Doped Graphene Nanoribbons". In: *J Am Chem Soc* 144.30 (2022), pp. 13696–13703. doi:10/grtt6j.

[57] Q. Sun, X. Yao, O. Groning, K. Eimre, C. A. Pignedoli, K. Mullen, A. Narita, R. Fasel, and P. Ruffieux. "Coupled Spin States in Armchair Graphene Nanoribbons with Asymmetric Zigzag Edge Extensions". In: *Nano Lett* 20.9 (2020), pp. 6429–6436. doi:10/gjn7qn.

[58] A. Yu Kitaev. "Unpaired Majorana fermions in quantum wires". In: *Physics-Uspekhi* 44.10 (2001), pp. 131–136. doi:10/fc6q65.

[59] O. Groning, S. Wang, X. Yao, C. A. Pignedoli, G. Borin Barin, C. Daniels, A. Cupo, V. Meunier, X. Feng, A. Narita, K. Mullen, P. Ruffieux, and R. Fasel. "Engineering of robust topological quantum phases in graphene nanoribbons". In: *Nature* 560.7717 (2018), pp. 209–213. doi:10/gdxvxn.

[60] M. Droth and G. Burkard. "Acoustic phonons and spin relaxation in graphene nanoribbons". In: *Physical Review B* 84.15 (2011). doi:10/fk3g86.

[61] M. Droth and G. Burkard. "Electron spin relaxation in graphene nanoribbon quantum dots". In: *Physical Review B* 87.20 (2013), p. 205432. doi:10/grtt4s.

[62] M. Slota, A. Keerthi, W. K. Myers, E. Tretyakov, M. Baumgarten, A. Ardavan, H. Sadeghi, C. J. Lambert, A. Narita, K. Mullen, and L. Bogani. "Magnetic edge states and coherent manipulation of graphene nanoribbons". In: *Nature* 557.7707 (2018), pp. 691–695. doi:10/gdm265.

[63] F. Lombardi, A. Lodi, J. Ma, J. Liu, M. Slota, A. Narita, W. K. Myers, K. Mullen, X. Feng, and L. Bogani. "Quantum units from the topological engineering of molecular graphenoids". In: *Science* 366.6469 (2019), pp. 1107–1110. doi:10/ggfmcq.

[64] X. Zhou and G. Yu. "Modified Engineering of Graphene Nanoribbons Prepared via On-Surface Synthesis". In: *Adv Mater* 32.6 (2020), e1905957. doi:10/gkb8f8.

[65] A. H. Castro Neto, F. Guinea, N. M. R. Peres, K. S. Novoselov, and A. K. Geim. "The electronic properties of graphene". In: *Reviews of Modern Physics* 81.1 (2009), pp. 109–162. doi:10/bgd7s4.

[66] Y. W. Son, M. L. Cohen, and S. G. Louie. "Energy gaps in graphene nanoribbons". In: *Phys Rev Lett* 97.21 (2006), p. 216803. doi:10/bk8cbg.

[67] Pooja Rani and V. K. Jindal. "Designing band gap of graphene by B and N dopant atoms". In: *RSC Adv.* 3.3 (2013), pp. 802–812. doi:10/gns2hm.

[68] Xiong Cao, Jun-jie Shi, Min Zhang, Xin-he Jiang, Hong-xia Zhong, Pu Huang, Yi-min Ding, and Meng Wu. "Band Gap Opening of Graphene by Forming Heterojunctions with the 2D Carbonitrides Nitrogenated Holey Graphene, g-C3N4, and g-CN: Electric Field Effect". In: *The Journal of Physical Chemistry C* 120.20 (May 26, 2016). Publisher: American Chemical Society, pp. 11299–11305. doi:10/f8qph3.

[69] Yuanbo Zhang, Tsung-Ta Tang, Caglar Girit, Zhao Hao, Michael C. Martin, Alex Zettl, Michael F. Crommie, Y. Ron Shen, and Feng Wang. "Direct observation of a widely tunable bandgap in bilayer graphene". In: *Nature* 459.7248 (June 2009). Number: 7248 Publisher: Nature Publishing Group, pp. 820–823. doi:10/b5ftfp.

[70] Hamed Abbasian. "Gap Opening in Graphene via Locally Introduced Electric Field". In: *physica status solidi (RRL) – Rapid Research Letters* 17.7 (2023). _eprint: https://onlinelibrary.wiley.com/doi/pdf/10.1002/pssr.202200302, p. 2200302. doi:10/gs2qb7.

[71] Katsunori Wakabayashi, Ken-ichi Sasaki, Takeshi Nakanishi, and Toshiaki Enoki. "Electronic states of graphene nanoribbons and analytical solutions". In: *Science and Technology of Advanced Materials* 11.5 (2010), p. 054504. doi:10/d7s58x.

[72] Stephanie Reich, Christian Thomsen, and Janina Maultzsch. *Carbon nanotubes: basic concepts and physical properties*. John Wiley & Sons, 2008.

[73] M. Fujita, K. Wakabayashi, K. Nakada, and K. Kusakabe. "Peculiar localized state at zigzag graphite edge". In: *Journal of the Physical Society of Japan* 65.7 (1996), pp. 1920–1923. doi:10/d6j3h9.

[74] M. Y. Han, B. Ozyilmaz, Y. Zhang, and P. Kim. "Energy band-gap engineering of graphene nanoribbons". In: *Phys Rev Lett* 98.20 (2007), p. 206805. doi:10/b9p9ks.

[75] C. G. Tao, L. Y. Jiao, O. V. Yazyev, Y. C. Chen, J. J. Feng, X. W. Zhang, R. B. Capaz, J. M. Tour, A. Zettl, S. G. Louie, H. J. Dai, and M. F. Crommie. "Spatially resolving edge states of chiral graphene nanoribbons". In: *Nature Physics* 7.8 (2011), pp. 616–620. doi:10/drh866.

[76] H. S. Wang, L. Chen, K. Elibol, L. He, H. Wang, C. Chen, C. Jiang, C. Li, T. Wu, C. X. Cong, T. J. Pennycook, G. Argentero, D. Zhang, K. Watanabe, T. Taniguchi, W. Wei, Q. Yuan, J. C. Meyer, and X. Xie. "Towards chirality control of graphene nanoribbons embedded in hexagonal boron nitride". In: *Nat Mater* 20.2 (2021), pp. 202–207. doi:10/ghfwn3.

[77] L. Yang, C. H. Park, Y. W. Son, M. L. Cohen, and S. G. Louie. "Quasiparticle energies and band gaps in graphene nanoribbons". In: *Phys Rev Lett* 99.18 (2007), p. 186801. doi:10/b856kp.

[78] F. Aryasetiawan and O. Gunnarsson. "The GW method". In: *Reports on Progress in Physics* 61.3 (1998), pp. 237–312. doi:10/dn4zkp.

[79] P. Ruffieux, J. Cai, N. C. Plumb, L. Patthey, D. Prezzi, A. Ferretti, E. Molinari, X. Feng, K. Mullen, C. A. Pignedoli, and R. Fasel. "Electronic structure of atomically precise graphene nanoribbons". In: *ACS Nano* 6.8 (2012), pp. 6930–5. doi:10/f36kkp.

[80] R. Denk, M. Hohage, P. Zeppenfeld, J. Cai, C. A. Pignedoli, H. Sode, R. Fasel, X. Feng, K. Mullen, S. Wang, D. Prezzi, A. Ferretti, A. Ruini, E. Molinari, and P. Ruffieux. "Exciton-dominated optical response of ultra-narrow graphene nanoribbons". In: *Nat Commun* 5.1 (2014), p. 4253. doi:10/f6dbtm.

[81] L. Brey and H. A. Fertig. "Electronic states of graphene nanoribbons studied with the Dirac equation". In: *Physical Review B* 73.23 (2006), p. 235411. doi:10/djh968.

[82] P. Marconcini and M. Macucci. "The k center dot p method and its application to graphene, carbon nanotubes and graphene nanoribbons: the Dirac equation". In: *Rivista Del Nuovo Cimento* 34.8 (2011), pp. 489–584. doi:10/gj597h.

[83] C. L. Kane and E. J. Mele. "Quantum spin Hall effect in graphene". In: *Phys Rev Lett* 95.22 (2005), p. 226801. doi:10/c3hxn6.

[84] C. L. Kane and E. J. Mele. "\Z_2\ Topological Order and the Quantum Spin Hall Effect". In: *Physical Review Letters* 95.14 (2005), p. 146802. doi:10/d82f8w.

[85] A. R. Akhmerov and C. W. J. Beenakker. "Boundary conditions for Dirac fermions on a terminated honeycomb lattice". In: *Physical Review B* 77.8 (2008), p. 085423. doi:10/cchxds.

[86] G. Tkachov. "Dirac fermion quantization on graphene edges: Isospin-orbit coupling, zero modes, and spontaneous valley polarization". In: *Physical Review B* 79.4 (2009). doi:10/cv7q4g.

[87] S. Ryu and Y. Hatsugai. "Topological origin of zero-energy edge states in particle-hole symmetric systems". In: *Phys Rev Lett* 89.7 (2002), p. 077002. doi:10/dx3g6v.

[88] L. Pisani, J. A. Chan, B. Montanari, and N. M. Harrison. "Electronic structure and magnetic properties of graphitic ribbons". In: *Physical Review B* 75.6 (2007), p. 064418. doi:10/fjnhk7.

[89] P. Delplace, D. Ullmo, and G. Montambaux. "Zak phase and the existence of edge states in graphene". In: *Physical Review B* 84.19 (2011). doi:10/chk4sn.

[90] Guido van Miert, Carmine Ortix, and Cristiane Morais Smith. "Topological origin of edge states in two-dimensional inversion-symmetric insulators and semimetals". In: *2D Materials* 4.1 (2016), p. 015023.

[91] O. V. Yazyev, R. B. Capaz, and S. G. Louie. "Theory of magnetic edge states in chiral graphene nanoribbons". In: *Physical Review B* 84.11 (2011), p. 115406. doi:10/bjhmsd.

[92] M. Kohmoto and Y. Hasegawa. "Zero modes and edge states of the honeycomb lattice". In: *Physical Review B* 76.20 (2007). doi:10/cj28fb.

[93] W. Jaskólski, A. Ayuela, M. Pelc, H. Santos, and L. Chico. "Edge states and flat bands in graphene nanoribbons with arbitrary geometries". In: *Physical Review B* 83.23 (2011). doi:10/fw4nhm.

[94] Keisuke Sawada, Fumiyuki Ishii, and Mineo Saito. “Band-Gap Tuning in Magnetic Graphene Nanoribbons”. In: *Applied Physics Express* 1 (2008), p. 064004. doi:10/dkfw6j.

[95] O. Hod, V. Barone, J. E. Peralta, and G. E. Scuseria. “Enhanced half-metallicity in edge-oxidized zigzag graphene nanoribbons”. In: *Nano Lett* 7.8 (2007), pp. 2295–9. doi:10/d2rpw8.

[96] E. J. Kan, Z. Li, J. Yang, and J. G. Hou. “Half-metallicity in edge-modified zigzag graphene nanoribbons”. In: *J Am Chem Soc* 130.13 (2008), pp. 4224–5. doi:10/bwjws2.

[97] S. Dutta and S. K. Pati. “Half-metallicity in undoped and boron doped graphene nanoribbons in the presence of semilocal exchange-correlation interactions”. In: *J Phys Chem B* 112.5 (2008), pp. 1333–5. doi:10/bk6mpn.

[98] A. Rycerz, J. Tworzydło, and C. W. J. Beenakker. “Valley filter and valley valve in graphene”. In: *Nature Physics* 3.3 (2007), pp. 172–175. doi:10/c45bpq.

[99] W. Yao, S. A. Yang, and Q. Niu. “Edge states in graphene: from gapped flat-band to gapless chiral modes”. In: *Phys Rev Lett* 102.9 (2009), p. 096801. doi:10/fqz9sr.

[100] K. Sasaki, J. Jiang, R. Saito, S. Onari, and Y. Tanaka. “Theory of superconductivity of carbon nanotubes and graphene”. In: *Journal of the Physical Society of Japan* 76.3 (2007), p. 033702. doi:10/crcj3q.

[101] D. E. Jiang, B. G. Sumpter, and S. Dai. “Unique chemical reactivity of a graphene nanoribbon’s zigzag edge”. In: *J Chem Phys* 126.13 (2007), p. 134701. doi:10/b5vx5p.

[102] B. Huang, F. Liu, J. Wu, B. L. Gu, and W. H. Duan. “Suppression of spin polarization in graphene nanoribbons by edge defects and impurities”. In: *Physical Review B* 77.15 (2008), p. 153411. doi:10/cpsqgg.

[103] P. Ruffieux, S. Wang, B. Yang, C. Sanchez-Sanchez, J. Liu, T. Dienel, L. Talirz, P. Shinde, C. A. Pignedoli, D. Passerone, T. Dumslaff, X. Feng, K. Mullen, and R. Fasel. “On-surface synthesis of graphene nanoribbons with zigzag edge topology”. In: *Nature* 531.7595 (2016), pp. 489–92. doi:10/f8fj8t.

[104] R. E. Blackwell, F. Zhao, E. Brooks, J. Zhu, I. Piskun, S. Wang, A. Delgado, Y. L. Lee, S. G. Louie, and F. R. Fischer. “Spin splitting of dopant edge state in magnetic zigzag graphene nanoribbons”. In: *Nature* 600.7890 (2021), pp. 647–652. doi:10/gnv7h9.

[105] V. Barone, O. Hod, and G. E. Scuseria. “Electronic structure and stability of semiconducting graphene nanoribbons”. In: *Nano Lett* 6.12 (2006), pp. 2748–54. doi:10/djdkdd.

[106] J. Cai, P. Ruffieux, R. Jaafar, M. Bieri, T. Braun, S. Blankenburg, M. Muoth, A. P. Seitsonen, M. Saleh, X. Feng, K. Mullen, and R. Fasel. “Atomically precise bottom-up fabrication of graphene nanoribbons”. In: *Nature* 466.7305 (2010), pp. 470–3. doi:10/fjq74g.

[107] Néstor Merino-Díez, Jingcheng Li, Aran Garcia-Lekue, Guillaume Vasseur, Manuel Vilas-Varela, Eduard Carbonell-Sanromà, Martina Corso, J. Enrique Ortega, Diego Peña, Jose I. Pascual, and Dimas G. De Oteyza. "Unraveling the Electronic Structure of Narrow Atomically Precise Chiral Graphene Nanoribbons". In: *The Journal of Physical Chemistry Letters* 9.1 (2018), pp. 25–30. doi:10/gcvwtb.

[108] A. Kimouche, M. M. Ervasti, R. Drost, S. Halonen, A. Harju, P. M. Joensuu, J. Sainio, and P. Liljeroth. "Ultra-narrow metallic armchair graphene nanoribbons". In: *Nat Commun* 6 (2015), p. 10177. doi:10/f75db2.

[109] Andrea Basagni, Francesco Sedona, Carlo A. Pignedoli, Mattia Cattelan, Louis Nicolas, Maurizio Casarin, and Mauro Sambi. "Molecules–Oligomers–Nanowires–Graphene Nanoribbons: A Bottom-Up Stepwise On-Surface Covalent Synthesis Preserving Long-Range Order". In: *Journal of the American Chemical Society* 137.5 (2015), pp. 1802–1808. doi:10/gkb9p7.

[110] Robert S. Jordan, Yolanda L. Li, Cheng-Wei Lin, Ryan D. McCurdy, Janice B. Lin, Jonathan L. Brosmer, Kristofer L. Marsh, Saeed I. Khan, K. N. Houk, Richard B. Kaner, and Yves Rubin. "Synthesis of $N = 8$ Armchair Graphene Nanoribbons from Four Distinct Polydiacetylenes". In: *Journal of the American Chemical Society* 139.44 (2017), pp. 15878–15890. doi:10/gcgvv5.

[111] X. Yang, X. Dou, A. Rouhanipour, L. Zhi, H. J. Rader, and K. Mullen. "Two-dimensional graphene nanoribbons". In: *J Am Chem Soc* 130.13 (2008), pp. 4216–7. doi:10/cjdt86.

[112] Z. Chen, H. I. Wang, J. Teyssandier, K. S. Mali, T. Dumslaff, I. Ivanov, W. Zhang, P. Ruffieux, R. Fasel, H. J. Rader, D. Turchinovich, S. De Feyter, X. Feng, M. Klaui, A. Narita, M. Bonn, and K. Mullen. "Chemical Vapor Deposition Synthesis and Terahertz Photoconductivity of Low-Band-Gap N = 9 Armchair Graphene Nanoribbons". In: *J Am Chem Soc* 139.10 (2017), pp. 3635–3638. doi:10/gkcbd6.

[113] L. Talirz, H. Sode, T. Dumslaff, S. Wang, J. R. Sanchez-Valencia, J. Liu, P. Shinde, C. A. Pignedoli, L. Liang, V. Meunier, N. C. Plumb, M. Shi, X. Feng, A. Narita, K. Mullen, R. Fasel, and P. Ruffieux. "On-Surface Synthesis and Characterization of 9-Atom Wide Armchair Graphene Nanoribbons". In: *ACS Nano* 11.2 (2017), pp. 1380–1388. doi:10/f9n4sf.

[114] Robert, Yue Wang, Ryan, Michael, Kristofer, Saeed, Richard, and Yves Rubin. "Synthesis of Graphene Nanoribbons via the Topochemical Polymerization and Subsequent Aromatization of a Diacetylene Precursor". In: *Chem* 1.1 (2016), pp. 78–90. doi:10/grwz5c.

[115] Y. C. Chen, D. G. de Oteyza, Z. Pedramrazi, C. Chen, F. R. Fischer, and M. F. Crommie. "Tuning the band gap of graphene nanoribbons synthesized from molecular precursors". In: *ACS Nano* 7.7 (2013), pp. 6123–8. doi:10/f46ksx.

[116] Nasiba Abdurakhmanova, Nadja Amsharov, Sebastian Stepanow, Martin Jansen, Klaus Kern, and Konstantin Amsharov. "Synthesis of wide atomically precise graphene nanoribbons from para-oligophenylene based molecular precursor". In: *Carbon* 77 (2014), pp. 1187–1190. doi:10/f6d6th.

[117] Mirella El Gemayel, Akimitsu Narita, Lukas F. Dössel, Ravi S. Sundaram, Adam Kiersnowski, Wojciech Pisula, Michael Ryan Hansen, Andrea C. Ferrari, Emanuele Orgiu, Xinliang Feng, Klaus Müllen, and Paolo Samorì. "Graphene nanoribbon blends with P3HT for organic electronics". In: *Nanoscale* 6.12 (2014), pp. 6301–6314. doi:10/gkb9kz.

[118] Zongping Chen, Hai I. Wang, Nerea Bilbao, Joan Teyssandier, Thorsten Prechtl, Nicola Cavani, Alexander Tries, Roberto Biagi, Valentina De Renzi, Xinliang Feng, Mathias Kläui, Steven De Feyter, Mischa Bonn, Akimitsu Narita, and Klaus Müllen. "Lateral Fusion of Chemical Vapor Deposited $N = 5$ Armchair Graphene Nanoribbons". In: *Journal of the American Chemical Society* 139.28 (2017), pp. 9483–9486. doi:10/gbsmxb.

[119] Néstor Merino-Díez, Aran Garcia-Lekue, Eduard Carbonell-Sanromà, Jingcheng Li, Martina Corso, Luciano Colazzo, Francesco Sedona, Daniel Sánchez-Portal, Jose I. Pascual, and Dimas G. De Oteyza. "Width-Dependent Band Gap in Armchair Graphene Nanoribbons Reveals Fermi Level Pinning on Au(111)". In: *ACS Nano* 11.11 (2017), pp. 11661–11668. doi:10/gcqb5d.

[120] Kewei Sun, Penghui Ji, Junjie Zhang, Jinxi Wang, Xuechao Li, Xin Xu, Haiming Zhang, and Lifeng Chi. "On-Surface Synthesis of 8- and 10-Armchair Graphene Nanoribbons". In: *Small* 15.15 (2019), p. 1804526. doi:10/gkb9qk.

[121] Okan Deniz, Carlos Sánchez-Sánchez, Tim Dumslaff, Xinliang Feng, Akimitsu Narita, Klaus Müllen, Neerav Kharche, Vincent Meunier, Roman Fasel, and Pascal Ruffieux. "Revealing the Electronic Structure of Silicon Intercalated Armchair Graphene Nanoribbons by Scanning Tunneling Spectroscopy". In: *Nano Letters* 17.4 (2017), pp. 2197–2203. doi:10/f94rtc.

[122] Patrick Han, Kazuto Akagi, Filippo Federici Canova, Hirotaka Mutoh, Susumu Shiraki, Katsuya Iwaya, Paul S. Weiss, Naoki Asao, and Taro Hitosugi. "Bottom-Up Graphene-Nanoribbon Fabrication Reveals Chiral Edges and Enantioselectivity". In: *ACS Nano* 8.9 (2014), pp. 9181–9187. doi:10/ghb23n.

[123] Dimas G. De Oteyza, Aran García-Lekue, Manuel Vilas-Varela, Néstor Merino-Díez, Eduard Carbonell-Sanromà, Martina Corso, Guillaume Vasseur, Celia Rogero, Enrique Guitián, Jose Ignacio Pascual, J. Enrique Ortega, Yutaka Wakayama, and Diego Peña. "Substrate-Independent Growth of Atomically Precise Chiral Graphene Nanoribbons". In: *ACS Nano* 10.9 (2016), pp. 9000–9008. doi:10/ghb3hw.

[124] S. Linden, D. Zhong, A. Timmer, N. Aghdassi, J. H. Franke, H. Zhang, X. Feng, K. Müllen, H. Fuchs, L. Chi, and H. Zacharias. "Electronic Structure of Spatially Aligned Graphene Nanoribbons on Au(788)". In: *Physical Review Letters* 108.21 (2012). doi:10/gkb95z.

[125] A. Narita, X. Feng, Y. Hernandez, S. A. Jensen, M. Bonn, H. Yang, I. A. Verzhbitskiy, C. Casiraghi, M. R. Hansen, A. H. Koch, G. Fytas, O. Ivasenko, B. Li, K. S. Mali, T. Balandina, S. Mahesh, S. De Feyter, and K. Mullen. "Synthesis of structurally well-defined and liquid-phase-processable graphene nanoribbons". In: *Nat Chem* 6.2 (2014), pp. 126–32. doi:10/gh3bqb.

[126] C. Bronner, S. Stremlau, M. Gille, F. Brausse, A. Haase, S. Hecht, and P. Tegeder. "Aligning the band gap of graphene nanoribbons by monomer doping". In: *Angew Chem Int Ed Engl* 52.16 (2013), pp. 4422–5. doi:10/f2bjft.

[127] Eduard Carbonell-Sanromà, Jeremy Hieulle, Manuel Vilas-Varela, Pedro Brandimarte, Mikel Iraola, Ana Barragán, Jingcheng Li, Mikel Abadia, Martina Corso, Daniel Sánchez-Portal, Diego Peña, and Jose Ignacio Pascual. "Doping of Graphene Nanoribbons *via* Functional Group Edge Modification". In: *ACS Nano* 11.7 (2017), pp. 7355–7361. doi:10/gkb9p2.

[128] Tomas Marangoni, Danny Haberer, Daniel J. Rizzo, Ryan R. Cloke, and Felix R. Fischer. "Heterostructures through Divergent Edge Reconstruction in Nitrogen-Doped Segmented Graphene Nanoribbons". In: *Chemistry – A European Journal* 22.37 (2016), pp. 13037–13040. doi:10/f3q4ff.

[129] Rebecca A. Durr, Danny Haberer, Yea-Lee Lee, Raymond Blackwell, Alin Miksi Kalayjian, Tomas Marangoni, Jisoon Ihm, Steven G. Louie, and Felix R. Fischer. "Orbitally Matched Edge-Doping in Graphene Nanoribbons". In: *Journal of the American Chemical Society* 140.2 (2018), pp. 807–813. doi:10/gkb69p.

[130] Giang D. Nguyen, Francesca M. Toma, Ting Cao, Zahra Pedramrazi, Chen Chen, Daniel J. Rizzo, Trinity Joshi, Christopher Bronner, Yen-Chia Chen, Marco Favaro, Steven G. Louie, Felix R. Fischer, and Michael F. Crommie. "Bottom-Up Synthesis of $N = 13$ Sulfur-Doped Graphene Nanoribbons". In: *The Journal of Physical Chemistry C* 120.5 (2016), pp. 2684–2687. doi:10/gmzpjg.

[131] Yan-Fang Zhang, Yi Zhang, Geng Li, Jianchen Lu, Yande Que, Hui Chen, Reinhard Berger, Xinliang Feng, Klaus Müllen, Xiao Lin, Yu-Yang Zhang, Shixuan Du, Sokrates T. Pantelides, and Hong-Jun Gao. "Sulfur-doped graphene nanoribbons with a sequence of distinct band gaps". In: *Nano Research* 10.10 (2017), pp. 3377–3384. doi:10/gbxhnb.

[132] Ryan R. Cloke, Tomas Marangoni, Giang D. Nguyen, Trinity Joshi, Daniel J. Rizzo, Christopher Bronner, Ting Cao, Steven G. Louie, Michael F. Crommie, and Felix R. Fischer. "Site-Specific Substitutional Boron Doping of Semiconducting Armchair Graphene Nanoribbons". In: *Journal of the American Chemical Society* 137.28 (2015), pp. 8872–8875. doi:10/f7mcpn.

[133] Z. Pedramrazi, C. Chen, F. Zhao, T. Cao, G. D. Nguyen, A. A. Omrani, H. Z. Tsai, R. R. Cloke, T. Marangoni, D. J. Rizzo, T. Joshi, C. Bronner, W. W. Choi, F. R. Fischer, S. G. Louie, and M. F. Crommie. "Concentration Dependence of Dopant Electronic Structure in Bottom-up Graphene Nanoribbons". In: *Nano Lett* 18.6 (2018), pp. 3550–3556. doi:10/gds6mg.

[134] X. Y. Wang, J. I. Urgel, G. B. Barin, K. Eimre, M. Di Giovannantonio, A. Milani, M. Tommasini, C. A. Pignedoli, P. Ruffieux, X. Feng, R. Fasel, K. Mullen, and A. Narita. "Bottom-Up Synthesis of Heteroatom-Doped Chiral Graphene Nanoribbons". In: *J Am Chem Soc* 140.29 (2018), pp. 9104–9107. doi:10/gd6x4m.

[135] Shigeki Kawai, Soichiro Nakatsuka, Takuji Hatakeyama, Rémy Pawlak, Tobias Meier, John Tracey, Ernst Meyer, and Adam S. Foster. "Multiple heteroatom substitution to graphene nanoribbon". In: *Science Advances* 4.4 (2018), eaar7181. doi:10/gkb9d9.

[136] Y. Fu, H. Yang, Y. Gao, L. Huang, R. Berger, J. Liu, H. Lu, Z. Cheng, S. Du, H. J. Gao, and X. Feng. "On-Surface Synthesis of NBN-Doped Zigzag-Edged Graphene Nanoribbons". In: *Angew Chem Int Ed Engl* 59.23 (2020), pp. 8873–8879. doi:10/gkcbd9.

[137] Fangping OuYang, Jin Xiao, Rui Guo, Hua Zhang, and Hui Xu. "Transport properties of T-shaped and crossed junctions based on graphene nanoribbons". In: *Nanotechnology* 20.5 (Jan. 9, 2009), p. 055202. doi:10/fbb2m2.

[138] D. Prezzi, D. Varsano, A. Ruini, and E. Molinari. "Quantum dot states and optical excitations of edge-modulated graphene nanoribbons". In: *Physical Review B* 84.4 (2011). doi:10/d8nztv.

[139] Xiao-Fei Li, Ling-Ling Wang, Ke-Qiu Chen, and Yi Luo. "Design of Graphene-Nanoribbon Heterojunctions from First Principles". In: *The Journal of Physical Chemistry C* 115.25 (2011), pp. 12616–12624. doi:10/cjfckq.

[140] J. Cai, C. A. Pignedoli, L. Talirz, P. Ruffieux, H. Sode, L. Liang, V. Meunier, R. Berger, R. Li, X. Feng, K. Mullen, and R. Fasel. "Graphene nanoribbon heterojunctions". In: *Nat Nanotechnol* 9.11 (2014), pp. 896–900. doi:10/gkb774.

[141] G. D. Nguyen, H. Z. Tsai, A. A. Omrani, T. Marangoni, M. Wu, D. J. Rizzo, G. F. Rodgers, R. R. Cloke, R. A. Durr, Y. Sakai, F. Liou, A. S. Aikawa, J. R. Chelikowsky, S. G. Louie, F. R. Fischer, and M. F. Crommie. "Atomically precise graphene nanoribbon heterojunctions from a single molecular precursor". In: *Nat Nanotechnol* 12.11 (2017), pp. 1077–1082. doi:10/gkcbgq.

[142] C. Bronner, R. A. Durr, D. J. Rizzo, Y. L. Lee, T. Marangoni, A. M. Kalayjian, H. Rodriguez, W. Zhao, S. G. Louie, F. R. Fischer, and M. F. Crommie. "Hierarchical On-Surface Synthesis of Graphene Nanoribbon Heterojunctions". In: *ACS Nano* 12.3 (2018), pp. 2193–2200. doi:10/gcxnjq.

[143] S. Wang, N. Kharche, E. Costa Girao, X. Feng, K. Mullen, V. Meunier, R. Fasel, and P. Ruffieux. "Quantum Dots in Graphene Nanoribbons". In: *Nano Lett* 17.7 (2017), pp. 4277–4283. doi:10/gkb84b.

[144] D. J. Rizzo, J. Jiang, D. Joshi, G. Veber, C. Bronner, R. A. Durr, P. H. Jacobse, T. Cao, A. Kalayjian, H. Rodriguez, P. Butler, T. Chen, S. G. Louie, F. R. Fischer, and M. F. Crommie. "Rationally Designed Topological Quantum Dots in Bottom-Up Graphene Nanoribbons". In: *ACS Nano* 15.12 (2021), pp. 20633–20642. doi:10/grtt7t.

[145] S. Blankenburg, J. Cai, P. Ruffieux, R. Jaafar, D. Passerone, X. Feng, K. Mullen, R. Fasel, and C. A. Pignedoli. "Intraribbon heterojunction formation in ultranarrow graphene nanoribbons". In: *ACS Nano* 6.3 (2012), pp. 2020–5. doi:10/gkb7bc.

[146] Y. C. Chen, T. Cao, C. Chen, Z. Pedramrazi, D. Haberer, D. G. de Oteyza, F. R. Fischer, S. G. Louie, and M. F. Crommie. "Molecular bandgap engineering of bottom-up synthesized graphene nanoribbon heterojunctions". In: *Nat Nanotechnol* 10.2 (2015), pp. 156–60. doi:10/gf3cgr.

[147] Paulo S. Costa, Jacob D. Teeter, Axel Enders, and Alexander Sinitskii. "Chevron-based graphene nanoribbon heterojunctions: Localized effects of lateral extension and structural defects on electronic properties". In: *Carbon* 134 (2018), pp. 310–315. doi:10/gdp6px.

[148] D. J. Rizzo, M. Wu, H. Z. Tsai, T. Marangoni, R. A. Durr, A. A. Omrani, F. Liou, C. Bronner, T. Joshi, G. D. Nguyen, G. F. Rodgers, W. W. Choi, J. H. Jorgensen, F. R. Fischer, S. G. Louie, and M. F. Crommie. "Length-Dependent Evolution of Type II Heterojunctions in Bottom-Up-Synthesized Graphene Nanoribbons". In: *Nano Lett* 19.5 (2019), pp. 3221–3228. doi:10/gkb98c.

[149] O. Hod, J. E. Peralta, and G. E. Scuseria. "Edge effects in finite elongated graphene nanoribbons". In: *Physical Review B* 76.23 (2007), p. 233401. doi:10/ckpwz3.

[150] M. Koch, F. Ample, C. Joachim, and L. Grill. "Voltage-dependent conductance of a single graphene nanoribbon". In: *Nat Nanotechnol* 7.11 (2012), pp. 713–7. doi:10/gf3cg8.

[151] C. Bronner, F. Leyssner, S. Stremlau, M. Utecht, P. Saalfrank, T. Klamroth, and P. Tegeder. "Electronic structure of a subnanometer wide bottom-up fabricated graphene nanoribbon: End states, band gap, and dispersion". In: *Physical Review B* 86.8 (2012). doi:10/gkqfvp.

[152] P. Shemella, Y. Zhang, M. Mailman, P. M. Ajayan, and S. K. Nayak. "Energy gaps in zero-dimensional graphene nanoribbons". In: *Applied Physics Letters* 91.4 (2007), p. 042101. doi:10/dz7sgw.

[153] M. Ijäs, M. Ervasti, A. Uppstu, P. Liljeroth, J. van der Lit, I. Swart, and A. Harju. "Electronic states in finite graphene nanoribbons: Effect of charging and defects". In: *Physical Review B* 88.7 (2013). doi:10/gkqd6c.

[154] S. Wang, L. Talirz, C. A. Pignedoli, X. Feng, K. Mullen, R. Fasel, and P. Ruffieux. "Giant edge state splitting at atomically precise graphene zigzag edges". In: *Nat Commun* 7.1 (2016), p. 11507. doi:10/f8njxj.

[155] X. Yao, W. Zheng, S. Osella, Z. Qiu, S. Fu, D. Schollmeyer, B. Muller, D. Beljonne, M. Bonn, H. I. Wang, K. Mullen, and A. Narita. "Synthesis of Nonplanar Graphene Nanoribbon with Fjord Edges". In: *J Am Chem Soc* 143.15 (2021), pp. 5654–5658. doi:10/gkb979.

[156] X. Wang, J. Ma, W. Zheng, S. Osella, N. Arisnabarreta, J. Droste, G. Serra, O. Ivasenko, A. Lucotti, D. Beljonne, M. Bonn, X. Liu, M. R. Hansen, M. Tommasini, S. De Feyter, J. Liu, H. I. Wang, and X. Feng. "Cove-Edged Graphene Nanoribbons with Incorporation of Periodic Zigzag-Edge Segments". In: *J Am Chem Soc* 144.1 (2022), pp. 228–235. doi:10/gpxp77.

[157] Wenhui Niu, Ji Ma, Paniz Soltani, Wenhao Zheng, Fupin Liu, Alexey A. Popov, Jan J. Weigand, Hartmut Komber, Emanuele Poliani, Cinzia Casiraghi, Jörn Droste, Michael Ryan Hansen, Silvio Osella, David Beljonne, Mischa Bonn, Hai I. Wang, Xinliang Feng, Junzhi Liu, and Yiyong Mai. "A Curved Graphene Nanoribbon with Multi-Edge Structure and High Intrinsic Charge Carrier Mobility". In: *Journal of the American Chemical Society* 142.43 (2020), pp. 18293–18298. doi:10/gkcbpt.

[158] J. Lawrence, P. Brandimarte, A. Berdonces-Layunta, M. S. G. Mohammed, A. Grewal, C. C. Leon, D. Sanchez-Portal, and D. G. de Oteyza. "Probing the Magnetism of Topological End States in 5-Armchair Graphene Nanoribbons". In: *ACS Nano* 14.4 (2020), pp. 4499–4508. doi:10/gkb9q3.

[159] R. Ortiz, N. A. Garcia-Martinez, J. L. Lado, and J. Fernandez-Rossier. "Electrical spin manipulation in graphene nanostructures". In: *Physical Review B* 97.19 (2018), p. 195425. doi:10/gkmbt5.

[160] X. Su, Z. Xue, G. Li, and P. Yu. "Edge State Engineering of Graphene Nanoribbons". In: *Nano Lett* 18.9 (2018), pp. 5744–5751. doi:10/gfbck8.

[161] K. V. Klitzing, G. Dorda, and M. Pepper. "New Method for High-Accuracy Determination of the Fine-Structure Constant Based on Quantized Hall Resistance". In: *Physical Review Letters* 45.6 (1980), pp. 494–497. doi:10/bttjkh.

[162] D. J. Thouless, M. Kohmoto, M. P. Nightingale, and M. Dennijs. "Quantized Hall Conductance in a Two-Dimensional Periodic Potential". In: *Physical Review Letters* 49.6 (1982), pp. 405–408. doi:10/d5fd7k.

[163] X. G. Wen. "Topological order and edge structure of nu =1/2 quantum Hall state". In: *Phys Rev Lett* 70.3 (1993), pp. 355–358. doi:10/dvktbn.

[164] Deepak Vaid. "Quantum Hall Effect and Black Hole Entropy in Loop Quantum Gravity". In: *arXiv pre-print server* (Aug. 16, 2012).

[165] Joseph E. Avron, Daniel Osadchy, and Ruedi Seiler. "A Topological Look at the Quantum Hall Effect". In: *Physics Today* 56.8 (2003), pp. 38–42. doi:10/fp6tpb.

[166] M. A. Paalanen, D. C. Tsui, and A. C. Gossard. "Quantized Hall effect at low temperatures". In: *Physical Review B* 25.8 (1982), pp. 5566–5569. doi:10/cdg5wv.

[167] Klaus Von Klitzing. "Developments in the quantum Hall effect". In: *Philosophical Transactions of the Royal Society A: Mathematical, Physical and Engineering Sciences* 363.1834 (2005), pp. 2203–2219. doi:10/b9t553.

[168] Charles Day. "Quantum spin Hall effect shows up in a quantum well insulator, just as predicted". In: *Physics Today* 61.1 (2008), pp. 19–23. doi:10/fmk9fc.

[169] Oleg Alexandrov. *Torus illustration*. 2007.

[170] Michael Victor Berry. "Quantal phase factors accompanying adiabatic changes". In: *Proceedings of the Royal Society of London. A. Mathematical and Physical Sciences* 392.1802 (1984), pp. 45–57. doi:10/cctx57.

[171] Michel Fruchart and David Carpentier. "An introduction to topological insulators". In: *Comptes Rendus Physique* 14.9 (2013), pp. 779–815. doi:10/f5n2qz.

[172] D. Xiao, M. C. Chang, and Q. Niu. "Berry phase effects on electronic properties". In: *Reviews of Modern Physics* 82.3 (2010), pp. 1959–2007. doi:10/bdr799.

[173] F. D. M. Haldane. "Model for a Quantum Hall-Effect without Landau-Levels - Condensed-Matter Realization of the Parity Anomaly". In: *Physical Review Letters* 61.18 (1988), pp. 2015–2018. doi:10/b3f6gt.

[174] J. Cayssol and J. N. Fuchs. "Topological and geometrical aspects of band theory". In: *Journal of Physics-Materials* 4.3 (2021), p. 034007. doi:10/gjsc6p.

[175] B. Andrei Bernevig, Taylor L. Hughes, and Shou-Cheng Zhang. "Quantum Spin Hall Effect and Topological Phase Transition in HgTe Quantum Wells". In: *Science* 314.5806 (2006), pp. 1757–1761. doi:10/cqx2x6.

[176] Markus König, Steffen Wiedmann, Christoph Brüne, Andreas Roth, Hartmut Buhmann, Laurens W. Molenkamp, Xiao-Liang Qi, and Shou-Cheng Zhang. "Quantum Spin Hall Insulator State in HgTe Quantum Wells". In: *Science* 318.5851 (2007), pp. 766–770. doi:10/c52bt8.

[177] L. Fu and C. L. Kane. "Topological insulators with inversion symmetry". In: *Physical Review B* 76.4 (2007), p. 045302. doi:10/bgf29k.

[178] L. Fu, C. L. Kane, and E. J. Mele. "Topological insulators in three dimensions". In: *Phys Rev Lett* 98.10 (2007), p. 106803. doi:10/c7t6tv.

[179] Haijun Zhang, Chao-Xing Liu, Xiao-Liang Qi, Xi Dai, Zhong Fang, and Shou-Cheng Zhang. "Topological insulators in Bi2Se3, Bi2Te3 and Sb2Te3 with a single Dirac cone on the surface". In: *Nature Physics* 5.6 (2009), pp. 438–442. doi:10/d8g6gq.

[180] Y. Xia, D. Qian, D. Hsieh, L. Wray, A. Pal, H. Lin, A. Bansil, D. Grauer, Y. S. Hor, R. J. Cava, and M. Z. Hasan. "Observation of a large-gap topological-insulator class with a single Dirac cone on the surface". In: *Nature Physics* 5.6 (2009), pp. 398–402. doi:10/d9wwpp.

[181] Y. L. Chen, J. G. Analytis, J. H. Chu, Z. K. Liu, S. K. Mo, X. L. Qi, H. J. Zhang, D. H. Lu, X. Dai, Z. Fang, S. C. Zhang, I. R. Fisher, Z. Hussain, and Z. X. Shen. "Experimental realization of a three-dimensional topological insulator, Bi2Te3". In: *Science* 325.5937 (2009), pp. 178–81. doi:10/dwkmvz.

[182] Y. L. Chen, Z. K. Liu, J. G. Analytis, J.-H. Chu, H. J. Zhang, B. H. Yan, S.-K. Mo, R. G. Moore, D. H. Lu, I. R. Fisher, S. C. Zhang, Z. Hussain, and Z.-X. Shen. "Single Dirac Cone Topological Surface State and Unusual Thermoelectric Property of Compounds from a New Topological Insulator Family". In: *Physical Review Letters* 105.26 (2010). doi:10/ddrgxm.

[183] Chao-Xing Liu, Xiao-Liang Qi, Xi Dai, Zhong Fang, and Shou-Cheng Zhang. "Quantum Anomalous Hall Effect inHg1-yMn". In: *Physical Review Letters* 101.14 (2008). doi:10/cp7fv8.

[184] Rui Yu, Wei Zhang, Hai-Jun Zhang, Shou-Cheng Zhang, Xi Dai, and Zhong Fang. "Quantized Anomalous Hall Effect in Magnetic Topological Insulators". In: *Science* 329.5987 (2010), pp. 61–64. doi:10/cfcqf5.

[185] Kentaro Nomura and Naoto Nagaosa. "Surface-Quantized Anomalous Hall Current and the Magnetoelectric Effect in Magnetically Disordered Topological Insulators". In: *Physical Review Letters* 106.16 (2011). doi:10/c8c9sp.

[186] Cui-Zu Chang, Jinsong Zhang, Xiao Feng, Jie Shen, Zuocheng Zhang, Minghua Guo, Kang Li, Yunbo Ou, Pang Wei, Li-Li Wang, Zhong-Qing Ji, Yang Feng, Shuaihua Ji, Xi Chen, Jinfeng Jia, Xi Dai, Zhong Fang, Shou-Cheng Zhang, Ke He, Yayu Wang, Li Lu, Xu-Cun Ma, and Qi-Kun Xue. "Experimental Observation of the Quantum Anomalous Hall Effect in a Magnetic Topological Insulator". In: *Science* 340.6129 (2013), pp. 167–170. doi:10/f4st8t.

[187] D. Xiao, W. Yao, and Q. Niu. "Valley-contrasting physics in graphene: magnetic moment and topological transport". In: *Phys Rev Lett* 99.23 (2007), p. 236809. doi:10/c4xxvh.

[188] Liang Fu. "Topological Crystalline Insulators". In: *Physical Review Letters* 106.10 (2011). doi:10/bjw5qj.

[189] S. Ryu, A. P. Schnyder, A. Furusaki, and A. W. W. Ludwig. "Topological insulators and superconductors: tenfold way and dimensional hierarchy". In: *New Journal of Physics* 12.6 (2010), p. 065010. doi:10/cd9ntq.

[190] C. K. Chiu, J. C. Y. Teo, A. P. Schnyder, and S. Ryu. "Classification of topological quantum matter with symmetries". In: *Reviews of Modern Physics* 88.3 (2016), p. 035005. doi:10/f82wvj.

[191] A. A. Soluyanov and D. Vanderbilt. "Computing topological invariants without inversion symmetry". In: *Physical Review B* 83.23 (2011), p. 235401. doi:10/b728jp.

[192] M. Taherinejad, K. F. Garrity, and D. Vanderbilt. "Wannier center sheets in topological insulators". In: *Physical Review B* 89.11 (2014), p. 115102. doi:10/gkrdb8.

[193] H. J. Zhang and S. C. Zhang. "Topological insulators from the perspective of first-principles calculations". In: *Physica Status Solidi-Rapid Research Letters* 7.1 (2013), pp. 72–81. doi:10/fz9kgz.

[194] F. Tang, H. C. Po, A. Vishwanath, and X. Wan. "Comprehensive search for topological materials using symmetry indicators". In: *Nature* 566.7745 (2019), pp. 486–489. doi:10/gfv4kc.

[195] M. G. Vergniory, L. Elcoro, C. Felser, N. Regnault, B. A. Bernevig, and Z. Wang. "A complete catalogue of high-quality topological materials". In: *Nature* 566.7745 (2019), pp. 480–485. doi:10/gfv4j4.

[196] T. Zhang, Y. Jiang, Z. Song, H. Huang, Y. He, Z. Fang, H. Weng, and C. Fang. "Catalogue of topological electronic materials". In: *Nature* 566.7745 (2019), pp. 475–479. doi:10/gfv4j7.

[197] Binghai Yan and Claudia Felser. "Topological Materials: Weyl Semimetals". In: *Annual Review of Condensed Matter Physics* 8.1 (2017), pp. 337–354. doi:10/ggbr49.

[198] Masatoshi Sato and Yoichi Ando. "Topological superconductors: a review". In: *Reports on Progress in Physics* 80.7 (2017), p. 076501. doi:10/gd236c.

[199] F.D.M. Haldane. "Continuum dynamics of the 1-D Heisenberg antiferromagnet: Identification with the O(3) nonlinear sigma model". In: *Physics Letters A* 93.9 (Feb. 14, 1983), pp. 464–468. doi:10/fgdpvp.

[200] I. Affleck. "Quantum Spin Chains and the Haldane Gap". In: *Journal of Physics-Condensed Matter* 1.19 (1989), pp. 3047–3072. doi:10/bmb2dv.

[201] L. Lu, J. D. Joannopoulos, and M. Soljacic. "Topological photonics". In: *Nature Photonics* 8.11 (2014), pp. 821–829. doi:10/f6ppxk.

[202] Sebastian D. Huber. "Topological mechanics". In: *Nature Physics* 12.7 (2016), pp. 621–623. doi:10/gghjrb.

[203] Takeshi Mizushima, Yasumasa Tsutsumi, Takuto Kawakami, Masatoshi Sato, Masanori Ichioka, and Kazushige Machida. "Symmetry-Protected Topological Superfluids and Superconductors —From the Basics to3He—". In: *Journal of the Physical Society of Japan* 85.2 (2016), p. 022001. doi:10/gdzz93.

[204] W{\textbackslash}textbackslash_P Su, JR Schrieffer, and Ao J Heeger. "Solitons in polyacetylene". In: *Physical review letters* 42.25 (1979), p. 1698. doi:10/fj76w9.

[205] Navketan Batra and Goutam Sheet. "Understanding Basic Concepts of Topological Insulators Through Su-Schrieffer-Heeger (SSH) Model". In: *arXiv preprint arXiv:1906.08435* (2019).

[206] J. Zak. "Berry's phase for energy bands in solids". In: *Phys Rev Lett* 62.23 (1989), pp. 2747–2750. doi:10/cztvbf.

[207] János K Asbóth, László Oroszlány, and András Pályi. "A short course on topological insulators". In: *Lecture notes in physics* 919 (2016), p. 166. doi:10/gc4n97.

[208] J. W. Rhim, J. Behrends, and J. H. Bardarson. "Bulk-boundary correspondence from the intercellular Zak phase". In: *Physical Review B* 95.3 (2017), p. 035421. doi:10/gkvzdc.

[209] R. Resta. "Manifestations of Berry's phase in molecules and condensed matter". In: *Journal of Physics-Condensed Matter* 12.9 (2000), R107–R143. doi:10/bhhxj4.

[210] A. Heimes, P. Kotetes, and G. Schon. "Majorana fermions from Shiba states in an antiferromagnetic chain on top of a superconductor". In: *Physical Review B* 90.6 (2014). doi:10/ggff7s.

[211] Y. H. Jeong and S. R. E. Yang. "Topological end states and Zak phase of rectangular armchair ribbon". In: *Annals of Physics* 385 (2017), pp. 688–694. doi:10/gcgxkp.

[212] Y. L. Lee, F. Zhao, T. Cao, J. Ihm, and S. G. Louie. "Topological Phases in Cove-Edged and Chevron Graphene Nanoribbons: Geometric Structures, [Formula: see text](2) Invariants, and Junction States". In: *Nano Lett* 18.11 (2018), pp. 7247–7253. doi:10/gfkj2t.

[213] K. S. Lin and M. Y. Chou. "Topological Properties of Gapped Graphene Nanoribbons with Spatial Symmetries". In: *Nano Lett* 18.11 (2018), pp. 7254–7260. doi:10/gfhqt9.

[214] F. M. Arnold, T. J. Liu, A. Kuc, and T. Heine. "Structure-Imposed Electronic Topology in Cove-Edged Graphene Nanoribbons". In: *Phys Rev Lett* 129.21 (2022), p. 216401. doi:10/grt3gp.

[215] F. Zhao, T. Cao, and S. G. Louie. "Topological Phases in Graphene Nanoribbons Tuned by Electric Fields". In: *Phys Rev Lett* 127.16 (2021), p. 166401. doi:10/gm5f56.

[216] J. P. Joost, A. P. Jauho, and M. Bonitz. "Correlated Topological States in Graphene Nanoribbon Heterostructures". In: *Nano Lett* 19.12 (2019), pp. 9045–9050. doi:10/gkb8hq.

[217] X. Zhu, H. Guo, and S. Feng. "Quantum magnetism of topologically-designed graphene nanoribbons". In: *J Phys Condens Matter* 31.50 (2019), p. 505601. doi:10/gkb9w3.

[218] D. X. Liu, X. F. Li, X. H. Zhang, X. R. Cao, X. J. Zhu, and D. Shi. "Interface Magnetism in Topological Armchair/Cove-Edged Graphene Nanoribbons". In: *Journal of Physical Chemistry C* 124.28 (2020), pp. 15448–15453. doi:10/gmzpdg.

[219] M. Ohfuchi and S. Sato. "Energetics and magnetism of topological graphene nanoribbons". In: *Journal of Applied Physics* 129.6 (2021), p. 064305. doi:10/gh227q.

[220] L. Talirz, H. Sode, J. Cai, P. Ruffieux, S. Blankenburg, R. Jafaar, R. Berger, X. Feng, K. Mullen, D. Passerone, R. Fasel, and C. A. Pignedoli. "Termini of bottom-up fabricated graphene nanoribbons". In: *J Am Chem Soc* 135.6 (2013), pp. 2060–3. doi:10/f4mps6.

[221] D. J. Rizzo, G. Veber, T. Cao, C. Bronner, T. Chen, F. Zhao, H. Rodriguez, S. G. Louie, M. F. Crommie, and F. R. Fischer. "Topological band engineering of graphene nanoribbons". In: *Nature* 560.7717 (2018), pp. 204–208. doi:10/gdxvx7.

[222] N. Friedrich, P. Brandimarte, J. Li, S. Saito, S. Yamaguchi, I. Pozo, D. Pena, T. Frederiksen, A. Garcia-Lekue, D. Sanchez-Portal, and J. I. Pascual. "Magnetism of Topological Boundary States Induced by Boron Substitution in Graphene Nanoribbons". In: *Phys Rev Lett* 125.14 (2020), p. 146801. doi:10/gjppvk.

[223] Q. Sun, O. Groning, J. Overbeck, O. Braun, M. L. Perrin, G. Borin Barin, M. El Abbassi, K. Eimre, E. Ditler, C. Daniels, V. Meunier, C. A. Pignedoli, M. Calame, R. Fasel, and P. Ruffieux. "Massive Dirac Fermion Behavior in a Low Bandgap Graphene Nanoribbon Near a Topological Phase Boundary". In: *Adv Mater* 32.12 (2020), e1906054. doi:10/gkb9cr.

[224] J. Li, S. Sanz, N. Merino-Diez, M. Vilas-Varela, A. Garcia-Lekue, M. Corso, D. G. de Oteyza, T. Frederiksen, D. Pena, and J. I. Pascual. "Topological phase transition in chiral graphene nanoribbons: from edge bands to end states". In: *Nat Commun* 12.1 (2021), p. 5538. doi:10/gnk4mb.

[225] Q. Sun, Y. Yan, X. Yao, K. Mullen, A. Narita, R. Fasel, and P. Ruffieux. "Evolution of the Topological Energy Band in Graphene Nanoribbons". In: *J Phys Chem Lett* 12.35 (2021), pp. 8679–8684. doi:10/gmwcfd.

[226] H. Gonzalez-Herrero, J. I. Mendieta-Moreno, S. Edalatmanesh, J. Santos, N. Martin, D. Ecija, B. de la Torre, and P. Jelinek. "Atomic Scale Control and Visualization of Topological Quantum Phase Transition in pi-Conjugated Polymers Driven by Their Length". In: *Adv Mater* 33.44 (2021), e2104495. doi:10/grsdpb.

[227] B. Cirera, A. Sanchez-Grande, B. de la Torre, J. Santos, S. Edalatmanesh, E. Rodriguez-Sanchez, K. Lauwaet, B. Mallada, R. Zboril, R. Miranda, O. Groning, P. Jelinek, N. Martin, and D. Ecija. "Tailoring topological order and pi-conjugation to engineer quasi-metallic polymers". In: *Nat Nanotechnol* 15.6 (2020), pp. 437–443. doi:10/grtt8b.

[228] S. Mishra, G. Catarina, F. Wu, R. Ortiz, D. Jacob, K. Eimre, J. Ma, C. A. Pignedoli, X. Feng, P. Ruffieux, J. Fernandez-Rossier, and R. Fasel. "Observation of fractional edge excitations in nanographene spin chains". In: *Nature* 598.7880 (2021), pp. 287–292. doi:10/gm4jw3.

[229] F. D. M. Haldane. "Nonlinear Field Theory of Large-Spin Heisenberg Antiferromagnets: Semiclassically Quantized Solitons of the One-Dimensional Easy-Axis Néel State". In: *Physical Review Letters* 50.15 (1983), pp. 1153–1156. doi:10/cj9nds.

[230] Ian Affleck, Tom Kennedy, Elliott H Lieb, and Hal Tasaki. "Rigorous results on valence-bond ground states in antiferromagnets". In: *Condensed Matter Physics and Exactly Soluble Models: Selecta of Elliott H. Lieb* (2004), pp. 249–252. doi:10/gr3rxg.

[231] Tom Kennedy. "Exact diagonalisations of open spin-1 chains". In: *Journal of Physics: Condensed Matter* 2.26 (1990), p. 5737. doi:10/bqgkrv.

[232] Steven R White and David A Huse. "Numerical renormalization-group study of low-lying eigenstates of the antiferromagnetic S= 1 Heisenberg chain". In: *Physical Review B* 48.6 (1993), p. 3844. doi:10/bdv8xk.

[233] Joel S Miller and Marc Drillon. *Magnetism: Molecules to materials IV*. Vol. 4. John Wiley & Sons, 2001.

[234] R. C. Williams, W. J. A. Blackmore, S. P. M. Curley, M. R. Lees, S. M. Birnbaum, J. Singleton, B. M. Huddart, T. J. Hicken, T. Lancaster, S. J. Blundell, F. Xiao, A. Ozarowski, F. L. Pratt, D. J. Voneshen, Z. Guguchia, C. Baines, J. A. Schlueter, D. Y. Villa, J. L. Manson, and P. A. Goddard. "Near-ideal molecule-based Haldane spin chain". In: *Physical Review Research* 2.1 (2020). doi:10/grtt6t.

[235] Graeme Allinson, Richard J Bushby, Jean Louis Paillaud, Duro Oduwole, and Keith Sales. "ESR spectrum of a stable triplet. pi. biradical: trioxytriangulene". In: *Journal of the American Chemical Society* 115.5 (1993), pp. 2062–2064. doi:10/d3dhwg.

[236] M. Atzori and R. Sessoli. "The Second Quantum Revolution: Role and Challenges of Molecular Chemistry". In: *J Am Chem Soc* 141.29 (2019), pp. 11339–11352. doi:10/gmkkm7.

[237] D. P. DiVincenzo. "The physical implementation of quantum computation". In: *Fortschritte Der Physik-Progress of Physics* 48.9 (2000), pp. 771–783. doi:10/fnmhpz.

[238] N. P. de Leon, K. M. Itoh, D. Kim, K. K. Mehta, T. E. Northup, H. Paik, B. S. Palmer, N. Samarth, S. Sangtawesin, and D. W. Steuerman. "Materials challenges and opportunities for quantum computing hardware". In: *Science* 372.6539 (2021), eabb2823. doi:10/gjqxb4.

[239] C. J. Yu, M. J. Graham, J. M. Zadrozny, J. Niklas, M. D. Krzyaniak, M. R. Wasielewski, O. G. Poluektov, and D. E. Freedman. "Long Coherence Times in Nuclear Spin-Free Vanadyl Qubits". In: *J Am Chem Soc* 138.44 (2016), pp. 14678–14685. doi:10/f9b9vm.

[240] Stefan Stoll and Daniella Goldfarb. *EPR spectroscopy: fundamentals and methods*. John Wiley & Sons, 2018.

[241] Alexander V. Khaetskii and Yuli V. Nazarov. "Spin relaxation in semiconductor quantum dots". In: *Physical Review B* 61.19 (May 15, 2000). Publisher: American Physical Society, pp. 12639–12642. doi:10/d22kjd.

[242] M. J. Graham, C. J. Yu, M. D. Krzyaniak, M. R. Wasielewski, and D. E. Freedman. "Synthetic Approach To Determine the Effect of Nuclear Spin Distance on Electronic Spin Decoherence". In: *J Am Chem Soc* 139.8 (2017), pp. 3196–3201. doi:10/f9qw4g.

[243] Jia Chen, Cong Hu, John F. Stanton, Stephen Hill, Hai-Ping Cheng, and Xiao-Guang Zhang. "Decoherence in Molecular Electron Spin Qubits: Insights from Quantum Many-Body Simulations". In: *The Journal of Physical Chemistry Letters* 11.6 (2020). Publisher: American Chemical Society (ACS), pp. 2074–2078. doi:10/gs25r5.

[244] F. Lombardi, J. Ma, D. I. Alexandropoulos, H. Komber, J. Z. Liu, W. K. Myers, X. L. Feng, and L. Bogani. "Synthetic tuning of the quantum properties of open-shell radicaloids". In: *Chem* 7.5 (2021), pp. 1363–1378. doi:10/grtt79.

[245] P. Recher and B. Trauzettel. "Quantum dots and spin qubits in graphene". In: *Nanotechnology* 21.30 (2010), p. 302001. doi:10/b8pc2t.

[246] Bowen Yang. "Spin-Orbit Coupling in Graphene and Transition Metal Dichalcogenides". Thesis. 2017.

[247] M. Droth and G. Burkard. "Spintronics with graphene quantum dots". In: *Physica Status Solidi-Rapid Research Letters* 10.1 (2016), pp. 75–90. doi:10/f3kn2h.

[248] S. Song, J. Su, M. Telychko, J. Li, G. Li, Y. Li, C. Su, J. Wu, and J. Lu. "On-surface synthesis of graphene nanostructures with pi-magnetism". In: *Chem Soc Rev* 50.5 (2021), pp. 3238–3262. doi:10/gjnzpb.

[249] Elliott H Lieb. "Two theorems on the Hubbard model". In: *Physical review letters* 62.10 (1989), p. 1201. doi:10/czvtpr.

[250] Eric Clar. "Aromatic sextet". In: (1972).

[251] M. Sola. "Forty years of Clar's aromatic pi-sextet rule". In: *Front Chem* 1 (2013), p. 22. doi:10/grtt5f.

[252] J. Fernandez-Rossier and J. J. Palacios. "Magnetism in graphene nanoislands". In: *Phys Rev Lett* 99.17 (2007), p. 177204. doi:10/b2bdng.

[253] S. Mishra, X. Yao, Q. Chen, K. Eimre, O. Groning, R. Ortiz, M. Di Giovannantonio, J. C. Sancho-Garcia, J. Fernandez-Rossier, C. A. Pignedoli, K. Mullen, P. Ruffieux, A. Narita, and R. Fasel. "Large magnetic exchange coupling in rhombus-shaped nanographenes with zigzag periphery". In: *Nat Chem* 13.6 (2021), pp. 581–586. doi:10/gjx42k.

[254] W. L. Wang, O. V. Yazyev, S. Meng, and E. Kaxiras. "Topological frustration in graphene nanoflakes: magnetic order and spin logic devices". In: *Phys Rev Lett* 102.15 (2009), p. 157201. doi:10/ds7ztq.

[255] S. Fajtlowicz, P. E. John, and H. Sachs. "On maximum matchings and eigenvalues of benzenoid graphs". In: *Croatica Chemica Acta* 78.2 (2005), pp. 195–201.

[256] S. Mishra, D. Beyer, R. Berger, J. Liu, O. Groning, J. I. Urgel, K. Mullen, P. Ruffieux, X. Feng, and R. Fasel. "Topological Defect-Induced Magnetism in a Nanographene". In: *J Am Chem Soc* 142.3 (2020), pp. 1147–1152. doi:10/gk7ssg.

[257] D. J. Rizzo, G. Veber, J. Jiang, R. McCurdy, T. Cao, C. Bronner, T. Chen, S. G. Louie, F. R. Fischer, and M. F. Crommie. "Inducing metallicity in graphene nanoribbons via zero-mode superlattices". In: *Science* 369.6511 (2020), pp. 1597–1603. doi:10/gkcbmz.

[258] T. Wang, S. Sanz, J. Castro-Esteban, J. Lawrence, A. Berdonces-Layunta, M. S. G. Mohammed, M. Vilas-Varela, M. Corso, D. Pena, T. Frederiksen, and D. G. de Oteyza. "Magnetic Interactions Between Radical Pairs in Chiral Graphene Nanoribbons". In: *Nano Lett* 22.1 (2022), pp. 164–171. doi:10/grtt6h.

[259] J. Li, N. Merino-Diez, E. Carbonell-Sanroma, M. Vilas-Varela, D. G. de Oteyza, D. Pena, M. Corso, and J. I. Pascual. "Survival of spin state in magnetic porphyrins contacted by graphene nanoribbons". In: *Sci Adv* 4.2 (2018), eaaq0582. doi:10/gc69pf.

[260] T. Yamabayashi, M. Atzori, L. Tesi, G. Cosquer, F. Santanni, M. E. Boulon, E. Morra, S. Benci, R. Torre, M. Chiesa, L. Sorace, R. Sessoli, and M. Yamashita. "Scaling Up Electronic Spin Qubits into a Three-Dimensional Metal-Organic Framework". In: *J Am Chem Soc* 140.38 (2018), pp. 12090–12101. doi:10/gd97qj.

[261] S. Carretta, D. Zueco, A. Chiesa, A. Gomez-Leon, and F. Luis. "A perspective on scaling up quantum computation with molecular spins". In: *Applied Physics Letters* 118.24 (2021), p. 240501. doi:10/gqp3mg.

[262] Haomin Wang, Hui Shan Wang, Chuanxu Ma, Lingxiu Chen, Chengxin Jiang, Chen Chen, Xiaoming Xie, An-Ping Li, and Xinran Wang. "Graphene nanoribbons for quantum electronics". In: *Nature Reviews Physics* 3.12 (2021), pp. 791–802. doi:10/gmxr4j.

[263] O. V. Yazyev and M. I. Katsnelson. "Magnetic correlations at graphene edges: basis for novel spintronics devices". In: *Phys Rev Lett* 100.4 (2008), p. 047209. doi:10/bxz2wn.

[264] M. Golor, S. Wessel, and M. J. Schmidt. "Quantum nature of edge magnetism in graphene". In: *Phys Rev Lett* 112.4 (2014), p. 046601. doi:10/f5zkg8.

[265] J. M. Zadrozny, A. T. Gallagher, T. D. Harris, and D. E. Freedman. "A Porous Array of Clock Qubits". In: *J Am Chem Soc* 139.20 (2017), pp. 7089–7094. doi:10/f96vcj.

[266] S. Bose. "Quantum communication through an unmodulated spin chain". In: *Phys Rev Lett* 91.20 (2003), p. 207901. doi:10/bwjr5r.

[267] S. Bose. "Quantum communication through spin chain dynamics: an introductory overview". In: *Contemporary Physics* 48.1 (2007), pp. 13–30. doi:10/cc8x4n.

[268] O. V. Marchukov, A. G. Volosniev, M. Valiente, D. Petrosyan, and N. T. Zinner. "Quantum spin transistor with a Heisenberg spin chain". In: *Nat Commun* 7.1 (2016), p. 13070. doi:10/f878s9.

[269] L. Fu and C. L. Kane. "Superconducting proximity effect and Majorana fermions at the surface of a topological insulator". In: *Physical Review Letters* 100.9 (2008), p. 096407. doi:10/bpmzx3.

[270] R. Gillen, M. Mohr, C. Thomsen, and J. Maultzsch. "Vibrational properties of graphene nanoribbons by first-principles calculations". In: *Physical Review B* 80.15 (2009). doi:10/djw5sk.

[271] R. Gillen, M. Mohr, and J. Maultzsch. "Symmetry properties of vibrational modes in graphene nanoribbons". In: *Physical Review B* 81.20 (2010). doi:10/fb37wn.

[272] J. Overbeck, G. B. Barin, C. Daniels, M. L. Perrin, O. Braun, Q. Sun, R. Darawish, M. De Luca, X. Y. Wang, T. Dumslaff, A. Narita, K. Mullen, P. Ruffieux, V. Meunier, R. Fasel, and M. Calame. "A Universal Length-Dependent Vibrational Mode in Graphene Nanoribbons". In: *ACS Nano* 13.11 (2019), pp. 13083–13091. doi:10/gkb98n.

[273] R. Saito, M. Furukawa, G. Dresselhaus, and M. S. Dresselhaus. "Raman spectra of graphene ribbons". In: *J Phys Condens Matter* 22.33 (2010), p. 334203. doi:10/ftt9qk.

[274] S. Ryu, J. Maultzsch, M. Y. Han, P. Kim, and L. E. Brus. "Raman spectroscopy of lithographically patterned graphene nanoribbons". In: *ACS Nano* 5.5 (2011), pp. 4123–30. doi:10/d8v97c.

[275] D. Bischoff, J. Guttinger, S. Droscher, T. Ihn, K. Ensslin, and C. Stampfer. "Raman spectroscopy on etched graphene nanoribbons". In: *Journal of Applied Physics* 109.7 (2011), p. 073710. doi:10/bfdftq.

[276] I. A. Verzhbitskiy, M. D. Corato, A. Ruini, E. Molinari, A. Narita, Y. Hu, M. G. Schwab, M. Bruna, D. Yoon, S. Milana, X. Feng, K. Mullen, A. C. Ferrari, C. Casiraghi, and D. Prezzi. "Raman Fingerprints of Atomically Precise Graphene Nanoribbons". In: *Nano Lett* 16.6 (2016), pp. 3442–7. doi:10/gkb9mm.

[277] Neil W. Aschcroft and N. David Mermin. *Solid States Physics*. 1980.

[278] David Vanderbilt. *Berry phases in electronic structure theory: electric polarization, orbital magnetization and topological insulators*. Cambridge University Press, 2018.

[279] Zheng-Zhong Li. "Solid state theory". In: *Chinese (Higher Education Press, Beijing, 1985)* (2002).

[280] Nick Papior. *sisl: v0.13.0*. 2022. doi:10.5281/zenodo.597181.

[281] Zheng Shi and Ian Affleck. "Effect of long-range interaction on graphene edge magnetism". In: *Physical Review B* 95.19 (2017). Publisher: American Physical Society (APS). doi:10/gs2wx6.

[282] Subir Sachdev. "Quantum phase transitions". In: *Physics World* 12.4 (Apr. 1, 1999), p. 33. doi:10/gsgdp6.

[283] Assa Auerbach. *Interacting electrons and quantum magnetism*. Springer Science & Business Media, 1998.

[284] K. Vijaya Sarathy, S. Parashar, A. R. Raju, and C. N. R. Rao. "Hopping conduction in charge-ordered rare-earth manganates Ln1-xCaxMnO3 (Lnrare earth)". In: *Solid State Sciences* 4.3 (2002), pp. 353–357. doi:10/fv22qw.

[285] Feliciano Giustino. *Materials modelling using density functional theory: properties and predictions*. Oxford University Press, 2014.

[286] Pierre Hohenberg and Walter Kohn. "Inhomogeneous electron gas". In: *Physical review* 136.3 (1964), B864. doi:10/csx7jx.

[287] J. P. Perdew and A. Zunger. "Self-Interaction Correction to Density-Functional Approximations for Many-Electron Systems". In: *Physical Review B* 23.10 (1981), pp. 5048–5079. doi:10/ft7cj6.

[288] J. P. Perdew, K. Burke, and M. Ernzerhof. "Generalized gradient approximation made simple". In: *Physical Review Letters* 77.18 (1996), pp. 3865–3868. doi:10/bppfwt.

[289] P. Verma and D. G. Truhlar. "Status and Challenges of Density Functional Theory". In: *Trends in Chemistry* 2.4 (2020), pp. 302–318. doi:10/gjxh29.

[290] A. D. Becke. "Perspective: Fifty years of density-functional theory in chemical physics". In: *J Chem Phys* 140.18 (2014), 18A301. doi:10/gfgqd9.

[291] A. J. Cohen, P. Mori-Sanchez, and W. Yang. "Challenges for density functional theory". In: *Chem Rev* 112.1 (2012), pp. 289–320. doi:10/fznx46.

[292] M. Vandescuren, P. Hermet, V. Meunier, L. Henrard, and P. Lambin. "Theoretical study of the vibrational edge modes in graphene nanoribbons". In: *Physical Review B* 78.19 (2008). doi:10/bnwnmf.

[293] J. Zhou and J. Dong. "Vibrational property and Raman spectrum of carbon nanoribbon". In: *Applied Physics Letters* 91.17 (2007), p. 173108. doi:10/bk2s23.

[294] Michele Lazzeri and Francesco Mauri. "First-principles calculation of vibrational Raman spectra in large systems: signature of small rings in crystalline S i O 2". In: *Physical review letters* 90.3 (2003), p. 036401. doi:10/b96kzs.

[295] A. J. Cohen, P. Mori-Sanchez, and W. Yang. "Insights into current limitations of density functional theory". In: *Science* 321.5890 (2008), pp. 792–4. doi:10/fqrfz2.

[296] S. Hammes-Schiffer. "A conundrum for density functional theory". In: *Science* 355.6320 (2017), pp. 28–29. doi:10/gf2bt2.

[297] P. Giannozzi, S. Baroni, N. Bonini, M. Calandra, R. Car, C. Cavazzoni, D. Ceresoli, G. L. Chiarotti, M. Cococcioni, I. Dabo, A. Dal Corso, S. de Gironcoli, S. Fabris, G. Fratesi, R. Gebauer, U. Gerstmann, C. Gougoussis, A. Kokalj, M. Lazzeri, L. Martin-Samos, N. Marzari, F. Mauri, R. Mazzarello, S. Paolini, A. Pasquarello, L. Paulatto, C. Sbraccia, S. Scandolo, G. Sclauzero, A. P. Seitsonen, A. Smogunov, P. Umari, and R. M. Wentzcovitch. "QUANTUM ESPRESSO: a modular and open-source software project for quantum simulations of materials". In: *J Phys Condens Matter* 21.39 (2009), p. 395502. doi:10/d7spb8.

[298] Georg Kresse and Jürgen Furthmüller. "Efficient iterative schemes for ab initio total-energy calculations using a plane-wave basis set". In: *Physical review B* 54.16 (1996), p. 11169. doi:10/fmrkzs.

[299] J. M. Soler, E. Artacho, J. D. Gale, A. Garcia, J. Junquera, P. Ordejon, and D. Sanchez-Portal. "The SIESTA method for ab initio order-N materials simulation". In: *Journal of Physics-Condensed Matter* 14.11 (2002), pp. 2745–2779. doi:10/dsbsq4.

[300] MJ ea Frisch, GW Trucks, HB Schlegel, GE Scuseria, MA Robb, JR Cheeseman, G Scalmani, VPGA Barone, GA Petersson, HJRA Nakatsuji, et al. *Gaussian 16, revision C. 01*. 2016.

[301] Frank Neese, Frank Wennmohs, Ute Becker, and Christoph Riplinger. "The ORCA quantum chemistry program package". In: *The Journal of chemical physics* 152.22 (2020). doi:10/gg53w7.

[302] K. N. Kudin, R. Car, and R. Resta. "Berry phase approach to longitudinal dipole moments of infinite chains in electronic-structure methods with local basis sets". In: *J Chem Phys* 126.23 (2007), p. 234101. doi:10/fb259h.

[303] N. Marzari and D. Vanderbilt. "Maximally localized generalized Wannier functions for composite energy bands". In: *Physical Review B* 56.20 (1997), pp. 12847–12865. doi:10/cbrkqq.

[304] A. A. Mostofi, J. R. Yates, Y. S. Lee, I. Souza, D. Vanderbilt, and N. Marzari. "wannier90: A tool for obtaining maximally-localised Wannier functions". In: *Computer Physics Communications* 178.9 (2008), pp. 685–699. doi:10/b6jm98.

[305] Ivo Souza, Nicola Marzari, and David Vanderbilt. "Maximally localized Wannier functions for entangled energy bands". In: *Physical Review B* 65.3 (2001), p. 035109. doi:10/ffcqhv.

[306] Arthur Schweiger and Gunnar Jeschke. *Principles of pulse electron paramagnetic resonance*. Oxford University Press on Demand, 2001.

[307] David J Griffiths and Darrell F Schroeter. *Introduction to quantum mechanics*. Cambridge university press, 2018.

[308] M Slota. "Manipulating the coupling between electronic and spin degrees of freedom in molecules". PhD thesis. University of Oxford, 2017.

[309] Stefan Stoll and Arthur Schweiger. "EasySpin, a comprehensive software package for spectral simulation and analysis in EPR". In: *Journal of magnetic resonance* 178.1 (2006), pp. 42–55. doi:10/d5rcsj.

[310] P. Gehring, J. M. Thijssen, and H. S. J. van der Zant. "Single-molecule quantum-transport phenomena in break junctions". In: *Nature Reviews Physics* 1.6 (2019), pp. 381–396. doi:10/ggkksg.

[311] M. L. Perrin, E. Burzuri, and H. S. van der Zant. "Single-molecule transistors". In: *Chem Soc Rev* 44.4 (2015), pp. 902–19. doi:10/grtt72.

[312] R. Gaudenzi, M. Misiorny, E. Burzuri, M. R. Wegewijs, and H. S. J. van der Zant. "Transport mirages in single-molecule devices". In: *Journal of Chemical Physics* 146.9 (2017), p. 092330. doi:10/f3vf94.

[313] C. Jia and X. Guo. "Molecule-electrode interfaces in molecular electronic devices". In: *Chem Soc Rev* 42.13 (2013), pp. 5642–60. doi:10/gf66vw.

[314] Jürgen Weis. "Single-electron devices". In: *CFN Lectures on Functional Nanostructures Vol. 1*. Springer, 2005, pp. 87–121.

[315] S. V. Aradhya and L. Venkataraman. "Single-molecule junctions beyond electronic transport". In: *Nat Nanotechnol* 8.6 (2013), pp. 399–410. doi:10/gfx27h.

[316] Mark Fox. *Optical properties of solids*. 2002.

[317] Susan B Piepho and Paul N Schatz. "Group theory in spectroscopy: with applications to magnetic circular dichroism". In: *(No Title)* (1983).

[318] Peter Larkin. *Infrared and Raman spectroscopy: principles and spectral interpretation*. Elsevier, 2017.

[319] Mildred S Dresselhaus, Gene Dresselhaus, and Ado Jorio. *Group theory: application to the physics of condensed matter*. Springer Science & Business Media, 2007.

[320] Z. Chen, A. Narita, and K. Mullen. "Graphene Nanoribbons: On-Surface Synthesis and Integration into Electronic Devices". In: *Adv Mater* 32.45 (2020), e2001893. doi:10/gkb9w6.

[321] X. L. Qi and S. C. Zhang. "Topological insulators and superconductors". In: *Reviews of Modern Physics* 83.4 (2011), p. 1057. doi:10/cfj5rr.

[322] Biao Lian, Xiao-Qi Sun, Abolhassan Vaezi, Xiao-Liang Qi, and Shou-Cheng Zhang. "Topological quantum computation based on chiral Majorana fermions". In: *Proceedings of the National Academy of Sciences* 115.43 (2018), pp. 10938–10942. doi:10/gfjn67.

[323] Z. F. Liu, Q. P. Wu, and X. B. Xiao. "Gate-tunable localization and delocalization of perfect valley-related topological edge states in zigzag graphene nanoribbons". In: *Surfaces and Interfaces* 25 (2021), p. 101300. doi:10/gkzsc2.

[324] The siesta group. *SIESTA website*.

[325] Marcelo Guzmán, Denis Bartolo, and David Carpentier. "Geometry and topology tango in chiral materials". In: *arXiv preprint arXiv:2002.02850* (2020).

[326] Tobias Wassmann, Ari P. Seitsonen, A. Marco Saitta, Michele Lazzeri, and Francesco Mauri. "Clar's Theory, π-Electron Distribution, and Geometry of Graphene Nanoribbons". In: *Journal of the American Chemical Society* 132.10 (2010), pp. 3440–3451. doi:10/cqxxht.

[327] F. Gutzeit, M. Dommaschk, N. Levin, A. Buchholz, E. Schaub, W. Plass, C. Nather, and R. Herges. "Structure and Properties of a Five-Coordinate Nickel(II) Porphyrin". In: *Inorg Chem* 58.19 (2019), pp. 12542–12546. doi:10/gmhcjw.

[328] Q. Sun, L. M. Mateo, R. Robles, P. Ruffieux, N. Lorente, G. Bottari, T. Torres, and R. Fasel. "Inducing Open-Shell Character in Porphyrins through Surface-Assisted Phenalenyl pi-Extension". In: *J Am Chem Soc* 142.42 (2020), pp. 18109–18117. doi:10/grtt53.

[329] Q. Sun, L. M. Mateo, R. Robles, P. Ruffieux, G. Bottari, T. Torres, R. Fasel, and N. Lorente. "Magnetic Interplay between pi-Electrons of Open-Shell Porphyrins and d-Electrons of Their Central Transition Metal Ions". In: *Adv Sci (Weinh)* 9.19 (2022), e2105906. doi:10/grpm4b.

[330] Giovanni Bressan, Martin D. Peeks, Harry L. Anderson, Stephen R. Meech, and Ismael A. Heisler. "Time-Resolved Structural Dynamics of Extended π-Electron Porphyrin Nanoring". In: *The Journal of Physical Chemistry C* 123.44 (2019), pp. 27222–27229. doi:10/gr933r.

[331] Chris J. Judd, Anton S. Nizovtsev, Rikke Plougmann, Dmitry V. Kondratuk, Harry L. Anderson, Elena Besley, and Alex Saywell. "Molecular Quantum Rings Formed from a π -Conjugated Macrocycle". In: *Physical Review Letters* 125.20 (2020). doi:10/gr933w.

[332] Sebastian M. Kopp, Henrik Gotfredsen, Jie-Ren Deng, Tim D. W. Claridge, and Harry L. Anderson. "Global Aromaticity in a Partially Fused 8-Porphyrin Nanoring". In: *Journal of the American Chemical Society* 142.45 (2020), pp. 19393–19401. doi:10/gr933v.

[333] S. Kawai, A. Ishikawa, S. I. Ishida, T. Yamakado, Y. Ma, K. Sun, Y. Tateyama, R. Pawlak, E. Meyer, S. Saito, and A. Osuka. "On-Surface Synthesis of Porphyrin-Complex Multi-Block Co-Oligomers by Defluorinative Coupling". In: *Angew Chem Int Ed Engl* 61.3 (2022), e202114697. doi:10/grpm4j.

[334] Y. Zhao, K. Jiang, C. Li, Y. Liu, G. Zhu, M. Pizzochero, E. Kaxiras, D. Guan, Y. Li, H. Zheng, C. Liu, J. Jia, M. Qin, X. Zhuang, and S. Wang. "Quantum nanomagnets in on-surface metal-free porphyrin chains". In: *Nat Chem* 15.1 (2023), pp. 53–60. doi:10/gq5g53.

[335] C. Chen, T. Joshi, H. Li, A. D. Chavez, Z. Pedramrazi, P. N. Liu, H. Li, W. R. Dichtel, J. L. Bredas, and M. F. Crommie. "Local Electronic Structure of a Single-Layer Porphyrin-Containing Covalent Organic Framework". In: *ACS Nano* 12.1 (2018), pp. 385–391. doi:10/gcqd69.

[336] L. M. Mateo, Q. Sun, S. X. Liu, J. J. Bergkamp, K. Eimre, C. A. Pignedoli, P. Ruffieux, S. Decurtins, G. Bottari, R. Fasel, and T. Torres. "On-Surface Synthesis and Characterization of Triply Fused Porphyrin-Graphene Nanoribbon Hybrids". In: *Angew Chem Int Ed Engl* 59.3 (2020), pp. 1334–1339. doi:10/gkb945.

[337] Qiang Chen, Alessandro Lodi, Heng Zhang, Alex Gee, Hai Wang, Fanmiao Kong, Michael Clarke, Matthew Edmondson, Jack Hart, James O'Shea, Wojciech Stawski, Jonathan Baugh, Akimitsu Narita, Alex Saywell, Mischa Bonn, Klaus Müllen, Lapo Bogani, and Harry Anderson. "Porphyrin-Fused Graphene Nanoribbons". Unpublished Work. Unpublished Work. Published: Unpublished Work. 2023. doi:10.26434/chemrxiv-2023-ghvdb.

[338] A. Tsuda and A. Osuka. "Fully conjugated porphyrin tapes with electronic absorption bands that reach into infrared". In: *Science* 293.5527 (2001), pp. 79–82. doi:10/d3cm99.

[339] Yoichi Yamaguchi. "Time-dependent density functional calculations of fully π-conjugated zinc oligoporphyrins". In: *The Journal of Chemical Physics* 117.21 (2002), pp. 9688–9694. doi:10/fjb738.

[340] V. Posligua, A. Aziz, R. Haver, M. D. Peeks, H. L. Anderson, and R. Grau-Crespo. "Band Structures of Periodic Porphyrin Nanostructures". In: *Journal of Physical Chemistry C* 122.41 (2018), pp. 23790–23798. doi:10/gfh637.

[341] J. Orenstein and A. J. Millis. "Advances in the Physics of High-Temperature Superconductivity". In: *Science* 288.5465 (Apr. 21, 2000), pp. 468–474. doi:10/dvxnf5.

[342] M. Pizzochero, N. V. Tepliakov, A. A. Mostofi, and E. Kaxiras. "Electrically Induced Dirac Fermions in Graphene Nanoribbons". In: *Nano Lett* 21.21 (2021), pp. 9332–9338. doi:10/grtt4p.

[343] Zibo Wang, Shuguang Cheng, Xiao Liu, and Hua Jiang. "Topological kink states in graphene". In: *Nanotechnology* 32.40 (2021), p. 402001. doi:10/gr96x7.

[344] Paola Gava, Michele Lazzeri, A. Marco Saitta, and Francesco Mauri. "Ab initiostudy of gap opening and screening effects in gated bilayer graphene". In: *Physical Review B* 79.16 (2009). doi:10/dgwr8x.

[345] Erika R. Bérczi-Kovács and Attila Bernáth. "The complexity of the Clar number problem and an exact algorithm". In: *Journal of Mathematical Chemistry* 56.2 (2018), pp. 597–605. doi:10/gcv5rv.

[346] Gary Weldon Atkinson. *Combinatorial optimization on planar bipartite graphs via unimodular matrices*. The George Washington University, 1998.

[347] Khaled Salem and Hernán Abeledo. "Hypergraphs and the Clar problem in hexagonal systems". In: *Discrete Optimization* 3.4 (2006), pp. 392–397. doi:10/djqcgr.

[348] Amna Ayub, Khurshid Ayub, Sehrish Gul, Muhammad Ali Hashmi, Ahmed Lakhani, Saleem Iqbal, and Javed Iqbal. "Hetero-porphyrin based channel for separation of proton isotope: A density functional theory study". In: *Microporous and Mesoporous Materials* 339 (2022), p. 111995. doi:10/gr98x7.

[349] W. D. Zeng, H. Phan, T. S. Herng, T. Y. Gopalakrishna, N. Aratani, Z. B. Zeng, H. Yamada, J. Ding, and J. S. Wu. "Rylene Ribbons with Unusual Diradical Character". In: *Chem* 2.1 (2017), pp. 81–92. doi:10/grtt7x.

[350] Q. Fan, D. Martin-Jimenez, D. Ebeling, C. K. Krug, L. Brechmann, C. Kohlmeyer, G. Hilt, W. Hieringer, A. Schirmeisen, and J. M. Gottfried. "Nanoribbons with Nonalternant Topology from Fusion of Polyazulene: Carbon Allotropes beyond Graphene". In: *J Am Chem Soc* 141.44 (2019), pp. 17713–17720. doi:10/ddch.

[351] P. H. Jacobse, Z. Jin, J. Jiang, S. Peurifoy, Z. Yue, Z. Wang, D. J. Rizzo, S. G. Louie, C. Nuckolls, and M. F. Crommie. "Pseudo-atomic orbital behavior in graphene nanoribbons with four-membered rings". In: *Sci Adv* 7.52 (2021), eabl5892. doi:10/grtt7g.

[352] Yonatan Plotnik, Mikael C. Rechtsman, Daohong Song, Matthias Heinrich, Julia M. Zeuner, Stefan Nolte, Yaakov Lumer, Natalia Malkova, Jingjun Xu, Alexander Szameit, Zhigang Chen, and Mordechai Segev. "Observation of unconventional edge states in 'photonic graphene'". In: *Nature Materials* 13.1 (2014), pp. 57–62. doi:10/gkkzhm.

[353] Matthieu Bellec, Ulrich Kuhl, Gilles Montambaux, and Fabrice Mortessagne. "Manipulation of edge states in microwave artificial graphene". In: *New Journal of Physics* 16.11 (Nov. 11, 2014), p. 113023. doi:10/gr98zp.

[354] X. Xi, J. Ma, S. Wan, C. H. Dong, and X. Sun. "Observation of chiral edge states in gapped nanomechanical graphene". In: *Sci Adv* 7.2 (2021), eabe1398. doi:10/grtt6w.

[355] J. Li, S. Sanz, M. Corso, D. J. Choi, D. Pena, T. Frederiksen, and J. I. Pascual. "Single spin localization and manipulation in graphene open-shell nanostructures". In: *Nat Commun* 10.1 (2019), p. 200. doi:10/gj35xk.

[356] Ryan, Aidan Delgado, Jingwei Jiang, Junmian Zhu, Ethan, Raymond, Gregory, Shenkai Wang, Steven, and Felix. "Engineering Robust Metallic Zero-Mode States in Olympicene Graphene Nanoribbons". In: *arXiv pre-print server* (Feb. 16, 2023).

[357] J. Hachmann, J. J. Dorando, M. Aviles, and G. K. Chan. "The radical character of the acenes: a density matrix renormalization group study". In: *J Chem Phys* 127.13 (2007), p. 134309. doi:10/dsj6hd.

[358] M. Vazdar, M. Eckert-Maksic, and H. Lischka. “The Antiferromagnetic Spin Coupling in Non-Kekule Acenes-Impressive Polyradical Character Revealed by High-Level Multireference Methods”. In: *Chemphyschem* 17.13 (2016), pp. 2013–21. doi:10/f3mfdz.

[359] F. Plasser, H. Pasalic, M. H. Gerzabek, F. Libisch, R. Reiter, J. Burgdorfer, T. Muller, R. Shepard, and H. Lischka. “The multiradical character of one- and two-dimensional graphene nanoribbons”. In: *Angew Chem Int Ed Engl* 52.9 (2013), pp. 2581–4. doi:10/fz96hp.

[360] Y. Ni, T. Y. Gopalakrishna, H. Phan, T. S. Herng, S. Wu, Y. Han, J. Ding, and J. Wu. “A Peri-tetracene Diradicaloid: Synthesis and Properties”. In: *Angew Chem Int Ed Engl* 57.31 (2018), pp. 9697–9701. doi:10/gdsftx.

[361] M. R. Ajayakumar, Y. Fu, J. Ma, F. Hennersdorf, H. Komber, J. J. Weigand, A. Alfonsov, A. A. Popov, R. Berger, J. Liu, K. Mullen, and X. Feng. “Toward Full Zigzag-Edged Nanographenes: peri-Tetracene and Its Corresponding Circumanthracene”. In: *J Am Chem Soc* 140.20 (2018), pp. 6240–6244. doi:10/gdg45d.

[362] J. Liu, A. Narita, S. Osella, W. Zhang, D. Schollmeyer, D. Beljonne, X. Feng, and K. Mullen. “Unexpected Scholl Reaction of 6,7,13,14-Tetraarylbenzo[k]tetraphene: Selective Formation of Five-Membered Rings in Polycyclic Aromatic Hydrocarbons”. In: *J Am Chem Soc* 138.8 (2016), pp. 2602–8. doi:10/f8c4qf.

[363] Z. Qiu, S. Asako, Y. Hu, C. W. Ju, T. Liu, L. Rondin, D. Schollmeyer, J. S. Lauret, K. Mullen, and A. Narita. “Negatively Curved Nanographene with Heptagonal and [5]Helicene Units”. In: *J Am Chem Soc* 142.35 (2020), pp. 14814–14819. doi:10/ghmncp.

[364] Y. Z. Dai, B. W. Dong, Y. Kao, Z. Y. Wang, H. I. Un, Z. Liu, Z. J. Lin, L. Li, F. B. Xie, Y. Lu, M. X. Xu, T. Lei, Y. J. Sun, J. Y. Wang, S. Gao, S. D. Jiang, and J. Pei. “Chemical Modification toward Long Spin Lifetimes in Organic Conjugated Radicals”. In: *Chemphyschem* 19.22 (2018), pp. 2972–2977. doi:10/gfgr98.

[365] S. K. Hoffmann, W. Hilczer, J. Goslar, S. Kiczka, and I. Polus. “Resonance-type effects in free radical electron spin lattice relaxation and electron spin echo dephasing due to a dynamics of a homogeneous-chain oligomeric system”. In: *Physical Chemistry Chemical Physics* 4.20 (2002), pp. 4944–4951. doi:10/d6kz3w.

[366] S. K. Hoffmann, W. Hilczer, T. Radczyk, and I. Polus. “Electron spin-lattice relaxation in polymers and crystals related to disorder and structure defects”. In: *Acta Physica Polonica A* 103.4 (2003), pp. 373–385. doi:10/grt3gr.

[367] S. S. Rao, A. Stesmans, J. van Tol, D. V. Kosynkin, A. Higginbotham-Duque, W. Lu, A. Sinitskii, and J. M. Tour. “Spin dynamics and relaxation in graphene nanoribbons: electron spin resonance probing”. In: *ACS Nano* 6.9 (2012), pp. 7615–23. doi:10/f378x2.

[368] M. Wencka, S. Lijewski, and S. K. Hoffmann. “Dynamics of CO2- radiation defects in natural calcite studied by ESR, electron spin echo and electron spin relaxation”. In: *Journal of Physics-Condensed Matter* 20.25 (2008), p. 255237. doi:10/fksv6p.

[369] N. Bloembergen, S. Shapiro, P. S. Pershan, and J. O. Artman. “Cross-Relaxation in Spin Systems”. In: *Physical Review* 114.2 (1959), pp. 445–459. doi:10/chqqww.

[370] M. Simenas, D. Klose, M. Ptak, K. Aidas, M. Maczka, J. Banys, A. Poppl, and G. Jeschke. "Magnetic excitation and readout of methyl group tunnel coherence". In: *Sci Adv* 6.18 (2020), eaba1517. doi:10/ghz6wh.

[371] S. von Kugelgen, M. D. Krzyaniak, M. Gu, D. Puggioni, J. M. Rondinelli, M. R. Wasielewski, and D. E. Freedman. "Spectral Addressability in a Modular Two Qubit System". In: *J Am Chem Soc* 143.21 (2021), pp. 8069–8077. doi:10/gj4wjj.

[372] M. Prada, L. Tiemann, J. Sichau, and R. H. Blick. "Dirac imprints on the g -factor anisotropy in graphene". In: *Physical Review B* 104.7 (2021). Publisher: American Physical Society (APS). doi:10/gmd8r7.

[373] Bruce H Robinson, John M Schurr, Alvin L Kwiram, Hans Thomann, Ho Kim, Anny Morrobel-Sosa, P Bryson, and Larry R Dalton. "Evidence for soliton-phonon interaction in trans-polyacetylene: temperature and frequency dependence of electron spin-lattice relaxation data". In: *The Journal of Physical Chemistry* 89.23 (1985), pp. 4994–5002. doi:10/dxg6hp.

[374] R. Gillen, M. Mohr, and J. Maultzsch. "Raman-active modes in graphene nanoribbons". In: *Physica Status Solidi B-Basic Solid State Physics* 247.11 (2010), pp. 2941–2944. doi:10/cthmjv.

[375] S. Malola, H. Hakkinen, and P. Koskinen. "Comparison of Raman spectra and vibrational density of states between graphene nanoribbons with different edges". In: *European Physical Journal D* 52.1 (2009), pp. 71–74. doi:10/dxftzb.

[376] A. Narita, I. A. Verzhbitskiy, W. Frederickx, K. S. Mali, S. A. Jensen, M. R. Hansen, M. Bonn, S. De Feyter, C. Casiraghi, X. Feng, and K. Mullen. "Bottom-up synthesis of liquid-phase-processable graphene nanoribbons with near-infrared absorption". In: *ACS Nano* 8.11 (2014), pp. 11622–30. doi:10/f6rqkp.

[377] P. L. Stiller, A. Dirnaichner, D. R. Schmid, and A. K. Huttel. "Magnetic field control of the Franck-Condon coupling of few-electron quantum states". In: *Physical Review B* 102.11 (2020). doi:10/gk6m4d.

[378] J. S. Seldenthuis, H. S. van der Zant, M. A. Ratner, and J. M. Thijssen. "Vibrational excitations in weakly coupled single-molecule junctions: a computational analysis". In: *ACS Nano* 2.7 (2008), pp. 1445–51. doi:10/fm82hn.

[379] R. Leturcq, C. Stampfer, K. Inderbitzin, L. Durrer, C. Hierold, E. Mariani, M. G. Schultz, F. von Oppen, and K. Ensslin. "Franck-Condon blockade in suspended carbon nanotube quantum dots". In: *Nature Physics* 5.5 (2009), pp. 327–331. doi:10/db86v5.

[380] F. Kuemmeth, S. Ilani, D. C. Ralph, and P. L. McEuen. "Coupling of spin and orbital motion of electrons in carbon nanotubes". In: *Nature* 452.7186 (2008), pp. 448–52. doi:10/fnhjnr.

[381] P. Gehring, J. K. Sowa, J. Cremers, Q. Wu, H. Sadeghi, Y. Sheng, J. H. Warner, C. J. Lambert, G. A. D. Briggs, and J. A. Mol. "Distinguishing Lead and Molecule States in Graphene-Based Single-Electron Transistors". In: *ACS Nano* 11.6 (2017), pp. 5325–5331. doi:10/f977nt.

[382] J. O. Thomas, B. Limburg, J. K. Sowa, K. Willick, J. Baugh, G. A. D. Briggs, E. M. Gauger, H. L. Anderson, and J. A. Mol. "Understanding resonant charge transport through weakly coupled single-molecule junctions". In: *Nature Communications* 10.1 (2019), pp. 1–9. doi:10/ghbshm.

[383] G. Zhou, C. Cen, S. Wang, M. Deng, and O. V. Prezhdo. "Electron-Phonon Scattering Is Much Weaker in Carbon Nanotubes than in Graphene Nanoribbons". In: *J Phys Chem Lett* 10.22 (2019), pp. 7179–7187. doi:10/gkb79v.

[384] Phaedon Avouris, Marcus Freitag, and Vasili Perebeinos. "Carbon-nanotube photonics and optoelectronics". In: *Nature Photonics* 2.6 (2008), pp. 341–350. doi:10/dpmmnw.

[385] Jacques Lefebvre, David G. Austing, Jeffery Bond, and Paul Finnie. "Photoluminescence Imaging of Suspended Single-Walled Carbon Nanotubes". In: *Nano Letters* 6.8 (2006), pp. 1603–1608. doi:10/dx8678.

[386] Adrian Nish, Jeong-Yuan Hwang, James Doig, and Robin J. Nicholas. "Highly selective dispersion of single-walled carbon nanotubes using aromatic polymers". In: *Nature Nanotechnology* 2.10 (2007), pp. 640–646. doi:10/cgw4gb.

[387] Shinichiro Mouri, Yuhei Miyauchi, and Kazunari Matsuda. "Dispersion-Process Effects on the Photoluminescence Quantum Yields of Single-Walled Carbon Nanotubes Dispersed Using Aromatic Polymers". In: *The Journal of Physical Chemistry C* 116.18 (2012), pp. 10282–10286. doi:10/f3x624.

[388] Arko Graf, Yuriy Zakharko, Stefan P. Schießl, Claudia Backes, Moritz Pfohl, Benjamin S. Flavel, and Jana Zaumseil. "Large scale, selective dispersion of long single-walled carbon nanotubes with high photoluminescence quantum yield by shear force mixing". In: *Carbon* 105 (Aug. 1, 2016), pp. 593–599. doi:10/gfz9x8.

[389] Sang-Yong Ju, William P. Kopcha, and Fotios Papadimitrakopoulos. "Brightly Fluorescent Single-Walled Carbon Nanotubes via an Oxygen-Excluding Surfactant Organization". In: *Science* 323.5919 (Mar. 6, 2009), pp. 1319–1323. doi:10/dp532k.

[390] S. Banerjee, T. Hemraj-Benny, and S. S. Wong. "Covalent Surface Chemistry of Single-Walled Carbon Nanotubes". In: *Advanced Materials* 17.1 (2005), pp. 17–29. doi:10/c5dmb3.

[391] Richard Martel. "Sorting Carbon Nanotubes for Electronics". In: *ACS Nano* 2.11 (2008), pp. 2195–2199. doi:10/dn7v6k.

[392] S. Zhao, L. Rondin, G. Delport, C. Voisin, U. Beser, Y. Hu, X. Feng, K. Mullen, A. Narita, S. Campidelli, and J. S. Lauret. "Fluorescence from graphene nanoribbons of well-defined structure". In: *Carbon* 119 (2017), pp. 235–240. doi:10/gbhgc3.

[393] John C. de Mello, H. Felix Wittmann, and Richard H. Friend. "An improved experimental determination of external photoluminescence quantum efficiency". In: *Advanced Materials* 9.3 (1997). _eprint: https://onlinelibrary.wiley.com/doi/pdf/10.1002/adma.19970090308, pp. 230–232. doi:10/c3bztm.

[394] Igor' S Osad'Ko. "Determination of electron-phonon coupling from structured optical spectra of impurity centers". In: *Soviet Physics Uspekhi* 22.5 (1979), pp. 311–329. doi:10/d32m9f.

[395] L. Yang, M. L. Cohen, and S. G. Louie. "Excitonic effects in the optical spectra of graphene nanoribbons". In: *Nano Lett* 7.10 (2007), pp. 3112–5. doi:10/dgnrtz.

[396] L. Yang, M. L. Cohen, and S. G. Louie. "Magnetic edge-state excitons in zigzag graphene nanoribbons". In: *Phys Rev Lett* 101.18 (2008), p. 186401. doi:10/dwmp6b.

[397] I. B. Mortimer and R. J. Nicholas. "Role of Bright and Dark Excitons in the Temperature-Dependent Photoluminescence of Carbon Nanotubes". In: *Physical Review Letters* 98.2 (2007). doi:10/cpsrm6.

[398] Jonah Shaver, Junichiro Kono, Oliver Portugall, Vojislav Krstić, Geert L. J. A. Rikken, Yuhei Miyauchi, Shigeo Maruyama, and Vasili Perebeinos. "Magnetic Brightening of Carbon Nanotube Photoluminescence through Symmetry Breaking". In: *Nano Letters* 7.7 (2007), pp. 1851–1855. doi:10/c4n8tq.

[399] H. Y. Fan. "Temperature Dependence of the Energy Gap in Semiconductors". In: *Physical Review* 82.6 (1951), pp. 900–905. doi:10/dcj32n.

[400] K. P. O'Donnell and X. Chen. "Temperature dependence of semiconductor band gaps". In: *Applied Physics Letters* 58.25 (June 24, 1991), pp. 2924–2926. doi:10/cdxcxq.

[401] Adam D. Wright, Carla Verdi, Rebecca L. Milot, Giles E. Eperon, Miguel A. Pérez-Osorio, Henry J. Snaith, Feliciano Giustino, Michael B. Johnston, and Laura M. Herz. "Electron–phonon coupling in hybrid lead halide perovskites". In: *Nature Communications* 7.1 (2016). doi:10/gc3hc2.

[402] S. Rudin, T. L. Reinecke, and B. Segall. "Temperature-dependent exciton linewidths in semiconductors". In: *Physical Review B* 42.17 (1990), pp. 11218–11231. doi:10/csgp8z.

[403] Annamraju Kasi Viswanath, Joo In Lee, Dongho Kim, C. R. Lee, and J. Y. Leem. "Exciton-phonon interactions, exciton binding energy, and their importance in the realization of room-temperature semiconductor lasers based on GaN". In: *Physical Review B* 58.24 (1998), pp. 16333–16339. doi:10/b3twcp.

[404] Ivan Yu. Eremchev, Arthur Yu. Neliubov, Kirill N. Boldyrev, Victor G. Ralchenko, Vadim S. Sedov, Lothar Kador, and Andrey V. Naumov. "Microscopic Insight into the Inhomogeneous Broadening of Zero-Phonon Lines of GeV– Color Centers in Chemical Vapor Deposition Diamond Films Synthesized from Gaseous Germane". In: *The Journal of Physical Chemistry C* 125.32 (2021), pp. 17774–17785. doi:10/gsfb9v.

[405] Yinjuan Huang, Fugui Xu, Lucia Ganzer, Franco V. A. Camargo, Tetsuhiko Nagahara, Joan Teyssandier, Hans Van Gorp, Kristoffer Basse, Lasse Arnt Straasø, Vaiva Nagyte, Cinzia Casiraghi, Michael Ryan Hansen, Steven De Feyter, Deyue Yan, Klaus Müllen, Xinliang Feng, Giulio Cerullo, and Yiyong Mai. "Intrinsic Properties of Single Graphene Nanoribbons in Solution: Synthetic and Spectroscopic Studies". In: *Journal of the American Chemical Society* 140.33 (2018), pp. 10416–10420. doi:10/gd4gmk.

[406] Michael S. Arnold, Jeffrey L. Blackburn, Jared J. Crochet, Stephen K. Doorn, Juan G. Duque, Aditya Mohite, and Hagen Telg. "Recent developments in the photophysics of single-walled carbon nanotubes for their use as active and passive material elements in thin film photovoltaics". In: *Physical Chemistry Chemical Physics* 15.36 (2013), p. 14896. doi:10/gcx5f4.

[407] Meidan Que, Boyue Zhang, Jin Chen, Xingtian Yin, and Sining Yun. "Carbon-based electrodes for perovskite solar cells". In: *Materials Advances* 2.17 (2021), pp. 5560–5579. doi:10/gq6qgt.

[408] Andrea C Ferrari, Francesco Bonaccorso, Vladimir Fal'Ko, Konstantin S Novoselov, Stephan Roche, Peter Bøggild, Stefano Borini, Frank HL Koppens, Vincenzo Palermo, Nicola Pugno, et al. "Science and technology roadmap for graphene, related two-dimensional crystals, and hybrid systems". In: *Nanoscale* 7.11 (2015), pp. 4598–4810. doi:10/2df.

[409] Shuo Diao, Jeffrey L Blackburn, Guosong Hong, Alexander L Antaris, Junlei Chang, Justin Z Wu, Bo Zhang, Kai Cheng, Calvin J Kuo, and Hongjie Dai. "Fluorescence imaging in vivo at wavelengths beyond 1500 nm". In: *Angewandte Chemie* 127.49 (2015), pp. 14971–14975. doi:10/f3gkst.

[410] Xuedan Ma, Nicolai F. Hartmann, Jon K. S. Baldwin, Stephen K. Doorn, and Han Htoon. "Room-temperature single-photon generation from solitary dopants of carbon nanotubes". In: *Nature Nanotechnology* 10.8 (2015), pp. 671–675. doi:10/gsfcc4.

[411] Mete Atatüre, Dirk Englund, Nick Vamivakas, Sang-Yun Lee, and Joerg Wrachtrup. "Material platforms for spin-based photonic quantum technologies". In: *Nature Reviews Materials* 3.5 (2018), pp. 38–51. doi:10/gdkgdc.

[412] S. L. Bayliss, D. W. Laorenza, P. J. Mintun, B. D. Kovos, D. E. Freedman, and D. D. Awschalom. "Optically addressable molecular spins for quantum information processing". In: *Science* 370.6522 (2020), pp. 1309–1312. doi:10/ghpgx7.

[413] Damian Bouwmeester, Talieh S. Ghiasi, Gabriela Borin Barin, Klaus Müllen, Pascal Ruffieux, Roman Fasel, and Herre S. J. Van Der Zant. "MoRe Electrodes with 10 nm Nanogaps for Electrical Contact to Atomically Precise Graphene Nanoribbons". In: *ACS Applied Nano Materials* (2023). doi:10/gsh9nm.